Improving the decision base for nuclear and radiological emergency management by modeling external radiation exposure

Hinrichsen, Yvonne

Publication date:
2019

Document Version
Publisher's PDF, also known as Version of record

Thesis for the Degree of Doctor of Philosophy
Center for Nuclear Technologies / Department of Physics
Technical University of Denmark

Improving the decision base for nuclear and radiological emergency management by modeling external radiation exposure

Yvonne Hinrichsen

To be presented for public criticism on February 25th, 2019
DTU Nutech, Roskilde, Denmark

Supervisor

Senior Scientist Kasper Grann Andersson
Center for Nuclear Technologies, Technical University of Denmark
Roskilde, Denmark

Co-Supervisor

Senior Scientist Per Roos
Center for Nuclear Technologies, Technical University of Denmark
Roskilde, Denmark

Supervisors during the external stay at Lund University

Senior Lecturer Christopher Rääf
Medical Radiation Physics, Department of Translational Medicine, Lund University
Malmö, Sweden

Researcher Robert Finck
Medical Radiation Physics, Department of Translational Medicine, Lund University
Malmö, Sweden

Opponents

Senior Scientist Erik Nonbøl
Center for Nuclear Technologies, Technical University of Denmark
Roskilde, Denmark

Professor Mats Isaksson
Department of Radiation Physics, Institute of Clinical Sciences, University of Gothenburg
Gothenburg, Sweden

Senior Physicist Jens Søgaard-Hansen
Danish Decommissioning
Roskilde, Denmark

αὐτοῦ γάρ ἐσμεν ποίημα, κτισθέντες ἐν Χριστῷ Ἰησοῦ ἐπὶ ἔργοις ἀγαθοῖς οἷς προητοίμασεν ὁ θεός, ἵνα ἐν αὐτοῖς περιπατήσωμεν.

ΠΡΟΣ ΕΦΕΣΙΟΥΣ 2,10

In memory of Bernd-Dieter Hinrichsen

* 27.05.1958 †29.10.2006

Resume

Forbedring af beslutningsgrundlaget for nukleart og radiologiskt beredskab ved modellering af ekstern strålingseksponering

I 'recovery' fasen efter en hændelse, hvor radioaktive isotoper er sluppet ud i miljøet, er værktøjer, som kan bruges til at forudsige den eksterne strålingseksponering baseret på eksisterende viden, essentielle for at retfærdiggøre og optimere strategier for modforholdsregler i forurenede beboede områder. For at demonstrere anvendelsen af Monte Carlo koden MCNP6 til dette formål blev afskærmningsfaktorer for en bygning med lette ydervægskontruktioner bestemt eksperimentelt, og sammenlignet med afskærmningsfaktorer baseret på teoretiske beregninger, som blev udført med Monte Carlo koden MCNP6. I den forbindelse blev kilder, som indeholder de gamma-emitterende radionuklider ^{60}Co og ^{137}Cs, placeret i forskellige positioner rundtomkring og oven på en modulær bygning for at repræsentere homogent nedfald. Den anvendte modulære bygning var af præfabrikeret standardtype leveret fra en kommerciel fabrikant. Gammastrålingsdetektorerne blev placeret i fire referencepositioner inde i bygningen. Resultaterne viser anvendeligheden af MCNP6 til teoretiske beregninger af scenarier med radioaktivt nedfald. Derefter blev ca. 30 år gamle beregnede kerma-konverteringsfaktorer for et standardbeboelsesmiljø genberegnet med MCNP6, og sammenligningen med de gamle værdier viste signifikante forskelle.

Da antallet af datasæt i de europæiske uheldshåndteringsbesluttningsstøttesystemer repræsenterende forskellige typer beboelses miljøer er begrænset, blev disse udvidet med beregniger for en ny, væsentlig form for beboelse. En model af et moderne kontor- eller boligbyggeri med glasfacader blev udviklet og opstillet med elleve forskellige bygningshøjder. Kerma-konverteringsfaktorer for etagerne inde i bygningen i forhold til stråling fra kontamination på forskellige overflader blev bestemt for de primære gamma-energier 0,3 MeV, 0,662 MeV og 3,0 MeV og for tre forskellige beboelsesmiljøscenarier ved anvendelse af MCNP6. Kerma-konverteringsfaktorerne blev udtrykt som formler for hver type overflade, hvor radioaktive stoffer kan deponeres. Betydningen af de derved bestemte faktorer blev illustreret ved sammenligning med tidligere almindeligt anvendte

faktorer for fleretagers husblokke.

I forbindelse med den videre anvendelse af kerma-konverteringsfaktorerne er kendskab til den miljømæssige opførsel af deponerede radioaktive materialer nødvendig for at forudsige den eksterne strålingseksponering. Det er her nødvendigt at estimere den relative fordeling af de radioaktive stoffer på forskellige typer overflader i miljøet efter deponering og de resulterende dosishastigheder for mennesker, som opholder sig i miljøet. De seneste parametriske forbedringer til brug i de europæiske beslutningsstøttesystemer for konsekvenshåndtering efter udslip er rapporteret. Disse viser en betydelig variation i forhold til den fysisk-kemiske form af de deponerede materialer. Det blev illustreret for et standardmiljø, at deponerede radioaktive stoffer på taget er af stor betydning for dosis til mennesker inde i bygningen.

For også at muliggøre estimering af tidsintegrerede eksterne doser til personer, som opholder sig i et miljø, som er blevet radioaktivt forurenet, behøver man yderligere viden om migration af forskellige slags af deponerede stoffer på de forskellige relevante typer miljøoverflader. Migrationsprocessen, som er modelleret dynamiskt i de europæiske beslutningsstøttesystemer, er beskrevet og de nyeste parametriske datasæt for disse modeller er præsenteret. Det forklares, hvordan modellerne kan bruges til at estimere doser, som befolkningen i radioaktivt kontaminerede beboede områder modtager med tiden fra deponerede radioaktive stoffer. Det blev vist for et standardmiljø, at udover kontaminering på hustaget, bidrager også kontaminering på jord/græsarealer betydeligt til den tidsintegrerede dosis til mennesker inde i bygningen.

Med fokus på bygningers skærmende effekt mod stråling fra forskellige retninger, udførtes en serie Monte Carlo beregninger, som giver detaljeret information om dosisbidragene forskellige steder i en bygning fra kontaminede udendørs områder. Konceptet isodosis blev udviklet for at optimere dekontamineringsaktiviteter, og blev anvendt i form af isodosislinjer, som definerer den ydre grænse af de mindste områder, hvor dekontaminering af områder omkring bygningen resulterer i en given dosisreduktion. Formen og positionen af isodosislinierne afhænger af bygningens geometri, vægtykkelsen og materialet og observationspunktet inde i bygningen. Beregninger gennemførtes med en kilde-overfladeopløsning på 1 m^2 for fire observationspunkter i en modulær bygning under antagelse af en deponering af henholdsvis ^{137}Cs og ^{60}Co på jordoverfladen. Geometriafskærmning blev identificeret som den væsentligste indflydelse på størrelsen af arealer omfattet af isodosislinierne, og barriereafskærmning som den væsentligste indflydelse på formen af isodosislinierne.

Yderligere blev isodosiskonceptet anvendt på typiske svenske boliger. Indflydelsen af træ og mursten som almindelige byggematerialer og betydningen af dør- og vinduespositioner for isodosislinierne blev demonstreret for specifikke positioner inde i husene

og for de hele huse, under antagelse af at beboerne har en typisk opholdsadfærd. Dekontaminering af arealer inden for isodosislinier er påvist at give en øget dosisreduktionseffekt sammenlignet med dekontaminering af et tilsvarende jordareal til en vis afstand omkring huset. Yderligere blev indflydelsen af den vertikale migration af deponerede materialer i jorden på isodosislinierne undersøgt, hvilket viser, hvordan de zoner, som er omfattet af isodosislinierne, bliver mindre over tid, efterhånden som de deponerede stoffer migrerer dybere ned i jorden. De resulterende isodosislinier og graden af deres transformation er domineret af nedtrængningen af kontamineringen i toplaget af jorden. Indflydelsen af naturlige variationer i kontamineringsgraden på isodosislinierne blev demonstreret med sin afhængighed af byggematerialer. Isodosiskonceptet ser således ud til at kunne blive et nyttigt instrument i forbindelse med optimering af modforholdsregler i radioaktivt kontaminerede beboede områder.

Abstract

Improving the decision base for nuclear and radiological emergency management by modeling external radiation exposure

In the recovery phase after a radioactive release incident, tools predicting the external radiation exposure based on existing knowledge are essential for justification and optimization of recovery countermeasure strategies for contaminated inhabited areas. To justify the application of the Monte Carlo code MCNP6 for this purpose, experimentally determined shielding factors for a common light construction dwelling type were obtained and compared to shielding factors based on theoretical calculations performed using the Monte Carlo code MCNP6. Therefore, sources of the gamma-emitting radionuclides ^{60}Co and ^{137}Cs were positioned around and on top of a modular building to represent homogeneous fallout. The modular building used was a standard prefabricated structure obtained from a commercial manufacturer. Four reference positions for the gamma radiation detectors were used inside the building. The results demonstrate the applicability of using MCNP6 for theoretical calculations of radioactive fallout scenarios. Subsequently, about 30 years old kerma conversion factors for one standard environment were re-calculated with MCNP6, showing significant differences compared to the old values.

As the number of data sets for different inhabited environments is limited, the estimation of external gamma irradiation from deposited radioactivity in urban environments was improved by developing a model of a modern office or residential building with glass facades which was set up with eleven different building heights. Kerma conversion factors for the floors inside the building from contamination on different types of surfaces were determined by using MCNP6 for the primary gamma energies 0.3 MeV, 0.662 MeV and 3.0 MeV and for three different environmental scenarios. The kerma conversion factors were expressed as formulas for each possible deposition area for contaminants. The importance of the determined factors was shown by comparing them to previously generally used factors for multistory house blocks.

In connection with the the kerma conversion factors knowledge on the environmental behavior of radiocontaminants is needed for predicting external radiation exposure. Therefore, one necessary requirement is to estimate the relative initial contaminant distribution on different types of surfaces in the environment and the resultant initial dose rates to humans staying in the environment. The latest parametric refinements for the use in the European emergency management decision support systems are reported, showing a considerable variation according to the physicochemical form of the contaminants. It was shown for a standard environment that contaminants deposited on the roof are of major concern in contributing dose to humans inside the building.

To also enable estimation of time-integrated external doses to persons staying in an environment that was radioactively contaminated, additional knowledge on the postdeposition migration of different types of contaminants on the various relevant types of environmental surface is needed. The migration process as it is modeled dynamically in the European decision support systems was described and the newest parametric datasets for these models reported. It is explained how the models can be used to estimate doses received over time by populations in radioactively contaminated inhabited areas in connection with the initial contaminant distribution. It was shown for a standard environment that additionally to the roof also contaminants deposited on a unpaved ground are of major concern in contributing dose to humans inside the building.

Focusing on the shielding effect of a building against radiation from various directions, further Monte Carlo simulations were applied that also give information on the dose contributions at various locations inside the building from specific areas outside. The concept of the isodose was developed to optimize decontamination activities, and was applied as isodose lines to define the smallest areas that lead to a certain dose reduction through decontamination of areas surrounding the building. The shape and position of the isodose lines depend on the geometry of the building, the wall thickness and material, and the observation point inside the building. Calculations have been made with a surface resolution of 1 m^2 for four observation points in a modular building, assuming depositions of ^{137}Cs and ^{60}Co on the ground surface. Geometry shielding was identified as main impact on the size of areas encompassed by the isodose lines and barrier shielding as main impact on the shape of the isodose lines.

Moreover, the isodose concept was applied to typical Swedish residential houses. The influence of wood and brick as common building materials and the importance of the positions of doors and windows on the isodose lines were demonstrated for specific positions inside the houses as well as for the entire houses assuming people having a typical residential behavior. Decontamination of areas within isodose lines is demonstrated to provide an increased dose reducing effect compared to decontaminating an equal area of soil to a certain distance around the house. Furthermore, the impact of vertical con-

taminant migration in soil on the isodose lines was studied, showing how the zones that are encompassed by the isodose lines are getting smaller over time as the contaminants migrate deeper into soil. The resulting isodose lines and the degree of their transformation are dominated by the downward movement of the contamination in the topsoil layer. The impact of contamination variability on the final result was demonstrated with its dependence on building materials. Thus, the isodose concept shows promise for becoming a useful tool for the optimization of countermeasures in cases of radioactive fallout in populated environments.

Preface

The work for this thesis was mainly carried out at the section for Radioecology of the Hevesy Laboratory at the Center for Nuclear Technologies at the Technical University of Denmark from 2015 to 2018. The respective PhD school was the Department of Physics of the Technical University of Denmark. Furthermore, parts of the work were carried out within a four month external in 2017 in the group for Medical Radiation Physics at the Department of Translational Medicine at Lund University, Sweden.

Yvonne Hinrichsen
Roskilde, December 2018

Acknowledgements

When I look back on the past three years, I am very grateful for all the experiences and persons that have allowed me to grow scientifically and personally. The following lines can only express a small share of my appreciation for all the things you have done and are for me.

First of all I want to thank my supervisor Kasper for all your work that you put in the success of my PhD studies. I have gained a lot from your experience and knowledge and I am thankful for all the care I received from you not just scientifically but also in many other ways. You definitely have done more for me than you have had to and as Eckart Witzigmann said: 'The student can only be as good as the teacher' - I have had the best teacher I can imagine.

Beyond an amazing main supervisor, I had Per as a brilliant co-supervisor. Thank you for always jumping in when Kasper has not been available, but also for raising my awareness about many things I have not thought about so far and taking care about that everything stayed on track. Moreover, I want to thank my supervisors Christopher and Robert during my external stay at Lund University for making it as convenient as possible, but also for all your valuable ideas and input to my work as well as allowing me to take part in really interesting projects and giving me a future perspective.

Furthermore, I like to thank my other colleagues at the Radioecology section, beginning with Jixin for keeping our bunch of different people with different backgrounds together and emphasizing on a friendly working atmosphere, followed by Helle, and Birgitte for magically solving all the problems that are beyond my capabilities, Claus for making sure that my bike has always been in perfect condition and showing me the beauty of Roskilde Fjord, Liga, Kristina, Lise, and Hanne for helping me improve my Danish, as well as my German sidekick Gunnar, Nikola, the one who went before me, Liuchao and Mu who came after me, Szabolcs, Cobus, Yusuf, Sven, Xiaolin, and our guests Dongxia and Xue.

Moreover, I like to thank my family at the First International Baptist Church of Copenhagen including Jessica for sharing the ‘Thesis-summer’ with me, all your precious thoughts and sense of humor, Anne for your unique mixture of playfulness and deep thoughts, Chris and Ira for your hospitality including physical and spiritual food, Jeroen for just being who you are, Shin-Young for your warm-hearted being, Ana for being one of the most giving persons I have ever met, Irashka for being so welcoming and connecting, Hartzel for being one of the cutest persons I have ever met as well as Dongah, Ida, Kelly, Dorotea, Emma, Keethe, Lenti, Nefeli, Adina, Lu, Ann, Fon, Guin, Évelyne... for all the enjoyable get togethers and a lot more.

Further I like to thank my friends that I have met while trying to keep the balance to all the brain work through dancing at Sceneindgangen. These are in particular Jenny for being an even better friend than teacher and for having become more to me than I imagined, my Shervonnija-sisters with Cija for sharing the Indian Groove and a lot more with me, and Sherwin for making me feel like being part of your family, Erato for allowing me to let the serious part of my life behind me every once in a while, Anastasia for making me feel a little less crazy in what I do, Lene for giving me lots of reasons to laugh, Andreea for really always being willing to chat with me as well as Celina, Hanna, Annette, Evi, Nadia, Andrea, Staša, Tuuli, Mette, Maria, Alix, Laisa, Susanne, Tine, Thomas, Deborah, Sarah, Amanda, Stephanie... for uncountable smiles and good conversations.

Before ending I want to express my gratefulness to my parents for providing me with everything that I needed to find my own way in life, my favorite brother Michael for being my constant companion in better and worse times, Birte and Harald for giving me a second home, Marcel for being a real gentleman, Dominik for your sense of humor, my family at Friedenskirche Lübeck for providing me a save place to grow from, Myriam for being the best friend in the worst times of my life, Tracey for our everlasting connection, Gaby for being some sort of foster mother to me, and Elly and Theresia for friendship beyond physical and temporal distances.

Thank you very much! Vielen Dank! Tusind tak!

List of publications

This thesis is based on the work contained in the following Papers:

I. Hinrichsen, Y., Finck, R., Östlund, K., Rääf, C., Andersson, K. G., Comparison of experimental and calculated shielding factors for modular buildings in a radioactive fallout scenario. Journal of Environmental Radioactivity 189 (2018) 146-155.

II. Hinrichsen, Y., Finck, R., Rääf, C., Andersson, K. G., Introducing the concept of the isodose for optimization of decontamination activities in a radioactive fallout scenario. Journal of Radiological Protection 38 (2018) 1293-1310.

III. Hinrichsen, Y., Andersson, K. G., Kerma conversion factors for modern urban glass buildings in radioactively contaminated areas. Accepted for publication by Journal of Radiological Protection.

IV. Hinrichsen, Y., Andersson, K. G., European decision support modelling of long-term external doses received in inhabited areas contaminated by a nuclear power plant accident - 1: initial relative dose rate contributions from different contaminated outdoor surfaces. Submitted to Journal of Environmental Radioactivity.

V. Hinrichsen, Y., Andersson, K. G., European decision support modelling of long-term external doses received in inhabited areas contaminated by a nuclear power plant accident - 2: post deposition contaminant mobility on outdoor surfaces. Submitted to Journal of Environmental Radioactivity.

VI. Hinrichsen, Y., Finck, R., Martinsson, J., Rääf, C., Andersson, K. G., Influence of the migration of radioactive contaminants in soil, resident occupancy, and variability in contamination on isodose lines for typical Swedish houses. Submitted to Scientific Reports.

In particular Section 2.1 is based on Paper I, Section 2.2 on parts of Paper IV, Chapter 3 on Paper III, Section 4.1 on the other parts of Paper IV, Section 4.2 on Paper V, Section 5.1 on Paper II, and Section 5.2 on Paper VI.

Contents

List of Abbreviations

AM	Arithmetic Mean
AMAD	Activity Median Aerodynamic Diameter
ARGOS	Accident Reporting and Guiding Operational System
DSS	Decision Support System
ERMIN	EuROpean Model for INhabited areas
GM	Geometric Mean
GSD	Geometric Standard Deviation
GSF	Gesellschaft für Strahlen- und Umweltforschung (now Helmholtz Zentrum München, German Research Center for for Environmental Health)
IAEA	International Atomic Energy Agency
ICRP	International Commission on Radiological Protection
MCNP	Monte Carlo N-Particle code
NPP	Nuclear Power Plant
OCD	Office of Civil Defence
RASTEP	RApid Source TErm Prediction
RODOS	Realtime Online DecisiOn Support
SD	arithmetic Standard Deviation
SOC	Soil Organic Carbon

Chapter 1

Introduction

Prior to 1986, it was in general thought that any significant airborne environmental contamination resulting from nuclear power plant accidents would be restricted to rural areas very near the power plant. However, the Chernobyl accident demonstrated that inhabited environments and even cities at considerable distances from the release point could become strongly affected. On the basis of the measurements and learning points after the Chernobyl accident, relatively simple calculation models were soon created to enable rough estimation of the external doses to urban and suburban populations (e.g., Crick & Brown 1990, Andersson 1990). When the much more comprehensive map based decision support systems ARGOS (Hoe et al. 2009) and RODOS (Ehrhardt et al. 1996) were developed, which are today integrated in the preparedness in practically all European countries as well as in, e.g., Canada, Brazil and Australia, essentially these models were first integrated. Furthermore, it was recently published (Howard et al. 2017) that the long term ingestion and external dose contributions received by inhabitants of areas contaminated by the Chernobyl accident was estimated to be about equal in magnitude, whereas the long term external dose contribution to the public in areas contaminated by the Fukushima accident has been estimated to be of the order of 80-90 %, and the corresponding ingestion dose only 10-20 %. In preparedness for possible future nuclear power plant accidents, it is thus highly important to be able to implement effective recovery strategies for contaminated inhabited areas.

The common model for external dose estimation in inhabited areas in the ARGOS and RODOS systems is the ERMIN model which was co-developed and coded at Public Health England (Charnock 2018, Andersson et al. 2009, Charnock et al. 2009). The model comprises the estimation of deposition of contaminants as it may be useful for several purposes in nuclear emergency management decision support, including rough early phase external dose prognoses when local measurements of deposits on different

representative surfaces have not yet been made, drills and competence building training sessions to assess possible consequences of different contamination scenarios and possibly to dimension an operational preparedness accordingly. It further includes a system of formulae reflecting the post deposition mobility of radiocontaminants on the different types of outdoor surface (Andersson 2009*a*, Andersson et al. 2002, Jones et al. 2007).

Another part of external dose estimation takes into account the shielding of gamma radiation by buildings as it can reduce the radiation exposure of the population and sheltering of inhabitants is one of the principal countermeasures considered for areas potentially affected by radioactive release. Thus, detailed knowledge of the shielding properties of buildings is therefore an important component of risk assessment in radiological emergency preparedness. As the geometry of building structures is too complex for simple methods such as the point kernel model (Spencer et al. 1980), Monte Carlo calculations are needed to calculate shielding factors as shown in a comparison performed by Jensen & Thykier-Nielsen (1989). The shielding properties can vary greatly for different types of buildings (e.g., Finck 1991) leading to the use of Monte Carlo simulations in the late 1980s at the GSF (now the Helmholtz Zentrum München – German Research Center for Environmental Health) (Jacob & Meckbach 1987, Meckbach & Jacob 1988, Meckbach et al. 1987, 1988). An early Monte Carlo code SAM-CE (Lichtenstein et al. 1979) was applied to calculations for four different types of houses. Inhabited area external dose estimates in the European standard decision support systems ARGOS and RODOS rely entirely on these few old datasets. Further Monte Carlo simulations were performed for an industrial area (Kis et al. 2003, 2004), for various scenarios of U.S. residential structures (Dickson & Hamby 2014, 2016, Dickson et al. 2017), for typical houses in Brazil (Salinas et al. 2006), and typical buildings in Japan (Furuta & Takahashi 2015).

The first step of this thesis is thus to prove the applicability of the Monte Carlo code MCNP6 (Goorley et al. 2012) for theoretical calculations of radioactive fallout scenarios. On this basis this thesis aims to improve nuclear and radiological emergency preparedness by adding new datasets for modern types of buildings to inhabited area external dose estimation as well as connecting them with data of initial relative contamination levels and post deposition mobility for different surfaces and radiocontaminants of different physicochemical properties. As the final part of this thesis a new approach for optimizing of decontamination activities will be introduced including an analysis of possibly influential parameters.

The following sections of this introduction will introduce to airborne radioactive contamination in general (Section 1.1), deal with the terminology regarding the shielding of buildings (Section 1.2), and describe the basic principle of Monte Carlo calculations with focus on the Monte Carlo code MCNP6 as it was employed in the work for this

thesis (Section 1.3).

1.1 Airborne radioactive contamination

The deposition of the contaminants is greatly dependent on their physicochemical properties and the types and orientations of the surfaces in the inhabited area to which the deposition occurs (Andersson 2009*a*). Thus, it should be considered which physicochemical forms the various likely contaminants from a major NPP (nuclear power plant) accident could be expected to have. A 'consensus' list of contaminants considered potentially important by Slovakia, France, Germany, Finland, Czech Republic and USA for evaluation of radiological consequences in case of severe NPP accidents comprises (apart from noble gases) radionuclides of the following elements: Am, Ba, Ce, Cs, Cm, I, La, Mo, Nb, Np, Pu, Rb, Ru, Sb, Sr, Te and Zr (Andersson 2016). The physicochemical forms of these in future accidental releases will depend on a complex of processes and conditions during the release, and are difficult to predict. However, the experience from history's two large nuclear power plant accidents, the Fukushima and the Chernobyl accident, provide very useful information on what might be expected in some different types of scenarios, and for instance which sizes, materials and thus aerodynamic behavior the produced aerosols might be expected to have under different conditions.

In addition to the deposition, there are also a range of publications that describe post-deposition transfer and natural removal of radiocontaminants that deposited in inhabited areas. Many of these are based again on studies of contamination from the Chernobyl accident. Unfortunately, measurements have not been made of the post-deposition migration of radioactive matter from the Fukushima accident on each of the various types of man-made surfaces representative of inhabited areas. Instead, the focus of the Japanese authorities has been on rapid carborne surveillance of dose rate in affected areas using KURAMA II detection systems (Kinase et al. 2015), which measure an uncollimated dose rate in a position close to the road surface. This provided valuable rough indications of the contamination pattern over large land areas. In relation to the actual average exposure of the local population, however, this measurement geometry would give an overrepresentation of the radiation from the nearby contaminated street surface. And since the natural decline in radioactivity on street surfaces has previously been found to be comparatively very rapid (Andersson 2009*a*), such repeated measurements would lead to overestimation of the rate at which the average dose rate declines in the area through natural processes. Qualitatively, however, these Japanese measurements illustrate that the decline in dose rate is as expected faster in urban areas, comprising surfaces with rapid natural weathering processes, than in rural areas, where the decline in dose rate level is largely dependent on the slow downward contaminant migration in soil (Kinase et al. 2015).

1.2 Shielding factors

Buildings naturally provide some shielding against radiation from the ground and from miscellaneous contamination of all outdoor surfaces (including soil, roofs, walls, windows and pavements), vegetation, and in the air (primary contaminant plume or resuspended radioactive matter). The degree of protection depends on the building material, its thickness and density and on the geometry of the building. Furthermore, it depends on the distribution of the source of radiation around the building, on the building and if any part of the source is also present inside the building. The protection can be described as a dose reduction effect. Several different, and sometimes confusing, terms have been used to describe the shielding effect of a building. The terms used in this thesis follow the terminology originally defined by Spencer (1962) and described in the OCD manual (OCD 1962) with some additions.

To quantitatively measure the effectiveness of shielding afforded by structures, by one structure relative to another, or one location in a structure relative to another, a standard 'unprotected' position is needed for comparison. Spencer (1962) assumed in the absence of specific information for a present radioactive fallout situation that the fallout is uniformly distributed horizontally over the exposed surfaces. Therefore, the standard D_0 or reference value was defined by the detector response at a point 1 m (originally 3 feet) above an infinite, smooth, uniformly contaminated plane.

The 'reduction factor' R was defined as

$$R = \frac{D}{D_0} \tag{1.1}$$

where D is the detector response in a protected position (e.g. inside a building), which is divided by the reference value D_0. Furthermore, the inverse of the reduction factor was termed 'protection factor' P, but is not employed in this thesis.

The reduction factor comprises two types of attenuation factors. The first factor is called the geometry shielding factor S_{geom} and can be seen as the exposure reduction effect of a building with its materials being replaced by air. The reduction here is caused by the assumption that the ground area and floors inside the building are clean from radioactive contamination or can be also caused by moving the detector further away from the contaminated area, e.g. by moving it to a higher floor. The geometry shielding factor S_{geom} is thus defined by the detector response at a certain position inside a building with its materials being replaced by air D_{geom} divided by the the reference value D_0:

$$S_{geom} = \frac{D_{geom}}{D_0} \tag{1.2}$$

The second factor is called barrier shielding factor S_{barr} and describes the reduction caused by the interaction of the radiation with the materials that the building is made of. The barrier shielding factor S_{barr} is thus defined by the detector response at a certain position inside a building D (protected position) divided by the the detector response at the same position inside the building with its materials being replaced by air D_{geom} as introduced for the geometry reduction:

$$S_{barr} = \frac{D}{D_{geom}} \tag{1.3}$$

Multiplying the geometry shielding factor with the barrier shielding factor leads to a total shielding factor of a building S_{bld} at a specific position inside it that equals the reduction factor R defined in Equation (1.1):

$$S_{bld} = S_{geom} \cdot S_{barr} = \frac{D_{geom}}{D_0} \cdot \frac{D}{D_{geom}} = \frac{D}{D_0} = R \tag{1.4}$$

1.3 Monte Carlo code MCNP6

The basis of the principle of the Monte Carlo method for particle transport is that a large number of particles are generated by a random source. Its principle is presented in Figure 1.1 an can be seen as a numerical experiment. The code follows each particle (exclusively photons for the calculations described in this thesis) from its source throughout its life interacting with media to its death in a terminal category like e.g. absorption or escape including possible secondary particles. The basic principle of the Monte Carlo method is the random selection of physical parameters according to given distributions for media m, energies E and directions Ω at a certain position r of each particle based on cross section data and physical models. The result is obtained by averaging over the scores of all particles with their paths and interaction histories that were calculated for the respective source and thus accompanied by a statistical uncertainty.

The Monte Carlo calculations for this thesis were performed with the transport code MCNP6 (Goorley et al. 2012), using the nuclear cross-section data set ENDF/B-VII.0 (Chadwick et al. 2006). Among other processes, it accounts for photon creation and loss through relevant mechanisms such as bremsstrahlung, fluorescence, Compton scattering, photon capture, pair production and p-annihilation. The code allows for the definition of complex 3-dimensional geometries through a combinatorial geometry technique. The regions in space were constructed by a logical combination (union, intersection, difference) of elementary geometric bodies and surfaces. Material specifications with definite atomic compositions and densities have to be assigned to the input for the different building structures and environmental regions.

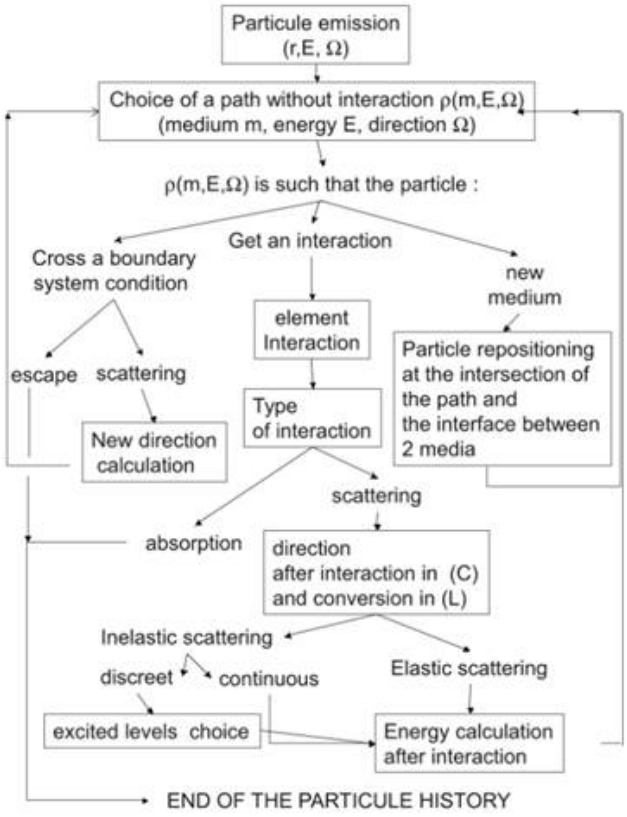

Figure 1.1: Flow chart of the calculation scheme of the Monte Carlo method used for the tracking of particles (Antoni & Bourgois 2017).

The geometry and the energy of sources were defined according to applied problem and are described in the respective chapters. This is also the case for position and size of the detector regions (called tally in MCNP). In the detector regions, the number and energies of the gamma 'particles' passing through are scored. By using conversion coefficients (ICRP 2010), the fluence was transferred to air kerma free-in-air. Furthermore, the code provides ten statistical tests that are performed on each defined detector region. Those tests are a valuable tool to ascertain reliable statistical quality of the respective results.

Furthermore, several techniques can be applied to reduce the variation in the results with acceptable computation times in MCNP6. The defined regions in space are called cells, and for some of the models weight windows were generated for each cell. The number of a particle's weight in MCNP6 represents the number of physical particles, which in the calculations this thesis were photons, where different random walks are represented by one MCNP particle. A lower bound on the weight of particles in each cell is defined by the user, and the upper weight bound is a specified multiple of the lower bound. These weight bounds define a window of acceptable weights. If the weight of a particle emitted from the source and generated by interactions with the materials is below the lower weight bound, then the weight of the particle is randomly increased to a value within the window, or it is not included in the calculations. If the weight of a particle is above the upper limit, it is split so that its parts are within the window. No action is taken for particles with weights within the window. The weight windows were determined using the Weight Window Generator, which estimates the importance of the cells in space. The importance of cells is defined as the expected score generated by a unit weight particle after entering the cell. The average importance of each cell can be estimated using the cell-based generator.

Chapter 2

Proving the method

2.1 Comparing MCNP6 with experimental results for a modular building

2.1.1 Description of the experiment and of the corresponding calculations

This thesis focuses on the modeling of external radiation exposure in emergency situations and one main part of it is the determination of the dose at various locations caused by radioactive sources of different kinds. For this purpose the Monte Carlo code MCNP6 (Goorley et al. 2012) that was described in Section 1.3 was employed. To study the applicability of the code in determining exposure reduction for buildings, a comparison of numerical simulation results from a theoretical calculation with practical measurements in a modular building geometry was performed by using point sources of ^{137}Cs and ^{60}Co distributed over an area of about 800 m^2 around the building to mimic a surface deposition. The comparison study was performed for a lightweight prefabricated modular building which was selected because this type of construction is not uncommon in Scandinavia as solutions for kindergartens, office-complexes and habitation in areas with rapid population growth. Another aspect of this type of building is the poor shielding provided by the light walls, and it is therefore of special concern in emergency preparedness. ^{137}Cs was chosen as it has been of main concern in connection with the Chernobyl and Fukushima incidents (Imanaka et al. 2015) and it furthermore is also represented among those important high-activity sealed sources that could become dispersed in an accident or as a consequence of a terrorist attack (Andersson et al. 2008). However, this study also considered ^{60}Co as a representative of higher-energetic sources, as it also is directly relevant to plausible terrorism scenarios (Ferguson et al. 2003).

The focus was on the barrier shielding factors considering contamination on outdoor horizontal surfaces (ground and roof). In fallout scenarios where the deposition mainly has arisen from rainout or washout of fission products from the passing plume, radionuclides on the ground and on the roof of buildings can be expected to contribute significantly to the total dose (Andersson 2009*b*), although buildings naturally also protect against radiation from contamination, e.g., on all vertical surfaces, on other indoor surfaces, on vegetation and in the air (primary contaminant plume or resuspended radioactive matter).

To experimentally determine the barrier shielding factors as described in Equation (1.3) by measuring dose rates with a dose rate instrument, it is necessary to separate the natural background component as defined by IAEA (IAEA 2007) from the signal originating from a specific radiation source. This is done in two steps. First, the natural background is measured both inside the building and outside using one location as a reference. Then, the shielding factor for the radiation from the source is calculated from the relationship

$$S_{barr} = \frac{\dot{D} - \dot{D}_{bgd}}{\dot{D}_{geom} - \dot{D}_{bgd,geom}} \tag{2.1}$$

where $\dot{D}$ and $\dot{D}_{geom}$ are the total measured absorbed dose rates inside the building and outside at the location chosen as reference with the radiation sources present. $\dot{D}_{bgd}$ and $\dot{D}_{bgd,geom}$ are the dose rate contributions from the natural background in the building and outside at the location chosen as reference as measured in the absence of the source.

The applied modular building consisted of two standard office modules with outer measurements 900 x 330 x 300 cm (L x W x H) rented by the company Bilsby® , that were fitted together side by side (Figure 2.1). The modules were placed in an open field (>100 m clear in all directions) and raised with wooden beams from the uneven ground to make them level. Each module had one window on each short side and one door on each long side. The outer dimensions of the windows were 140 x 120 cm (W x H) and of the doors 90 x 200 cm (W x H), so the fraction of windows was about 7% of the wall surface of the entire modular building and that of the doors was about 4%. The outer wall thickness was 12.5 cm and it consisted mainly of wood and mineral wool. The combination thus had four windows, two doors, and one opening between the modules. The inner wall thickness was 25 cm. Inside one of the modules an “inner room” of lightweight expanded clay aggregate (LECA) was set up (Figure 2.2) to investigate the impact of heavier material for constructing buildings. This room had a wall thickness of 15 cm, height of 152 cm, and outer dimensions of 103 x 88 cm due to the sizes of the used bricks.

Dose rate instruments (Automess Dose Rate Meter 6150 AD 6/H with a plastic scin-

Figure 2.1: Setup of the modular building

tillator probe 6150 AD-b/H) were used to experimentally determinate the dose rates. They were calibrated to the ambient dose rate, H*(10), according to the ICRP definition (ICRP 2010). This is the absorbed dose rate at a point 10 mm below the surface in the 300 mm diameter ICRU sphere (consisting of tissue-equivalent matter) subjected to a parallel and aligned radiation field. One detector was calibrated by the Swedish Radiation Safety Authority (SSM) for calibration factors regarding the ambient dose rate equivalent, H*(10), and the angular efficiency (30^o, 60^o, and 90^o) for ^{241}Am, ^{137}Cs, and ^{60}Co. The calibration factors for the other detectors were determined by placing a source at 1 m distance from the center of a scintillator crystal at 0^oin a low background level room, with the calibrated detector as a reference instrument for ^{60}Co and ^{137}Cs. The deviations were within a range of 10%. It is assumed that the ratio of ambient dose, with and without shielding, at a given observation point, is the same as the corresponding ratio of the absorbed dose at that point. In the same low-background-level room, sources were also placed at 30^o, 60^o, and $90^o$to assess the angular efficiency. The results of those measurements were within a range of 6%. Four detectors were positioned inside the modules (Figure 2.2) and one detector outside, about 14 m away from the modules. All detectors were placed 1 m above the floor surface in the modules. The bottom level of the modules was 26 cm beneath the floor surface and was used as ground surface, as the ground was uneven and thus the modules had to be put on beams.

^{137}Cs and ^{60}Co point sources as well as one point source with physical diameter <10 mm of ^{60}Co were used in the experiments. The respective details including uncertainties

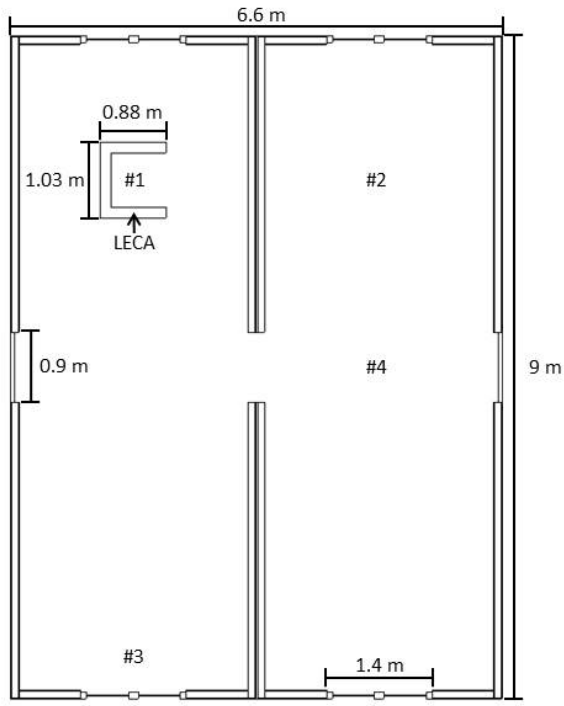

Figure 2.2: Detector positions inside the modular building. The top and bottom wall have two windows each. The left and right wall have one door each, and there is a doorway connecting both modules where the modules are fitted together. The U-shape in the top-left corner represents the clay brick structure (LECA).

are presented in Table 2.1.

The measurement scheme used in the study followed a grid system that was 29 m x 26.5 m, as represented in Figure 2.3 for the source positions. The red grid in Figure 2.3 represents a distance between the source points of 4 m and the blue grid represents a subdivision of the red grid to a distance between the source points of 2 m. Every crossing between the red, blue, and red-blue lines in the figure represents a source point. Thus, the frequency of source points is higher along the short side of the module configuration in order to reduce systematic uncertainties for measurements of radiation penetrating the windows. The 4 m density of source points is also too coarse for measuring the barrier shielding factor on the roof; hence, it was decreased to a 2 m frequency as seen by the

Table 2.1: Sources used for the measurement of barrier shielding factors. The uncertainties represent a coverage factor of k=2.

Radionuclide	Source number	Activity in MBq
^{137}Cs	1	1400 ± 200
	2	880 ± 80
	3	850 ± 150
^{60}Co	4	6100 ± 1600
	5	45 ± 4
	6	45 ± 4
	7	94 ± 9
	8	94 ± 9

crossings of the red, blue, and red-blue lines in Figure 2.3. The height of the positioned sources was chosen to be on a plane that would have been level with the ground if the modules were placed on a level ground surface.

To calculate the barrier shielding factor, the background values for all detectors and their respective positions were recorded daily prior to the measurements with the sources present. These values were eventually subtracted from the instrument reading of the source points. The ambient dose rate was also corrected with the calibration factors and the angular efficiencies via a calculation of the incident angle from each source point.

The $H^*(10)$ rates measured with the detector outside the modules were also corrected using the same method mentioned above (subtraction of measured background values and correction with calibration factors and angular efficiencies). Ambient dose rates for different source points were compiled and the data set was used to fit a mathematical expression that displayed $H^*(10)$ as a function of distance. This expression was then used to extract the reference $H^*(10)$ for the exact distance from each detector to each source point. The measured $H^*(10)$ from each source point and each detector was then divided by this value to determine the barrier shielding factor.

Measurements for the following four setups were performed:

Setup 1: All 92 grid points on the ground according to Figure 3 were measured with three ^{137}Cs point sources totaling 3.1 GBq (Sources number 1-3 in Table 2.1) placed in a 200 mL plastic container (inner wall $\varnothing$ = 67 mm and inner wall thickness = 1.9 mm). This container was placed on a height-adjustable tripod in order to place the sources in the measurement plane.

Setup 2: ^{137}Cs measurements were taken of the 15 grid points on the roof of the

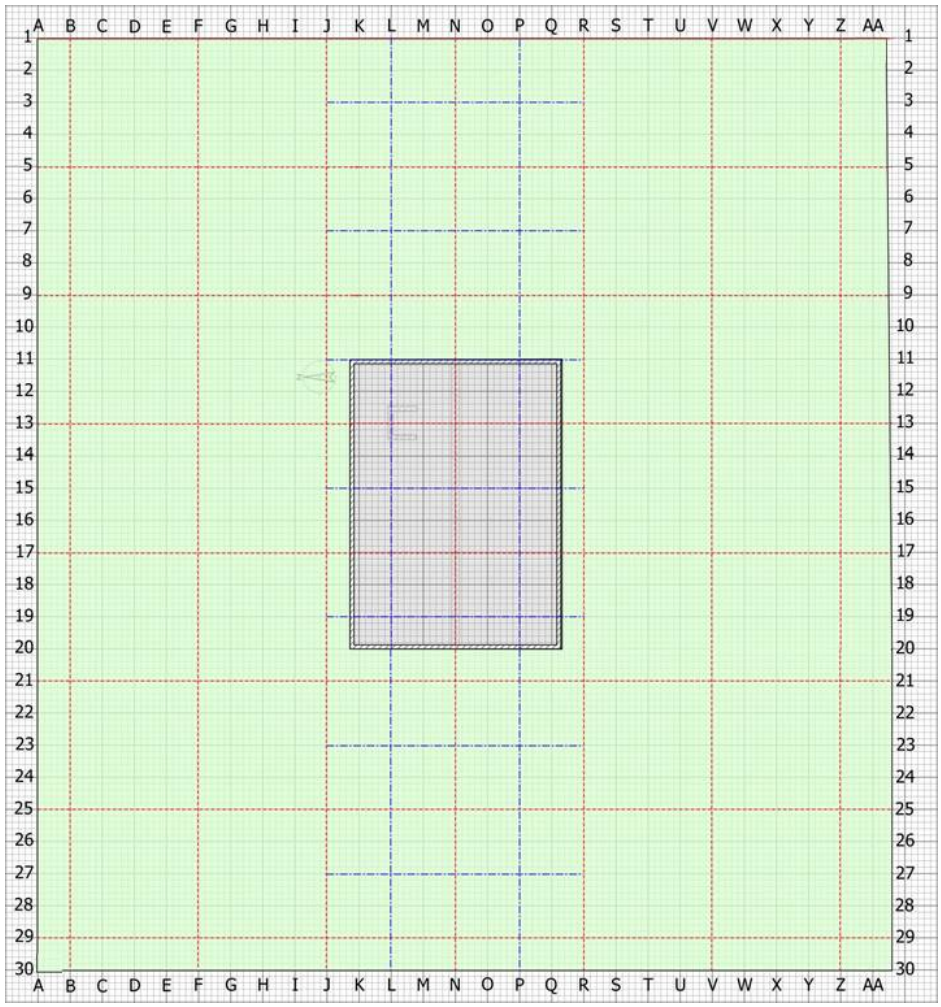

Figure 2.3: Schematic overview of the measurement grid. All crossings of red and blue lines indicate source position points. The width of one row and column represented by the letters and numbers at the frame is 1 m.

modules (L11 to P19 in Figure 2.3). The scintillators were now re-oriented so that their front surfaces were directed towards the ceiling of the building, instead of downwards as in the previous experiments with the center of the plastic crystal remaining 1 m above the floor surface. For these measurements, one point source was used with activity 880 MBq (Source number 2 in Table 2.1), and it was also placed in a 200 mL plastic container.

Setup 3: All 92 source points on the ground, according to Figure 2.3, were measured with the point source of 6100 MBq (^{60}Co - source number 4 in Table 2.1). Due to its high activity, complementary measurements were made with weaker sources at the points closer to the modules in order to avoid saturating the detectors. The source points where one or more detectors saturated and for which complementary measurements were necessary were N9, L9, P9, R9, J11, R11, J13, R13, J15, R15, J17, R17, J19, R19, J21, L21, N21, P21, J23, L23 and N23 (Figure 2.3). Measurements were taken by using three point sources of ^{60}Co that contained a total 180 MBq (Sources number 5, 6, and 7 or 8 in Table 2.1). The sources were placed in a 200 mL plastic container with inner wall diameter 67 mm, which, in turn, was placed on a height-adjustable tripod.

Setup 4: For the ^{60}Co measurements of the 15 grid points on the roof of the modules (L11 to P19 in Figure 2.3), the detectors were turned 180^{o} with the center of the plastic crystal remaining 1 m above the floor surface. Two point sources totaling an activity of 190 MBq (Sources number 7 and 8 in Table 2.1) were used for the measurements on the roof. As in Setup 3, the sources were placed in a 200 mL plastic container.

For all the measurements that used the 200 mL plastic container, the maximum displacement of the sources within the container was 30 mm. Source number 4 in Table 2.1 was somewhat more difficult to place in exact position because of its higher activity and attached handling equipment. Because of this, the displacement varied from measurement point to measurement point, in the range 10 cm to 40 cm.

The definition of the geometry for the Monte Carlo calculations is based on the construction drawings and descriptions made available by Bilsby® (Bilsby® -), and measurements for the real modules included an additional construction made of clay bricks (Figure 2.4). Various databases (in particular McConn Jr et al. 2011) were used to assign the material specifications with definite atomic compositions and densities as summarized in Table 2.2 to the input data for the different building structures and environmental regions.

For each setup separate computations were performed for the different source positions and for reference values without the building structure. The setups corresponded to the four different measurement setups. The source regions were defined in all calcu-

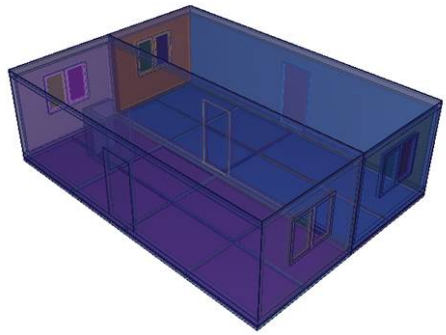

Figure 2.4: Birds-eye view of the modular building model.

lations as cylinders with a diameter and height of 1 cm. The source energies were either monoenergetic sources of 0.662 MeV representing the ^{137}Cs sources, or they were multi-energetic sources with energies of 1.173 MeV and 1.332 MeV representing the ^{60}Co sources, also taking into account the emission probability of both energies. Internal scatter within the source material was neglected, and there was no extra material composition attached to the source regions apart from the surrounding air, but from a simple comparison calculation without building can be assumed that about 12 % of the calculated ambient dose is caused by gamma radiation that was scattered by the soil for ^{137}Cs and about 8 % for ^{60}Co.

The detection regions were defined as air-filled spheres with a diameter of 30 cm. Four detector regions were positioned according to the detector positions in the real modular building 1 m above floor level of the modules (Figure 2.2).

2.1.2 Results of the comparison

The barrier shielding factors determined from the experiment were compared to those calculated theoretically. This was done by using the ratio of the experimentally and computationally determined shielding factors.

Table 2.2: Material specifications with definite atomic compositions (rounded) and densities that were used for the Monte Carlo calculations.

Material	Atomic composition	Density in kg/L
Particle board	46.24 % H; 32.34 % C;	0.7
Profile boards	0.28 % N; 20.88 % O;	0.6
Plywood	0.06 % Mg; 0.12 % S;	0.5
Window frame	0.04 % K; 0.04 % Ca	0.45
Mineral wool	42.5 % O; 1.7 % Na; 5.4 % Mg; 10.6 % Al; 18.2 % Si; 1.9 % K; 14.3 % Ca; 0.5 % Mn; 4.9 % Fe	0.167
Glas	60.39 % O; 8.81 % Na; 25.18 % Si; 5.62 % Ca	2.4
Plastic	50.00 % H; 33.33 % C; 16.67 % Cl	1.51
LECA bricks	63.33 % O; 0.69 % Na; 0.92 % Mg; 9.47 % Al; 21.91 % Si; 0.01 % P; 1.09 % K; 0.99 % Ca; 0.20 % Ti; 0.01 % Mn; 1.38 % Fe	2.2
Steel	3.41 % C; 4.87 % N; 0.97 % Si; 0.05 % P; 0.03 % S; 18.88 % Cr; 8.69 % Mn; 65.92 % Fe; 4.65 % Ni	7.86
Soil	31.69 % H; 50.16 % O; 4.00 % Al; 14.16 % Si	1.52
Air	0.02 % C; 78.44 % N; 21.07 % O; 0.47 % Ar	0.001205

Setup 1: The resulting ratios of the experimentally determined to the theoretically calculated shielding factors for ^{137}Cs were plotted in heat maps, in which individual values are represented graphically by a color code, for the corresponding distances from the respective detector region. This allowed an investigation into any possible influence of the different source positions around the modules (Figure 2.5) on the ratio. The ranges of the plotted ratios show that the clay bricks in the real modules provided less shielding than those in the theoretical model. Measurements of the real clay bricks showed that their density was $\rho = 0.65 kg/L$, which is lower than the clay density applied to the model: $\rho = 2.20 kg/L$ taken from a material compendium (McConn Jr et al. 2011). On average, the shielding factor over all source and detector regions was experimentally determined to be 0.66 ± 0.02 and theoretically calculated to be 0.60 ± 0.02.The overall ratio of the experimentally determined to the theoretically calculated shielding factors was determined to be 1.39 ± 0.04. If the combinations of source positions to detector regions are divided into those that cross the clay bricks looking at the direct line and those that do not cross the clay bricks at the direct line the ratios are determined to be 1.03 ± 0.02 without and 2.53 ± 0.06 with the clay bricks.

Setup 2: The resulting ratios of the experimentally determined to the theoretically calculated shielding factors for ^{137}Cs were plotted in heat maps for the corresponding source positions on top of the modules to the respective detector region. This allowed

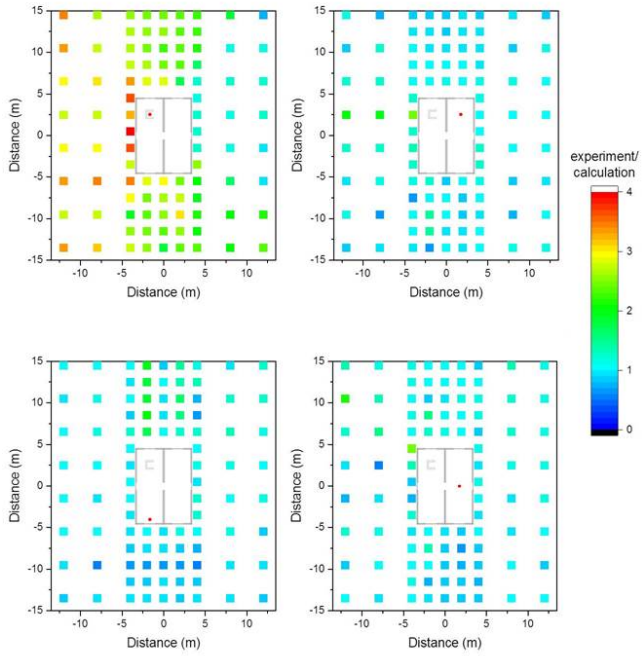

Figure 2.5: Ratio of the experimentally determined to the theoretically calculated shielding factor according to source region position around the modules, for four different detector regions inside the modules (red spot) for Setup 1 (^{137}Cs). According to a material compendium (McConn Jr et al. 2011), the density of the clay bricks in the calculations was assumed to be $\rho = 2.20 kg/L$, and it was later measured to be $\rho = 0.65 kg/L$.

an investigation into any possible influence of different source positions on top of the modules (Figure 2.6) on the ratio. The ranges of the plotted ratios show that the clay bricks in the real modules provide less shielding than those in the theoretical model, as the clay density was assumed to be higher in the model than that of the real bricks. The ranges of the plotted ratios also show that the sources that were positioned on the line where the two modules were fitted together lead to greater shielding from the real modules than that seen in the theoretical model. This can be explained because the edges of the real modules are encased in metal, which was not included in the model. The overall ratio of the experimentally determined to the theoretically calculated shielding factors was determined to be 1.24 ± 0.10. If the combinations of source positions to detector regions are divided into those that cross the clay bricks looking at the direct

line and those that do not cross the clay bricks as well as those where the sources were positioned on the metal case the ratios are determined to be 1.10 ± 0.03 without the clay bricks or metal case, 2.68 ± 0.20 with the clay bricks and 0.64 ± 0.04 with the metal case.

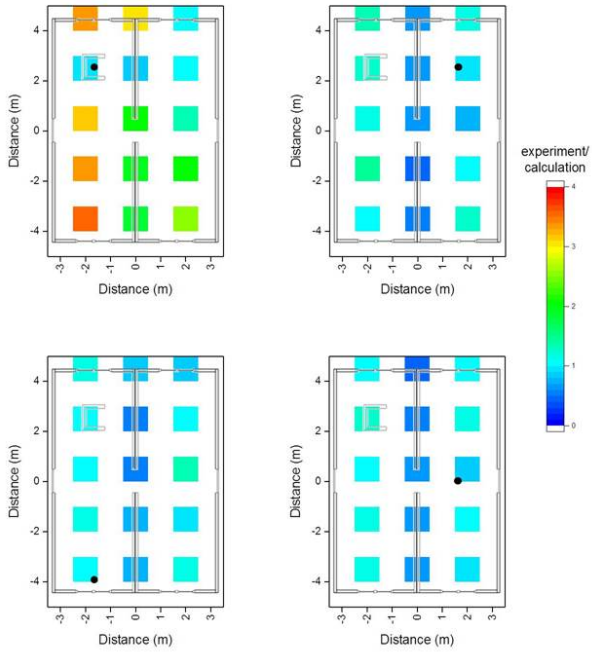

Figure 2.6: Ratio of the experimentally determined to the theoretically calculated shielding factor according to source region position on top of the modules, for four different detector regions inside the modules (black spot) for Setup 2 (^{137}Cs). According to a material compendium (McConn Jr et al. 2011), the density of the clay bricks in the calculations was assumed to be $\rho = 2.20 kg/L$, and it was later measured to be $\rho = 0.65 kg/L$.

Setup 3: The resulting ratios of the experimentally determined to the theoretically calculated shielding factors for ^{60}Co were plotted in heat maps as in Setup 1 (Figure 2.7). The ranges of the plotted ratios show again that the clay bricks in the real modules provide less shielding than those in the theoretical model, as the clay density was assumed to be higher in the model than that of the real bricks. On average, the shielding factor over all source and detector regions was experimentally determined to be 0.73 ± 0.02 and theoretically calculated to be 0.65 ± 0.02. This resulted in an overall ratio and the

standard error of the mean of the experimentally determined to the theoretically calculated shielding factors of 1.33 ± 0.04. If the combinations of source positions to detector regions are divided into those that cross the clay bricks looking at the direct line and those that do not cross the clay bricks at the direct line the ratios are determined to be 1.04 ± 0.02 without and 2.22 ± 0.05 with the clay bricks.

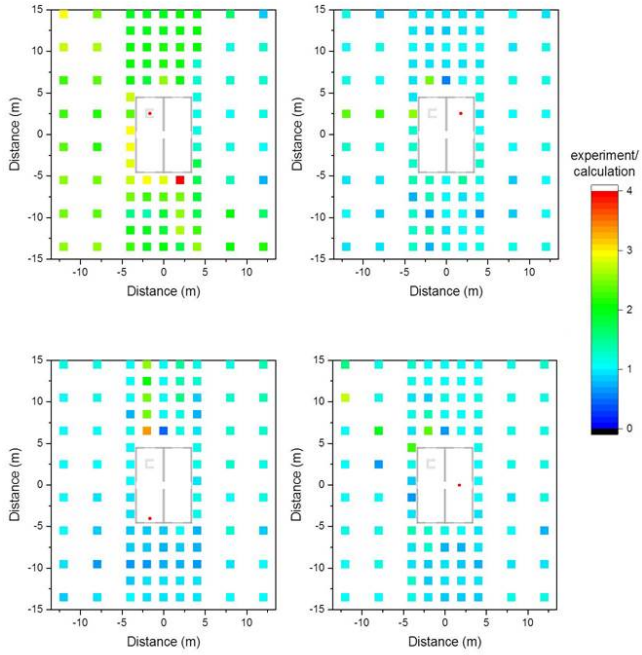

Figure 2.7: Ratio of the experimentally determined to the theoretically calculated shielding factor according to source region position around the modules, for four different detector regions inside modules (red spot) for Setup 3 (^{60}Co). According to a material compendium (McConn Jr et al. 2011), the density of the clay bricks in the calculations was assumed to be $\rho = 2.20 kg/L$, and it was later measured to be $\rho = 0.65 kg/L$.

Setup 4: The resulting ratios of the experimentally determined to the theoretically calculated shielding factors for ^{60}Co were plotted in heat maps as in Setup 2 (Figure 2.8). The ranges of the plotted ratios show again that the clay bricks in the real modules provide less shielding than those in the theoretical model, as the clay density was assumed to be higher in the model than that of the real bricks. Furthermore, the ranges of the

plotted ratios again show that the sources that were positioned on the line where the two modules were fitted together lead to greater shielding of the real modules than that seen in the theoretical model. This can be explained because the edges of the real modules are encased in metal which was not included in the model. The overall ratio of the experimentally determined to the theoretically calculated shielding factors was found to be 1.12 ± 0.07. If the combinations of source positions to detector regions are divided into those that cross the clay bricks looking at the direct line and those that do not cross the clay bricks, as well as those where the sources were positioned on the metal case the ratios are determined to be 1.02 ± 0.02 without the clay bricks or metal case, 2.17 ± 0.15 with the clay bricks and 0.67 ± 0.03 with the metal case.

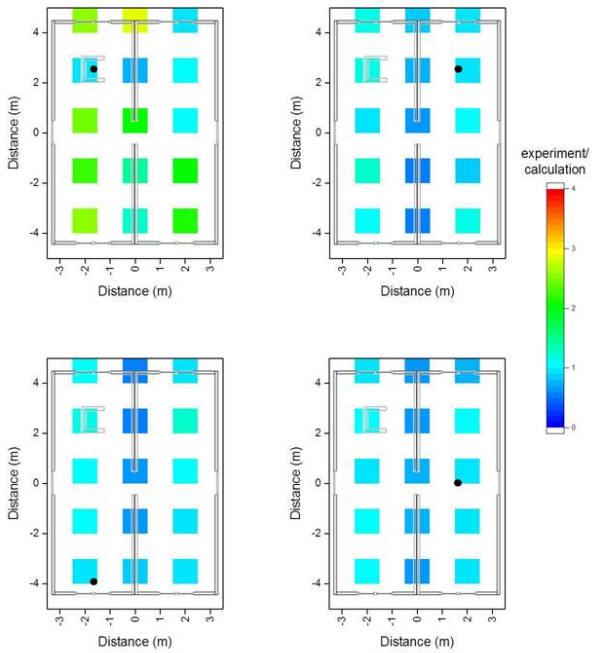

Figure 2.8: Ratio of the experimentally determined to the theoretically calculated shielding factor according to source region position on top of the modules, for four different detector regions inside the modules (black spot) for Setup 4 (^{60}Co). According to a material compendium (McConn Jr et al. 2011), the density of the clay bricks in the calculations was assumed to be $\rho = 2.20 kg/L$, and it was later measured to be $\rho = 0.65 kg/L$.

Table 2.3 provides a summary of the ratios of the compared experimentally determined and theoretically calculated shielding factors.

Table 2.3: Ratios and standard error of the mean of the experimentally determined and theoretically calculated shielding factors for different scenarios for a density of the clay bricks (LECA) of $\rho = 2.20 kg/L$ if not a different value is mentioned.

Gamma source	Influences assumed	Source region	
		Ground	Roof
^{137}Cs	None	1.39 ± 0.04 ($\rho_{LECA} = 2.20 kg/L$)	1.24 ± 0.10
		1.00 ± 0.01 ($\rho_{LECA} = 0.65 kg/L$)	
	Without clay bricks or metal case	1.03 ± 0.02	1.10 ± 0.03
	Clay bricks	2.53 ± 0.06	2.68 ± 0.20
	Metal case	–	0.64 ± 0.04
^{60}Co	None	1.33 ± 0.04	1.12 ± 0.07
	Without clay bricks or metal case	1.02 ± 0.05	1.02 ± 0.02
	Clay bricks	2.22 ± 0.05	2.17 ± 0.15
	Metal case	–	0.67 ± 0.03

To find a suitable and representative indoor point for the shielding factor the overall ratios were also determined per detector region and are summarized in Table 2.4. The ratios are the highest for detector #1 as it was almost surrounded by the clay bricks and thus its shielding factor was the most affected. The ratios determined for the source positions on the roof were lower than the respective ratios for source positions on the ground, since one third of the source positions on the roof were affected by the metal case.

For studying the impact of the clay density it has to be kept in mend that for various brick clays, the firing temperature has a high impact on the development of their pore structure (Hill 1960) and correspondingly their density. Moreover, some clay brick types have large perforations that enhance their thermal insulating capacity (Gosmartbricks 2017), which naturally also considerably reduces the bulk density of the brick. To investigate the impact of the different densities of clay bricks in this case and to show that the Monte Carlo calculations are also applicable for the clay brick structure, additional calculations were performed for clay brick densities of $\rho = 2.20 kg/L$and $\rho = 0.65 kg/L$. The ratio comparing $H^*(10)$ caused by ^{60}Co and ^{137}Cs crossing a clay brick for both densities was calculated using the MCNP6 code (Goorley et al. 2012). The ratios were determined for different thicknesses of clay brick (Figure 2.9), as the radiation can cross the clay brick structure in the building model at different angles. The ratio of the difference of the shielding factor ratios for the respective source point detector combinations

Table 2.4: Ratios and standard error of the mean of the experimentally determined and theoretically calculated shielding factors for the different setups and detectors for a density of the clay bricks (LECA) of $\rho = 2.20 kg/L$ if not a different value is mentioned.

Setup		Detector			
		#1	#2	#3	#4
^{137}Cs	Ground ($\rho_{LECA} = 2.20 kg/L$)	2.38 ± 0.08	1.07 ± 0.03	1.05 ± 0.03	1.06 ± 0.03
	Ground ($\rho_{LECA} = 0.65 kg/L$)	0.95 ± 0.02	1.02 ± 0.02	0.99 ± 0.02	1.03 ± 0.02
	Roof	2.14 ± 0.25	0.96 ± 0.08	0.95 ± 0.06	0.91 ± 0.06
^{60}Co	Ground	2.02 ± 0.06	1.10 ± 0.04	1.10 ± 0.05	1.10 ± 0.04
	Roof	1.76 ± 0.18	0.92 ± 0.06	0.90 ± 0.06	0.88 ± 0.06

that were affected by the clay brick structure are in the right range.

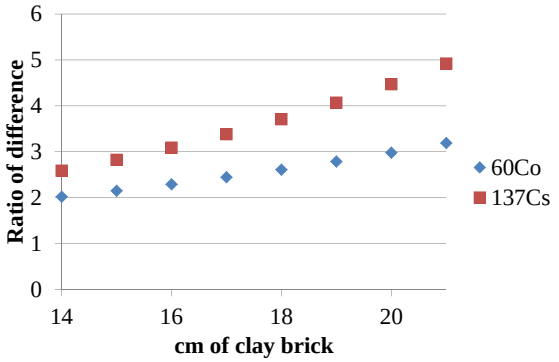

Figure 2.9: Ratio of the difference in H*(10) after crossing clay bricks with a density $\rho = 0.65 kg/L$ to bricks with density $\rho = 2.20 kg/L$.

Additionally, the calculations were repeated for all source points that were influenced by the clay brick structure according to Setup 1, but this time using the measured density of the clay brick structure. The resulting ratios of the experimentally determined to the theoretically calculated shielding factors for ^{137}Cs were plotted in heat maps for the corresponding distances from the respective detector region, as they were for the first

calculations (Figure 2.10). The presented results show good agreement with the measurements (slight variations will always be expected due to small imperfections in the model compared with real life, due to ground unevenness, surface texture, etc.). The ratio of the experimentally determined to the theoretically calculated shielding factors was now determined to be 0.95 ± 0.02 for detector #1, 1.02 ± 0.02 for detector #2, 0.99 ± 0.02 for detector #3, 1.03 ± 0.02 for detector #4 (Table 2.4), and 1.00 ± 0.01 averaging over all detector regions (Table 2.3). The results show that all detector regions are of similar quality. The average theoretical shielding factor increased with the new calculations to 0.68 ± 0.02.

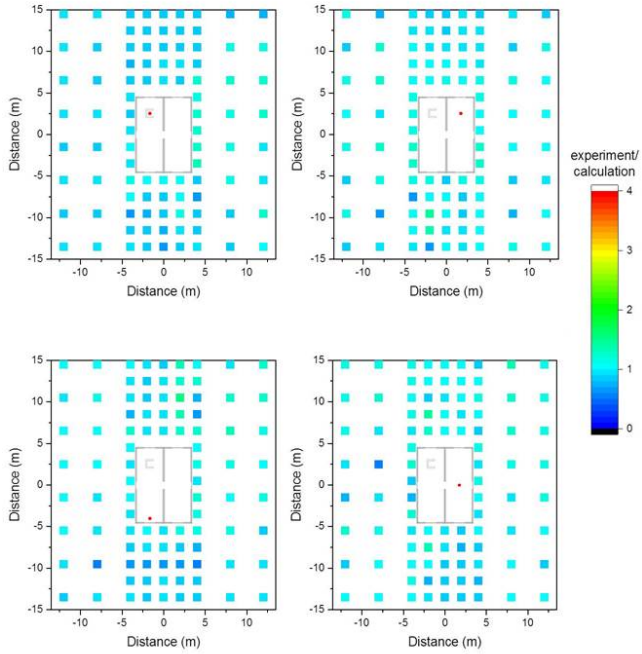

Figure 2.10: Ratio of the experimentally determined to the theoretically calculated shielding factor according to source region position around the modules for four different detector regions inside the modules (red spot) for Setup 1 with corrected density of the clay bricks (^{137}Cs).

Concluding this section, the theoretically calculated shielding factors showed good agreement with the experimentally determined shielding factors for the modular building in case of source point and detector area combinations that were not directly influenced

by the clay brick structure or the metal case. The ratios determined for the source points, for which the direct radiation path crosses the clay structure before reaching the detector, were within the predicted range, considering the clay density in the model and the density in the experiment. Further calculations also showed the agreement between the model and experiment. For future calculations, it will be important to know the actual density of bricks and other important construction elements used in building houses. If not properly accounted for, construction materials with highly deviating density or atomic composition may strongly affect the accuracy in the calculated shielding factors of a building, depending on the choice of reference point in the building. In the present study, however, the metal case only influenced the result when the source was directly positioned on top of it. For future models has to be considered, that a structure of this type might have to be included, especially when a major part of the unscattered radiation crosses the structure before reaching the detector, which is usually not the case as the metal case normally only covers a very small part of a modular building as in the presented case.

The difference between the calculated and experimentally determined shielding for two different radionuclides with primary gamma energies of 0.662 to 1.25 MeV appeared to be negligible for the reference points not directly affected by the clay brick (Detector points 2-4). As an example, the ratio between the measured and calculated shielding factors ranged from 1.06 to 1.10 for the ground source geometry (Table 2.4). Hence, the results showed that the gamma energy, in practice, has no influence on the level of agreement between experiment and calculation, provided that the construction materials are accurately characterized in terms of density and atomic composition. Therefore, the applicability of theoretical calculations using MCNP6 for radioactive fallout scenarios has been demonstrated in practice.

2.2 Comparing previous results with MCNP6

Regarding the theoretical determination of exposure reduction for buildings it has to be considered that the ERMIN model currently largely relies on a series of Monte Carlo computed kerma conversion factors, which date more than 30 years back and where performed by GSF (Jacob & Meckbach 1987, Meckbach & Jacob 1988, Meckbach et al. 1987, 1988). To investigate the quality of the Monte Carlo calculations, they were repeated for one of the building types (semidetached house) using the modern code MCNP6 (Goorley et al. 2012) for which its applicability was just demonstrated in Section 2.1.

The house type and the surfaces and neighboring buildings (see Figure 2.11) were modeled based on the data published by Meckbach et al. (1987, 1988), who also provided, e.g., highly detailed descriptions of the assumed construction materials with di-

mensions, material specifications and densities. Atomic composition data of the different materials were added from a compilation by Pacific Northwest National Laboratory (McConn Jr et al. 2011). The source and detector regions were defined according to the data given by (Meckbach et al. 1988).

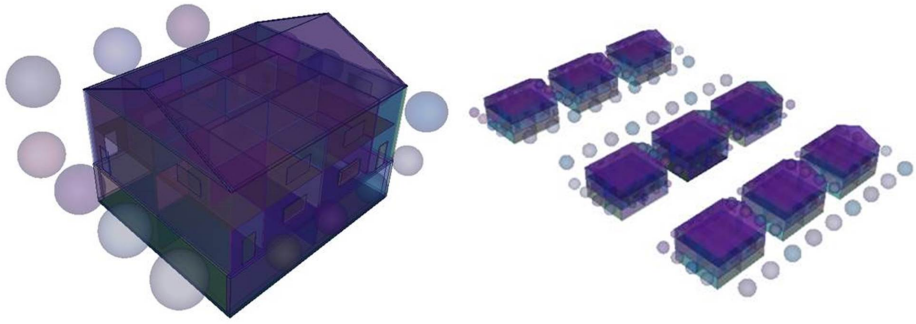

Figure 2.11: Birds-eye view of the semidetached house without (left) and with (right) neighboring buildings. The spheres indicate the position of the trees.

The calculated air kerma values per photon emitted per unit source area were compared to those published at GSF (Meckbach et al. 1988). The ratios of the two data were calculated for different source and detector areas and averaged over three different photon energies – 0.3 MeV, 0.662 MeV and 3.0 MeV (Table 2.5). The new calculations only comprise indoor detection positions, as the publications of Meckbach did not disclose the positions assumed for detection in outdoor locations.

Naturally, part of the difference may be attributable to differences in assumptions regarding atomic compositions of materials, which were not specified in the old publication. However, the rather substantial differences between the calculations for particularly walls and doors show that something more fundamental may be at play, possibly due to the old and perhaps incorrect cross-section libraries that were used with the SAM-CE code (Lichtenstein et al. 1979). The wall material in this case provides better shielding against radiation than does the roof, and comparatively smaller radiation tallies would thus be scored, and longer computing time required for a good result. Also estimates of contributions to the air kerma from radiation from neighboring areas (where comparatively small radiation tallies would also be expected) are generally not in good agreement. The results of the new calculations of kerma rate conversion factors in the format applied by Meckbach et al. (1988) and used in the ERMIN data libraries are reported in Tables 2.6 to 2.8 for the photon energies 0.3 MeV, 0.662 MeV and 3.0 MeV.

Table 2.5: Ratios of newly calculated air kerma rate conversion factors divided by those previously reported by Meckbach et al. (1988) for the same scenario. Figures are given according to source and detection area.

Source area	Detection area			
	Basement	Ground floor	First floor	Attic
On the house:				
Windows	1.11	0.41	0.78	0.68
Walls and doors	0.36	0.41	0.16	0.23
Roof	1.01	0.82	0.92	1.06
Without neighboring buildings:				
Ground	0.51	0.37	0.27	0.81
With neighboring buildings:				
Ground	0.42	0.36	0.13	0.13
Neighboring buildings	0.35	0.22	0.35	0.53
Trees	0.38	0.28	0.06	0.24

In conclusion, the new dose rate factors differed significantly from the old ones, particularly when the radiation passed through substantial masses like outer house walls, but the agreements and deviations lie within the order of magnitude. The explanation might possibly lie in the programming, and could also reflect differences in cross-section data libraries or unreported case-specific assumptions.

Table 2.6: Contribution of the various deposition areas to the kerma at several locations inside a semidetached house for a source energy of 0.3 MeV in pGy per γ/cm^2.

Source area	Detection area			
	Basement	Ground floor	First floor	Attic
On the house:				
Windows	0.026	2.8	6.2	1.5
Walls and doors	0.008	4.0	1.4	1.2
Roof	0.116	7.3	24.0	84.0
Without neighboring buildings:				
Ground	0.013	13.6	10.4	29.8
With neighboring buildings:				
Ground	0.004	8.8	2.6	3.1
Neighboring buildings	0.001	1.0	1.9	3.9
Trees	0.002	1.4	0.3	0.7

Table 2.7: Contribution of the various deposition areas to the kerma at several locations inside a semidetached house for a source energy of 0.662 MeV in pGy per γ/cm^2.

Source area	Detection area			
	Basement	Ground floor	First floor	Attic
On the house:				
Windows	0.159	6.2	20.5	4.0
Walls and doors	0.054	7.9	3.0	3.5
Roof	0.753	17.5	57.5	198.8
Without neighboring buildings:				
Ground	0.060	31.0	19.4	73.1
With neighboring buildings:				
Ground	0.020	18.9	5.3	7.7
Neighboring buildings	0.007	2.3	4.2	12.1
Trees	0.012	3.2	0.5	1.9

Table 2.8: Contribution of the various deposition areas to the kerma at several locations inside a semidetached house for a source energy of 3.0 MeV in pGy per γ/cm^2.

Source area	Detection area			
	Basement	Ground floor	First floor	Attic
On the house:				
Windows	2.37	20.9	66.2	14
Walls and doors	1.10	23.1	11.0	19
Roof	9.79	69.3	218.3	722
Without neighboring buildings:				
Ground	0.95	108.2	46.4	416
With neighboring buildings:				
Ground	0.71	59.8	16.7	31
Neighboring buildings	0.15	7.9	14.5	66
Trees	0.31	11.2	1.2	9

Chapter 3

Application to modern types of buildings

3.1 Kerma conversion factors for modern glass buildings

Apart from the ERMIN model relying on old data sets of kerma conversion factors for buildings, the number of different types of inhabited environment is limited. For instance, city centers contain many tall buildings of modern construction (e.g., with much glass). To the best of our knowledge Monte Carlo simulations have not previously been performed for buildings with glass facades or buildings with similar shielding properties. Therefore, the next step was to set up a model of a modern glass building and derive the kerma conversion factors from different contaminated surfaces.

3.1.1 Description of the model

The definition of the geometry is leaned on the construction drawings and descriptions of a real glass building in the city of Copenhagen that were made available by the Technical and Environmental Administration of the Municipality of Copenhagen (Teknik- og Miljøforvaltning – Københavns Kommune) and was applied to 11 different heights of the building from one story till 11 storys for a single house scenario that stands alone, for a park scenario with 3 houses in a row, and for a city scenario with a square of 3 x 3 houses (Figures 3.1 to 3.4). The outer walls are made of 2 layers of 1.2 cm thick glass with 97.6 cm air in between them. In the middle of the building (see Figures 3.1 and 3.2) is an atrium covered by a roof of 2.4 cm thick glass. It is not surround by any wall as it is usually surrounded by railings on the different floors. The house contains

six shafts for stairs and elevators going from the basement up to the top of the building (see Figures 3.1 and 3.2). Their surrounding walls are made of 30 cm thick concrete. The building is furthermore based on sixty concrete columns (indicated by small circles in Figure 3.1) with a diameter of 60 cm going from the basement building. The intermediate floors and the roof are made 22 cm thick concrete and the basement is surrounded by 40 cm thick concrete to the bottom and to the sides. The spheres in Figures 3.1 to 3.4 indicate the positions of the tree canopies. As foliage on trees constitute a very efficient aerosol/rain filter, the contamination on the stem and branches will be of comparatively little importance (Roed 1988) and is not considered in the model.

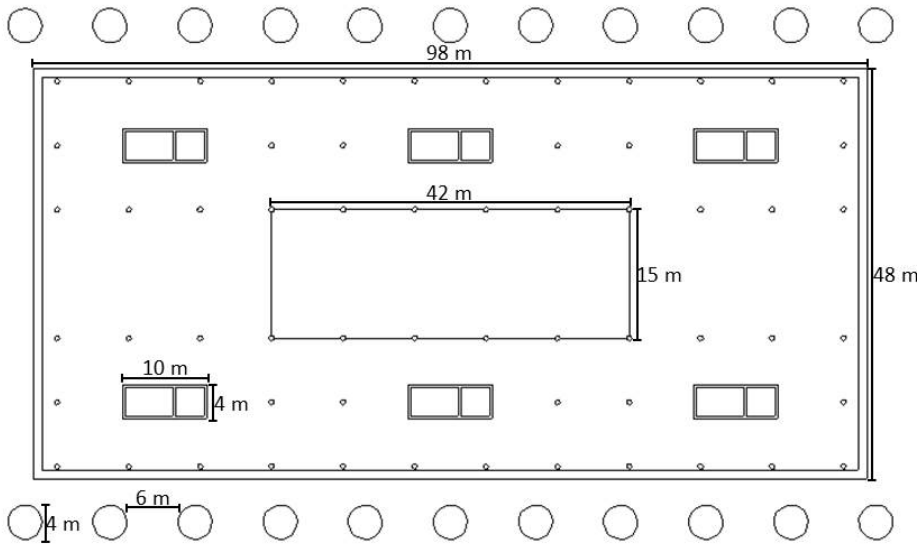

Figure 3.1: Horizontal cut of the glass building. The spheres indicate the positions of the trees.

Data from a material compendium (McConn Jr et al. 2011) was used to assign the material specifications with definite atomic compositions and densities as summarized in Table 3.1 to the input for the different building structures and environmental regions.

For each height and scenario separate computations were performed for sources that were defined as surfaces on top of the ground, trees, walls, and roofs. The source energies were monoenergetic sources of 0.662 MeV representing ^{137}Cs, which has been of main concern in connection with the Chernobyl and Fukushima incidents, 0.3 MeV or

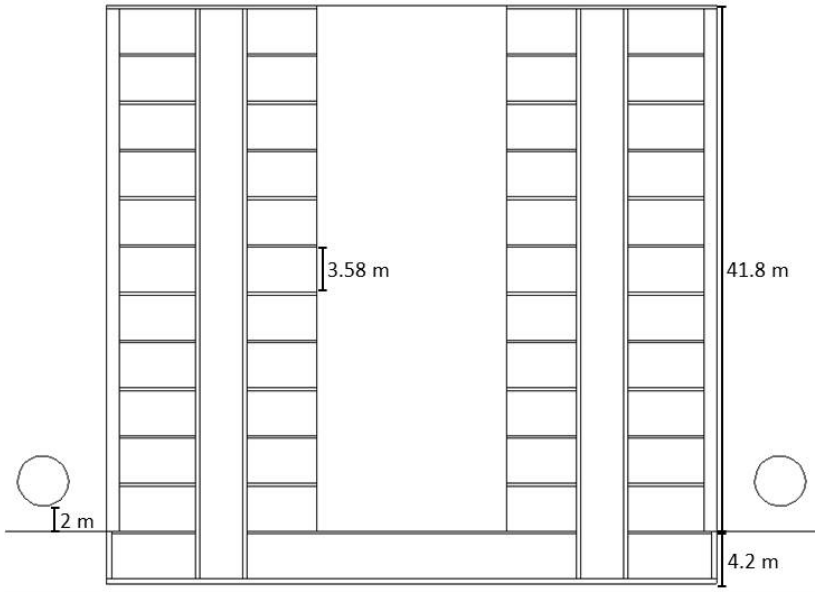

Figure 3.2: Vertical cut of the glass building for the largest height of eleven storys. The spheres indicate the positions of the trees.

3.0 MeV to get an impression of the behavior of the kerma for lower and higher primary gamma energies. The detector regions were defined as air-filled spheres with a diameter of 30 cm and eighteen of them were positioned in various part of each floor 1 m above the level of the respective floor of the building.

Internal walls inside the building were not modeled, because in these modern buildings they are not part of the building. They are usually made of gypsum (around 12 cm thick) and can be built up and removed quickly. To get an idea about their shielding effect extra simulations were performed leading to the results that the kerma will be reduced by a factor of 0.72 for a primary gamma energy of 0.3 MeV, by 0.77 for a primary gamma energy of 0.662 MeV and by 0.86 for a primary gamma energy of 3.0 MeV after passing one gypsum wall of 12 cm thickness.

3.1.2 Resulting formulas for glass buildings of different heights

With these Monte Carlo calculations the kerma (pGy) per emitted gamma photon (γ) on the source was determined. This factor was multiplied with the size of the respective source area (mm^2) to determine the kerma (pGy) for a source strength of one gamma

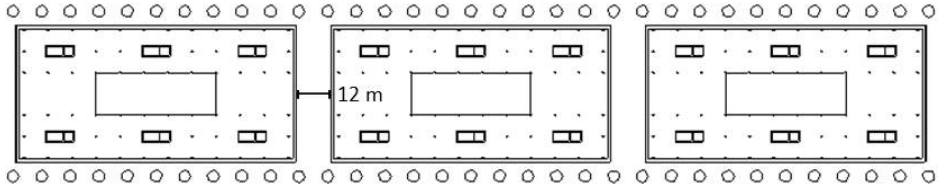

Figure 3.3: Horizontal cut of the park scenario. The spheres indicate the positions of the trees.

Table 3.1: Material specifications with definite atomic compositions (rounded) and densities that were used for the Monte Carlo calculations.

Material	Atomic composition	Density in kg/l
Air	0.02 % C; 78.44 % N; 21.07 % O; 0.47 % Ar	0.001205
Concrete	8.47 % H; 60.41 % O; 1.25 % Na; 2.48 % Al; 24.19 % Si; 2.72 % Ca; 0.47 % Fe	2.25
Glass	60.39 % O; 8.81 % Na; 25.18 % Si; 5.62 % Ca	2.4
Soil	31.69 % H; 50.16 % O; 4.00 % Al; 14.16 % Si	1.52

photon per unit area (γmm^{-2}) represented by K. These values were used as a basis to fit a mathematical model for the kerma over them for each type of surface at a given floor F inside a building of a height H with the smallest possible deviations.

The following mathematical expressions describe the kerma for all floors of the glass building for all building heights, environmental scenarios, source energies and source areas. H represents in the equations the height in terms of number of storys above ground level (excluding the basement there are $H+1$ storys). F represents the floor inside the building from $F=-1$ (basement) through $F=0$ (ground floor) to higher floors (e.g. $F=5$ is the fifth floor). F is of course restricted by the height of the building ($F \leq H$). All equations determine the kerma (pGy) for a source strength of one gamma photon per unit area (γmm^{-2}) (K). By multiplying this factor with a given contamination level (Bq mm^{-2}) and the number of photons per disintegration (γ) of the respective gamma energy, the kerma rate contribution for each gamma energy emitted with determined kerma factors can be calculated. As the basement of the building is more shielded than the rest of the building, an extra equation is necessary for all contamination scenarios.

The development of the kerma per source strength inside a glass building caused by contamination on the roof can be described by Equation (3.1) with the values of the variables given in Table 3.2. The variable a expresses the kerma per source strength in the floor directly under the roof, the term $\exp(-b\cdot(H-F)^c)$ the decrease of the kerma

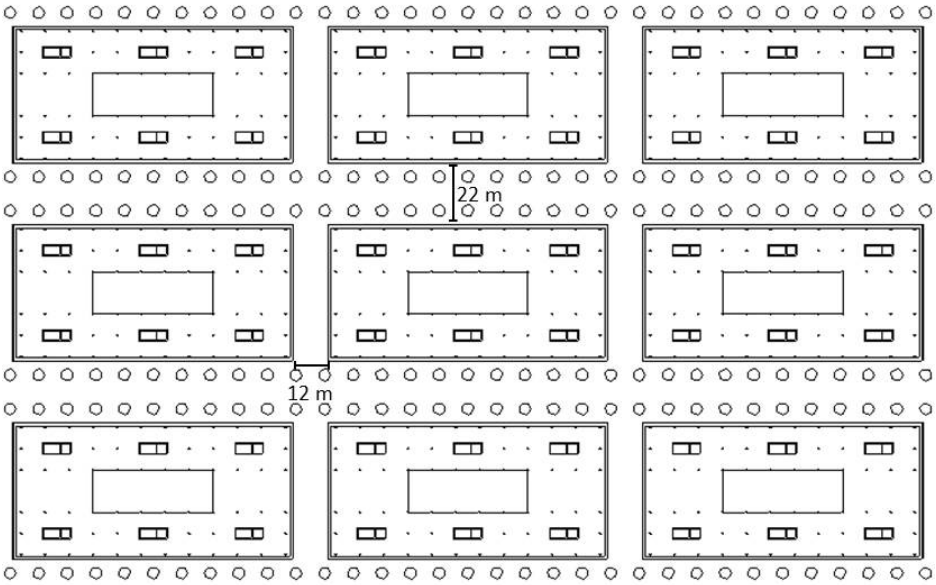

Figure 3.4: Horizontal cut of the city scenario. The spheres indicate the positions of the trees.

with distance to the roof, and the term $(1+d\cdot\exp(-e\cdot F^f))$ the backscattered radiation from the ground. The kerma in the basement decreases with the height of the building as the distance to the basement increases $(g\cdot\exp(-h\cdot H^i))$.

$$K(F,H)=\begin{cases} a\cdot\exp(-b\cdot(H-F)^c)\cdot(1+d\cdot\exp(-e\cdot F^f)), & \forall F\geq 0 \\ g\cdot\exp(-h\cdot H^i), & \forall F=-1 \end{cases} \tag{3.1}$$

Equation (3.2) with the values of the variables given in Table 3.3 describes the development of the kerma per source strength inside a glass building caused by contamination on the walls. The variable a expresses the maximal kerma per source strength in a floor with several floors under and over it. The term $(1-b\cdot\exp(-c\cdot F^d))$ expresses the decrease of the kerma because of decreasing distance to the ground and therefore smaller area of contaminated wall below this floor, and the term $(1-e\cdot\exp(-f\cdot(H-F)^g))$ the same effect of decreasing distance towards the roof of the building. Furthermore, the term $(1-h\cdot\exp(-i\cdot H^j))$ expresses the impact of the height of the building as the source area of the walls increases with height. The kerma in the basement increases with the height and source area of the building $(1-l\cdot\exp(-m\cdot H^n))$ towards a maximum value

Table 3.2: Values of the variables in Equation (3.1) describing the kerma per unit source strength inside a glass building caused by contamination on the roof. 'a' and 'g' have the dimension pGy per $\gamma\,\mathrm{mm}^{-2}$. All other variables are dimensionless.

	0.3 MeV	0.662 MeV	3.0 MeV
a	4.70	15.3	126
b	0.80	1.05	1.33
c	0.78	0.74	0.70
d	0.11	0.073	0.018
e	1.29	1.27	0.95
f	1.03	0.63	0.30
g	0.040	0.39	14.6
h	0.35	0.59	0.96
i	0.87	0.69	0.60

of k.

$$K(F,H) = \begin{cases} a \cdot (1 - b \cdot \exp(-c \cdot F^d)) \\ \cdot (1 - e \cdot \exp(-f \cdot (H-F)^g)) \cdot (1 - h \cdot \exp(-i \cdot H^j)), & \forall F \geq 0 \\ k \cdot (1 - l \cdot \exp(-m \cdot H^n)), & \forall F = -1 \end{cases} \tag{3.2}$$

The development of the kerma per source strength inside a glass building caused by contamination on the ground can be described by Equations (3.3) and (3.4) with the respective values of the variables given in Tables 3.4 to 3.6 depending on the environmental scenario. The variable a represents the kerma at the ground floor and the term $\exp(-b \cdot F^c)$ the decrease of it towards the roof. In the scenarios with neighboring buildings skyshine has an impact on the floors closest to the roof, which is expressed by the term $(1 + d \cdot \exp(-e \cdot (H-F)^f))$. The kerma in the basement is independent from the height of the buildings and therefore stable. It is expressed by the value d in the scenario without neighboring buildings and by the value g in the scenarios with neighboring buildings.

$$K(F,H) = \begin{cases} a \cdot \exp(-b \cdot F^c), & \forall F \geq 0 \\ d, & \forall F = -1 \end{cases} \tag{3.3}$$

$$K(F,H) = \begin{cases} a \cdot \exp(-b \cdot F^c) \cdot (1 + d \cdot \exp(-e \cdot (H-F)^f)), & \forall F \geq 0 \\ g, & \forall F = -1 \end{cases} \tag{3.4}$$

Neighboring buildings contribute to the kerma by contamination on their roofs and walls. Equation (3.5) with the respective values of the variables given in Tables 3.7

Table 3.3: Values of the variables in Equation (3.2) describing the kerma per unit source strength inside a glass building caused by contamination on the walls. 'a' and 'k' have the dimension pGy per $\gamma\,\mathrm{mm}^{-2}$. All other variables are dimensionless.

	0.3 MeV	0.662 MeV	3.0 MeV
a	17.0	36.7	132
b	0.066	0.065	0.098
c	1.76	2.64	1.41
d	0.0064	0.45	0.87
e	0.12	0.12	0.15
f	1.84	1.92	1.62
g	0.39	0.42	0.74
h	0.096	0.037	0.025
i	0.25	0.59	1.46
j	0.60	0.71	0.86
k	0.040	0.30	7.42
l	0.34	0.35	0.41
m	1.40	2.38	1.63
n	0.17	0.31	1.33

and 3.8 describe the development of the kerma per source strength inside a glass building caused by contamination on the roofs of those neighboring buildings. The variable a expresses the kerma per source strength in the floor directly under the roof, the term $\exp(-b\cdot(H-F)^c)$ the decreasing of the kerma with distance to the roof, and the term $(1+d\cdot\exp(-e\cdot F^f))$ the backscattered radiation from the ground. The kerma in the basement decreases with the height of the building as the distance to the basement increases ($g\cdot\exp(-h\cdot H^i)$) for primary gamma energies of 0.3 and 0.662 MeV. For primary gamma energies of 3.0 MeV an extra of $-j\cdot\exp(-k\cdot H^l)$ has to be added to model the development of the kerma in the basement for different heights of the buildings. This

Table 3.4: Values of the variables in Equation (3.3) describing the kerma per unit source strength inside a glass building caused by contamination on the ground for a single house without any neighboring buildings. 'a' and 'd' have the dimension pGy per $\gamma\,\mathrm{mm}^{-2}$. 'b' and 'c' are dimensionless.

	0.3 MeV	0.662 MeV	3.0 MeV
a	41.1	115	572
b	0.64	0.67	0.62
c	0.51	0.53	0.58
d	0.019	0.093	0.63

Table 3.5: Values of the variables in Equation (3.4) describing the kerma per unit source strength inside a glass building caused by contamination on the ground for a house in a park scenario with two neighboring buildings. 'a' and 'g' have the dimension pGy per γ mm^{-2}. All other variables are dimensionless.

	0.3 MeV	0.662 MeV	3.0 MeV
a	34.5	95.7	475
b	0.70	0.73	0.69
c	0.50	0.51	0.54
d	0.035	0.026	0.015
e	0.37	0.48	0.52
f	1.88	1.51	1.33
g	0.017	0.082	0.55

Table 3.6: Values of the variables in Equation (3.4) describing the kerma per unit source strength inside a glass building caused by contamination on the ground for a house in a city scenario with eight neighboring buildings. 'a' and 'g' have the dimension pGy per γ mm^{-2}. All other variables are dimensionless.

	0.3 MeV	0.662 MeV	3.0 MeV
a	23.8	61.5	267
b	1.18	1.36	1.46
c	0.49	0.48	0.49
d	0.12	0.13	0.084
e	0.60	0.68	0.88
f	1.56	1.49	1.57
g	0.011	0.056	0.36

may reflect a second relevant factor apart from the distance of source and detector position. By looking at the direct line between source and detector position it can be seen that the distance of soil that has to be crossed, before the radiation reaches the basement, decreases with increasing height of the building. Therefore, the kerma in the basement at the beginning increases with increasing distance to the source as this shielding effect seems to have a higher impact on the kerma development in these ranges than the

distance to the source which additionally seems to be only relevant for higher energies.

$$K(F,H) = \begin{cases} a \cdot \exp(-b \cdot (H-F)^c) & \\ \cdot(1 + d \cdot \exp(-e \cdot F^f)), & \forall F \geq 0 \\ g \cdot \exp(-h \cdot H^i) & \forall F = -1 \\ & (0.3 \text{ and } 0.662 \text{ MeV}) \\ g \cdot \exp(-h \cdot H^i) - j \cdot \exp(-k \cdot H^l) & \forall F = -1 \\ & (3.0 \text{ MeV}) \end{cases} \tag{3.5}$$

Table 3.7: Values of the variables in Equation (3.5) describing the kerma per unit source strength inside a glass building caused by contamination on the roof of two neighboring buildings in a park scenario. 'a', 'g' and 'j' have the dimension pGy per γ mm^{-2}. All other variables are dimensionless.

	0.3 MeV	0.662 MeV	3.0 MeV
a	0.37	0.64	1.38
b	0.74	0.84	0.70
c	0.59	0.58	0.79
d	0.034	0.039	0.039
e	0.017	0.31	0.37
f	4.95	1.78	1.45
g	0.00043	0.0018	0.077
h	0.45	0.38	0.10
i	0.90	0.85	1.61
j	-	-	0.067
k	-	-	0.20
l	-	-	2.38

The development of the kerma per source strength inside a glass building caused by contamination on the walls of neighboring buildings can be described by Equation (3.2) with the respective values of the variables given in Tables 3.9 and 3.10 depending on the environmental scenario. The variable a expresses the maximal kerma per source strength in a floor with several floors under and over it. The term $(1 - b \cdot \exp(-c \cdot F^d))$ expresses the decrease of the kerma because of decreasing distance to the ground and therefore less area of contaminated walls on this side of the floor, and the term $(1 - e \cdot \exp(-f \cdot (H-F)^g))$ the same effect of decreasing distance towards the roof of the buildings. Furthermore, the term $(1 - h \cdot \exp(-i \cdot H^j))$ expresses the impact of the heights of the buildings as the source area of the walls increases with height. The kerma in the basement increases with the height and source area of the building $(1 - l \cdot \exp(-m \cdot H^n))$ towards a maximum value of k.

Table 3.8: Values of the variables in Equation (3.5) describing the kerma per unit source strength inside a glass building caused by contamination on the roof of eight neighboring buildings in a city scenario. 'a', 'g' and 'j' have the dimension pGy per $\gamma\,\mathrm{mm}^{-2}$. All other variables are dimensionless.

	0.3 MeV	0.662 MeV	3.0 MeV
a	1.48	2.64	5.53
b	0.55	0.61	0.52
c	0.85	0.85	0.93
d	0.063	0.066	0.037
e	0.67	0.39	0.57
f	1.56	1.91	1.26
g	0.0014	0.0079	0.39
h	0.072	0.32	0.12
i	1.78	0.96	1.26
j	-	-	0.36
k	-	-	0.16
l	-	-	1.44

Equation (3.6) with the respective values of the variables given in Tables 3.11 to 3.13 describe the development of the kerma per source strength inside a glass building caused by contamination on trees depending on the environmental scenario. The term $a \cdot \exp(-b \cdot F^c)$ describes the decreasing of the kerma with distance to the trees for buildings of heights $H \geq 1$ at the floors $F \geq 1$. The value of the variable d expresses the kerma at the ground floor for a building height of $H = 0$ and e the kerma at the ground floor for higher buildings. The kerma in the basement is independent from the height of the buildings and expressed by the value f.

$$K(F,H) = \begin{cases} a \cdot \exp(-b \cdot F^c), & \forall F,H \geq 0 \\ d & \forall F,H = 0 \\ e & \forall F = 0 \wedge H \geq 1 \\ f & \forall F = -1 \end{cases} \tag{3.6}$$

With the determined kerma conversion factors for a modern glass building that can be found in a similar way in many modern cities now, the knowledgebase for external dose estimations in inhabited areas can be improved. Therefore, those factors support the progress of decision making in long term management in modern cities after an airborne release of radionuclides as e.g. a nuclear power plant accident. The description as formulas allows the further application of the glass building model regardless of the height of the building and detection area.

Table 3.9: Values of the variables in Equation (3.2) describing the kerma per unit source strength inside a glass building caused by contamination on the walls of two neighboring buildings in a park scenario. 'a' and 'k' have the dimension pGy per γ mm^{-2}. All other variables are dimensionless.

	0.3 MeV	0.662 MeV	3.0 MeV
a	4.62	10.8	36.9
b	0.21	0.20	0.20
c	1.11	1.34	1.52
d	0.75	0.70	0.44
e	0.37	0.38	0.40
f	0.89	0.94	0.99
g	1.20	1.19	1.13
h	0.51	0.46	0.31
i	0.45	0.51	0.74
j	0.55	0.40	0.43
k	0.0071	0.053	1.61
l	0.92	0.94	0.98
m	0.19	0.15	0.11
n	1.24	1.60	1.88

3.2 Comparison with previous values for a multistory house block

To show the relevance of the determined kerma factors they were compared to respective factors calculated by Meckbach et al. (1988) for a multistory house block, which is the closest of the building models that were developed so far compared to the glass building model described in Section 3.1.1. The multistory house was five storys high and therefore the values are compared to the values of the glass building with a height of $H = 4$. Furthermore, kerma factors inside the multistory house block were determined for the basement ($F = -1$), the ground floor ($F = 0$), the second floor ($F = 2$), and the fourth floor ($F = 4$) and thus compared to the respective floors inside the glass building. Regarding the source areas on the building both factors for the roof were compared as well as the factor for the walls of the glass building with the sum of the factors for walls and windows of the multistory house block. In case of the ground as source area the respective factors were compared for the park and the city scenario that were for the multistory house block the sum of the factors for the street and the park in the park scenario and the factor for the street in case of the city scenario. For the neighboring buildings (Meckbach et al. 1988) calculated factors for walls and windows as well as for the roof and for both park and city scenario. Therefore, all four could directly be

Table 3.10: Values of the variables in Equation (3.2) describing the kerma per unit source strength inside a glass building caused by contamination on the walls of eight neighboring buildings in a city scenario. 'a' and 'k' have the dimension pGy per γ mm^{-2}. All other variables are dimensionless.

	0.3 MeV	0.662 MeV	3.0 MeV
a	15.3	36.4	142
b	0.23	0.22	0.22
c	0.85	1.02	1.06
d	0.90	0.99	1.07
e	0.41	0.43	0.47
f	0.51	0.51	0.50
g	1.11	1.15	1.07
h	0.61	0.56	0.46
i	0.41	0.47	0.66
j	0.69	0.64	0.62
k	0.024	0.24	6.42
l	0.94	0.97	0.99
m	0.079	0.061	0.039
n	1.47	1.40	1.73

compared to the respective ones determined for the glass building. Regarding the factors for the trees the respective ones for a park scenario were compared.

The comparison took place by dividing the factor for the glass building by the respective one for the multistory house block for all values available. This was performed for all three primary gamma energies and the resulting ratios are presented in Tables 3.14 to 3.16.

The numbers show that the kerma factor is larger, apart from nine cases for the glass building than for the multistory house block. Two extreme cases were determined with a ratio of 271 for the roof to second floor factor for a primary gamma energy of 0.662 MeV and with a ratio of 383 for the roof to ground floor factor for a primary gamma energy of 3.0 MeV. The other ratios vary between 0.22 and 35.4 with an averaged ratio and standard error of the mean of 6.11 ± 0.73 (excluding the two extreme values).

Looking into the details the average ratio over each primary gamma energy decreases with increasing primary energy excluding the two extreme values as the averaged values are 7.72 ± 1.34 for a primary gamma energy of 0.3 MeV, 6.76 ± 1.36 for a primary gamma energy of 0.662 MeV and 4.05 ± 0.99 for a primary gamma energy of 3.0 MeV. Looking at the source areas of course the roof of the building has the highest averaged

Table 3.11: Values of the variables in Equation (3.6) describing the kerma per unit source strength inside a glass building caused by contamination on trees for a single house without any neighboring buildings. 'a', 'd', 'e' and 'f' have the dimension pGy per γ mm^{-2}. 'b' and 'c' are dimensionless.

	0.3 MeV	0.662 MeV	3.0 MeV
a	$1.42 \cdot 10^{17}$	$6.50 \cdot 10^{9}$	$1.12 \cdot 10^{10}$
b	39.4	21.6	20.8
c	0.048	0.10	0.12
d	1.07	2.66	10.2
e	1.12	2.77	10.6
f	0.0020	0.014	0.38

Table 3.12: Values of the variables in Equation (3.6) describing the kerma per unit source strength inside a glass building caused by contamination on trees for a house in a park scenario with two neighboring buildings. 'a', 'd', 'e' and 'f' have the dimension pGy per γ mm^{-2}. 'b' and 'c' are dimensionless.

	0.3 MeV	0.662 MeV	3.0 MeV
a	$4.24 \cdot 10^{18}$	$3.58 \cdot 10^{9}$	$3.90 \cdot 10^{42}$
b	42.7	20.9	95.6
c	0.041	0.095	0.025
d	1.19	2.98	11.7
e	1.23	3.09	12.1
f	0.0020	0.015	0.39

ratio because of the two extreme values with 116 ± 77 (without them it is still 10.5 ± 5.1). This source area in terms of the averaged ratio is followed by the ground in the city scenario with 16.7 ± 3.2, the ground in the park scenario with 7.32 ± 0.78, the walls and windows of the building with 6.54 ± 1.54, the roofs of neighboring buildings in the city scenario with 5.95 ± 2.18, the walls and windows of neighboring buildings in the city scenario with 3.75 ± 0.47, the walls and windows of neighboring buildings in the park scenario with 3.26 ± 0.48, the roofs of neighboring buildings in the park scenario with 1.67 ± 0.38 and at last the trees in the park scenario with 1.49 ± 2.18. The averaging of the ratio over the detection areas excluding the two extreme values shows less variety with the values for ground floor (6.60 ± 1.49), second floor (6.70 ± 1.38) and fourth floor (6.65 ± 1.56) being similar. Only the basement showed a lower averaged ratio of 4.04 ± 1.12.

Apart from the building material, the deviations of the two building models are caused e.g. by different building sizes. Furthermore, the glass building had an atrium

Table 3.13: Values of the variables in Equation (3.6) describing the kerma per unit source strength inside a glass building caused by contamination on trees for a house in a city scenario with eight neighboring buildings. 'a', 'd', 'e' and 'f' have the dimension pGy per $\gamma\,\mathrm{mm}^{-2}$. 'b' and 'c' are dimensionless.

	0.3 MeV	0.662 MeV	3.0 MeV
a	$4.70 \cdot 10^{20}$	$3.01 \cdot 10^{9}$	$9.10 \cdot 10^{9}$
b	47.0	20.3	20.0
c	0.030	0.078	0.092
d	1.78	4.55	18.6
e	1.83	4.65	18.9
f	0.0025	0.017	0.41

instead of a courtyard inside multistory house block and the multistory house block had light-shafts to the basement apart from the glass building. Moreover, the calculations were performed with different codes as the influence was already described in Section 2.2. Finally, those ratios underpin the importance of the determined factors for decision support systems as the kerma factors for the multistory house block were calculated for only one building height.

In conclusion, the results of this comparison emphasize the importance of taking into account adequate representations of construction geometries and materials when estimating kerma.

Table 3.14: Ratios of the kerma factor for the glass building divided by the respective factor for a multistory house block (Meckbach et al. 1988). The figures are given according to source and detection area for a primary gamma energy of 0.3 MeV.

	Basement	Ground floor	Second floor	Forth floor
On the building:				
Roof	-	-	-	7.85
Walls and windows	12.3	4.39	4.49	4.38
Ground:				
Park scenario (street and park)	7.65	11.6	9.42	8.14
City scenario (street)	2.76	24.1	21.6	30.2
Neighboring buildings:				
Roofs in a park scenario	-	2.25	2.88	3.68
Roofs in a city scenario	-	24.3	11.6	4.90
Walls and windows in a park scenario	1.62	4.16	4.91	5.83
Walls and windows in a city scenario	1.19	4.46	5.55	6.34
Trees:				
Park scenario	0.510	1.90	2.25	2.02

Table 3.15: Ratios of the kerma factor for the glass building divided by the respective factor for a multistory house block (Meckbach et al. 1988). The figures are given according to source and detection area for a primary gamma energy of 0.662 MeV.

	Basement	Ground floor	Second floor	Forth floor
On the building:				
Roof	-	-	271	4.04
Walls and windows	17.5	3.94	4.20	3.77
Ground:				
Park scenario (street and park)	4.88	11.0	8.62	8.66
City scenario (street)	2.83	23.9	21.1	35.4
Neighboring buildings:				
Roofs in a park scenario	-	1.86	2.09	2.55
Roofs in a city scenario	-	4.36	5.82	4.37
Walls and windows in a park scenario	1.77	3.47	4.12	5.95
Walls and windows in a city scenario	2.06	4.25	4.72	5.62
Trees:				
Park scenario	1.14	1.71	2.06	1.88

Table 3.16: Ratios of the kerma factor for the glass building divided by the respective factor for a multistory house block (Meckbach et al. 1988). The figures are given according to source and detection area for a primary gamma energy of 3.0 MeV.

	Basement	Ground floor	Second floor	Forth floor
On the building:				
Roof	-	383	27.7	2.26
Walls and windows	16.5	2.37	2.45	2.24
Ground:				
Park scenario (street and park)	2.03	6.13	4.74	5.06
City scenario (street)	1.14	11.2	9.47	16.3
Neighboring buildings:				
Roofs in a park scenario	0.223	0.250	0.319	0.649
Roofs in a city scenario	0.412	0.838	1.27	1.64
Walls and windows in a park scenario	1.08	1.93	2.27	2.02
Walls and windows in a city scenario	1.39	2.98	3.19	3.21
Trees:				
Park scenario	1.93	1.21	0.635	0.665

Chapter 4

Physicochemical properties of contaminants

By multiplication of kerma conversion factors with initial relative contamination levels, the initial relative kerma contributions to persons staying in given types of inhabited areas from different contaminated surfaces in the area can be estimated. Apart from drills and training purposes, detailed kerma modeling is an essential requirement in estimating any future doses to people living in a contaminated area, as these can obviously not be measured (e.g., residual doses in considering different recovery intervention strategies on different contaminated surfaces; ICRP 2007). This further includes the identification of appropriate time functions representing the natural weathering and migration processes of contaminants on each type of surface as it is essential in enabling estimation of future time integrated doses and for instance residual doses received by people after treatment in a prescribed way of a given type of surface in the inhabited environment. Both the initial levels and the post-deposition migration of the contaminants depend on their physicochemical characteristics.

4.1 Relative deposition of contaminants

To shed light on possible physicochemical forms of different contaminants potentially released in a nuclear power plant accident, the experience in this context from the Chernobyl and Fukushima accidents was first assessed. The radionuclide composition of released contaminants will depend on the source, while contaminant characteristics such as particle/gas release fractions, particle size distribution, solubility and oxidation states will also depend on the release processes, in particular on the temperature, pressure and the presence of air/oxygen (Lind 2006, Lind et al. 2009, Salbu 2001).

One of the most volatile contaminants (except noble gases) is iodine, which may be released in its elemental gas form (which has a very high deposition velocity to surfaces), in organic gas forms (where the deposition velocity is comparatively insignificant and thus in practice unimportant), and as condensed vapour on ambient aerosols, typically resulting in an AMAD (activity median aerodynamic diameter) in the range of 0.5-1 μm, which would have an intermediate deposition velocity (Andersson 2009*a*). Comparatively very high release fractions of iodine were as expected reported both in connection with the Chernobyl (0.2; IAEA 1991) and Fukushima (0.0002; Le Petit et al. 2014) accident. Iodine aerosol spectra obtained at different distances after the Chernobyl accident show a perfect Gaussian distribution with no signs of bimodality (e.g., Reineking et al. 1987, Jost et al. 1986), with an AMAD of about 0.5 μm, which is slightly smaller than that of the corresponding Cs aerosol. This iodine aerosol size distribution compares well with that registered after the Fukushima accident (Kaneyasu et al. 2012). However in these measurements the size distribution is a complete match with that for cesium, indicating that insignificant quantities of larger (fuel fragment) particles containing traces of cesium were at the times of measurement released at Fukushima. This suggests that the aerosol iodine can essentially be assumed to be purely condensed mode (on ambient particles). This is in-line with the high solubility and initial post-deposition mobility recorded for all the deposited iodine from Chernobyl at different distances (see, e.g., Roed 1990).

At the other end of the volatility spectrum, it was in connection with the Chernobyl accident found that contaminants of certain elements, which were not reported after the Fukushima accident, where the explosions were less powerful, were only released to the atmosphere in the form of comparatively large low solubility fuel particles, indicating that these would in general be expected to be highly refractory (undepleted from the fuel). These comprised ^{95}Zr, ^{95}Nb, ^{140}Ba, ^{140}La, $^{141/144}$Ce, $^{237/239}$Np, $^{238\text{-}242}$Pu, $^{241/243}$Am and $^{242/244}$Cm (Bobovnikova et al. 1990, Loshchilov et al. 1991, Kuriny et al. 1993, Kashparov et al. 2003, Salbu et al. 1994). It can not be ruled out that future accident scenarios might lead to releases of fuel particles. Apart from the fuel particles with sizes allowing them to follow air streams, part of the released fuel from the Chernobyl accident was in the form of either very large fuel fragments spread ballistically by the power of the release process, or very large conglomerates of nuclear fuel fused with melted zirconium (Kashparov et al. 2003). This part of the contamination was mainly in a form with a size range from several tens to more than a thousand microns (Kashparov et al. 2003), and mostly deposited within the nearest 2 km (Kashparov et al. 2003) - a zone where it makes absolutely no sense to attempt to model the contaminant distribution through atmospheric dispersion modeling. These huge particles/fragments, although probably locally dominant in some areas over very small distances, are estimated to contain only a small fraction of the total contamination (Kashparov et al. 2000). It

can thus be assumed that nearly all atmospherically dispersed particles carrying Zr, Nb, Ba, La, Ce, Np, Pu, Am and Cm are fuel aerosol particles. Measurements made after the Chernobyl accident showed that the smallest of these particles (which reached great distances) had a size of about 4 μm (Reineking et al. 1987, Rulik et al. 1989, Mala et al. 2013). Kashparov et al. (1996, 2000) reported of a fuel aerosol particle median diameter of some 5-6 μm corresponding to a crystallite size of the fuel. This actually seems consistent with results of smaller explosive tests (although clearly much less powerful) interacting on a matrix of uranium dioxide (Harper et al. 2007), where the smallest particles were found to be some 4 μm, but the greatest part of the aerosolized mass was in the ca. 5-20 μm range. In addition to pure fuel (uranium oxides) particles, also fuel mixes with construction materials and fire extinguishing materials have been reported in the near zones after the Chernobyl accident, which could have a different environmental mobility (Dobrovolsky & Lyalko 1995, Lind 2006).

Quite large (and comparable) fractions of Cs, Te and Rb (and to a somewhat lesser extent Sb and Mo) were released in connection with the Fukushima accident (Le Petit et al. 2014), and these should, based on Chernobyl data (e.g., Bobovnikova et al. 1990, Loshchilov et al. 1991, Kuriny et al. 1993) be expected to a considerable extent (probably somewhat less for Sb and Mo) to be volatilized from the fuel, forming submicroneous condensation particles. In the powerful Chernobyl explosion case investigations by Kuriny et al. (1993) show that even at distances up to about 50-60 km in some directions from the Chernobyl NPP, most of the deposited cesium was in the form of fuel particles. This agrees with results of experimental investigations of the effect of decontamination operations (water hosing on impermeable surfaces) carried out in Pripyat and hundreds of km away from the Chernobyl NPP, where the contamination was much easier removed in the nearest areas where it was associated with large low-solubility fuel particles (Andersson 2009*a*). The data of Salbu et al. (1994) show that the relationship between ^{90}Sr and ^{137}Cs in fuel particle deposition dominated areas was roughly 10 times higher than that in condensation particle deposition dominated areas. This can be taken as an indication that the fuel particles may have been depleted about 10 times more with respect to Cs than with respect to Sr. Some association with fuel particles could explain the slightly bimodal ^{137}Cs aerosol distribution measured by Reineking et al. (1987) as far away as Göttingen in central Germany after the Chernobyl accident, clearly showing the presence of some supermicron particles, which would be expected to have low solubility (Andersson 2009*a*). Again, the depletion fraction would be expected to vary according to the exact accident scenario conditions. The cesium aerosol measured after the Fukushima accident was generally submicron and characteristic of condensation mode (Kaneyasu et al. 2012), even though surprising processes some days after the start of the Fukushima accident also seem to have resulted in creation of some homogeneously cesium-containing spherical low solubility particles in the 2 μm range (Adachi et al. 2013). In connection with the Chernobyl accident, single element particles (e.g., ruthe-

nium, cesium) were recorded more than a thousand km from Chernobyl (Salbu 1988), indicating the complexity of processes during the release.

As for strontium, both fuel particle and small condensation aerosol fallout has been reported from the Chernobyl accident (Kashparov et al. 2003, Salbu et al. 1994). In the Chernobyl 30 km zone Konoplev et al. (1992), Askbrant et al. (1996) reported that 80-90 % of the strontium was associated with fuel particles. Even more than a hundred km away from the Chernobyl NPP, fuel particles constituted a significant part of the strontium contamination (Kuriny et al. 1993). The 'duality' of the fuel particles and condensation aerosols carrying strontium from the Chernobyl accident can be illustrated through the results of modified 'Tessier type' sequential extractions (see Tessier et al. 1979) carried out on soils contaminated with Chernobyl Sr at various distances from the Chernobyl NPP (Salbu et al. 1994). In the nearest investigated areas (at 50 km distance), by far the greatest part of the strontium in the soil was in strongly bound forms that could only be extracted with hydrogen peroxide or nitric acid, whereas in areas at greater distances (170-450 km), by far the majority of the strontium was in much more easily soluble forms. Parallel tests with stable Sr were employed to rule out effects of the different specific soil types. It should be noted that since ^{89}Sr, ^{90}Sr and ^{90}Y can not be determined in straightforward gamma spectrometry, but usually require chemical separation of strontium from other radionuclides in the sample, prior to radiometric analysis, they are 'inconvenient type' to study for instance in aerosol samples, where they have to a large extent been ignored both after the Chernobyl and the Fukushima accident (Steinhauser 2014). However, even in the Fukushima case, also ^{90}Sr contamination has been measured, in the vicinity of the Fukushima NPP Steinhauser (2014), at reported levels of about 1 kBq/kg soil (note: as this figure was published without indications of the depth/dimensions of the soil sample taken, it only qualitatively indicates the presence of strontium).

Ruthenium is special in that it has a very high elemental boiling point (2700°C), which would in practically any conceivable incident scenario prevent it from being volatilized and depleted from fuel material. However, if oxygen is present, it can be oxidized to its tetraoxide form, which is highly volatile (Kashparov et al. 1996, Hunt et al. 1991). From the Chernobyl accident, ruthenium radionuclides were in great amounts dispersed as condensation particles. This would be expected to have occurred in connection with the fire that followed the explosion. In fact, more ruthenium than cesium was released in connection with the Chernobyl accident (IAEA 1991), and this had a considerable impact on doses over the first few years (^{106}Ru has a half-life of very close to 1 year). The explanation offered by Le Petit et al. (2014) as to why only small amounts of ruthenium were measured in the environment after the Fukushima accident was that it seems that the fuel remained under water in the spent fuel pools (thus no air ingress). Instead the low volatility of ruthenium is reported to be consistent with overheating and

fuel melting of reactor cores. Oxidation could in reality occur in all accident scenarios currently represented in RODOS Andersson (2016). However, since this is a critical parameter, and oxidation obviously may not always be expected, it would be useful to run the DSS with different assumptions in this respect, both for training purposes and for early prognostic runs, when actual scenario specific processes have not yet been disclosed through measurements. It is well known that ruthenium in irradiated UO_2 fuel appears in small metallic alloy precipitations together with other fission product elements such as molybdenum, technetium, rhodium, and palladium (Ver et al. 2007). Such precipitations are in metallographic images seen as generally spherical white inclusions.

It is difficult to predict the physicochemical forms that would arise in any future nuclear power plant accidents, as these would be largely dependent on the exact inventory and accident processes at the NPP. Although for example the international Phebus Fission Product Programme (Gonfiotti & Paci 2018) shed some new light on possible releases in different NPP accident processes, the results reflect specific conditions and do not provide the range of details needed in operational nuclear preparedness for a specific NPP construction. However, perhaps in the future, results of such investigations could be used together with for example the Rapid Source Term Prediction (RASTEP) system (Knochenhauer et al. 2013), focusing on estimating the state of the specific NPP at the time of the accident using a Bayesian belief network to provide a probabilistic overview of possible accident states. By estimating the processes at the NPP, also the physicochemical forms of the various potentially released contaminants could be estimated. In a recent publication Sørensen et al. (2018) comment on the requirements to do this.

4.1.1 Distribution of contaminants for dry deposition

It is important to note that the background data for the derived deposition parameter values given in Table 4.1 may possibly not reflect the full range of possible parametric variation, as they are generally taken from a limited number of actual sets of environmental observations of deposition velocity of elemental iodine and relevant aerosols with different AMADs on different surfaces in connection with the Chernobyl accident, the Fukushima accident and various experimentation (Atkins et al. 1967, Belot 1977, Bonka 1989, Bonka & Horn 1980, Chamberlain 1953, 1967, Clough 1975, Collins et al. 2004, Freer-Smith et al. 2004, Garland 2001, Horn et al. 1988, Jonas 1984, Jonas & Vogt 1982, Kashparov et al. 2000, Lai & Nazaroff 2005, Little 1977, McMahon & Denison 1979, Mück et al. 2002, Nicholson 1988, Nicholson & Watterson 1992, Petroff 2005, Roed 1985, 1987*a*, 1988, 1990, Schwartz 1986, Sehmel 1973, Tschiersch & Georgi 1987, Vargas et al. 2016, Watterson & Nicholson 1996). However, these relations between deposition on different surfaces in the same scenario are obviously associated with comparatively much less variation than would relations between deposition velocities in

general to these surfaces. For example, deposition velocity depends on atmospheric stability. It has been demonstrated that under moderately stable atmospheric conditions (e.g., night time with clear sky), the friction velocity will only be about half of its value under neutral conditions (Jensen 1981). This in turn means that the eddy diffusion part of the deposition velocity will be reduced to about a quarter (IAEA 1994).

Also wind velocity can greatly influence deposition velocity. It has been demonstrated (Ahmed 1979) that between wind velocities of 2 and 14 m s^{-1}, the deposition velocity of naturally occurring radioactive aerosols increases by about a factor of 3, both to smooth (e.g., filter paper) and rough (grass) surfaces. It has also been shown (Freer-Smith et al. 2004, Slinn 1982) that deposition velocities of ca. 0.8 μm particles to trees can increase by a factor of 3-4 between wind velocities of 3-9 m s^{-1}. Even at moderate wind velocities (<5 m s^{-1}), the deposition of particles on walls facing the wind direction can be several times higher than that on leeside walls, for particles of sizes between about 10^{-2} and 20 μm (Freer-Smith et al. 2004). As the particle size increases beyond about 20 μm, the influence of wind speed on deposition increases markedly, due to the significance of the inertial impaction mechanism (Ahmadi & Li 2000). However, such large particles will in any case only remain airborne for short time, due to their large mass, and radionuclides associated with these would thus only contaminate rather small areas, depending on, e.g., the initial plume rise height (Hage 1961).

Finally, surface roughness is an important parameter. An indication of this influence can be seen from measurements made in the Roskilde area after the Chernobyl accident. Here deposition velocities to grassed surfaces varied rather widely (Roed 1990) between 1.8 and 8.8 m s^{-1}. However, if the length of the grass is taken into account (by dividing with the grass mass per unit area), the results are consistent within 10 %. It should therefore be noted that grassed areas in inhabited environments must be well-defined with respect to roughness (grass length). Differences of up to about a factor of 2 have been recorded (Lai & Nazaroff 2005) for deposition velocities of 0.9-9.1 μm particles to vertical sandpaper surfaces, ranging from Sand 60 to Sand 220. As shown in Table 4.1, dry deposition will vary to roof pavings of different materials having different roughness.

Deposition to coniferous trees and deciduous trees in leaf would according to available literature be similar Jonas (1984). However, during the winter period where deciduous trees are leafless, the deposition to these would be very low. According to measurements made after the Chernobyl accident Roed (1988), the needles or leaves receive some 98 % of the bulk 0.7 μm aerosol deposition on a tree. However, relatively not quite insignificant deposition velocities of trace particles have been reported to bare trees in forests (Höfken et al. 1981) (ca. 10-30 % of that to the same trees in leaf). This is explained by a higher wind speed in a forest with bare trees, but this effect would not be expected to be relevant for single trees in an inhabited area (Jonas 1984). Only trees

Table 4.1: Values for deposition to different surfaces relative to that on the grassed reference surface, for situations when dry deposition dominates. The term 'sd' denotes one standard deviation. All distributions are assumed to be normal. Values are given for elemental iodine gas and for particles with AMAD < 2 μm, 2-5 μm, 5-10 μm and 10-20 μm.

Surface	Elemental iodine		AMAD <2 μm		AMAD 2-5 μm		AMAD 5-10 μm		AMAD 10-20 μm	
	Mean	sd	Mean	sd	Mean	sd	Mean	sd	Mean	sd
Short grass	1.0	Ref. surf.	1.0	Ref. surf.	1.0	Ref. surf.	1.0	Ref. surf.	1.0	Ref. surf.
Bare soil	0.6	0.4	0.3	0.15	0.3	0.15	0.17	0.10	0.23	0.12
Soil and short grass	1.0	-	1.0	-	1.0	-	1.0	-	1.0	-
Small plants	0.8	0.5	1.4	0.7	1.6	0.8	1.0	0.5	1.2	0.7
Trees and shrubs	0.4	0.25	2.5	1.2	4.3	2.5	1.7	1.2	1.5	1.1
Paved area	0.2	0.1	0.25	0.15	0.75	0.35	0.3	0.15	0.3	0.25
Clay tile roof	1.5	0.3	0.8	0.1	3.0	0.8	1.9	0.5	1.5	0.4
Concrete tile roof	1.8	0.4	1.0	0.2	4.0	1.0	2.2	0.6	1.6	0.4
Fibre cement roof	1.6	0.3	0.9	0.1	3.6	0.9	2.1	0.5	1.6	0.4
Silicon covered fibre cement roof	1.0	0.2	0.7	0.1	2.5	0.6	1.7	0.4	1.4	0.4
Glass roof	0.5	0.1	0.4	0.1	1.4	0.4	1.5	0.4	1.3	0.3
Smooth metal roof	0.7	0.1	0.5	0.1	1.6	0.4	1.6	0.4	1.3	0.3
External walls	0.15	0.1	0.03	0.02	0.07	0.04	0.1	0.07	0.05	0.03

in leaf are thus considered in the table. In the period where they are not in leaf, the deposition to these surfaces may be assumed to be comparatively negligible. Unfortunately, no measurements of deposition velocities on surfaces in inhabited areas were reported after the Fukushima accident.

In the ERMIN model deposition on different surfaces in the inhabited environment is dealt with relatively to the deposition to a defined reference surface - in this case a newly shortcut lawn was selected (here a quick measurement the relationship between deposition on the grass and the underlying soil can also give a useful indication of the local extent of dry and wet deposition). In ARGOS and RODOS, the deposition process to the reference surface is dealt with in the applied atmospheric dispersion model tool, and not in ERMIN. ERMIN has been designed on the background of the Chernobyl and Fukushima experience to hold information for elemental iodine gas and for aerosols in four characteristic groups with different size ranges (AMAD less than 2 μm, 2 - 5 μm, 5 - 10 μm and 10 - 20 μm). The initial surface contamination relations within each group are all assumed to be representable by normal distributions. Typically reported values of the dry deposition velocity in units of 10-4 m s^{-1} to the reference surface are for these contaminant groups respectively of the order of 20, 4, 7, 30 and 130 (see references above), but case-specific factorial dependencies and thus overall uncertainties are large as explained above.

4.1.2 Distribution of contaminants for wet deposition

Table 4.2 shows estimates of the relative wet depositions to the different surfaces for each type of contaminant (again, the modeling of deposition to the shortcut grassed reference surface is in ARGOS and RODOS included in the atmospheric dispersion estimation tool). Also shown in this table is the fraction of the deposition to each surface which is practically instantaneously carried away, e.g., to sewers, with run-off water. Even during periods of strong rain, deposition to surfaces occurs through a combination of wet and dry deposition. However, unless the rain is extremely light or brief during such a phase or only leads to slight contaminant scavenging from the plume (not assumed for this deposition weather category), wet deposition will clearly be the dominant contamination process. Dry deposition contributions can thus be assumed to be negligible for the deposition weather category covered in this section. The initial run-off of contaminants in rainwater during the wet deposition process may depend on the surface roughness/permeability/porosity and rainfall intensity immediately before as well as during the wet deposition episode (Bonka & Horn 1980, Karlberg 1986, Sartor et al. 1974, Shaw et al. 2006). Further, the surface material type has been reported to be able to influence run-off through pH (Göbel et al. 2007).

On roofs compared with the grassed reference surface, the rain intensity incident per

Table 4.2: Values for initial deposition to different surfaces relative to that on the grassed reference surface, for situations when wet deposition dominates. The term 'sd' denotes one standard deviation. Also given are the fractions of the contaminants that immediately run off the surface with rain water during the deposition process.

Surface	Elemental iodine		Cationic ceasium		Other contaminants		Elemental iodine		Cationic ceasium		Other contaminants	
	Rel. deposition		Rel. deposition		Rel. deposition		Runoff fraction		Runoff fraction		Runoff fraction	
	Mean	sd	Mean	sd	Mean	sd	Mean	sd	Mean	sd	Mean	sd
Short grass	1.0	-	1.0	-	1.0	-	0.9	0.1	0.8	0.1	1.0	0.2
Bare soil	1.0	-	1.0	-	1.0	-	0	-	0	-	0	-
Soil and short grass	1.0	Ref. surf.	1.0	Ref. surf.	1.0	Ref. surf.	0	-	0	-	0	-
Small plants	1.0	-	1.0	-	1.0	-	0.99	0.01	0.7	0.2	0.8	0.2
Trees and shrubs	1.0	-	1.0	-	1.0	-	0.99	0.01	0.5	0.3	0.8	0.2
Paved area	1.0	-	1.0	-	1.0	-	0.97	0.03	0.55	0.15	0.55	0.15
Clay tile roof	0.8	0.2	0.8	0.2	0.8	0.2	0.99	0.01	0.3	0.04	0.35	0.05
Concrete tile roof	0.8	0.2	0.8	0.2	0.8	0.2	0.99	0.01	0.4	0.05	0.45	0.06
Fibre cement roof	0.8	0.2	0.8	0.2	0.8	-	0.9	0.1	0.8	0.1	1.0	0.2
Silicon covered fibre cement roof	0.8	0.2	0.8	0.2	0.8	0.2	0.99	0.01	0.8	0.1	0.9	0.1
Glass roof	0.8	0.2	0.8	0.2	0.8	0.2	0.99	0.01	0.95	0.05	0.95	0.05
Smooth metal roof	0.8	0.2	0.8	0.2	0.8	0.2	0.99	0.01	0.9	0.07	0.9	0.07
External walls	0.01	0.01	0.01	0.01	0.01	0.01	0	-	0	-	0	-

unit roof area will be less by cos(v), where v is the roof angle. It is assumed that common roofs have a slope of between 0 and 45 degrees. The initial retention after wet deposition of a range of Chernobyl contaminants (^{134}Cs, ^{137}Cs, ^{103}Ru, ^{106}Ru, ^{140}La and ^{140}Ba) with different physicochemical characteristics was recorded on different types of roof pavements with different slopes in Denmark following the Chernobyl accident (Roed 1987*a*). Cesium, which is in cationic form retained selectively and strongly in many building materials (Andersson 2009*a*), seems to be somewhat more efficiently retained on the roof than other contaminants. In general, the initial retention after the deposition process varies greatly with the roof material. For a range of materials and radionuclides, in the region of one-sixth to half of the contaminants were instantaneously removed with the run-off rain water. The exception from this was silicon-treated very smooth roofs with extremely low open porosity, where the run-off percentage was as high as 70-80 %. The main cause of variation here was by far the roof material and not the roof angle nor the radionuclide. Corresponding measurements made in Germany and the United Kingdom of wet-deposited Chernobyl radiocesium on clay and concrete roofs showed similar values (Roed & Jacob 1991, Sandalls & Gaudern 1988). It should be noted that contaminant run-off in rainwater is likely to be more dominant when the roof pores are already filled by rain than when contaminated rain falls on a dry roof (Roed 1987*a*). Ritchie et al. (1978) found that run-off from artificial surfaces in an urban area (e.g., roofs) would be virtually 100 % for all rainfall above an initially accumulated 3 mm, and if there has been rain within the previous hour the run-off will occur sooner.

Wet contamination levels on walls would in general be expected to be low, but associated with some variation according to factors such as the wind speed and direction during the contaminating process. In the Gävle area, which was wet-contaminated by the Chernobyl accident, a cesium contamination level on walls of slightly less than 1 % relative to the reference surface was recorded in 1988 (Andersson 1991). Figures reported by Roed & Jacob (1991) for the same location were by mistake somewhat higher (up to 3 %), as the contamination estimate for the grassed reference surface originated from a direct measurement, not allowing for contaminant penetration.

Only a couple of weeks after the Chernobyl accident, the initial retention on street pavings of wet deposited contaminants was measured in Sweden (Karlberg 1986, 1992). It was found that at this point, some 40-70 % of the radiocesium incident on asphalt and differently textured concrete street pavings had been removed, most likely to a very high extent already during the deposition phase, with the run-off water. Somewhat less had been removed from rough concrete paving slabs. Similar figures were found for the more refractory ^{140}Ba and ^{110m}Ag that were according to Rulik et al. (1989) associated with particles with a size of several microns after Chernobyl, indicating that particle size within the range of interest has little influence on the fraction of contamination lost with run-off water. Also Jacob et al. (1987) reported results of measurements of wet deposi-

tion of Chernobyl cesium, on different urban pavings in Germany. After 32 days, 28-32 % of the cesium remained on concrete pavings, and 36 % in an asphalted parking lot. A measurement after 40 days in an asphalted square showed 32 % retention. In a different area, the retention on concrete pavings after 160 days was found to be 33 %. By extrapolation from the curves obtained for the different locations, it could be estimated that the initial retention was in the German region of 35-50 %.

Experience with non-radioactive pollutants demonstrates that rain often leaves comparatively little contamination on vegetation (Gravenhorst & Höfken 1982). The deposition before run-off for trees is interpreted as the deposition per unit ground area covered by the tree. Contaminants in the precipitation above the tree canopy will either be intercepted by the tree, lost by throughfall (falling directly through leaf gaps or dripping from leaves, needles, twigs and branches), or lost by stemflow (flow down stems or boles). It has been reported (Alexander & Cresser 1995) that both for birch trees (Betula pubescens) and pine trees (Pinus sylvestris L.) the throughfall precipitation fraction is some 80 % of the incident precipitation. This is an average figure for a two-year study in the English Midlands, in an area with an annual precipitation of 930 mm. The interception was greatest for the pine tree during summer. This is in agreement with findings of other workers of 80-90 % throughfall and 2-5 % stemflow (Carlyle-Moses 2004, Kryshev 1996, Neal et al. 1993, Pryor & Barthelmie 2005). However, contaminants do not follow the water fractions evenly. Ronneau et al. (1987) reported that for Belgian spruce contaminated by a 7.4 mm rainfall episode after the Chernobyl accident significantly less ruthenium and lanthanum than cesium was intercepted. The explanation offered was biological absorption, e.g., by cesium exchange with potassium. It is also known that the rate of penetration of cations through the cuticle of vegetation is inversely related to the radius of the ion, and thus strongly favors cesium (Carini & Bengtsson 2001). Similar figures have been reported by other workers for cesium on spruce, whereas deciduous trees have somewhat lower cesium interception (Schell et al. 1996). Schimmack et al. (1991) have reported a cesium interception fraction of 20 % for beech trees. Deciduous trees would in winter conditions be expected to intercept considerably less than indicated by the numbers in Table 4.2. A rain interception fraction for a leafless pear tree has been reported, which was about half of that of an evergreen oak (Xiao et al. 2000). The same workers stress that interception fractions vary significantly dependent on factors like the structure of the tree and amount of rainfall.

Small plants would in general in the context interception be expected to be well represented by agricultural crops, due to sizes, shapes and textures. It has been reported that interception fractions will depend on the amount of rainfall, and plant type, as well as the stage of plant development (Müller & Pröhl 1993). It would seem that a likely interception range relevant to urban small plants would be 10-30 % for most radionuclides (IAEA 1994, Schell et al. 1996). This would correspond to assuming a leaf area index

value of about 5; retention coefficient of 0.2-0.3 mm, and rainfall of 4-10 mm (Müller & Pröhl 1993). The leaf area index is the total one-sided leaf canopy area per projected area ground covered by the plant.

For relatively short urban grass, the leaf area index would be of the order of 1-3 Kammann et al. (2005), Müller & Pröhl (1993), Rodriguez et al. (1999), and the retention coefficient would be 0.2 for most radionuclides (Müller & Pröhl 1993). With the same assumptions as for small plants regarding rainfall, this would give the retention/run-off expressed by the values in Table 4.2 (Müller & Pröhl 1993).

4.1.3 Distribution of contaminants for equal amounts of wet and dry deposition

ERMIN also operates with a case, where contributions of wet and dry deposition are of approximately the same magnitude. Since precipitation is very effective in washing out contaminants from a plume, this case would be associated with very little rain, and comparatively rather little contamination would be removed with the run-off water during the deposition process. This is for instance clear from investigations in areas in Russia, which received some rain as the contaminated plume carrying primarily cesium condensation particles passed from Chernobyl. Here, dry deposition rarely contributed more than one or two percent to the total deposition on the reference surface (Andersson et al. 2002). It would thus in most cases only take very little precipitation during the plume passage to make wet deposition the dominant mechanism of contamination. Table 4.3 shows estimates of the relative depositions to the different surfaces for each type of contaminant assuming that half of the deposition is wet and the other dry (simple averaging with parameters described above). Also the fractions of the deposit removed by run-off water during the contamination process are estimated on the basis of the same literature as used for the wet deposition mode, but assuming very little water. The rainfall rate is here assumed to be well below 1 mm per hour. Experimental and theoretical work has demonstrated that at low precipitation values (< ca. 0.5 mm), the majority of a contamination deposited in solution on a grassed area will remain on the grass (Bonka & Horn 1980).

Other modes of deposition (e.g., deposition in fog, deposition in snow and deposition to snow covered landscape) still remain to be implemented in the ERMIN model, although some parametric reviews have been conducted.

4.1.4 Application on a semidetached house

As pointed out in the introduction of this chapter the initial relative kerma contributions to persons staying in given types of inhabited areas caused by different contaminated

Table 4.3: Values for initial deposition of different contaminant groups to different surfaces relative to that on the grassed reference surface, for situations when wet and dry deposition are about equal in magnitude. The term 'sd' denotes one standard deviation. All distributions are assumed to be normal. Also given are the fractions of the contaminants that immediately run off the surface with rain water during the deposition process.

Surface	Elemental iodine		AMAD <2 μm		AMAD 2-5 μm		AMAD 5-10 μm		AMAD 10-20 μm		Elemental iodine		Cationic ceasium (<2 μm)		Other contaminants	
	Rel. deposition Meansd		Rel. deposition Meansd		Rel. deposition Meansd		Rel. deposition Meansd		Rel. deposition Meansd		Runoff fraction Meansd		Runoff fraction Meansd		Runoff fraction Meansd	
Short grass	1.0	Ref. surf.	1.0	-	1.0	-	1.0	-	1.0	-	0.3	0.1	0.2	0.1	0.2	0.2
Bare soil	0.8	0.2	0.7	0.2	0.7	0.2	0.6	0.2	0.6	0.2	0	-	0	-	0	-
Soil and short grass	1.0	-	1.0	Ref. surf.	1.0	Ref. surf.	1.0	Ref. surf.	1.0	Ref. surf.	0	-	0	-	0	-
Small plants	0.9	0.3	1.2	0.4	1.3	0.4	1.0	0.3	1.1	0.4	0.3	0.3	0.1	0.1	0.15	0.15
Trees and shrubs	0.7	0.2	1.8	1.0	2.5	1.0	1.4	0.7	1.2	0.6	0.3	0.3	0.05	0.05	0.15	0.15
Paved area	0.6	0.1	0.7	0.2	0.9	0.2	0.7	0.1	0.7	0.1	0.3	0.3	0.05	0.05	0.05	0.05
Clay tile roof	1.2	0.8	0.8	0.3	1.8	0.5	1.3	0.4	1.2	0.4	0.3	0.2	0.1	0.06	0.1	0.06
Concrete tile roof	1.5	0.9	0.9	0.3	2.4	0.6	1.5	0.4	1.2	0.3	0.3	0.2	0.2	0.1	0.2	0.1
Fibre cement roof	1.3	0.8	0.8	0.3	2.2	0.5	1.5	0.4	1.2	0.3	0.3	0.2	0.03	0.02	0.03	0.02
Silicon covered fibre cement roof	1.4	0.8	0.7	0.2	1.7	0.4	1.3	0.3	1.1	0.2	0.5	0.3	0.4	0.2	0.4	0.2
Glass roof	0.7	0.2	0.5	0.1	0.7	0.2	0.6	0.2	1.0	0.3	0.6	0.3	0.6	0.2	0.6	0.2
Smooth metal roof	0.9	0.2	0.6	0.2	1.2	0.3	1.2	0.3	1.1	0.3	0.6	0.3	0.55	0.2	0.55	0.2
External walls	0.07	0.05	0.02	0.015	0.04	0.03	0.06	0.04	0.03	0.02	0	-	0	-	0	-

surfaces can be determined by multiplying kerma conversion factors with initial relative contamination levels. As an example, this was performed for a semidetached house as it is described in Section 2.2. This type of urban environment with neighboring buildings was useful for demonstration as all possibly kerma contributing surfaces are included in this scenario. Furthermore, 0.662 MeV was chosen as an example source energy representing the contamination of ^{137}Cs as it has been of main concern in connection with the Chernobyl and Fukushima incidents (Imanaka et al. 2015). Thus, the employed kerma conversion factors are those given in Table 2.7 and were multiplied by the initial contamination level for all deposition scenarios and particle characteristics given in Tables 4.1 to 4.3 mentioning that the respective value for the roof is based on averaging over all roof materials. The results are presented in diagrams for the different parts of the semidetached house assuming once the ground to be paved (Figure 4.1) and once to be grassed (Figure 4.2), but it has to be mentioned that some of the particle characteristics occur less likely as e.g. in Section 4.1 was mentioned that the cesium aerosol measured after the Fukushima accident was generally submicron.

The results show that particles of AMAD >2 μm would cause the highest kerma to a person inside a semidetached house in relation to contamination level, especially those of AMAD $2-5$ μm. Looking at contributing surfaces the bars show that apart from the ground floor the kerma inside a semidetached house would be caused almost exclusively by deposited particles on the roof. Therefore, only by looking at the ground floor a difference between paved and grassed ground can be seen as fewer particles deposit on paved areas than on grassed areas.

4.2 Post-deposition contaminant mobility on outdoor surfaces

As described in Section 4.1, experience from Chernobyl and Fukushima has shown that a large nuclear power plant accident can lead to airborne releases of a wide range of radionuclides with different physicochemical forms (more or less reactive gases, aerosols of different sizes and with different features with respect to environmental mobility). In general, it is for the purpose of modeling post-deposition migration processes important to distinguish between elemental iodine, which may deposit in large amounts, but will in general be rapidly removed by natural processes (precipitation) on impermeable surfaces (Roed 1987*b*), and deposited contaminant particles with different characteristics. Radioiodine dose rate contributions may be high in an early phase, but due to the short physical half-life of the most abundant iodine isotopes in a nuclear power reactor, radioiodine would not be likely to have important influence on external doses in later (recovery) time phases, particularly if also other radionuclides than iodine and noble gases (notably cesium isotopes) are released.

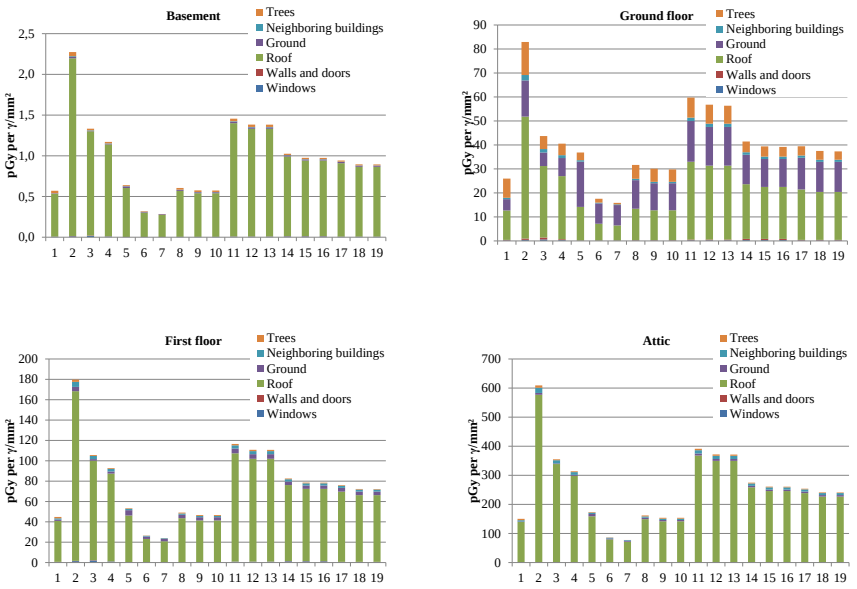

Figure 4.1: Initial air kerma after deposition in parts of a semidetached house distributed on different source areas in an urban environment with a paved ground, neighboring buildings and trees for different deposition scenarios. Bars $1-4$ represent dry, bars $5-7$ wet and bars $8-19$ an equal amount of dry and wet deposition. Different particle sizes with AMADs of <2 μm in bars 1 and $8-10$, for $2-5$ μm in bars 2 and $11-13$, for $5-10$ μm in bars 3 and $14-16$ and for $10-20$ μm in bars 4 and $17-19$. The first run–off of rain water is represented in bars 6, 9, 12, 15, 18 for cesium cations and in bars 7, 10, 13, 16, 19 low solubility particles. The results are given in pGy per emitted photon of 0.662 MeV on a grassed reference surface of 1 mm^2.

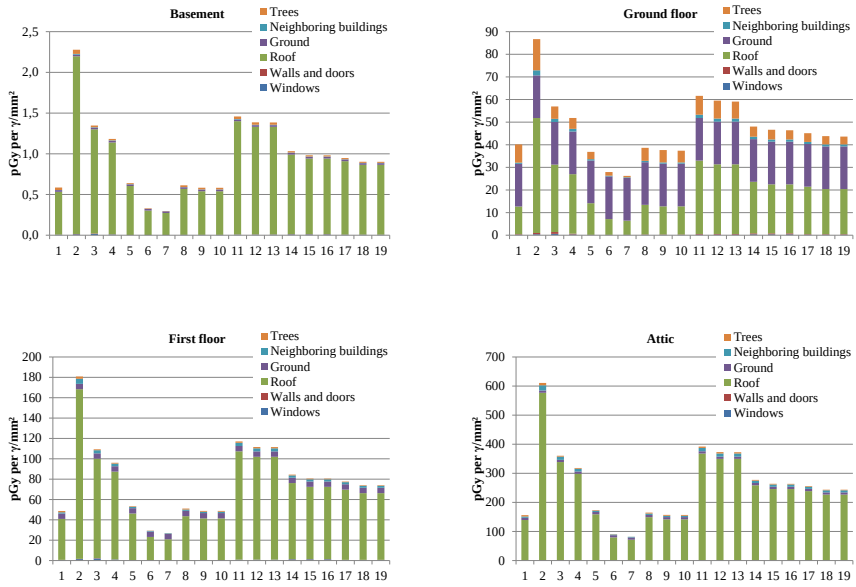

Figure 4.2: Initial air kerma after deposition in parts of a semidetached house distributed on different source areas in an urban environment with a grassed ground, neighboring buildings and trees for different deposition scenarios. Bars $1-4$ represent dry, bars $5-7$ wet and bars $8-19$ an equal amount of dry and wet deposition. Different particle sizes with AMADs of <2 μm in bars 1 and $8-10$, for $2-5$ μm in bars 2 and $11-13$, for $5-10$ μm in bars 3 and $14-16$ and for $10-20$ μm in bars 4 and $17-19$. The first run–off of rain water is represented in bars 6, 9, 12, 15, 18 for cesium cations and in bars 7, 10, 13, 16, 19 low solubility particles. The results are given in pGy per emitted photon of 0.662 MeV on a grassed reference surface of 1 mm^2.

If we, as argued in Section 4.1, concentrate on those particles that have a size that allows them to follow air streams over longer distances, these may be split into four different categories or model 'bins' (the general approach adopted in the ERMIN model). This includes a group of particles ranging in size between 0 and 2 μm, which is particularly representative of condensation mode contamination attached to ambient particles (Andersson 2009*a*). As mentioned in Section 4.1 these typically had a radius of the order of half a micron in the Chernobyl and Fukushima cases. The contaminants associated with condensation mode particles are assumed to be rather readily soluble and would thus rapidly be on ionic form after deposition in the outdoor environment, as frequently reported after the Chernobyl accident (Andersson 2009*a*, Roed 1987*b*). Nevertheless, to illustrate the complexity of these issues, it should be mentioned that in an area very far from the release point from the Chernobyl accident, some low solubility cesium particles of this size range have been found, and increasing soil to milk contaminant transfer factors in that area over the first two years after the accident suggested that natural particle dissolution in the environment took considerable time (Hansen & Hove 1991). However, focusing on external dose, contaminants embedded in low solubility particles would in general be expected to be more rapidly weathered away from an impermeable surface than cesium on cationic form (Andersson 2009*a*). Therefore, modeling post-deposition mobility of such small low solubility particles in the same way as cationic cesium, which will be very strongly fixed in upper layers of many types of urban surface, may make the dose contribution estimates somewhat conservative.

Radiocesium has a particularly great importance in modeling external doses after nuclear power plant accidents, as it will evaporate at comparatively low temperatures, and thus be likely to be released in great quantities from large accidents. At the same time, the decays of the key isotopes of concern in this context, ^{134}Cs and ^{137}Cs, lead to emission of gamma photons with quite high energy and photon yield, particularly ^{137}Cs has a long physical half-life of ca. 30 years and the cesium cation has a rare marked tendency to be fixed in a range of minerals and also to be retained in the upper soil layers (Andersson 2009*a*). External dose rate contributions from cesium thus only slowly decline through natural processes, and would be of major concern in recovery (late phase) decisions for management of contaminated inhabited areas, as seen after both the Fukushima and Chernobyl accidents.

There is currently insufficient data available to enable specific detailed modeling of the retention of other radionuclides on ionic form on urban surfaces. However, high specific binding strength of cesium compared with any other potentially relevant ions has also been reported in laboratory studies of many urban construction materials (De Preter 1990). Further, it has been demonstrated in field studies after the Chernobyl accident that the retention of cationic cesium in a variety of construction materials is consid-

erably greater than that of, e.g., ruthenium (Roed 1987*b*), which was released in even greater quantity from the Chernobyl accident than was cesium (IAEA 1991), but where the relevant isotopes, ^{103}Ru and ^{106}Ru are considerably more short-lived (physical half-lives of respectively 39.5 d and 1.0 y). Strontium deposited in water solution has for example been found to weather off a clay roof with a half-life of only ca. 2.5 months (Brown et al. 2016), whereas most of the cesium deposited in solution on a clay roof would remain over decades (Andersson 2009*a*). Thus modeling retention of all ionic contaminants using parameters derived for cesium would be expected to make the dose estimates somewhat conservative.

Larger low solubility particles will generally be expected to be removed from impermeable surfaces at a much faster rate than cationic cesium (Andersson 2009*a*). The main mechanisms driving the 'natural' removal of all contaminants are in general precipitation and anthopogenic impact such as traffic and routine cleaning (Wilkins 1987, Andersson 2009*a*). Although time, rain intensity and rain frequency all have importance (Madoz-Escande et al. 2004, 2005), data is not available to allow quantitative modeling according to these factors, and in any case, weather predictions over long time periods would be too uncertain to make use of such data. Therefore empirical formulae based on typical observations of the overall natural weathering process are used in the ERMIN model. The following sections report on the newest version of weathering parameter formulae and datasets, which have been derived for use in ERMIN. In the event of a new contaminating incident, case specific parameter studies should be made to continuously further improve and target model parameters. Also, an investigation of aerosol characteristics (including solubility) should be made so that the user could for the purpose of long-term dose prediction target the model assumptions for different aerosol groups to the specific case.

4.2.1 Contaminant mobility from paved areas

For modeling the mobility of contaminants on paved areas, such as streets and walkways, the primary dataset of interest reflects the results of in situ measurements on such surfaces of radiocesium in the town of Gävle, Sweden, which received one of the highest levels of contamination outside the former Soviet Union from the Chernobyl accident (Andersson 2009*a*). These measurements were made with collimated germanium detectors over a period stretching from the first week after the accident to more than ten years later (Karlberg 1988, Andersson 1991, Andersson et al. 2002).

The weathering process has generally been found to be rapid on such surfaces, although a bit of variation has been observed due to differences in traffic intensity, and also precipitation rates and routine street cleaning would play a role. Experiments have shown that there are no strong binding mechanisms of cationic cesium in asphalt bitumen

(Andersson 1991), as there are in for example soil or common roof tiles. It has also been demonstrated that the downward penetration of cesium into an asphalted road surface can over a 2-year weathering period be expected to be less than one millimeter (Andersson 1991). Although the cesium may be selectively bound to street dust (De Preter 1990), this does not slow down the removal rate, as the street dust is not strongly attached to the road surface (Andersson 1991).

As there does not appear to be significant contaminant ion specific fixation mechanisms at play on these surfaces, the results recorded for cationic cesium should apply also to other contaminant ions. This agrees with the results of (Warming 1982, 1984) in a tracer experiment where ^{86}Rb, ^{103}Ru and ^{140}Ba were sprayed onto asphalt and concrete pavements in a solution, and a very large part of all tracers could be removed by simple firehosing some days later.

The empirical weathering formula that was derived from the measurement time series recorded in Gävle was found to be generally consistent with information from in situ measurements over shorter periods of time of Chernobyl cesium weathering in Bavaria (Jacob et al. 1987). This formula is used in ERMIN for all contaminants deposited in more or less readily soluble form:

$$C(t) = C_0 \cdot \exp(-\ln(2) \cdot t/T_{1/2}) \cdot (f_1 \cdot \exp(-\ln(2) \cdot t/T_{w1}) + f_2 \cdot \exp(-\ln 2 \cdot t/T_{w2})) \quad (4.1)$$

where $C(t)$ is the contaminant concentration at time t, C_0 is the initial contaminant concentration after the deposition process, $T_{1/2}$ is the physical half-life of the radionuclide, f_1 is the fraction (on average ca. 0.7 on streets; estimated standard deviation 0.2) of the contamination removed with a short half-life of T_{w1} (ca. 120 days on streets; estimated standard deviation 40 days), and $f2$ is the fraction $(1 - f_1)$ of the contamination removed with a longer half-life of T_{w2} (on average ca. 3 years on streets; estimated standard deviation 1 year). The weathering process may take considerably longer, if there is very little human activity in the area, as recorded in areas deserted after the Chernobyl accident (Andersson 2009*a*).

The case is different if low solubility fuel particles are at play. Sartor et al. (1974) found experimentally that removal of contaminants in particle form from impermeable road surfaces was largely independent of particle size, when the particles were larger than about 10 μm. Smaller particles are however increasingly difficult to remove, as they can enter cavities in structures, and be less prone to weathering. According to aerosol spectra recorded after the Chernobyl accident, ^{140}La and ^{140}Ba were representatives of the more refractory element radionuclides released (in fuel particles), having a contaminant AMAD (activity median aerodynamic diameter) of several microns (typically 2-5) even in the most remote areas to which dispersion was recorded (Rulik et al.

1989, Nair & Darley 1986). This indicates that fuel particles may be expected to be supermicroneous, in-line with findings from explosions impacting on materials that do not undergo phase transition during the explosion (Andersson et al. 2008). This would also be expected to have been the case in Denmark, where ^{140}La and ^{140}Ba contaminants were recorded to have different characteristics with respect to surface weathering, than did for instance the radiocesium isotopes that predominantly deposited in readily soluble submicron particle form. Over the first 22 days that followed the initial contamination deposition in Roskilde, Denmark, from the Chernobyl accident, some 22 % of the lanthanum and barium was washed off concrete surfaces through natural processes (Roed 1987*b*, 1990). This corresponds to a weathering half-life of about 60 days. It is likely that routine street cleaning would speed up this process further, so that the value of T_{w3} of 60 days (with an estimated standard deviation of 20 days) may be seen as a conservative estimate for dose estimation from particles in the 2-5 μm range.

On the basis of experimental investigations of attachment of particles of different sizes to street surfaces (Sartor & Gaboury 1984, Sartor et al. 1974, Bender & Terstriep 1984, Owen et al. 1960, Terstriep et al. 1982), it would be expected that particles in the 5-10 μm range (and thus according to Sartor et al. (1974), also likely the particles in the 10-20 μm range) would have a half-life, T_{w3}, of the order of 30 days (standard deviation estimated to 15 days). The environmental dissolution timespans in soils reported by Kashparov et al. (2004) are long compared with the time constants determining natural removal of deposited fuel particles, and may thus be ignored in this context.

The general formula for contaminants deposited in fuel particle form becomes:

$$C(t) = C_0 \cdot \exp(-\ln(2) \cdot t/T_{1/2}) \cdot \exp(-\ln(2) \cdot t/T_{w3}) \tag{4.2}$$

4.2.2 Contaminant mobility from roofs

Measurement series performed in Denmark over a period of nearly 15 years after the Chernobyl accident of the level of radiocesium contamination level on a range of common roof materials (concrete, slate, clay tile) showed that whereas the initial retention on the roof of contaminants after a wet deposition process varies considerably between roofing materials (see Section 4.1.2), the subsequent long-term weathering rates were after the Chernobyl accident found to vary rather little between the examined range of materials (Andersson 2009*a*). A shorter time-series of measurements made on German roofs (Roed & Jacob 1991) support the general validity of these findings, although only done for concrete and clay tile roofs. Common to these materials is that they generally contain minerals, which selectively and strongly fix and retain cesium cations (De Preter 1990, Andersson 1991). Other radionuclide ions would be expected to be less strongly held (Andersson 2009*a*, Brown et al. 2016), although it has been demonstrated that

ruthenium in representative ionic forms is not very easily removed from a roof clay or concrete tile surface (Andersson 1991). ERMIN uses weathering data based on the Chernobyl time series cesium measurements (Andersson 2009*a*) for all radionuclides in ionic form for these types of roof materials. This may lead to conservative estimates of long term doses for other radionuclides, which are in reality weathered off faster. However, the physical half-lives of other radionuclides that would on the basis of past experience be expected to be potentially released in relatively large amounts and could impinge on external dose (see part 1 of the paper) are considerably shorter than that of ^{137}Cs, and cesium is among the more volatile elements with generally comparatively high release probability.

The empirical formula thus applied in ERMIN for all contaminant ions deposited in more or less readily soluble form on many types of roofs (clay, concrete, slate) is:

$$C(t) = C_0 \cdot \exp(-\ln(2) \cdot t/T_{1/2}) \cdot (f_1 \cdot \exp(-\ln 2 \cdot t/T_{w1}) + f_2 \cdot \exp(-\ln(2) \cdot t/T_{w2})) \quad (4.3)$$

where $C(t)$ is the contaminant concentration at time t, C_0 is the initial contaminant concentration after the deposition process, $T_{1/2}$ is the physical half-life of the radionuclide, f_1 is the fraction (on average ca. 0.5 on these roof types; estimated standard deviation 0.1) of the contamination removed with a short half-life of T_{w1} (ca. 730 days; estimated standard deviation 85 days), and f_2 is the fraction $(1-f_1)$ of the contamination removed with a longer half-life of T_{w2} (on average ca. 35 years; estimated standard deviation 7 years). Also sandstone roof tiles contain intact micaceous substances (De Preter 1990), and would be expected to retain cesium in the same way.

The exception regarding radionuclide ions concerns very smooth (non-porous) surfaces, where experimentation suggests that the weathering of cationic cesium (and very likely also other ions) on a glass roof would occur with a half-life of the order of 95 days (Brown et al. 2016), and investigations from the European ECP-4 project (Mamaev et al. 1993) suggest a similar value for smooth (uncorroded) metal roof covers.

Regarding low solubility particle contamination, these types of surfaces would not constitute an environment that could over a reasonable time (compared with weathering half-lives) lead to very much fuel particle dissolution (Kashparov et al. 2004). For the parameterization time series data exists for Chernobyl lanthanum and barium, associated with 2-5 μm particles, as measured on roof pavings (concrete, slate, clay tile) in Denmark. These contaminants were found to be weathered off the surface much more rapidly than cesium (Roed 1987*b*). A reasonable weathering half-life, T_{w3}, would on the basis of that data seem to be of the order of 100 days. A probably dose conservative estimate of the weathering half-life for 5-10 μm (and larger) particles would judging from the data for paved horizontal surfaces be expected to be of the order of 60 days.

The general formula for contaminants deposited in fuel particle form becomes:

$$C(t) = C_0 \cdot \exp(-\ln(2) \cdot t/T_{1/2}) \cdot \exp(-\ln(2) \cdot t/T_{w3}) \tag{4.4}$$

4.2.3 Contaminant mobility from outer walls

For weathering of contamination on outdoor walls, generally very sparse information is available, primarily from measurements over time in Gävle (Andersson et al. 2002). It is clear that the weathering function on walls is not subject to strong fixation mechanisms, as construction bricks used for building walls are typically fired at such high temperatures that no specific strong ionic fixation sites remain (Andersson 2009*a*), and no significant difference was recorded in Gävle between plastered walls and clay brick walls (Andersson et al. 2002). The slow removal is largely due to wind abrasion and any horizontal precipitation components. It can not be ruled out that larger particles may be more prone to wind-driven abrasion than small ones, which might be more protected in material cavities of suitable sizes, but the required data is not available to allow distinguishing on this parameter. Again a dose conservative approach is used, assuming that the larger particle contamination is weathered off walls at the same rate as is small particle contamination.

The generally assumed formula for contaminants deposited walls is (Andersson et al. 2002):

$$C(t) = C_0 \cdot \exp(-\ln(2) \cdot t/T_{1/2}) \cdot \exp(-\ln(2) \cdot t/T_{w1}) \tag{4.5}$$

where $C(t)$ is the contaminant concentration at time t, C_0 is the initial contaminant concentration after the deposition process, $T_{1/2}$ is the physical half-life of the radionuclide, and T_{w1} is the weathering half-life of ca. 7 years (estimated standard deviation 2 years).

4.2.4 Contaminant mobility from grass and small plants

A large number of workers have over the years estimated the weathering half-life of contaminants on grass and small plants according to experimentation, as such data is needed in traditional radioecology studies. The majority of experiments were carried out prior to the Chernobyl accident, but also some later studies have been made (Martin 1963, Cline et al. 1965, Milbourn & Taylor 1965, Heinemann & Vogt 1980, Kirchmann et al. 1966, Chadwick & Chamberlain 1970, Krieger & Burmann 1969, Aarkrog et al. 1988, BIOMOVS 1991, Mück et al. 1994, Eriksson & Rosén 1998, IAEA 2009). There is no clear trend from this data with respect to dependence on physicochemical characteristics, where these have been specified, and it is thus assumed in the modeling that

all the contaminant material is washed off vegetation at the same rate. Based on the above references, the default value in the ERMIN model of the natural weathering half-life of contaminants from grass is $T_w = 16$ days (with a standard deviation of 7 days). This value is somewhat shorter than the value of 25 days that has been recommended by Müller & Pröhl (1993) for the purpose of the ECOSYS ingestion dose model. However, the 25 days correspond to the results of a field study where the field was completely protected against rain (Krieger & Burmann 1969). It should be noted that in case of prolonged rain, the natural weathering half-life may be shortened considerably (Madoz-Escande et al. 2004, 2005, Madoz-Escande & Santucci 2005). On small plants, a similar typical value of $T_w = 12$ days (estimated standard deviation of 5 days) was derived from the same literature.

The formula applied in ERMIN to describe the concentration of contaminants on these surfaces at any time t is of the form

$$C(t) = C_0 \cdot \exp(-\ln(2) \cdot t/T_{1/2}) \cdot \exp(-\ln(2) \cdot t/T_w) \tag{4.6}$$

where $C(t)$ is the contaminant concentration at time t, C_0 is the initial contaminant concentration after the deposition process, $T_{1/2}$ is the physical half-life of the radionuclide, and T_w is the weathering half-life.

4.2.5 Contaminant mobility from trees and shrubs

Nearly half of the contamination on trees or shrubs will according to literature generally be removed with a short half-life, of about 30 days with a standard deviation of about 2 weeks (Mamikhin & Klyashtorin 2000, Nygren et al. 1994, Roed 1988). It would seem reasonable to assume that the mechanism largely responsible for this transfer is the first heavy rainshowers (Roed 1988). A small part of the order of 4 % (estimated standard deviation of 4 %) is assumed to remain on the tree/shrub largely until it is felled (Mamikhin & Klyashtorin 2000, Roed 1988), and the rest is assumed to have a weathering half-life of some 1.7 years, with an estimated standard deviation of about 1 year (Mamikhin & Klyashtorin 2000, Linkov et al. 1997). There may possibly be some species of trees for which this is not quite true, but the data available is sparse. On top of this, for coniferous trees, the shedding of needles will occur continuously with a half-life that depends on the exact species and climate, but can be assumed to be of the order of 4 years, with a standard deviation of about 2 years (Laboratory 2018). For deciduous trees/shrubs (in leaf at deposition), it is assumed that they shed their leaves during the first autumn, where nearly all the contamination is on the leaves (Roed 1988). The time may here be assumed to vary rather homogeneously within about 8 weeks of the autumn.

It should be noted that the above parameter values were based almost exclusively on data for deposited soluble radiocesium aerosols, and only Roed (1988)reported di-

rectly applicable information for garden trees. The mechanisms and/or rates of loss may well be different in forests. However, the values for cesium fit reasonably with results obtained after artificial contamination of respectively pine and birch forest tree crowns with ^{90}Sr in soluble form (Alexakhin & Naryshkin 1977). It is assumed that all contaminants behave in this way on trees and shrubs. No data is available for large low solubility contaminant particles, but these would be assumed to be removed somewhat more easily from the trees by precipitation, as they are on for example street surfaces. Applying values for cesium in solution would thus make the tree/shrub dose contribution estimates somewhat conservative.

Small amounts of long-lived radionuclides in soil will be transferred from the soil to trees/shrubs by root uptake. This will correspond to only few percent of the material initially deposited directly on the tree (Linkov et al. 1997), and is not considered in ERMIN. Unlike forested areas, leaves/needles in urban areas are generally not left to form a litter layer after they are shed. Therefore urban tree/shrub soil uptake will be much less than that in forests. The focus in the context of urban external dose is on the initially potentially very high tree/shrub canopy contamination due to the very effective aerosol filter constituted by foliage if the tree/shrub was in leaf at deposition Roed (1990). Only trees in leaf during deposition are considered in ERMIN, as the contamination level will otherwise be much less significant.

The formula applied in ERMIN to describe the concentration of contaminants on these surfaces at any time t is of the form

$$\begin{aligned} C(t) = C_0 \cdot \exp(-\ln(2) \cdot t/T_{1/2}) \\ \cdot (f_1 \cdot \exp(-\ln(2) \cdot t/T_{w1}) + f_2 \cdot \exp(-\ln(2) \cdot t/T_{w2}) + f_3) \end{aligned} \tag{4.7}$$

where $C(t)$ is the contaminant concentration at time t, C_0 is the initial contaminant concentration after the deposition process, $T_{1/2}$ is the physical half-life of the radionuclide, f_1 is the fraction (on average ca. 0.46, standard deviation of ca. 0.07) of the contamination removed with a half-life of T_{w1} = ca. 30 days, f_2 is the fraction $(1 - f_1 \check{} f_3)$ of the contamination removed with a half-life of T_{w2} (on average ca. 1.7 years for deciduous and ca. 1.2 years for coniferous trees/shrubs taking into account continuous needle shedding), f_3 is the fraction (0.04) of the contamination assumed to stay until the tree/shrub is removed, and T_{w1} and T_{w2} are the corresponding removal half-lives, as given above. Deciduous foliage shedding in the first autumn after the deposition occurred is assumed to change f_1 and f_2 to 0.

4.2.6 Contaminant mobility in soils

The concentration of contaminants in soil is described in ERMIN as a function of time and vertical soil depth by a convection-dispersion model, as suggested by Schuller et al. (1997), Bunzl et al. (2000), Kirchner et al. (2009):

$$C(x,t) = C_0 \exp(-\ln(2) \cdot t/T_{1/2}) \cdot (\frac{1}{\sqrt{\pi D_s t}} \cdot \exp(-\frac{(x-v_s t)^2}{4D_s t}) - \frac{v_s}{2D_s} \cdot \exp(\frac{v_s}{D_s} x) \cdot erfc(\frac{x+v_s}{2\sqrt{D_s t}})) \quad (4.8)$$

Here $T_{1/2}$ is again the physical half-life, whereas D_s is the effective dispersion coefficient, and v_s is the convective velocity, defined respectively as

$$D_s = \frac{D}{1 + K_d \frac{\rho}{\varepsilon}} \quad (4.9)$$

and

$$v_s = \frac{v_w}{1 + K_d \frac{\rho}{\varepsilon}} \quad (4.10)$$

where D is the dispersion coefficient, v_w is the mean pore water velocity, K_d is the distribution coefficient of the contaminant in the soil, ρ is the bulk soil density, and ε is the soil porosity.

Bossew & Kirchner (2004), Kirchner et al. (2009) have made thorough reviews of D_s and vs by soil type on the basis of numerous assessments over different parts of Europe. For radiocesium from Chernobyl, the resultant values were found to be as shown in Table 4.4. These values are in agreement with those reported by Ivanov (2009).

Of course the downward migration of contaminants in fuel particles is governed by entirely different physicochemical processes. Ivanov (2009) recorded much lower effective diffusion coefficients for contaminants contained in dispersed fuel particles deposited on soil. For sandy, loamy and peaty soils, these were all found to be of the order of 0.015 cm^2 per year. The dispersed fuel particles measured by Ivanov (2009) were found to range up to about 18 μm in size, and the larger of these (>4 μm) seem as might be expected to be somewhat better retained in very top layers of undisturbed soils. Based on these results, the downward migration of fuel particles is seen to be exceedingly slow, and it could only lead to limited conservatism in external dose estimates to assume that the particles remain in the very top of the soil until they dissolve over months or years.

However, once the radionuclides are released from the fuel particles, other relevant contaminants can generally be expected to migrate faster than cesium (Andersson

Table 4.4: Results of a review of values of D_s and v_s by soil type in different types of soil, based on Chernobyl (cationic) cesium assessment (Bossew & Kirchner 2004, Kirchner et al. 2009).

Soil group	GM	GSD	AM	SD	Min	Max
Parameter: D_s (cm^2 per year)						
All soils	0.22	3.1	0.37	0.4	0.02	1.9
Clay/Loam	0.20	4.6	0.36	0.3	0.02	0.8
Sand	0.11	2.3	0.16	0.2	0.03	0.6
Organic	0.94	1.8	1.07	0.7	0.63	1.9
Unspecified	0.27	2.6	0.37	0.3	0.04	0.8
Parameter: v_s (cm per year)						
All soils	0.18	3.3	0.27	0.2	0.00	0.9
Clay/Loam	0.06	17.5	0.24	0.3	0.00	0.6
Sand	0.15	1.7	0.17	0.1	0.07	0.6
Organic	0.69	1.6	0.73	0.3	0.40	0.9
Unspecified	0.22	1.6	0.24	0.1	0.09	0.5

GM: geometric mean; GSD: geometric standard deviation; AM: arithmetic mean; SD: arithmetic standard deviation

2009*a*) as reflected by the differences in Table 4.5 of soil K_d. The dissolution of fuel particles in soil has in the Chernobyl case been reported by Kashparov et al. (2004) to take place according to the formulae below, which are used in ERMIN:

If the material was initially oxidized, the dissolution rate constant after deposition in soil will be:

$$k(\text{years}^{-1}) = 0.6 \cdot 10^{(-0.15 \cdot \text{pH})} \text{ at pH} < 7.0, \text{ and } k = 0.05 \text{ at pH} > 7.0 \qquad (4.11)$$

If the material was NOT initially oxidized, the dissolution rate constant after deposition in soil will be:

$$k(\text{years}^{-1}) = 40 \cdot 10^{(-0.45 \cdot \text{pH})} \text{ at pH} < 6.5, \text{ and } k = 0.05 \text{ at pH} > 6.5 \qquad (4.12)$$

The pH values to be used in Kasparov et al.'s formulae would be based on easily made actual measurements in case of an accident, but may be assumed to mostly be in the range of 5.0-6.5 for mineral soils and 6.5-8.0 for more organic soils.

Theoretically, there should be some dependence of particle dissolution rates on particle sizes (Mercer 1967). However, such data are not apparent from the data published

Table 4.5: Results of a review of values of K_d for 3 important elements by soil type in different types of soil, based on hundreds (for Cs and I) of field assessments (in units of L/kg = cm^3/g).

Soil group	GM	GSD	AM	SD	Min	Max
Contaminant: Cs						
All soils	$1.2 \cdot 10^3$	7	$6.1 \cdot 10^3$	$2.1 \cdot 10^4$	4.3	$3.8 \cdot 10^5$
Clay/Loam	$5.5 \cdot 10^3$	4	$2.2 \cdot 10^4$	$6.7 \cdot 10^4$	$5.7 \cdot 10^2$	$3.8 \cdot 10^5$
Sand	$5.3 \cdot 10^2$	6	$2.2 \cdot 10^3$	$5.0 \cdot 10^3$	$1.0 \cdot 10^1$	$3.5 \cdot 10^4$
Organic	$2.7 \cdot 10^2$	7	$3.0 \cdot 10^3$	$1.2 \cdot 10^4$	4.3	$9.5 \cdot 10^4$
Unspecified	$1.7 \cdot 10^3$	5	$6.7 \cdot 10^3$	$1.5 \cdot 10^4$	$4.0 \cdot 10^1$	$5.5 \cdot 10^4$
Contaminant: I						
All soils	5.4	6	$2.5 \cdot 10^1$	$7.0 \cdot 10^1$	$1.0 \cdot 10^{-2}$	$5.8 \cdot 10^2$
Clay/Loam	6.8	6	$2.1 \cdot 10^1$	$3.0 \cdot 10^1$	1.0	$1.2 \cdot 10^2$
Sand	3.6	8	$1.3 \cdot 10^1$	$2.0 \cdot 10^1$	$1.0 \cdot 10^{-2}$	$1.3 \cdot 10^2$
Organic	$3.6 \cdot 10^1$	4	$9.3 \cdot 10^1$	$1.8 \cdot 10^2$	8.5	$5.8 \cdot 10^2$
Unspecified	2.6	6	$2.0 \cdot 10^1$	$7.0 \cdot 10^1$	$1.0 \cdot 10^{-1}$	$3.7 \cdot 10^2$
Contaminant: Ru						
All soils	$2.7 \cdot 10^2$	8	$4.7 \cdot 10^3$	$1.7 \cdot 10^4$	5.0	$6.6 \cdot 10^4$
Clay/Loam	$5.0 \cdot 10^2$	2	$6.0 \cdot 10^2$	$3.6 \cdot 10^2$	$2.0 \cdot 10^2$	$9.9 \cdot 10^2$
Sand	$3.6 \cdot 10^1$	6	$7.7 \cdot 10^1$	$9.0 \cdot 10^1$	5.0	$6.6 \cdot 10^4$
Organic	-	-	$6.6 \cdot 10^4$	-	-	-
Unspecified	$1.4 \cdot 10^2$	3	$2.3 \cdot 10^2$	$2.1 \cdot 10^2$	$3.4 \cdot 10^1$	$4.9 \cdot 10^2$

GM: geometric mean; GSD: geometric standard deviation; AM: arithmetic mean; SD: arithmetic standard deviation

by Kashparov et al. (2004).

It may be noted that values for the groups 'all soils' and 'unspecified soil type' are generally in reasonable agreement, as they would be if the unspecified category in reality spans representatively over different soil types. Also values reported for weapons fallout have been reported by Kirchner et al. (2009), and these are in most cases comparable with those for Chernobyl data. A lognormal distribution (using the geometric mean) is assumed in ERMIN (as favored by Kirchner et al. 2009). Minimum and maximum values are used as boundaries.

Values of D_s and v_s for other radioelements than cesium can be found by multiplying the values in Table 4.4 for cesium by the 'retardation factor' relationship ($R = 1 + K_d \frac{\rho}{\varepsilon}$) (Kirchner et al. 2009) (i.e. by the 'retardation factor' for the new element divided by that for cesium), applying appropriate values for all parameters (see above) for the soil type

and element in question.

For the K_d values in Equations (4.9) and (4.10), a wide range of data is available (also by soil type) from a relatively recent review by IAEA (2009). Table 4.5 shows the values for the 3 radioelements that would be thought to be of primary importance for external dose, but data for other elements of any potential significance (Am, Ba, Ce, Cm, La, Mo, Nb, Np, Pu, Rb, Sb, Sr, Te, U and Zr) are also available for use in the specified format from the report from IAEA (2009), although generally based on much fewer data and often without soil type specific data or standard deviations. All values of K_d are assumed to be lognormally distributed based on the Central Limit Theorem, and the assumption of lognormal is generally supported by empirical evidence (Sheppard et al. 2009).

As for bulk soil density, this normally varies within a short range of 1.4-1.7 g/cm^3 for sandy soil, whereas it is typically 1.1-1.4 g/cm^3 for clay/loam soil (Brewer 1965, Chesworth 2008). An assumption of uniform distribution seems reasonable over these rather small intervals. The relationship between bulk soil density and porosity is given by:

$$\text{Soil porosity} = 1 - (\text{Bulk soil density}/\text{particle density}) \tag{4.13}$$

(Blake & Hartge 1986, Brady & Weil 1996). In most soils the particle density can be assumed to be around 2.65 g/cm^3 (Brady & Weil 1996). This is the density of quartz, which is the dominant mineral in most soils.

For organic soils, the porosity has on the basis of 180 soil samples been shown to have the following dependence on soil organic carbon (SOC) (Franzluebbers 2011):

$$\text{Soil porosity}(m^3/m^3) = -0.20 + 0.89 \cdot (1 - \exp(-0.067 \cdot \text{SOC}\,[g/kg])) \tag{4.14}$$

whereas the bulk soil density depends on the soil organic C in the following way (Hossain et al. 2015):

$$\text{Bulk soil porosity}(g/cm^3) = 1.56 \cdot \exp(-0.0063 \cdot \text{SOC}\,[g/kg]) \tag{4.15}$$

By including these formulas in ERMIN the user can specify the values for organic soils directly from the soil organic C content, which is easily measurable by ignition (remembering the rule of thumb – the van Bemmelen factor - that organic matter generally contains about 58 percent organic carbon (Périé & Ouimet 2008)).

4.2.7 Application on a semidetached house

In continuation of Section 4.1.4 kerma contributions according to deposition scenarios and contaminated surfaces were also determined for different timescales after the ini-

tial deposition applying the formulas described in the previous sections. As the kerma conversion factors for the ground were determined for a source on top of the surface Equation (4.8) cannot be applied for the migration of contamination on grassed areas. Instead an empirical formula determined by Bunzl et al. (1997) was applied:

$$K(t) = \Gamma \cdot C_0 \cdot (f_1 \cdot \exp(-\ln(2) \cdot t/T_{w1}) + f_2 \cdot \exp(-\ln(2) \cdot t/T_{w2})) \tag{4.16}$$

$K(t)$ is the the kerma at time t, Γ the kerma conversion factor and C_0 is the initial contaminant concentration after the deposition process multiplied by a factor accommodating the reductive influence on the initial kerma rate level of surface roughness and possibly penetration with rain water early after the deposition compared with a situation where all contamination was initially located on top of a smooth surface. Based on the findings of Roed (1990) for a dry deposition scenario, it was estimated that the assumption of a reduction factor of about 80 % is reasonable. Therefore, the applied values in these calculations are f_1 = 0.46, T_{w1} = 3.3 y, f_2 = 0.34, T_{w2} = 21 y.

The deposition on a grassed surface at the initial time of deposition is used as a reference and as in Section 4.1.4 the calculations were performed for an urban environment with neighboring buildings and an source energy of 0.662 MeV. To show the development of air kerma over time the ground floor was chosen as location inside a semidetached as apart from the other building parts more different surfaces contribute to the air kerma in that part. Furthermore, a dry deposition scenario with its four different particle sizes was chosen as also the trees show a higher contribution to the air kerma. The results are presented in Figure 4.3 assuming the ground to be paved and in Figure 4.4 assuming the ground to be grassed.

For the assumption that the ground is paved, the graphs show regardless of AMAD that after ca. 1 year apart from the roof the other source areas that contribute air kerma to the ground floor become more and more negligible. Looking at a grassed ground surface, the graphs show again that the roof is a important source area that contributes air kerma to the ground floor, but in contrast to the scenario with a paved ground the contaminants on the ground continuously cause an important contribution to the air kerma in the ground floor.

In conclusion, the application of initial relative contamination levels and post deposition migration of contaminants in connection with kerma conversion factors shows importance of the roof as main contributor to the air kerma inside the semidetached house, keeping in mind that if the ground surface is grassed, it is of similar importance in contributing air kerma to the ground floor.

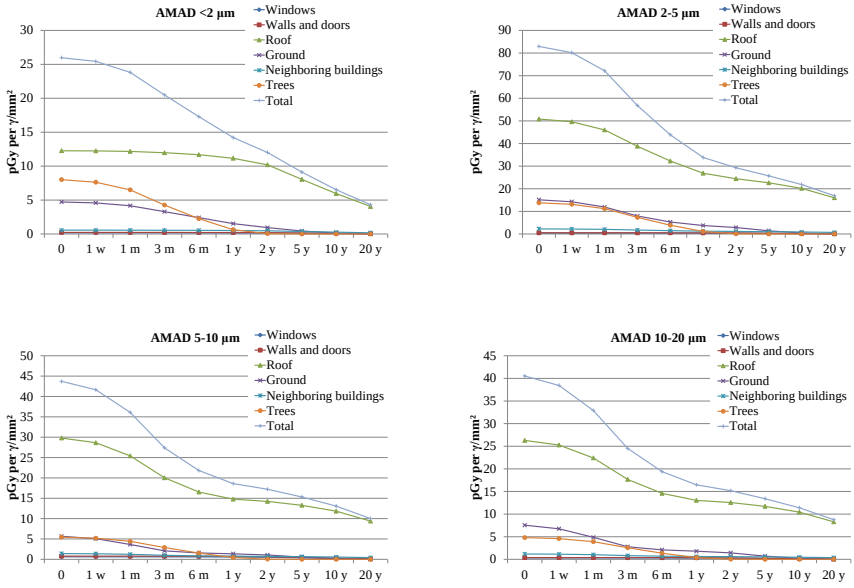

Figure 4.3: Air kerma development caused by different source areas over different time scales at the ground floor of a semidetached house for a dry deposition scenario with its four different particle sizes. The results are given in pGy per emitted photon of 0.662 MeV on a grassed reference surface of 1 mm^2 at the time of initial deposition. The ground surface was assumed to be paved.

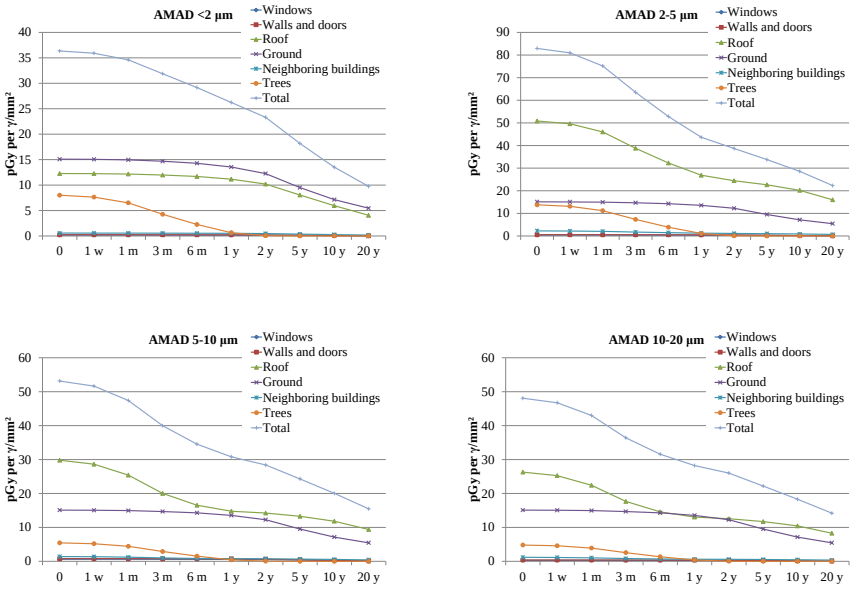

Figure 4.4: Air kerma development caused by different source areas over different time scales at the ground floor of a semidetached house for a dry deposition scenario with its four different particle sizes. The results are given in pGy per emitted photon of 0.662 MeV on a grassed reference surface of 1 mm^2 at the time of initial deposition. The ground surface was assumed to be grassed.

Chapter 5

Optimization of decontamination activities

In the previous chapter initial relative contamination levels and time functions representing the natural weathering and migration processes of contaminants were determined that can applied for detailed kerma modeling in connection with kerma conversion factors that can further give knowledge about which surfaces contribute mostly to the external radiation exposure and enables to optimize decontamination activities. Based on shielding factors for different source and detector positions, the isodose concept is introduced in this chapter as it illustrates the extent to which the specific areas contribute to the external radiation exposure at the observation points inside a building. This could, in turn, be used to show how the decontamination of surfaces or replacement of topsoil can be optimized in an emergency situation by determining the part of surfaces that contribute most to the external radiation exposure at the various observation points.

5.1 Introducing the concept of the isodose

5.1.1 Shielding factors around and on top of a modular building

First, in order to illustrate the influence of the position of the sources around the building on the shielding factor (Equation (1.3) for barrier shielding) the calculated shielding factors that were determined for a modular building as described in Section 2.1.1 were used again. The results for ^{137}Cs and ^{60}Co are plotted in heat maps for all 4 observation points defined above (Figure 5.1). The shielding factor is substantially lower at observation point No. 1 (inside the breeze block construction) than at the other observation points. At this point, the overall average shielding factor is 0.29 ± 0.20 (1 SD) for ^{137}Cs and 0.37 ± 0.21 for ^{60}Co. The shielding factors at the other points were about 0.72 ± 0.22

for ^{137}Cs and 0.77 ± 0.21 for ^{60}Co.

For ^{137}Cs, the shielding factor of one module wall is 0.90 ± 0.01 and for one breeze block wall 0.25 ± 0.01; while the corresponding values for ^{60}Co are 0.94 ± 0.01 and 0.32 ± 0.01, respectively. As can be seen from the plots in Figure 5.1, even the doors and windows provide slightly better shielding than the module walls. The shielding factors determined for the doors and windows are 0.89 ± 0.01 and 0.85 ± 0.01 in case of ^{137}Cs, and 0.93 ± 0.01 and 0.87 ± 0.01 in case of ^{60}Co. All other shielding factors can be determined from combinations of these factors and the angles at which the radiation passes through the different materials. The impact of the angle of incidence at the observation point on the shielding factor depends on the increasing septum length of the material traversed by the gamma photons as the distance between the surface source element and the observation point decreases (close to the building). This effect is especially evident when the breeze block structure is in the line of sight between the source and the observation point. Hence, as the angle between the incoming radiation and wall approaches 90°, while moving further away from the observation point, the radiation penetrates less material, and thus the shielding factor is higher.

Furthermore, in order to demonstrate the influence on the shielding factor of different source positions on top of the building, the results for ^{137}Cs and ^{60}Co are plotted for the 4 observation points, as in case of the surrounding deposition (Figure 5.2). The shielding factor is substantially lower at observation point No. 1 (inside the breeze block construction) than for the other observation points. At this point, the overall average shielding factor is 0.32 ± 0.30 (1 SD) for ^{137}Cs and 0.38 ± 0.29 for ^{60}Co. The shielding factors for the other points were about 0.59 ± 0.22 for ^{137}Cs and 0.66 ± 0.19 for ^{60}Co.

All other shielding factors can be determined as combinations of radiation passing through the roof and then a module or brick wall, taking the angles at which the radiation passes through the different materials into account, as well as backscattering effects.

5.1.2 Describing the concept of the isodose

Examination of the distribution of angular shielding factors around building structures leads to the conclusion that some contaminated areas have a higher influence on the radiation exposure inside the building than others. Considering that the distance between a given observation point inside the building and a given surface source element outside the building also influences the radiation exposure at the observation point, it is interesting to study which contaminated areas have the highest impact on the radiation exposure indoors. This could be helpful in optimizing decontamination activities after the release of radioactive substances and reducing the resulting waste.

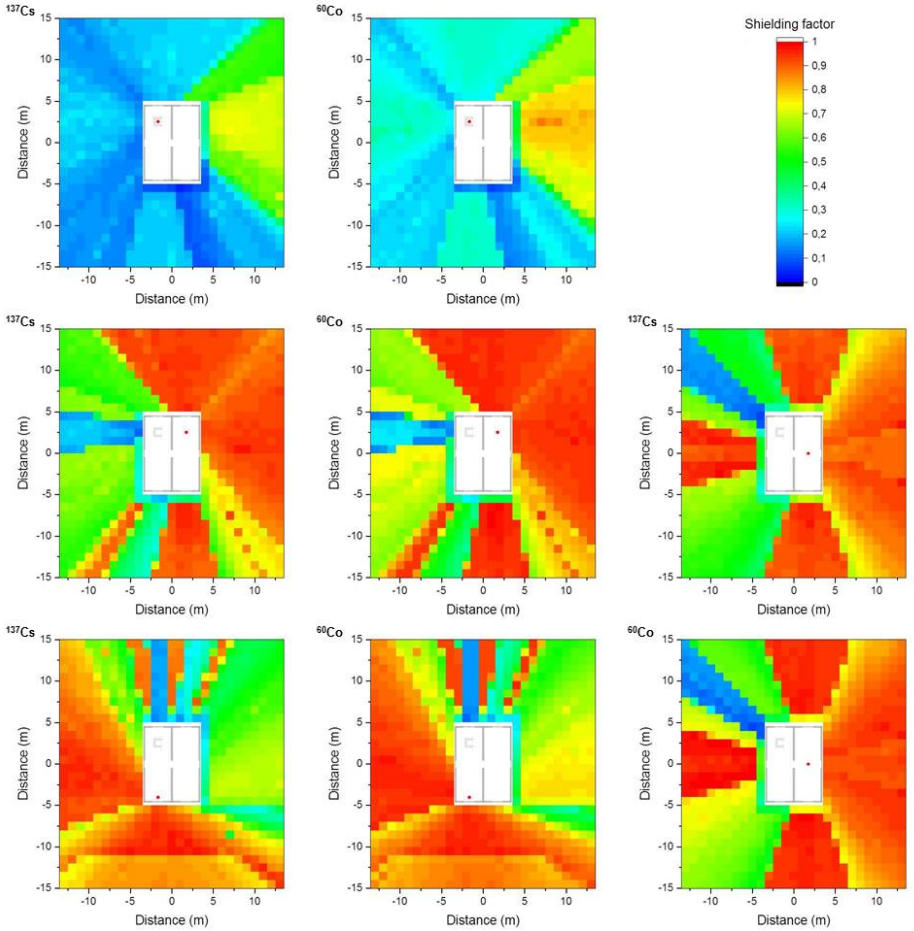

Figure 5.1: Computed angular shielding factors according to source region position around a modular building, at four different observation points inside the building (indicated by the red dots) for ^{137}Cs and ^{60}Co.

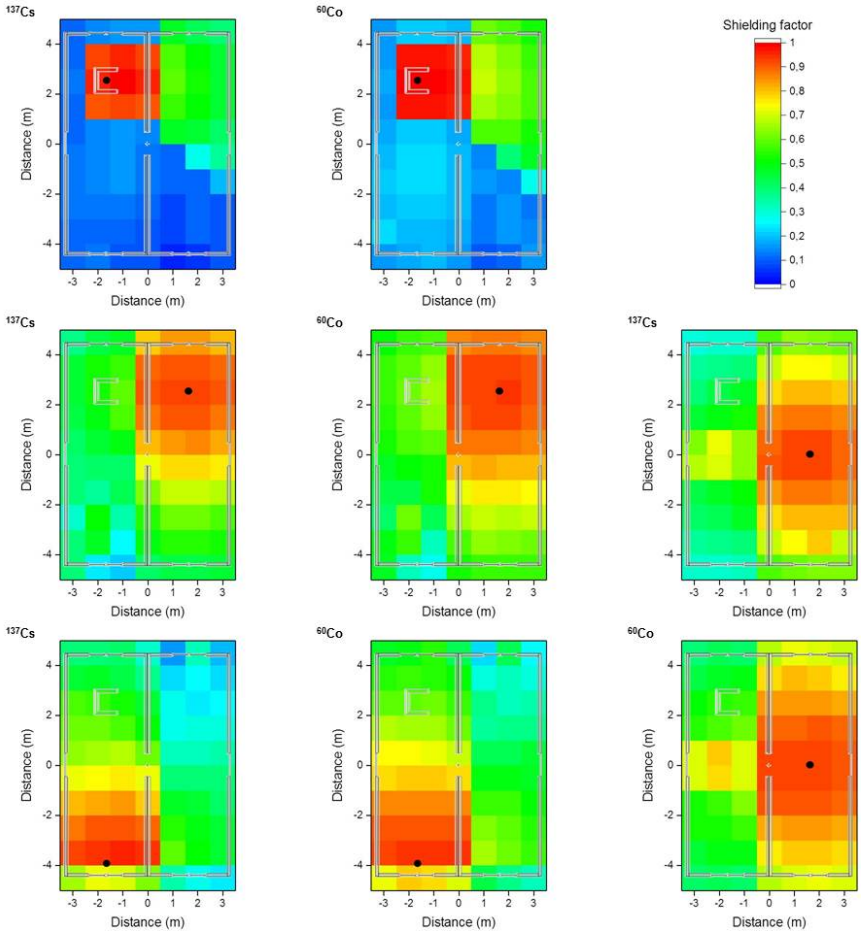

Figure 5.2: Computed angular shielding factors according to source region position on top of a modular building at four different observation points inside the building (black dots) for ^{137}Cs and ^{60}Co.

For this concept, an observation point i is defined such that it can be inside or outside the building, and its position is described by the vector $\vec{r}_i$ in 3-dimensional space. The absorbed dose resulting from gamma-emitting radionuclides over an infinitesimal volume, dV, located at the positions $\vec{r}$, can be determined at this point. The dose contribution from dV to the observation point i, here denoted the dose contribution density $\rho_{D,i}(\vec{r})$, can be determined at each point in space by, for example, defining a certain radionuclide contamination on a surface, or by defining it as 0 inside the building. Thus, the total dose $D_{i,\infty}$ at observation point i can be determined by the following integral:

$$D_{i,\infty} = \int \rho_{D,i}(\vec{r})dV \quad IF \lim_{|\vec{r}_i - \vec{r}| \to \infty} \rho_{D,i}(\vec{r}) = 0 \tag{5.1}$$

To determine the areas with the highest dose contribution, the concept of the "isodose" was developed, as defined below.

Definition: The isodose $ID_{i,k}$ is defined by the outer boundary of one or more zones in space that contribute, for the most part, a given fraction k to the dose at the observation point i. In the case when $\rho_{D,i}(\vec{r})$ is a continuous function with the maximum $\rho_{D,i,max} < \infty$, the isodose $ID_{i,k}$ can be chosen from the range $0 < ID_{i,k} < \rho_{D,i,max}$ and the fraction of dose contribution k_i resulting from the zone or zones determined by the isodose is given by:

$$k_i = \int f(\rho_{D,i}(\vec{r}))dV / D_{i,\infty} \quad FOR \quad f(\rho_{D,i}(\vec{r})) = \begin{cases} \rho_{D,i}(\vec{r}), & \rho_{D,i}(\vec{r}) \geq ID_{i,k} \\ 0, & \rho_{D,i}(\vec{r}) < ID_{i,k} \end{cases} \tag{5.2}$$

In the case when $\rho_{D,i}(\vec{r})$ is not a continuous function for the entire space, for example, due to limitations of the considered space, the concept of the isodose is still applicable for jump discontinuities. In such a case, the left- and right-hand limits exist, and the respective point can be applied over the entire range of dose contribution densities that lie within the left- and right-hand limits.

These equations apply to a single observation point inside the building, but in a real fallout situation, decontamination must be performed in such way that a substantial dose reduction is achieved in an entire building. To obtain a measure of the effective shielding obtained in a building by a given decontamination measure, the times spent by the residents in various parts of the building must be accounted for. Therefore, so-called occupancy factors p_i for various observation points can be applied to Equation

(5.2) resulting in:

$$
\begin{aligned}
k &= \int f(\rho_D(\vec{r}))dV / \sum_i D_{i,\infty} \cdot p_i \quad \forall \quad 1 = \sum_i p_i \\
FOR \quad f(\rho_D(\vec{r})) &= \begin{cases} \sum_i \rho_{D,i}(\vec{r}) \cdot p_i, & \sum_i \rho_{D,i}(\vec{r}) \cdot p_i \geq ID_k \\ 0, & \sum_i \rho_{D,i}(\vec{r}) \cdot p_i < ID_k \end{cases}
\end{aligned}
\tag{5.3}
$$

Based on this definition, the concept of the isodose can also be applied to 2-dimensional dose contribution densities $\rho_{D,i}(\vec{r})$, for example, on specific surfaces or on the ground surrounding the building. This can be done in some cases for the sake of simplification, when the depth distribution under a surface (e.g. fallout in the ground) is neglected.

5.1.3 Applying the concept of the isodose

In reality, we do not know the dose contribution density of the space (Equations (5.1) to (5.3)), and thus the concept must be applied for different scenarios. The first scenario could be a contaminated ground surface around a building. The depth distribution is neglected for the sake of simplification as it differs from point to point in a real fallout situation (see e.g., Östlund et al. 2017). Therefore, this application of the isodose concept is 2-dimensional, and the areas giving the highest dose contribution for a given source–building geometry can be determined using the following step-by-step procedure. To provide a better understanding, the relevant quantities are listed in Table 5.1.

Step 1: The dose resulting from the entire contaminated surface at the observation point i, $D_{i,\infty}$, is determined, as well as the contribution to the dose from smaller parts of the surface $D_{i,j}$. The size of the areas A_j is chosen by reasonability based on the applied scenario. The dose contribution density is then calculated for each subarea using the relation $\rho_{D,i,j} = D_{i,j}/A_j$. If more than one observation point is considered, this process must be repeated for all points, and the results weighted with their respective occupancy factors p_i: $D_j = \sum_i D_i \cdot p_i$ for the dose contribution and by $\rho_{D,j} = \sum_i D_{i,j} \cdot p_i/A_j$ for the dose contribution density.

Step 2: The subarea j with the highest dose contribution density for the observation point $\rho_{D,i,j}$ or weighted dose contribution density $\rho_{D,j}$ is then determined.

Step 3: The fraction of dose contribution k_i is then calculated by dividing the dose contribution $D_{i,j}$ by the dose resulting from the entire contaminated surface $D_{i,\infty}$ for one observation point, or for the weighted fraction of dose contribution k by dividing $D_{i,j}$ by $D_\infty = \sum_i D_{i,\infty} \cdot p_i$.

Table 5.1: Overview of the relevant quantities in the determination of the isodose.

Symbol	Name
A_j	Size of subarea j
D_∞	Total dose weighted for several observation points
D_i	Dose at observation point i
$D_{i,j}$	Dose at observation point i resulting from contamination of subarea j
$D_{i,\infty}$	Total dose at observation point i
D_j	Dose weighted for several observation points resulting from contamination of subarea j
i	Observation point index
j	Subarea index
$ID_{i,k}$	Isodose for the fraction of dose contribution k to the observation point i
ID_k	Isodose for the fraction of dose contribution k weighted for several observation points
k	Fraction of dose contribution weighted for several observation points
k_i	Fraction of dose contribution to the observation point i
p_i	Occupancy factors
$\vec{r}$	Any point in the defined space
$\vec{r}_i$	Position of the observation point i
ρ_D	Dose contribution density weighted for several observation points
$\rho_{D,i}$	Dose contribution density to the observation point i
$\rho_{D,i,j}$	Dose contribution density for the observation point i resulting from contamination of subarea j
$\rho_{D,j}$	Dose contribution density weighted for several observation points resulting from contamination of subarea j

Step 4: This subarea j now represents the area with a fraction of dose contribution k_i or k surrounded by the isodose criterion $ID_{i,k}$ and ID_k. $ID_{i,k}$ and ID_k are in turn defined here by their respective dose contribution densities $\rho_{D,i,j}$ or $\rho_{D,j}$.

Step 5: The subarea j with the next highest dose contribution density for the observation point $\rho_{D,i,j}$ or weighted dose contribution density $\rho_{D,j}$ is then determined.

Step 6: The fraction of dose contribution k_i is calculated by dividing the sum of all dose contributions from the subareas determined in Step 2 or 5 so far, $\sum_j D_{i,j} \forall j : \rho_{D,i,j} \geq ID_{i,k}$, by the dose resulting from the entire contaminated surface $D_{i,\infty}$ for one observation point using the isodose $ID_{i,k}$ as the criterion equalling the dose contribution density $\rho_{D,i,j}$ of the subarea j that was determined in Step 5. This must be done for the weighted fraction of dose contribution k by dividing the weighted sum of all dose contributions

considered $\sum_j D_j \forall j : \rho_{D,j} \geq ID_k$ by the weighted dose resulting from the infinite contaminated surface D_∞, again using the isodose ID_k as the criterion equalling the dose contribution density $\rho_{D,j}$ of the subarea j that was determined in Step 5.

Step 7: The subareas $j : \rho_{D,i,j} \geq ID_{i,k}$ or $j : \rho_{D,j} \geq ID_k$that were determined in Step 2 or 5 now represent the area or areas with a fraction of dose contribution k_i or k surrounded by the isodose criterion $ID_{i,k}$ or ID_k which are defined here by their respective dose contribution densities, $\rho_{D,i,j}$ or $\rho_{D,j}$ as in Step 6.

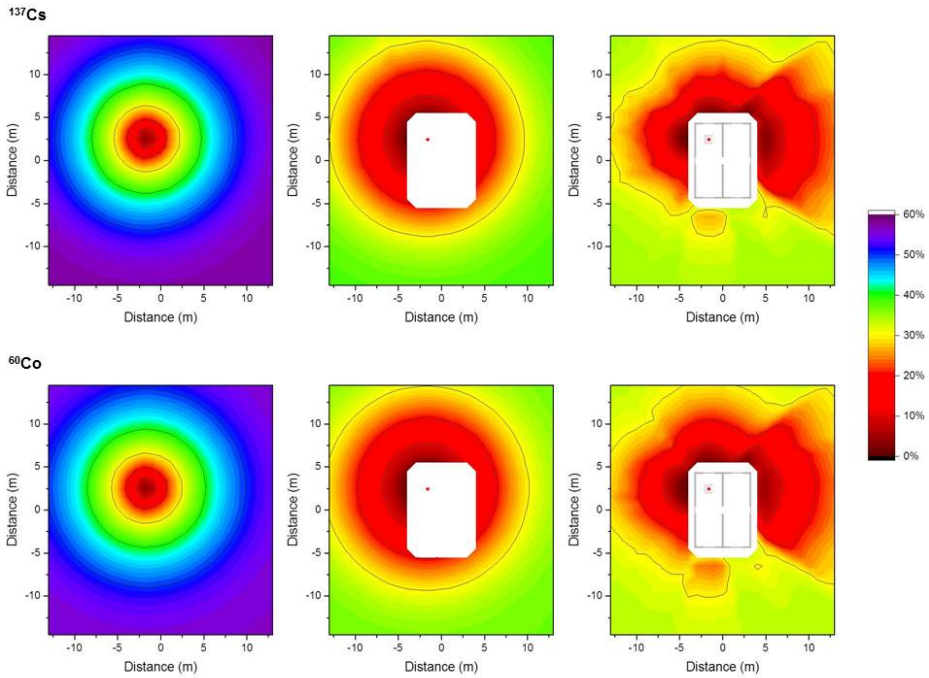

Figure 5.3: Isodose lines around a modular building at observation point # 1 (Figure 2.2) for homogenous contamination of ^{137}Cs (top) and ^{60}Co on the ground assuming no shielding (left), geometry shielding (middle), and combined geometry and barrier shielding (right) according to the definition in Section 1.2. The shading indicates the fraction of dose contribution to the observation point including the areas that are surrounded by the respective one. When the outside line for a certain dose reduction reaches the limit of the calculation grid, its shape might differ for a larger calculation grid.

Step 8: Repeat Steps 4-7 until all subareas have been considered.

These Steps can be expressed more mathematically for one observation point by:

$$k_i = \sum_j D_{i,j}/D_{i,\infty} \quad \forall \quad j : \rho_{D,i,j} \geq ID_{i,k} \tag{5.4}$$

and for more than one observation point by:

$$k = \sum_j D_j/D_\infty \quad \forall \quad j : \rho_{D,j} \geq ID_k \tag{5.5}$$

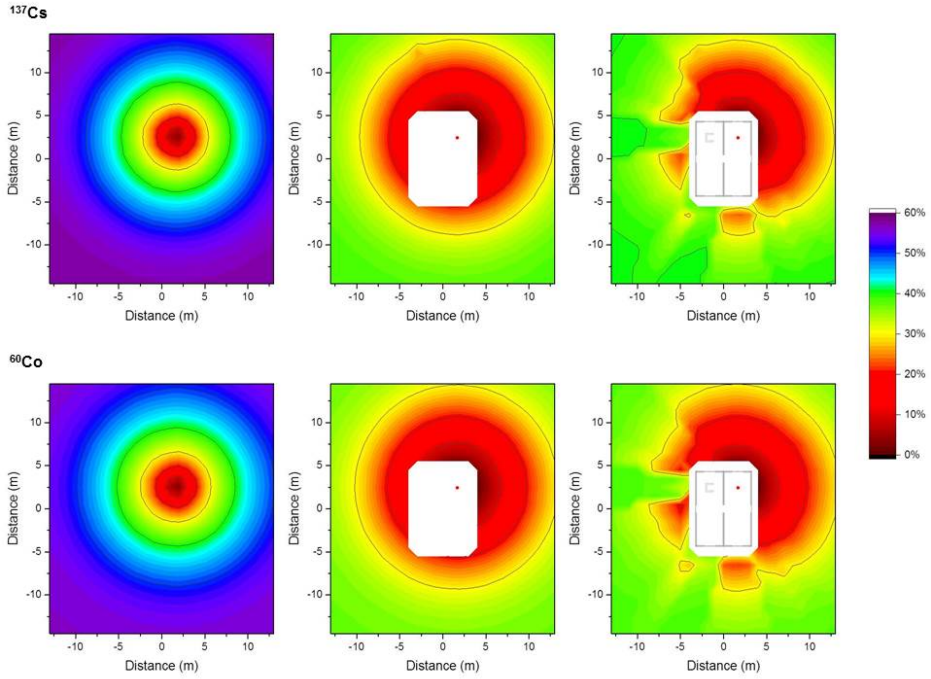

Figure 5.4: Isodose lines around a modular building at observation point # 2 (Figure 2.2) for homogenous contamination of ^{137}Cs (top) and ^{60}Co on the ground assuming no shielding (left), geometry shielding (middle), and combined geometry and barrier shielding (right) according to the definition in Section 1.2. The shading indicates the fraction of dose contribution to the observation point including the areas that are surrounded by the respective one. When the outside line for a certain dose reduction reaches the limit of the calculation grid, its shape might differ for a larger calculation grid.

If the sizes of the areas A_j are numerically equal, the procedure can be simplified as the determination of the dose contribution density for each subarea becomes unnecessary, and the dose contribution per subarea can be compared with the isodose $ID_{i,k}$ multiplied by the size of one subarea A. Mathematically, Equation (5.4) for one observation point can be transformed into:

$$k_i = \sum_j D_{i,j}/D_{i,\infty} \quad \forall \quad j : D_{i,j} \geq ID_{i,k} \cdot A \quad \wedge \quad A_j = A \tag{5.6}$$

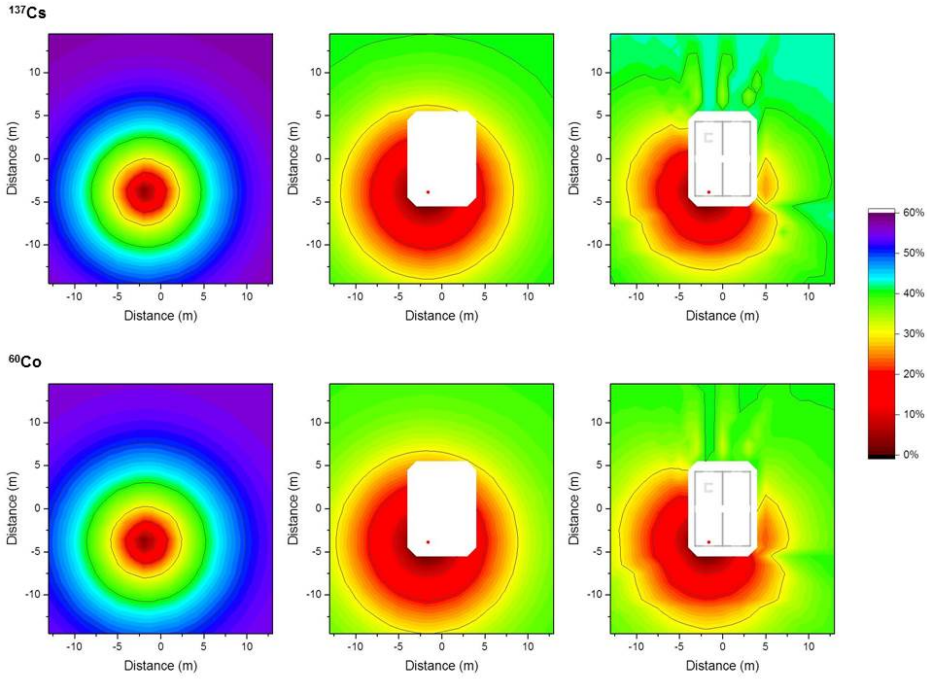

Figure 5.5: Isodose lines around a modular building at observation point # 3 (Figure 2.2) for homogenous contamination of ^{137}Cs (top) and ^{60}Co on the ground assuming no shielding (left), geometry shielding (middle), and combined geometry and barrier shielding (right) according to the definition in Section 1.2. The shading indicates the fraction of dose contribution to the observation point including the areas that are surrounded by the respective one. When the outside line for a certain dose reduction reaches the limit of the calculation grid, its shape might differ for a larger calculation grid.

and Equation (5.5) for more than one observation point into:

$$k = \sum_j D_j / D_\infty \quad \forall \quad j : D_j \geq ID_k \cdot A \quad \wedge \quad A_j = A \tag{5.7}$$

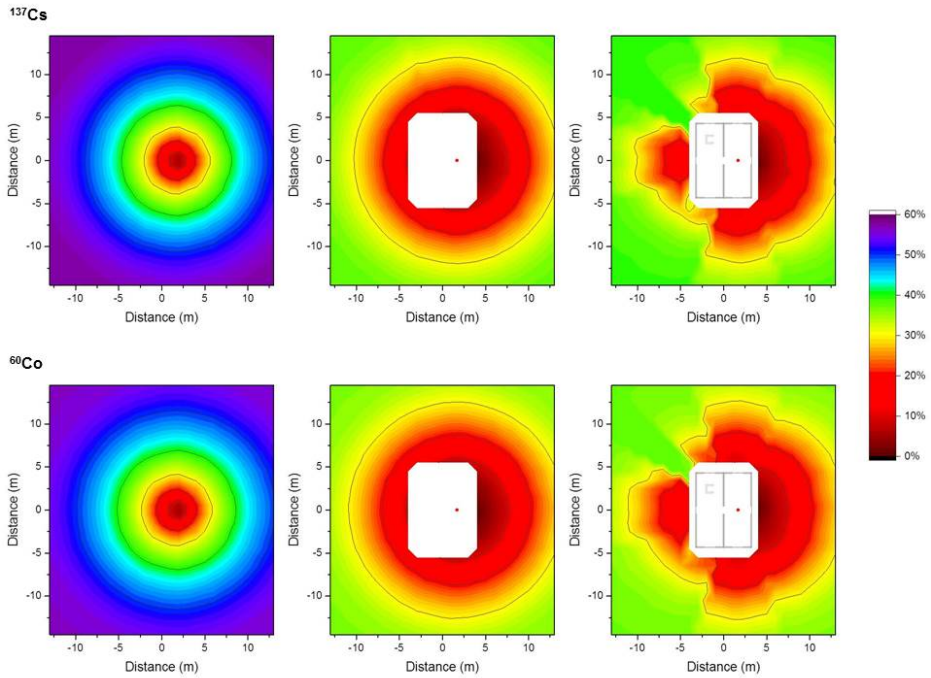

Figure 5.6: Isodose lines around a modular building at observation point # 4 (Figure 2.2) for homogenous contamination of ^{137}Cs (top) and ^{60}Co on the ground assuming no shielding (left), geometry shielding (middle), and combined geometry and barrier shielding (right) according to the definition in Section 1.2. The shading indicates the fraction of dose contribution to the observation point including the areas that are surrounded by the respective one. When the outside line for a certain dose reduction reaches the limit of the calculation grid, its shape might differ for a larger calculation grid.

5.1.4 Isodose lines for different shielding factors

The concept of the isodose, in its simplified application for same-sized subareas, described in Equation (5.6), was applied to the modular building that was described in

Section 2.1.1 and employed again in Section 5.1.1 to illustrate the influence of the position of the sources around the building on the (barrier) shielding factor. To study to which extent geometry and barrier shielding as defined in Section 1.2 have an impact on isodose lines, they were determined for no shielding, geometry shielding, and combined geometry and barrier shielding in case of homogeneous contamination of ^{137}Cs or ^{60}Co on the ground for all four observation points (see Figure 2.2). The results are presented graphically in Figures 5.3 to 5.6.

It can be seen in Figures 5.3 to 5.6 that the shapes of the zones encompassed by the isodose lines for a given observation point are relatively similar for both radionuclides. The zones are larger for ^{60}Co as the source energy is higher than in the case of ^{137}Cs. Regarding the type of shielding, geometry shielding causes a stronger impact on the size of the zones compared to barrier by moving the isodose lines to larger distance from the observation point as the areas that are closest to the observation point are not part of the source area. Barrier shielding gives the isodose lines their characteristic shapes as almost no transformation can be seen comparing the isodose lines determined for combined geometry and barrier shielding with those determined for geometry shielding in the directions of the building with less shielding and repectively more transformation in the directions of the building with more shielding.

To give a better idea of the size of the area that would have to be decontaminated to achieve a certain reduction in relative dose assuming the modular building being in place (combined geometry and barrier shielding), the respective values are presented in Table 5.2, together with the primary dose factor calculated for an infinite contaminated ground surface. The primary dose factor is directly related to the dose to the residents when no decontamination measures are taken and is given in pGy per γ/mm^2 representing the dose (pGy) that would be caused by a homogeneous ground contamination for an source strength of one gamma photon per unit area (γ/mm^2).

The values vary significantly depending on the observation point, especially regarding the influence of the breeze block structure or walls, which cause backscattering of the radiation. There also appears to be an inverse correlation between the primary dose factor at a given observation point attributed to an infinite contaminated ground and the size of the decontaminated surface required to reduce this dose by a certain fraction. The lower the unremediated dose, the larger the size of the area that must be decontaminated to achieve a certain percentage of dose reduction.

5.2 Influence of various factors on isodose lines

As a next step the isodose concept was applied to two typical Swedish residential houses to determine isodose lines for the various parts of the houses as well as the combined

Table 5.2: Area (m^2) that would hypothetically have to be decontaminated to achieve various degrees of dose reduction at the four observation points in case of ^{137}Cs and ^{60}Co contamination. All contamination is assumed to be on the soil surface.
*The values for 30 % dose reduction at observation point # 1 were determined using a limited calculation grid, and the results may differ with a larger calculation grid.

Observation point	Radionuclide	Primary dose factor before decontamination (pGy per γ/mm^2)	Dose reduction 10 %	20 %	30 %
1	^{137}Cs	173	48	155	396*
	^{60}Co	394	51	168	450*
2	^{137}Cs	446	23	88	251
	^{60}Co	829	27	106	303
3	^{137}Cs	489	15	58	172
	^{60}Co	908	18	73	221
4	^{137}Cs	425	30	117	292
	^{60}Co	804	37	140	349

effect of living in the houses by applying data about typical residential behavior. Furthermore, the impact of vertical migration and variability of the contaminants on the isodose lines is studied.

5.2.1 Description of the Swedish standard house models

The definition of the geometries for a wooden and a brick house of similar shape are leaned on the construction drawings and descriptions of authentic Swedish houses that were made available by the Urban Planning Department of the Municipality of Hässleholm (Stadsbyggnadskontoret Hässleholms kommun) (Figure 5.7). The houses have a ground area of 10 m x 15 m and an overview over the construction details is given in Table 5.3. Wooden frames were assumed to be negligible and are not part of the models. All windows and doors comprise an area of 25.3 m^2 of the outside walls.

Data from a material compendium (McConn Jr et al. 2011) was used to assign the material specifications with definite atomic compositions and densities as summarized in Table 5.4 to the input for the different building structures and environmental regions.

The source energies were representative of monoenergetic sources of 0.662 MeV representing ^{137}Cs, which has been of main concern in connection with the Chernobyl and Fukushima accidents. The source regions were defined as 1 m x 1 m plane squares

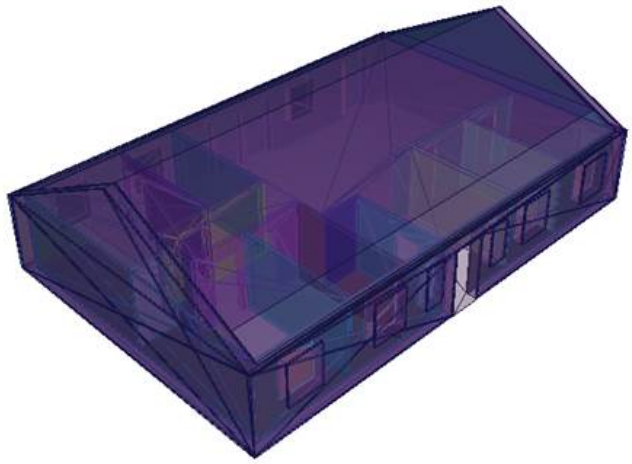

Figure 5.7: Birds-eye view of a Swedish standard house.

in a 1 m x 1 m grid up to a lateral distance of 10 m from the sides of the houses on the ground level as well as 2.5 cm and 5 cm beneath ground level. Separate Monte Carlo computations for reference values were performed for an infinite horizontal plane source area on the ground level as well as 2.5 cm and 5 cm beneath ground level.

The detector regions were defined as air-filled spheres with a diameter of 30 cm and positioned 1 m above ground level according to the observation points for the different parts of the building (Figure 5.8). Observation point # 1 represents a bedroom, # 2 a bathroom, # 3 a second bedroom (for e.g. a child or guests), # 4 a dressing room, # 5 a corridor, # 6 a restroom, # 7 a hall, # 8 a workroom, # 9 a kitchen, # 10 a living room, and # 11 a dining room.

5.2.2 Isodose lines around Swedish standard houses

The concept of the isodose, in its simplified application for same-sized subareas, described in (5.6), was applied for a case where decontamination would lead to different reductions of the absorbed dose depending on which of the eleven different observation points is taken into account. A homogenous ^{137}Cs-contamination on the ground level as well as 2.5 cm and 5 cm beneath ground level surrounding the wooden and the brick house was assumed. The results are graphically presented as isodose lines in Figures 5.9 to 5.14.

Table 5.3: Construction details for the wooden and the brick house.

	Wooden house	Brick house
Outer walls	2.2 cm wood, 4 cm air, 0.9 cm gypsum, 26 cm mineral wool, 2.8 cm air layer, 1.1 cm wood, 1.3 cm gypsum	12 cm brick, 4 cm air, 0.9 cm gypsum, 23 cm mineral wool, 1.3 cm gypsum
Inside walls	12 cm or 17 cm gypsum	
Roof	5.4 cm concrete, 2.7 cm wood	5.4 cm concrete, 3.5 cm wood
Ceiling	1.3 cm gypsum, 2.8 cm air layer, 40 cm mineral wool	
Windows and doors	0.8 cm glass	

The shape of the areas encompassed by the isodose lines of a given observation point are relatively similar in shape for all depth-levels of the contamination and both simulated houses. The shape of the isodose lines themselves reflects the different materials as well as the position of doors and windows. The respective zones for deposited contamination beneath ground level are smaller as less gamma photons from remote areas reach the observation point because of losing energy by interacting with the soil. To further get an idea about the size of the area that would need to be decontaminated to get a certain relative dose reduction for contamination at different depth the values of the primary dose factor that was calculated for an infinite contaminated surface are presented in Table 5.5. It has to be kept in mind as the isodose lines illustrate relative dose reduction and not total dose reduction.

The values of the different observation points vary within a factor of five. Furthermore, the primary dose factor for contamination at ground level is around about 5-6 times higher than the respective factor assuming the contamination 2.5 cm beneath ground level and this factor is about 2 times higher than the respective factor assuming the contamination 5 cm beneath ground level. Moreover, the primary dose factor inside a wooden house is about 2 times higher compared to the respective factor in a brick house.

5.2.3 Isodose lines according to residential behavior

So far eleven separate observation points representing the different parts of the building have been used to determine isodose lines. As a next step occupancy factors p_i as in Equation (5.7) are applied for the determination of isodose lines to obtain corresponding lines that are more representative of the building as a whole. To determine the isodose lines for typical living conditions, the choice of the occupancy factors p_i was based the data published in the European EXPOLIS project (see e.g. Jantunen et al. 1998, Rotko et al. 2000, Schweizer 2004), where thousands of people in seven European

Table 5.4: Material specifications with definite atomic compositions (rounded) and densities that were used for the Monte Carlo calculations.

Material	Atomic composition	Density in kg/l
Air	0.02 % C; 78.44 % N; 21.07 % O; 0.47 % Ar	0.001205
Brick	66.34 % O; 0.37 % Al; 32.32 % Si; 0.71 % Ca; 0.25 % Fe	1.8
Concrete	8.47 % H; 60.41 % O; 1.25 % Na; 2.48 % Al; 24.19 % Si; 2.72 % Ca; 0.47 % Fe	2.25
Glass	60.39 % O; 8.81 % Na; 25.18 % Si; 5.62 % Ca	2.4
Gypsum	33.33 % H; 50.00 % O; 8.33 % S; 8.33 % Ca	2.32
Mineral wool	42.50 % O; 1.70 % Na; 5.40 % Mg; 10.60 % Al; 18.20 % Si; 1.90 % K; 14.30 % Ca; 0.50 % Mn; 4.90 % Fe	0.1666667
Soil	31.69 % H; 50.16 % O; 4.00 % Al; 14.16 % Si	1.52
Wood	46.24 % H; 32.34 % C; 0.28 % N; 20.88 % O; 0.06 % Mg; 0.12 % S; 0.04 % K; 0.04 % Ca	0.64

cities (Athens, Basel, Grenoble, Helsinki, Milan, Oxford and Prague), were studied with respect to their time budgets, and the hours they spent in various microenvironments. Averaging over the values people spend about 14 h indoor at home and spend about 1 h preparing food (kitchen) within this time period. Further surveys show that people spend about 1 h eating (see USDA 2018, dining room), about 8 h sleeping (see OECD 2018, bedroom) and about 0.5 h in the bathroom (see Scotsman 2008), leaving about 3.5 h to be spend in the living room. The resulting isodose lines are graphically presented in Figure 5.15.

The calculated isodose lines show a mixture of the influence of the time spend in one (e.g. bedroom) and continuous influence of building materials (e.g. door and window in the kitchen). Comparing the results, the isodose lines for a wooden house are gentler than those for a brick house as the wooden materials provide less shielding and therefore have less impact on the isodose lines. Furthermore, the respective zones for a brick house are larger compared to the respective zones for a wooden house. Comparing the zones for contamination at ground level with those with contamination 2.5 cm beneath it, the size of the zones decrease with entering the soil. However, by getting deeper still (contaminated layer at 5 cm depth) the zones appear to slightly increase again, as the contribution from areas far away become insignificant.

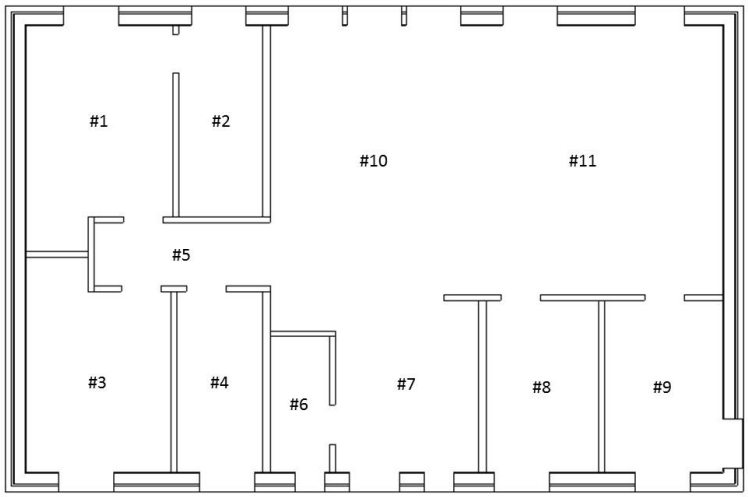

Figure 5.8: Observation points inside a Swedish standard house.

5.2.4 Impact of vertical migration of contaminants in the soil on the isodose lines

As contaminants migrate downwards in the ground over time, the impact of the position of the contamination on the isodose lines is of interest. The parameters D_s and v_s for the model described in Equation (4.8) were chosen to be the most extreme value combinations determined for ^{137}Cs by Almgren & Isaksson (2006) for sampling sites in western Sweden (D_s=0.06 cm^2 a^{-1}, v_s=0.17 cm a^{-1}and D_s=2.63 cm^2 a^{-1} and v_s=0.00 cm a^{-1}). The contaminant distributions were calculated for the first 5 cm of soil depth for the timescales 0.1 a, 1 a, and 5a after deposition and multiplied with the air kerma free-in-air values interpolated from the calculations at ground level, 2.5 cm and 5 cm beneath it. The results are graphically presented as isodose lines in Figure 5.16 for a wooden house and in Figure 5.17 for a brick house.

In the comparison of the wooden and the brick house similar differences can be seen as described before. The parameter combination shows that the isodose lines are similar for a short timescale like 0.1 a. Over longer timescales the respective zones become smaller as the contaminants migrate to deeper soil level. This effect is stronger for the parameter combination D_s=2.63 cm^2 a^{-1} and v_s=0.00 cm a^{-1} than for D_s=0.06 cm^2 a^{-1}, v_s=0.17 cm a^{-1}. Moreover, the dominance of the top soil layer can be seen as it contributes more to the air kerma free-in-air than the lower soil level as shown for the primary dose factor presented in Table 5.5.

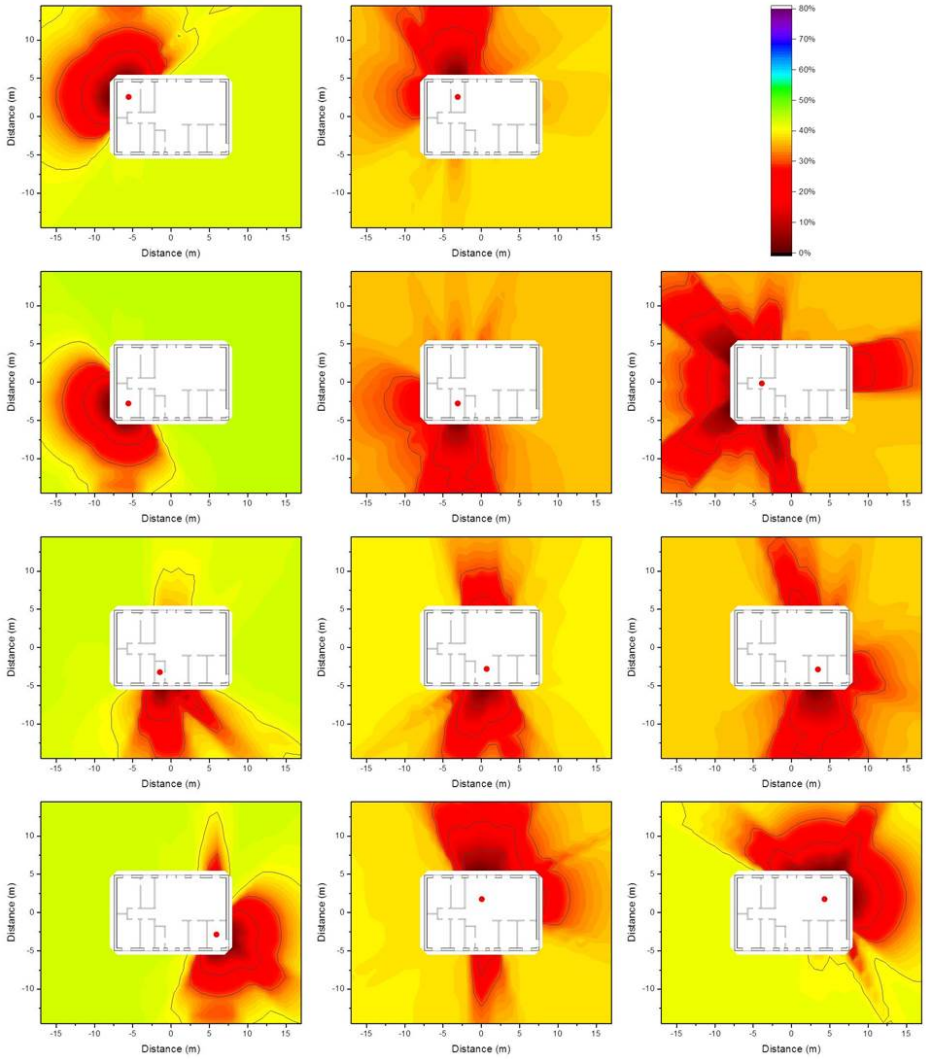

Figure 5.9: Isodose lines around a wooden house at eleven different observation points inside it (red dots) for homogenous ^{137}Cs-contamination on the ground level. The shading indicates the fraction of dose contribution to the observation point including the areas that are surrounded by the respective one. When the outside line for a certain dose reduction reaches the limit of the calculation grid, its shape might differ for a larger calculation grid.

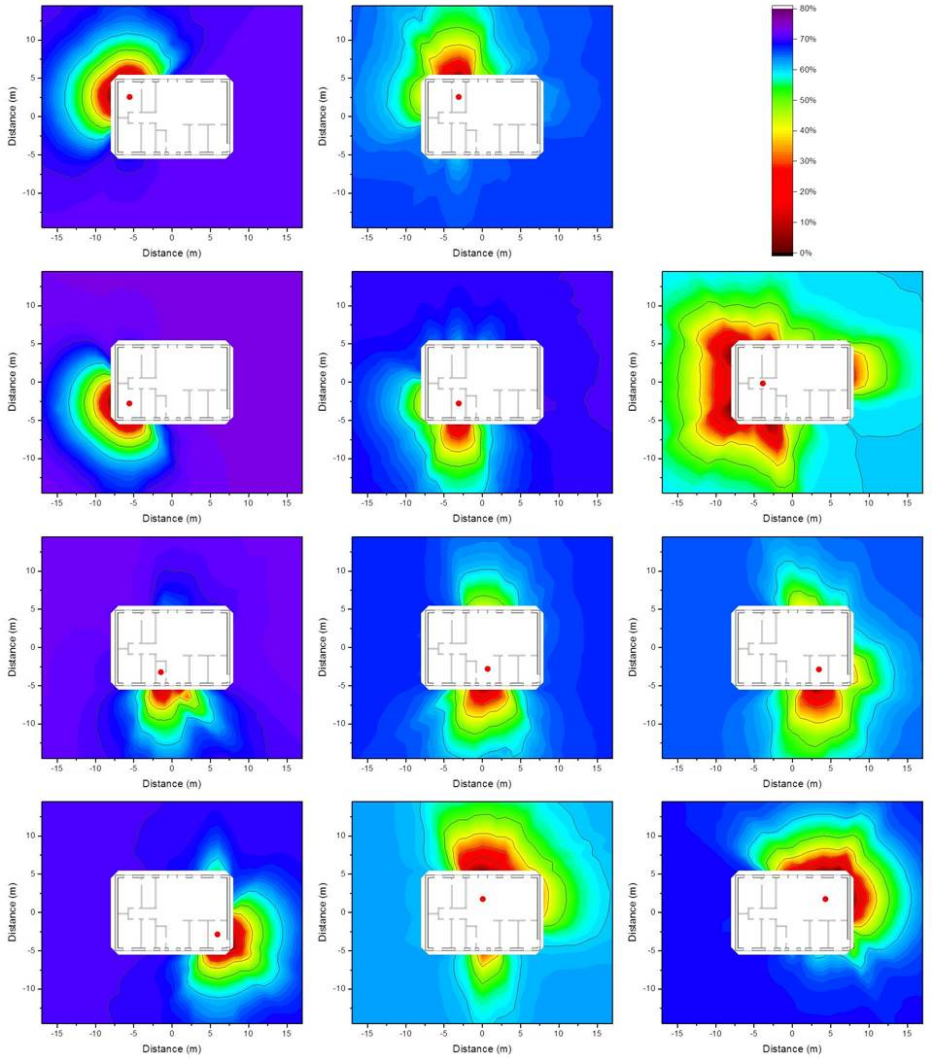

Figure 5.10: Isodose lines around a wooden house at eleven different observation points inside it (red dots) for homogenous ^{137}Cs-contamination 2.5 cm beneath ground level. The shading indicates the fraction of dose contribution to the observation point including the areas that are surrounded by the respective one. When the outside line for a certain dose reduction reaches the limit of the calculation grid, its shape might differ for a larger calculation grid.

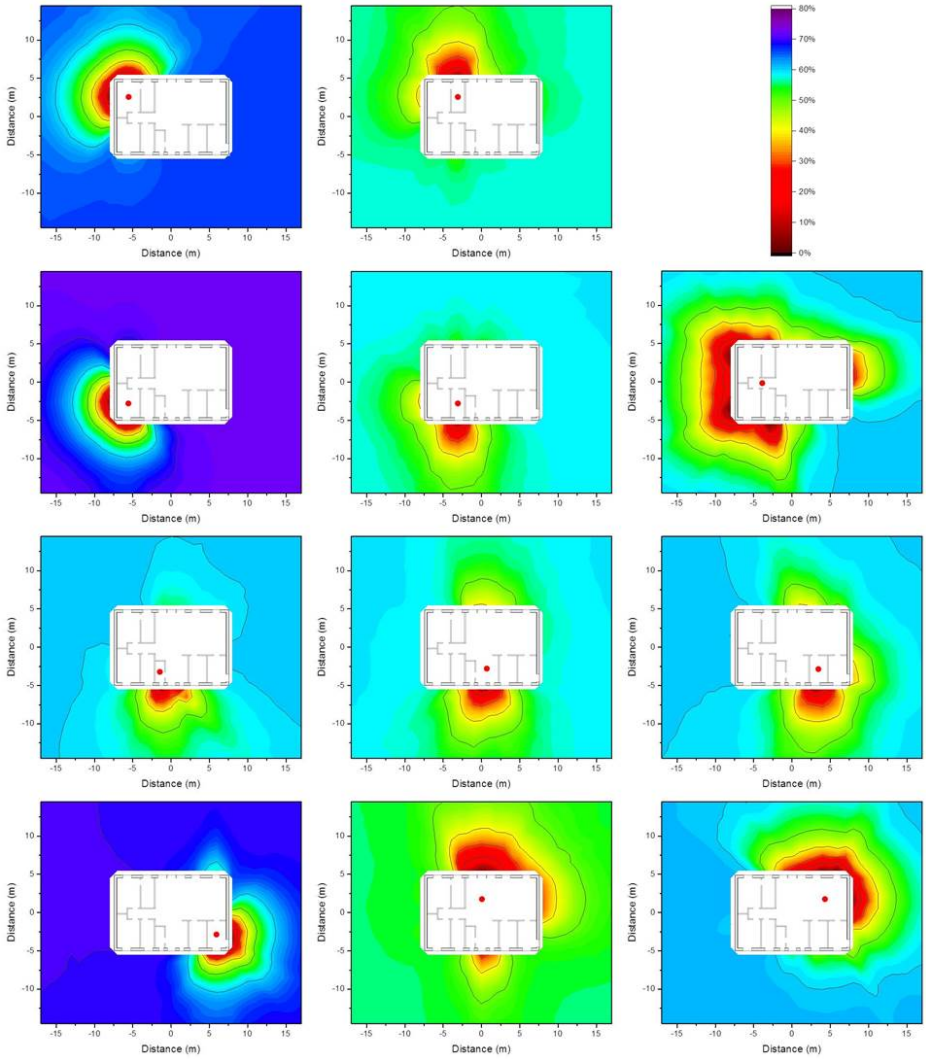

Figure 5.11: Isodose lines around a wooden house at eleven different observation points inside it (red dots) for homogenous ^{137}Cs-contamination 5 cm beneath ground level. The shading indicates the fraction of dose contribution to the observation point including the areas that are surrounded by the respective one. When the outside line for a certain dose reduction reaches the limit of the calculation grid, its shape might differ for a larger calculation grid.

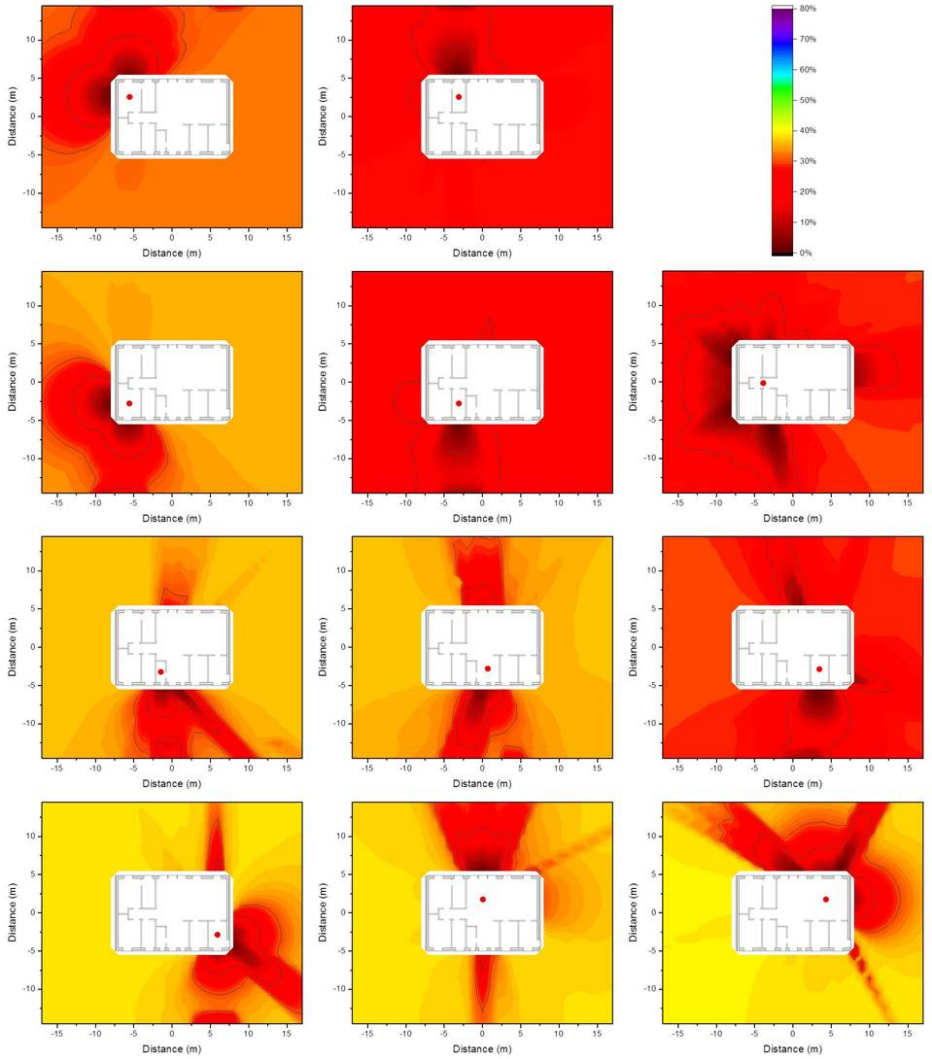

Figure 5.12: Isodose lines around a brick house at eleven different observation points inside it (red dots) for homogenous ^{137}Cs-contamination on the ground level. The shading indicates the fraction of dose contribution to the observation point including the areas that are surrounded by the respective one. When the outside line for a certain dose reduction reaches the limit of the calculation grid, its shape might differ for a larger calculation grid.

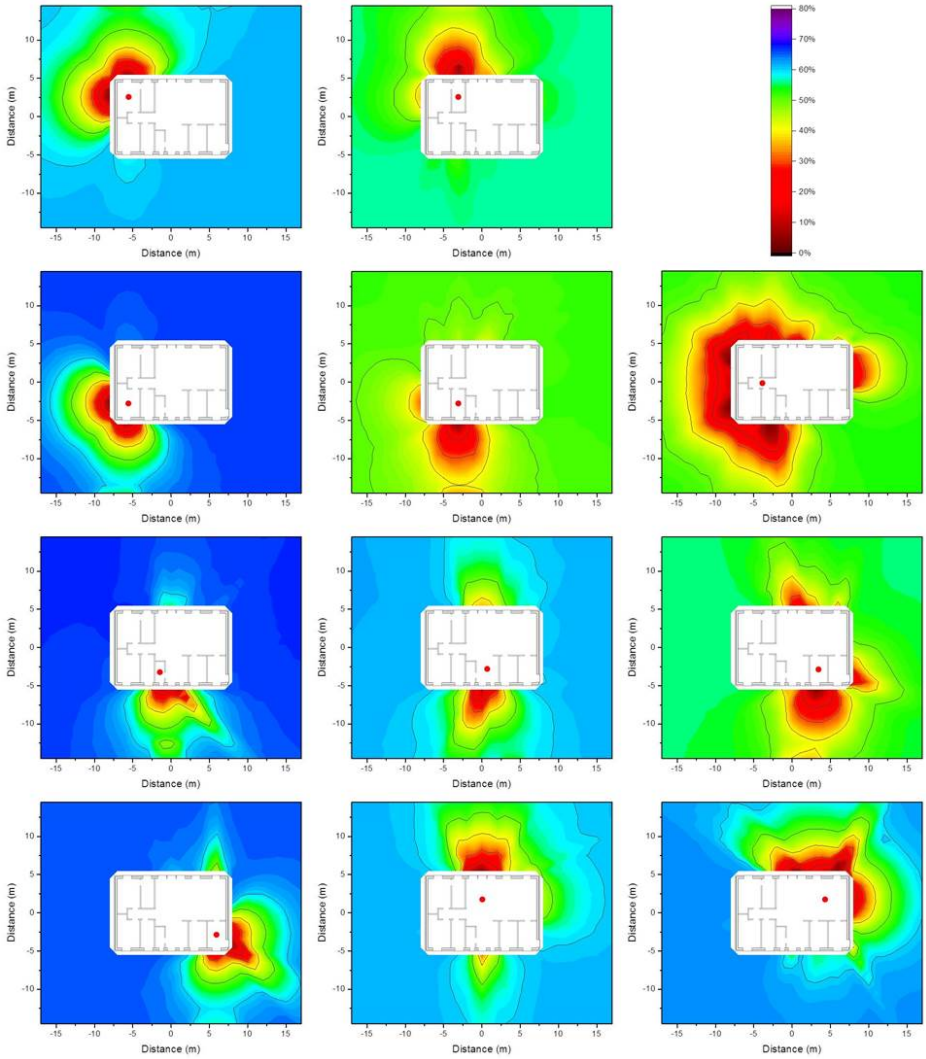

Figure 5.13: Isodose lines around a brick house at eleven different observation points inside it (red dots) for homogenous ^{137}Cs-contamination 2.5 cm beneath ground level. The shading indicates the fraction of dose contribution to the observation point including the areas that are surrounded by the respective one. When the outside line for a certain dose reduction reaches the limit of the calculation grid, its shape might differ for a larger calculation grid.

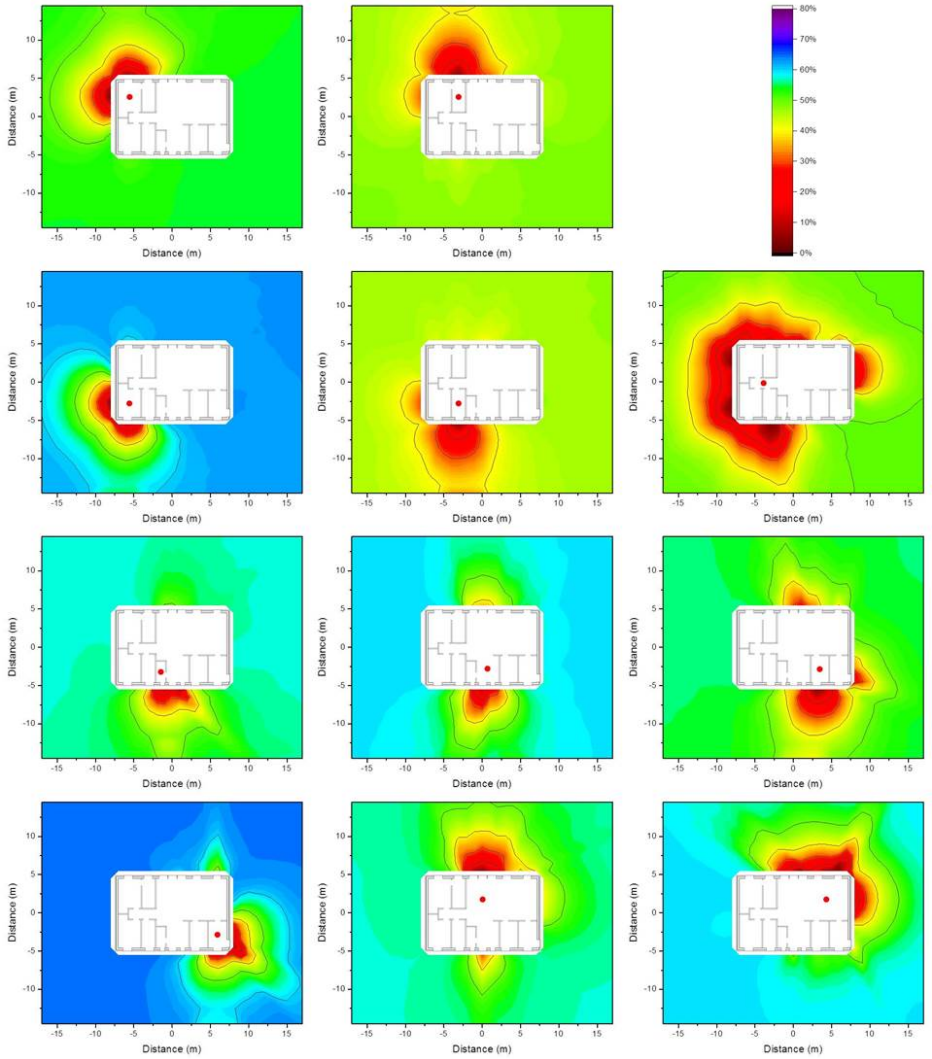

Figure 5.14: Isodose lines around a brick house at eleven different observation points inside it (red dots) for homogenous ^{137}Cs-contamination 5 cm beneath ground level. The shading indicates the fraction of dose contribution to the observation point including the areas that are surrounded by the respective one. When the outside line for a certain dose reduction reaches the limit of the calculation grid, its shape might differ for a larger calculation grid.

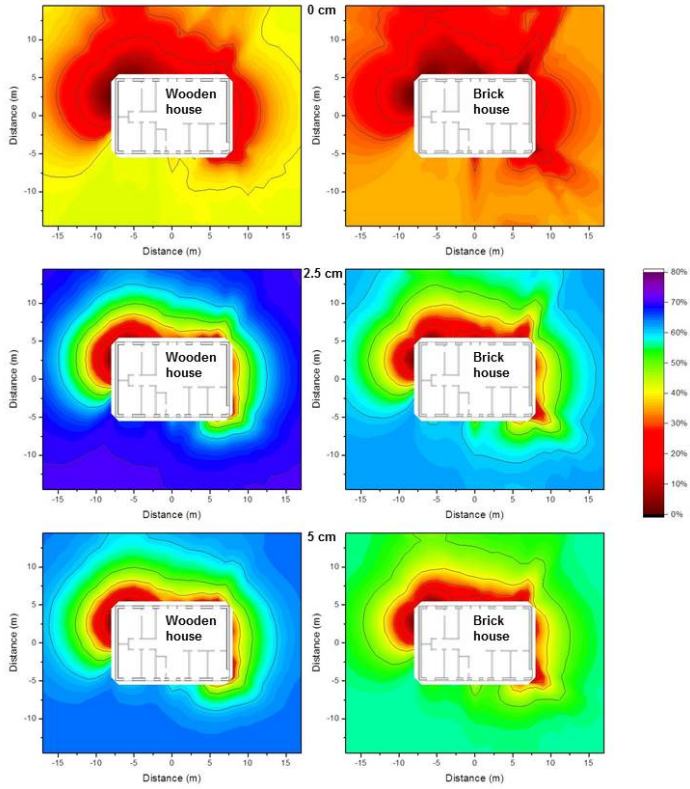

Figure 5.15: Isodose lines around a wooden (left) and a brick house (right) using occupancy factors representing typical residential behavior for homogenous ^{137}Cs-contamination at ground level (top), 2.5 cm beneath (middle), and 5 cm beneath ground level (bottom). The shading indicates the fraction of dose contribution to the observation point including the areas that are surrounded by the respective one. When the outside line for a certain dose reduction reaches the limit of the calculation grid, its shape might differ for a larger calculation grid.

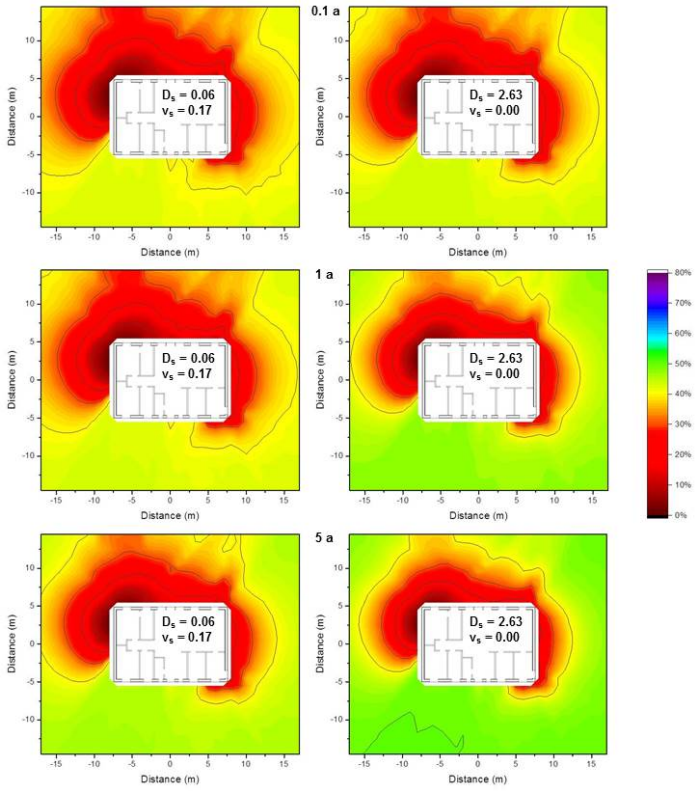

Figure 5.16: Isodose lines around a wooden house using occupancy factors representing typical residential behavior for homogenous ^{137}Cs-contamination for a vertical distribution 0.1 a (top), 1 a (middle), and 5 a after deposition (bottom) based on the two most extreme parameter combination determined in western Sweden. The shading indicates the fraction of dose contribution to the observation point including the areas that are surrounded by the respective one. When the outside line for a certain dose reduction reaches the limit of the calculation grid, its shape might differ for a larger calculation grid.

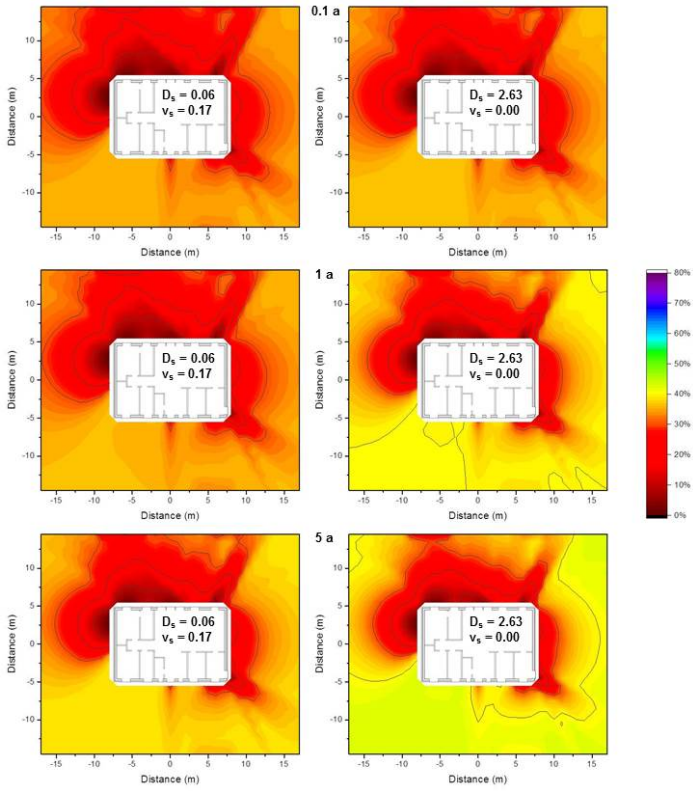

Figure 5.17: Isodose lines around a brick house using occupancy factors representing typical residential behavior for homogenous ^{137}Cs-contamination for a vertical distribution 0.1 a (top), 1 a (middle), and 5 a after deposition (bottom) based on the two most extreme parameter combination determined in western Sweden. The shading indicates the fraction of dose contribution to the observation point including the areas that are surrounded by the respective one. When the outside line for a certain dose reduction reaches the limit of the calculation grid, its shape might differ for a larger calculation grid.

Table 5.5: Primary dose factor before decontamination (pGy per γmm^{-2}) for eleven different observation points inside a wooden and a brick house for contamination on the ground level as well as 2.5 cm and 5 cm beneath ground level.

Observation point	Wooden house Contamination depth			Brick house Contamination depth		
	0 cm	2.5 cm	5 cm	0 cm	2.5 cm	5 cm
1	216	42.4	23.5	94.0	16.8	10.1
2	99.0	17.2	9.87	54.0	8.60	5.16
3	201	40.9	21.4	85.0	15.2	8.54
4	93.1	15.1	9.07	54.9	8.45	5.03
5	84.1	12.3	6.04	34.6	5.55	3.04
6	108	20.4	12.5	66.5	11.0	6.73
7	156	26.7	15.4	112	19.1	10.1
8	132	21.9	12.1	80.5	11.6	6.05
9	246	51.6	27.0	134	26.1	13.9
10	183	29.3	16.1	131	22.3	11.6
11	208	34.2	18.6	110	18.3	9.76

5.2.5 Impact of contamination variability on the isodose lines

The model of inhomogeneous contamination is based on measurements of ^{137}Cs fallout in settlements in Russia and Belarus (Bernhardsson et al. 2015), where dose rate levels represented by ^{137}Cs peak gamma signals ranging from 0 till 5 kcps were measured 0.1 m above an 9 m x 9 m open and untouched grass surface. Therefore, a random number generator picking values from 0 till 5 was applied to the 1 m x 1 m grid that was already used for the Monte Carlo calculations with the restriction that the values in all neighboring fields on a horizontal or vertical line are allowed to differ at most a value of ± 1 and on a diagonal line at most a value of ± 1.4. These values were applied as dimensionless scaling factors by multiplying the Monte Carlo calculated air kerma free-in-air values for the respective field for the wooden and the brick house that were determined for contamination at ground level (as this geometry is the most impactful one in terms of radiation dose to resident) with them. The primary dose factors were determined by subtracting the one for homogeneous contamination by the sum of determined air kerma free-in-air values without multiplication factor, then multiplied by the average of the randomly generated multiplication factors and finally the sum of determined air kerma free-in-air values with multiplication factor was added. This was done for three different contamination variability scenarios based on the random number generator (Figure 5.18). The resulting isodose lines are graphically presented Figure 5.19 for the wooden house and

in Figure 5.20 for the brick house.

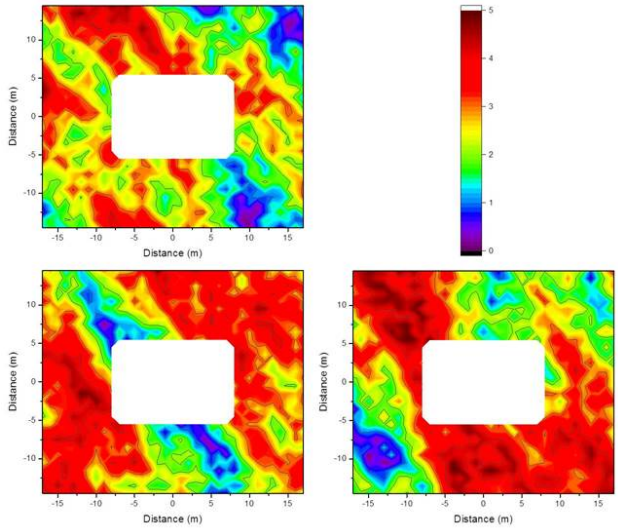

Figure 5.18: Three different possibilities of variability in ^{137}Cs contamination based on a random number generator.

By comparing the resulting isodose lines for different contamination variability scenarios with the determined isodose lines for homogenous contamination (see Figure 5.15) it can be seen that the original shape is still visible. Furthermore, as the shielding of the wooden house is lower, the effect of contamination variability has a higher impact on the change of the isodose lines compared to the brick house. The calculation of the Pearson correlation coefficient underpins this with values for the three different contamination variability scenarios of 0.96, 0.93, and 0.95 for the wooden house and 0.96, 0.94, and 0.95 for the brick house, respectively.

To see more clearly the impact of contamination variability on the quality of using zones determined by isodose lines for homogeneous contamination, the dose factors after decontamination of up to a distance of 2 m from the houses (116 m^2) were calculated as well as the respective dose factor after decontamination according to isodose lines that were determined for homogeneous contamination. The values are summarized in Table 5.6 for both houses and for homogeneous contamination as well as the three contamination variability scenarios (see Figure 5.18). The primary dose factors, the relative dose reduction and the ratio comparing the relative dose reductions for optimised and for normal decontamination are included in Table 5.6 as well.

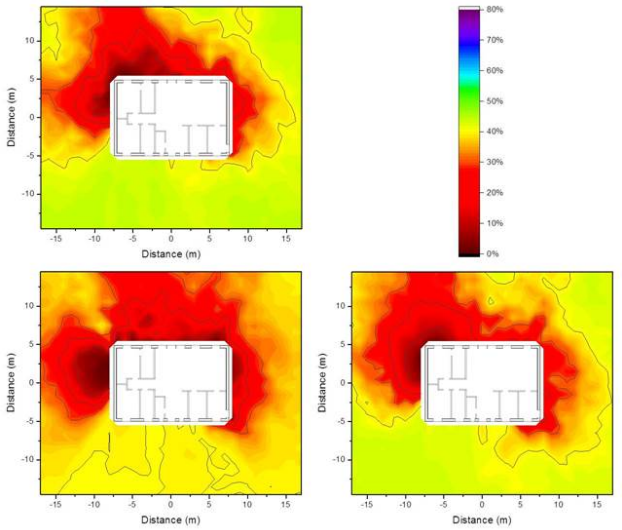

Figure 5.19: Isodose lines around a wooden house using occupancy factors representing typical residential behavior for three different possibilities of variability scenarios of ^{137}Cs-contamination according to Figure 5.18. The shading indicates the fraction of dose contribution to the observation point including the areas that are surrounded by the respective one. When the outside line for a certain dose reduction reaches the limit of the calculation grid, its shape might differ for a larger calculation grid.

The values in Table 5.6 show that the relative dose reduction for the optimized decontamination is on average 51$\pm$8 % higher compared to the normal decontamination for a fixed area size of 116 m^2 to the same distance around the house being decontaminated. This leads to the conclusion that in an authentic fallout scenario with contamination variability the decontamination of areas determined with isodose lines for homogeneous contamination are still a better choice compared to decontaminating within a certain distance of a building.

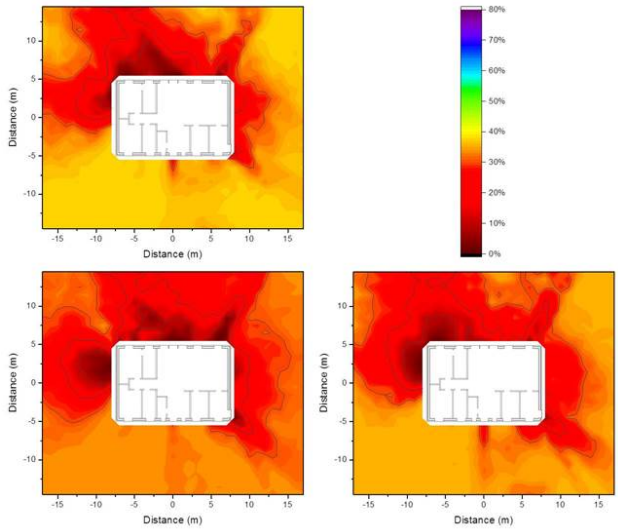

Figure 5.20: Isodose lines around a brick house using occupancy factors representing typical residential behavior for three different possibilities of variability scenarios of ^{137}Cs-contamination according to Figure 5.18. The shading indicates the fraction of dose contribution to the observation point including the areas that are surrounded by the respective one. When the outside line for a certain dose reduction reaches the limit of the calculation grid, its shape might differ for a larger calculation grid.

Table 5.6: Primary dose factor before decontamination (pGy per γmm^{-2}) for homogenous and three different variability scenarios of ^{137}Cs-contaminations at ground level using occupancy factors representing typical residential behavior in a wooden and a brick house compared to dose factors after decontaminating an area of 116 m^2 directly around the houses or optimized according to the isodose lines presented in Figure 5.15, including relative dose reductions and comparison of the relative dose reductions.

	Primary dose factor	After normal decontamination		After optimised decontamination		Comparison of relative dose reductions
		Dose factor	Relative dose reduction	Dose factor	Relative dose reduction	
Wooden house:						
Homogeneous scenario	209	177	15.5 %	165	21.2 %	1.37
Variability scenario 1	217	184 6	15.3 %	167	23.0 %	1.50
Variability scenario 2	202	178	12.1 %	168	17.1 %	1.42
Variability scenario 3	213	178	16.3 %	165	22.8 %	1.39
Brick house:						
Homogeneous scenario	102	90	12.3 %	84	18.4 %	1.47
Variability scenario 1	106	93	12.5 %	85	20.3 %	1.62
Variability scenario 2	100	90	9.6 %	85	15.2 %	1.55
Variability scenario 3	103	90	12.1 %	84	18.4 %	1.50

Chapter 6

Conclusions and perspectives

One requirement for modeling external radiation exposure is to calculate it based on given source types for a specified geometry. By comparing measured and calculated shielding factors (see Table 2.4), it was shown that an agreement within 2 % can be obtained using Monte Carlo simulations, provided that the atomic composition and density of the majority of the construction materials are accurately specified. This agreement appears to be independent of the primary photon energy of the surrounding gamma sources. The applicability of theoretical calculations using MCNP6 for radioactive fallout scenarios has thus been demonstrated in practice. Based on these findings MCNP6 was used to re-calculate the about 30 year-old dose rate (kerma rate in air) conversion factor estimates (made with the Monte Carlo code SAM-CE) for one of the standard inhabited environments integrated in the European decision support systems. The new dose rate factors differed significantly from the old ones, particularly when the radiation passed through substantial masses like outer house walls. The explanation might possibly lie in the programming as in the past 30 years milestones in computing power were taken, but could also be differences in cross-section data libraries or unreported case-specific assumptions.

Those kerma conversion factors support the progress of decision making in long term recovery management in modern cities after an airborne release of radionuclides e.g. from a nuclear power plant accident. Therefore, MCNP6 was employed to extend the knowledgebase for external dose estimations in inhabited areas by determining respective factors for a modern glass building that can be found in a similar way in many modern cities now. The factors were described as formulas as this allows the further application of the glass building model regardless of the height of the building and detection area. The importance of this building model was shown by comparing its results for kerma factors with those calculated by Meckbach et al. (1988) for a multistory house

block. The results of this comparison show the importance of taking into account adequate representations of construction geometries and materials when estimating kerma. The kerma conversion factors are given in a format that can in practice readily be implemented in the European decision support systems for management of the radiological consequences of airborne urban contamination.

To predict the external gamma exposure kerma conversion factors have to be connected with contamination levels on the various surfaces in inhabited areas. Therefore, an overview of primary contaminants with different physicochemical forms produced in the Chernobyl and Fukushima accidents was given, but it has to be noted that future accidents would be likely to have different features and might lead to different types of contaminants. Nevertheless, the lessons from these two major accidents are of great importance and on the basis of available knowledge, the relative deposition of various groups of possible contaminants on the different surfaces in the inhabited environment is estimated. This is an essential requirement in predicting initial dose rates to inhabitants from different contaminated surfaces in representative housing environments as Tables 4.1 to 4.3 show that the relative distribution of contaminants on different surfaces can vary considerably according to the physicochemical form (notably elemental iodine gas fraction, aerosol sizes) of the contaminants. The connection of this data on initial contamination levels with kerma conversion factors for a semidetached house reveals that apart from the ground the kerma inside the house would be almost exclusively caused by particles on the roof.

Moreover, to determine the fate over time of radioactive substances after deposition formulae for the decline in contamination level on different surfaces in the inhabited environment, under different conditions were given. The most recent parameter datasets derived for use in the European inhabited area decision support model, ERMIN, are reported, including estimates of uncertainties, which are often rather rough, due to the scarcity of available relevant data. Recently,refinements to the modeling have also been made to reduce overall uncertainties by better distinguishing between for instance construction material types, and soil type categories. Also, data libraries have been created for ERMIN with values reflecting the latest state of knowledge. A calculation example is given in connection with kerma conversion factors for a semidetached house. They illustrate that the post-deposition migration, and thereby doses to affected persons, may greatly depend on contaminant characteristics and assumptions regarding the surface characteristics. Furthermore, they underpin the importance of the roof as main contributor to the air kerma inside in case of this semidetached house, keeping in mind that if the ground surface is grassed, it is of similar importance in contributing air kerma to the ground floor. This knowledge is of importance in optimizing decontamination activities.

Furthermore, the influence of various building materials and the angle of incidence

of radiation on the shielding factor in case of a modular building was demonstrated. For example, the breeze block structure provides the most efficient shielding, with about 3 times lower shielding factor than the walls of the house modules. Even the doors and windows exhibit slightly lower shielding factors than the walls. To define an area with a given dose contribution to a defined observation point inside the building, the concept of the isodose was introduced. In form of isodose lines it can be used to illustrate the extent of surrounding areas that must be decontaminated to achieve a certain dose reduction, depending on the observation point. It was found that the shape of the surface encompassed by the isodose lines did not change with increasing gamma energy of the incident photons, but the area requiring decontamination to achieve the same percentage of dose reduction increased with higher gamma energies. An inverse correlation was found between the primary dose factor (dose when no decontamination measures are taken) and the size of the area that has to be decontaminated to achieve a certain dose reduction. Moreover, analyzing the impact of the type of shielding showed that geometry shielding has a high impact on the size of areas encompassed by the isodose lines, whereas barrier shielding gives the isodose lines their characteristic shapes.

As a last step the influence of wood and brick as common building materials as well as the positions of doors and windows on the shape of the isodose lines was demonstrated by applying the isodose concept to a typical Swedish residential house. Relating the determined data with data describing typical residential occupancy in the various rooms of the houses shows the mixture of the influence of the time spent in a specific part of a house and the continuous influence of building materials as well as positions of doors and windows. In addition, connecting the data with a model for vertical migration of contaminants showed the impact of increasing migration depth of the source in the soil on the decrease rate of the zones that are encompassed by the isodose lines as well as the dominance of the contamination in the topsoil layer on the total result. Eventually, the impact of contamination variabilty on the final result was demonstrated with its dependence on building materials. It was possible to show here that decontamination according to isodose lines determined for homogeneous contamination is also the better choice for a realistic contamination variability compared to decontaminating within a certain distance of the house.

In future investigations that will use MCNP6 and models connected to the contaminants characteristics, further methodologies can be demonstrated to enable further optimization of dose reductive interventions in contaminated inhabited areas as, for example, further studies are required to be able generalize the identified influences on the isodose lines, in order to further develop this method into a practical and useful tool for the optimization of countermeasures in cases of radioactive fallout in populated environments. Moreover, estimates based on Monte Carlo calculations are important, as the justification and optimization of an intervention should be based on estimates of residual dose

(ICRP 2007), and the dose rate conversion factors for the gamma exposure inside and outside resulting from radionuclides deposited on different surfaces at the required level of detail are available for only a limited number of different building types. With modern day computing power, much less time is required to obtain reliable Monte Carlo model estimates with good statistics, and with constant improvements to model data libraries, tools such as MCNP6 will play an increasing role in the optimization of an intervention.

Chapter 7

Bibliography

Aarkrog, A., Bøtter-Jensen, L., Chen, Q., Dahlgaard, H., Hansen, H., Holm, E., Lauridsen, B., Nielsen, S. P. & Søgaard-Hansen, J. (1988), 'Environmental radioactivity in denmark in 1986', *RisøReport R-549* .

Adachi, K., Kajino, M., Zaizen, Y. & Igarashi, Y. (2013), 'Emission of spherical cesium-bearing particles from an early stage of the fukushima nuclear accident', *Scientific Reports* **3**(1), 2554.

Ahmadi, G. & Li, A. (2000), 'Computer simulation of particle transport and deposition near a small isolated building', *Journal of Wind Engineering and Industrial Aerodynamics* **84**(1), 23–46.

Ahmed, A.-R. A.-A. (1979), Untersuchungen zur Aerosoldeposition an Oberflächen (in German), PhD thesis, Justus-Liebig-Universität Gießen.

Alexakhin, R. M. & Naryshkin, M. A. (1977), 'Migration of radionuclides in forest biogeocenoses', *Science* p. 144.

Alexander, C. E. & Cresser, M. S. (1995), 'An assessment of the possible impact of expansion of native woodland cover on the chemistry of scottish freshwaters', *Forest Ecology and Management* **73**(1-3), 1–27, 1–27.

Almgren, S. & Isaksson, M. (2006), 'Vertical migration studies of cs-137 from nuclear weapons fallout and the chernobyl accident', *Journal of Environmental Radioactivity* **91**(1-2), 90–102.

Andersson, K. G. (1990), 'Tactus: A code for simulation of the flow of caesium-137 in urban surroundings', *Recovery Operations in the Event of a Nuclear Accident or Radiological Emergency* pp. 217–228.

Andersson, K. G. (1991), Contamination and decontamination of urban areas, PhD thesis, Laboratory, RisøNational and of Denmark, Technical University and DTH.

Andersson, K. G. (2009*a*), Chapter 5 migration of radionuclides on outdoor surfaces, *in* K. G. Andersson, ed., 'Airborne Radioactive Contamination in Inhabited Areas', Vol. 15 of *Radioactivity in the Environment*, Elsevier, pp. 107 – 146.

Andersson, K. G. (2009*b*), Chapter10 strategies for restoration of contaminated inhabited areas, *in* K. G. Andersson, ed., 'Airborne Radioactive Contamination in Inhabited Areas', Vol. 15 of *Radioactivity in the Environment*, Elsevier, pp. 297 – 326.

Andersson, K. G. (2016), 'Physico-chemical properties of radionuclides emitted as particulate matter', *Radioprotection* **51**(2), S97–S99.

Andersson, K. G., Jones, J. A. & Charnock, T. W. (2009), Chapter 6 estimation of doses in inhabited areas, *in* K. G. Andersson, ed., 'Airborne Radioactive Contamination in Inhabited Areas', Vol. 15 of *Radioactivity in the Environment*, Elsevier, pp. 147 – 185.

Andersson, K. G., Mikkelsen, T., Astrup, P., Thykier-Nielsen, S., Jacobsen, L., Schou-Jensen, L., Hoe, S. & Nielsen, S. P. (2008), 'Estimation of health hazards resulting from a radiological terrorist attack in a city', *Radiation Protection Dosimetry* **131**(3), 297–307.

Andersson, K. G., Roed, J. & Fogh, C. (2002), 'Weathering of radiocaesium contamination on urban streets, walls and roofs', *Journal of Environmental Radioactivity* **62**(1), 49–60.

Antoni, R. & Bourgois, L. (2017), *Principle of the Monte-Carlo Method Applied to Dosimetry and Radiation Protection*, Springer International Publishing, Cham, pp. 387–465.

Askbrant, S., Melin, J., Sandalls, J., Rauret, G., Vallejo, R., Hinton, T., Cremers, A., Vandecastelle, C., Lewyckyj, N., Ivanov, Y., Firsakova, S., Arkhipov, N. & Alexakhin, R. (1996), 'Mobility of radionuclides in undisturbed and cultivated soils in ukraine, belarus and russia six years after the chernobyl fallout', *Journal of Environmental Radioactivity* **31**(3), 287–312.

Atkins, D. H. F., Chadwick, R. C. & Chamberlain, A. C. (1967), 'Deposition of radioactive methyl iodine to vegetation', *Health Physics* **13**(1), 91–92.

Belot, Y. (1977), Etude de la captation des polluants atmosphériques par les végétaux (in French), PhD thesis, Centre dÉtudes Nucléaires de Fontenay-aux-Roses, Département de Protection.

Bender, G. & Terstriep, M. (1984), 'Effectiveness of street sweeping in urban runoff pollution control', *Science of the Total Environment* **33**(33), 185–192.

Bernhardsson, C., Rääf, C. L. & Mattsson, S. (2015), 'Spatial variability of the dose rate from cs-137 fallout in settlements in russia and belarus more than two decades after the chernobyl accident', *Journal of Environmental Radioactivity* **149**, 144–149.

Bilsby® (-), 'Snittegning af kontormoduler - stabelbare; konstruktionsbeskrivelse - kontormoduler - stabelbare (in danish)'.

BIOMOVS (1991), 'Scenario 4. multiple model testing using chernobyl fallout data of i-131 and cs-137 in forage, milk, beef and grain', *H. Kohler, S.-R. Peterson & F.O. Hoffmann (eds.). Technical Report 13, vols. I and II, Stockholm: National Institute of Radiation Protection* .

Blake, G. R. & Hartge, K. H. (1986), 'Bulk density', *Klute, A., Ed., Methods of Soil Analysis, Part 1—Physical and Mineralogical Methods, 2nd Edition, Agronomy Monograph 9, American Society of Agronomy—Soil Science Society of America, Madison* pp. 363–382.

Bobovnikova, C., Virichenko, E., Konoplev, A., Siverina, A. & Shkurotova, I. (1990), 'Chemical forms of long-term radionuclides and theier transformation in the soils of accidental zone of the chernobyl npp', *Pochvovedenie* **10**, 20–29.

Bonka, H. (1989), 'Measured radioecological paramters after the chernobyl accident', *The Radioecology of Natural and Artificial Surfaces (edited by W. Feldt), TÜV Rheinland, Germany* .

Bonka, H. & Horn, M. (1980), 'Review on dry and wet deposition of aerosol particles', *Lehrgebiet Strahlenschutz in der Kerntechnik, Rheinisch-Westfälische Technische Hochschule, Aachen, Germany.* .

Bossew, P. & Kirchner, G. (2004), 'Modelling the vertical distribution of radionuclides in soil. part 1: the convection-dispersion equation revisited', *Journal of Environmental Radioactivity* **73**(2), 127–150.

Brady, N. C. & Weil, R. R. (1996), *The nature and properties of soils*, Prentice-Hall, Inc.,.

Brewer, R. (1965), 'Fabric and mineral analysis of soils', *Soil Science* **100**(1), 73.

Brown, J., Ewers, L. & Youngman, M. (2016), 'An experimental study on natural weathering of radionuclides from urban surfaces for aerosols deposited in wet and dry conditions', *Radioprotection* **51**(HS2), S109–S112.

Bunzl, K., Jacob, P., Schimmack, W., Alexakhin, R. M., Arkhipov, N. P., Ivanov, Y. & Kruglov, S. V. (1997), '137cs mobility in soils and its long-term effect on the external radiation exposure', *Radiation and Environmental Biophysics* **36**(1), 31–37.

Bunzl, K., Schimmack, W., Zelles, L. & Albers, B. P. (2000), 'Spatial variability of the vertical migration of fallout 137cs in the soil of a pasture, and consequences for long-term predictions', *Radiation and Environmental Biophysics* **39**(3), 197–205.

Carini, F. & Bengtsson, G. (2001), 'Post-deposition transport of radionuclides in fruit', *Journal of Environmental Radioactivity* **52**(2-3), 215–236.

Carlyle-Moses, D. (2004), 'Throughfall, sternflow, and canopy interception loss fluxes in a semi-arid sierra madre oriental matorral community', *Journal of Arid Environments* **58**(2), 181–202.

Chadwick, M., Obložinský, P., Herman, M., Greene, N., McKnight, R., Smith, D., Young, P., MacFarlane, R., Hale, G., Frankle, S., Kahler, A., Kawano, T., Little, R., Madland, D., Moller, P., Mosteller, R., Page, P., Talou, P., Trellue, H., White, M., Wilson, W., Arcilla, R., Dunford, C., Mughabghab, S., Pritychenko, B., Rochman, D., Sonzogni, A., Lubitz, C., Trumbull, T., Weinman, J., Brown, D., Cullen, D., Heinrichs, D., McNabb, D., Derrien, H., Dunn, M., Larson, N., Leal, L., Carlson, A., Block, R., Briggs, J., Cheng, E., Huria, H., Zerkle, M., Kozier, K., Courcelle, A., Pronyaev, V. & van der Marck, S. (2006), 'Endf/b-vii.0: Next generation evaluated nuclear data library for nuclear science and technology', *Nuclear Data Sheets* **107**(12), 2931 – 3060. Evaluated Nuclear Data File ENDF/B-VII.0.

Chadwick, R. C. & Chamberlain, A. C. (1970), 'Field loss of radionuclides from grass', *Atmospheric Environment* **4**(1), 51–56.

Chamberlain, A. C. (1953), Aspects of travel and deposition of aerosol and vapour clouds, aere, hp/r 1261, Technical report, Harwell Lab., UK.

Chamberlain, A. C. (1967), 'Transport of lycopodium spores and other small particles to rough surfaces', *Proceedings of the Royal Society of London. Series A, Mathematical and Physical Sciences* **296**(1444), 45–70.

Charnock, T. (2018), 'Concise description of ermin 2.1', *The European inhabited dose and decontamination model, Draft report, Centre for Radiation, Chemical and Environmental Hazards, Public Health England, Chilton, Didcot, Oxfordshire, OX11 0RQ, UK* .

Charnock, T., Jones, J., Singer, L., Andersson, K. G., Roed, J., Thykier-Nielsen, S., Mikkelsen, T., Astrup, P., Kaiser, J., Müller, H., Pröhl, G., Raskob, W., Hoe, S., Jacobsen, L., Schou-Jensen, L. & Gering, F. (2009), 'Calculating the consequences of recovery, a european model for inhabited areas', *Radioprotection - Revue De La Societé Francaise De Radioprotection* **44**(5), 407–412.

Chesworth, W. (2008), 'Encyclopedia of soil science', *Springer Netherlands* .

Cline, J. F., Wilson, D. O. & Hungate, F. P. (1965), 'Effect of physical and biological conditions on deposition and retention of 131i on plants', *Health Physics* **11**(8), 713–717.

Clough, W. (1975), 'The deposition of particles on moss and grass surfaces', *Atmospheric Environment* **9**(9), 1113–1119.

Collins, C., Gravett, A. & Bell, J. (2004), 'The deposition and translocation of methyl iodide by crops', *Health Physics* **87**(5), 512–516.

Crick, M. J. & Brown, J. (1990), 'Expurt - a model for evaluating exposure from radioactive material deposited in the urban environment', *NRPB Report, R-235. National RadiationProtection Board, Chilton* .

De Preter, P. (1990), Radiocesium retention in the aquatic, terrestrial and urban environment: a quantitative and unifying analysis, PhD thesis, Fakulteit der Landbouwwetenschappen, Katholieke Universiteit Leuven.

Dickson, E. D. & Hamby, D. M. (2014), 'Cloud immersion building shielding factors for us residential structures', *Journal of Radiological Protection* **34**(4), 853–871.

Dickson, E. D. & Hamby, D. M. (2016), 'Building protection- and building shielding-factors for environmental exposure to radionuclides and monoenergetic photon emissions', *Journal of Radiological Protection* **36**(3), 579–615.

Dickson, E. D., Hamby, D. M. & Eckerman, K. F. (2017), 'Contaminant deposition building shielding factors for us residential structures (vol 35, pg 317, 2015)', *Journal of Radiological Protection* **37**(4), 961–962.

Dobrovolsky, E. & Lyalko, V. (1995), 'Acidification of soils and radioactive hot particles behavior: A macrokinetic approach', *Water Air and Soil Pollution* **85**(2), 767–772.

Ehrhardt, J., Shershakov, V., Zhelenyak, M. & Mikhalevitch, A. (1996), 'Rodos: decision support system for off-site emergency management in europe', *Radiological Consequences of the Chernobyl Accident. Proceedings of the First International Conference (eur 16544 En)* pp. 1087–95, 1087–1095.

Eriksson, r. & Rosén, K. andnHaak, E. (1998), 'Eriksson, Å, rosén, k. & haak, e.', *Retention of simulated fallout nuclides in agricultural crops, Swedish University of Agricultural Sciences, Uppsala, Sweden, Report SLU-REK-80* .

Ferguson, C., Kazi, T. & Perera, J. (2003), 'Commercial radioactive sources, occasional paper no. 11. center for nonproliferation studies, monterey institute of international studies'.

Finck, R. (1991), Shielding factors for gamma radiation, experiments and calculations for swedish dwellings, *in* L. Moberg, ed., 'Results from a research programme on environmental radioecology', The Swedish Radiation Protection Institute, pp. 489–526.

Franzluebbers, A. J. (2011), *Stratification of Soil Porosity and Organic Matter*, Springer Netherlands, Dordrecht, pp. 858–861.

Freer-Smith, P., El-Khatib, A. & Taylor, G. (2004), 'Capture of particulate pollution by trees: A comparison of species typical of semi-arid areas (ficus nitida and eucalyptus globulus) with european and north american species', *Water Air and Soil Pollution* **155**(1-4), 173–187.

Furuta, T. & Takahashi, F. (2015), 'Study of radiation dose reduction of buildings of different sizes and materials', *Journal of Nuclear Science and Technology* **52**(6), 897–904.

Garland, J., A. (2001), 'On the size dependence of particle deposition', *Water, Air and Soil Pollution: Focus* **1**(5), 323–332.

Göbel, P., Dierkes, C. & Coldewey, W. G. (2007), 'Storm water runoff concentration matrix for urban areas', *Journal of Contaminant Hydrology* **91**(1-2), 26–42.

Gonfiotti, B. & Paci, S. (2018), 'Stand-alone containment analysis of phébus fpt tests with astec and melcor codes: the fpt-2 test', *Heliyon* **4**(3), e00553, e00553.

Goorley, T., James, M., Booth, T., Brown, F., Bull, J., Cox, L. J., Durkee, J., Elson, J., Fensin, M., Forster, R. A., Hendricks, J., Hughes, H. G., Johns, R., Kiedrowski, B., Martz, R., Mashnik, S., McKinney, G., Pelowitz, D., Prael, R., Sweezy, J., Waters, L., Wilcox, T. & Zukaitis, T. (2012), 'Initial mcnp6 release overview', *Nuclear Technology* **180**(3), 298–315.

Gosmartbricks (2017), 'Why bricks have holes?'.
URL: *http://gosmartbricks.com/why-bricks-have-holes/*

Gravenhorst, G. & Höfken, K. D. (1982), 'Concentration of aerosol constituents above and beneath a beech and a spruce forest canopy', *Deposition of Atmospheric Pollutants, Proceedings of a Colloquium* pp. 187–190.

Hage, K. D. (1961), 'On the dispersion of large particles from a 15-m source in the atmosphere', *Journal of Meteorology* **18**(4), 534–539.

Hansen, H. S. & Hove, K. (1991), 'Radiocesium bioavailability - transfer of chernobyl and tracer radiocesium to goat milk', *Health Physics* **60**(5), 665–673.

Harper, F. T., Musolino, S. V. & Wente, W. B. (2007), 'Realistic radiological dispersal device hazard boundaries and ramifications for early consequence management decisions', *Health Physics* **93**(1), 1–16.

Heinemann, K. & Vogt, K. J. (1980), 'Measurements of the deposition of iodine onto vegetation and of the biological half-life of iodine on vegetation', *Health Physics* **39**(3), 463–474.

Hill, R. D. (1960), 'A study of pore-size distribution of fired clay bodies', *Transactions and Journal of the Britsh Ceramic Society* (59), 189–197.

Hoe, S., McGinnity, P., Charnock, T., Gering, F., Schou Jacobsen, L. H., Havskov Sørensen, J., Andersson, K. G. & Astrup, P. (2009), 'Argos decision support system for emergency management', *Proceedings (online)* .

Höfken, K. D., Georgii, H. W. & Gravenhorst, G. (1981), 'Untersuchung über die depositon atmosphärischer spurenstoffe an buchen- und fichtenwald (in german)', *Berichte des Instituts für Meteorologie und Geophysik der Universität Frankfurt/Main, nr. 46, Frankfurt, Germany* .

Horn, H. G., Maqua, M. & Bonka, H. (1988), 'Nasse und trockene ablagerung radioaktiver stoffe auf die vegetation und den erdboden (in german)', *Schriftenreihe Reaktorsicherheit und Strahlenschutz, BMU 199-195, ISSN 0724-3316* .

Hossain, M. F., Chen, W. & Zhang, Y. (2015), 'Bulk density of mineral and organic soils in the canada's arctic and sub-arctic', *Information Processing in Agriculture* **2**(3-4), 183–190.

Howard, B. J., Fesenko, S., Balonov, M. I., Proehl, G. & Nakayama, S. (2017), 'A comparison of remediation after the chernobyl and fukushima daiichi accidents', *Radiation Protection Dosimetry* **173**(1-3), 170–176.

Hunt, C., Cox, D. & Iglesias, F. (1991), 'Fission-product release during accidents. an accident management perspective', *Atomic Energy of Canada Limited, Aecl (report)* (10481), 1–12.

IAEA (1991), 'The international chernobyl project', *Technical Report* .

IAEA (1994), 'Modelling the depositon of airborne radionuclides into the urban environment', *First report of the VAMP Urban Working Group, IAEA TECDOC 760* .

IAEA (2007), 'Terminology used in nuclear safety and radiation protection', *IAEA Safety Glossary* .

IAEA (2009), 'Quantification of radionuclide transfer in terrestrial and freshwater environments for radiological assessments', *IAEA TECDOC No. 1616* .

ICRP (2007), 'The 2007 recommendations of the international commission on radiological protection', *Annals of the ICRP* **37**(2-7), 1 – 332. ICRP Publication 103.

ICRP (2010), 'Conversion coefficients for radiological protection quantities for external radiation exposures', *Annals of the ICRP* **40**(2), 1 – 257. ICRP Publication 116.

Imanaka, T., Hayashi, G. & Endo, S. (2015), 'Comparison of the accident process, radioactivity release and ground contamination between chernobyl and fukushima-1', *Journal of Radiation Research* **56**(Suppl. 1, Sp. Iss. SI), I56–I61.

Ivanov, Y. (2009), 'Migration of fuel particles of chnpp fallout and leached radionuclides in soils and soil-to-plant system', *Nato Security Through Science Series C: Environmental Security* pp. 123–137, 123–137.

Jacob, P. & Meckbach, R. (1987), 'Shielding factors and external dose evaluation', *Radiation Protection Dosimetry* **21**(1-3), 79–85.

Jacob, P., Meckbach, R. & Müller, H. M. (1987), 'Reduction of external exposure from deposited chernobyl activity by run-off, weathering, street cleaning and migration in the soil', *Radiation Protection Dosimetry* **21**(1-3), 51–57.

Jantunen, M., Hanninen, O., Katsouyanni, K., Knoppel, H., Kuenzli, N., Lebret, E., Maroni, M., Saarela, K., Sram, R. & Zmirou, D. (1998), 'Air pollution exposure in european cities: The "expolis" study', *Journal of Exposure Analysis and Environmental Epidemiology* **8**(4), 495–518.

Jensen, N. O. (1981), 'A micrometeorological perspective on deposition', *Health Physics* **40**(6), 887–91, 887–891.

Jensen, P. H. & Thykier-Nielsen, S. (1989), 'Shielding factor calculation for plume radiation', *Radiation Protection Programme. Progress Report 1988* pp. 1561–1565.

Jonas, R. (1984), Ablagerung und Bindung von Luftverunreinigungen an Vegetation und anderen atmosphärischen Grenzflächen (in German), PhD thesis, Kernforschungsanlage Jülich GmbH, Abteilung Sicherheit und Strahlenschutz, Jül-1949, ISSN 0366-0885.

Jonas, R. & Vogt, K. J. (1982), Untersuchungen zur Ermittlung der Ablagerungsgeschwindigkeit von Aerosolen auf Vegetation und anderen Probenahmeflächen (in German), PhD thesis, Kernforschungsanlage Jülich GmbH, Abteilung Sicherheit und Strahlenschutz, Jül-1780, ISSN 0366-0885.

Jones, A., Charnock, T., Singer, L., Roed, J., Andersson, K. G., Thykier-Nielsen, S., Mikkelsen, T., Astrup, P., Kaiser, J., Müller, H., Pröhl, G., Raskob, W., Hoe, S., Jacobsen, L., Schou-Jensen, L. & Gering, F. (2007), 'Description of the modelling

of transfer and dose calculations within ermin', *Deliverable report D5C2R2 of the CEC-EURANOS project, EURANOS(CAT2)-TN(05)-04* .

Jost, D., Gäggeler, H. W., Baltensperger, U., Zinder, B. & Haller, P. (1986), 'Chernobyl fallout in size-fractionated aerosol', *Nature* **324**(6092), 22–23.

Kammann, C., Grunhage, L., Gruters, U., Janze, S. & Jager, H. (2005), 'Response of aboveground grassland biomass and soil moisture to moderate long-term co2 enrichment', *Basic and Applied Ecology* **6**(4), 351–365.

Kaneyasu, N., Ohashi, H., Suzuki, F., Okuda, T. & Ikemori, F. (2012), 'Sulfate aerosol as a potential transport medium of radiocesium from the fukushima nuclear accident', *Environmental Science & Technology* **46**(11), 5720–5726. PMID: 22533383.

Karlberg, O. (1986), 'Avrinning och retention av chernobyl nedfallet i stadsmiljö - fält-mätningar med gamma spectrometer (in swedish)', *Technical Note, Studsvik AB, Nyköping, Sweden* .

Karlberg, O. (1988), 'Weathering and migration of chernobyl fallout in sweden', *Studsvik report NP 216 EA, Studsvik, Sweden* .

Karlberg, O. (1992), 'The environmental behaviour of chernobyl deposition in a high fallout region of sweden - measurements and analysis of the urban programme 1986-1989', *Studsvik Nuclear, Stockholm, Sweden, Report NS-92/1, ISBN 91-7010-184-1* .

Kashparov, V. A., Ahamdach, N., Zvarich, S. I., Yoschenko, V. I., Maloshtan, I. M. & Dewiere, L. (2004), 'Kinetics of dissolution of chernobyl fuel particles in soil in natural conditions', *Journal of Environmental Radioactivity* **72**(3), 335–353.

Kashparov, V., Ivanov, Y., Zvarisch, S., Protsak, V., Khomutinin, Y., Kurepin, A. & Pazukhin, E. (1996), 'Formation of hot particles during the chernobyl nuclear power plant accident', *Nuclear Technology* **114**(2), 246–253.

Kashparov, V., Lundin, S., Zvarych, S., Yoshchenko, V., Levchuk, S., Khomutinin, Y., Maloshtan, I. & Protsak, V. (2003), 'Territory contamination with the radionuclides representing the fuel component of chernobyl fallout', *Science of the Total Environment* **317**(1-3), 105–119.

Kashparov, V., Protsak, V., Ahamdach, N., Stammose, D., Peres, J., Yoshchenko, V. & Zvarich, S. (2000), 'Dissolution kinetics of particles of irradiated chernobyl nuclear fuel: influence of ph and oxidation state on the release of radionuclides in the contaminated soil of chernobyl', *Journal of Nuclear Materials* **279**(2-3), 225–233.

Kinase, S., Takahashi, T., Sato, S., Yamamoto, H. & Saito, K. (2015), 'Prediction of ambient dose equivalent rates for the next 30 years after the accident', *Takahashi, T., Yamana, H., Tsukada, H., Sato, N., Nakatani, M.: Proceedings of the International Symposium on Radiological Issues for Fukushima's Revitalized Future, Paruse Iizaka, Fukushima City, Japan, May 30-31, 2015, KUR Research Program for Scientific Basis of Nuclear Safety, Osaka, Japan* .

Kirchmann, R., Fagniart, E. & van Puymbroeck, S. (1966), 'Studies on foliar contamination by radiocaesium and radio-strontium', *Radioecological concentration processes, Proceedings of an international symposium held in Stockholm, Sweden, 25-29 April 1966, Pergamon Press, London* pp. 475–483.

Kirchner, G., Strebl, F., Bossew, P., Ehlken, S. & Gerzabek, M. H. (2009), 'Vertical migration of radionuclides in undisturbed grassland soils', *Journal of Environmental Radioactivity* **100**(9), 716–720.

Kis, Z., Eged, K., Meckbach, R. & Müller, H. (2003), 'Guidelines for planning interventions against external exposure in industrial area after a nuclear accident. pt. 2. calculation of doses using monte carlo method. institut für strahlenschutz, gsf - forschungszentrum für umwelt und gesundheit gmbh'.

Kis, Z., Eged, K., Voigt, G., Meckbach, R. & Müller, H. (2004), 'Modeling of an industrial environment: External dose calculations based on monte carlo simulations of photon transport', *Health Physics* **86**(2), 161–173.

Knochenhauer, M., Hedtjärn Swaling, V., Di Dedda, F., Hansson, F., Sjökvist, S. & Sunnegård, K. (2013), 'Using bayesian belief network (bbn) modelling for rapid source term prediction - final report', *NKS report 293, NKS, Roskilde, Denmark, ISBN 978-87-7893-369-0* .

Konoplev, A. V., Bulgakov, A. A., Popov, V. E. & Bobovnikova, T. I. (1992), 'Behaviour of long-lived chernobyl radionuclides in a soil-water system', *Analyst* **117**(6), 1041–7, 1041–1047.

Krieger, H. L. & Burmann, F. J. (1969), 'Effective half-times of 85sr and 134cs for a contaminated pasture', *Health Physics* **17**(6), 811–824.

Kryshev, I. I. (1996), 'Dose reconstruction for the areas of russia affected by 131i contamination', *Radiation Protection Dosimetry* **64**(1-2), 93–96.

Kuriny, V. D., Ivanov, Y. A., Kashparov, V. A., Loshchilov, N. A., Protsak, V. P., Yudin, E. B., Zhurba, M. A. & Parshakov, A. E. (1993), 'Particle-associated chernobyl fallout in the local and intermediate zones', *Annals of Nuclear Energy* **20**(6), 415–420.

Laboratory, H. D. (2018), 'Normal needle & foliage shedding on evergreens', *Cornell University, Cooperative Extension of Suffolk University, NY* .

Lai, A. C. K. & Nazaroff, W. W. (2005), 'Supermicron particle deposition from turbulent chamber flow onto smooth and rough vertical surfaces', *Atmospheric Environment* **39**(27), 4893–4900.

Le Petit, G., Douysset, G., Ducros, G., Gross, P., Achim, P., Monfort, M., Raymond, P., Pontillon, Y., Jutier, C., Blanchard, X., Taffary, T. & Moulin, C. (2014), 'Analysis of radionuclide releases from the fukushima dai-ichi nuclear power plant accident part i', *Pure and Applied Geophysics* **171**(3-5), 629–644.

Lichtenstein, H., Cohen, M., Steinberg, H., Troubetzkoy, E. & Beer, M. (1979), 'The sam-ce monte carlo system for radiation transport and criticality calculations in complex configurations (revision 7.0). mathematical application group, inc.'.

Lind, O. C. (2006), Chracterisation of radioactive particles in the environment using advanced techniques, PhD thesis, Norwegian University of Life Sciences.

Lind, O. C., Salbu, B., Skipperud, L., Janssens, K., Jaroszewicz, J. & De Nolf, W. (2009), 'Solid state speciation and potential bioavailability of depleted uranium particles from kosovo and kuwait', *Journal of Environmental Radioactivity* **100**(4), 301–307.

Linkov, I., Morel, B. & Schell, W. R. (1997), 'Remedial policies in radiologically-contaminated forests: Environmental consequences and risk assessment', *Risk Analysis* **17**(1), 67–75.

Little, P. (1977), 'Deposition of 2.75, 5.0 and 8.5 μm particles to plant and soil surfaces', *Environmental Pollution (1970)* **12**(12), 293–305.

Loshchilov, N. A., Kashparov, V. A., B., Y. Y., Prostsak, V. P., Zhurba, M. A. & Parshakov, A. E. (1991), 'Experimental assessment of radioactive fallout from the chernobyl accident', *Sicurezza e protezione* (25-26), 46–50.

Madoz-Escande, C., Garcia-Sanchez, L., Bonhomme, T. & Morello, M. (2005), 'Influence of rainfall characteristics on elimination of aerosols of cesium, strontium, barium and tellurium deposited on grassland', *Journal of Environmental Radioactivity* **84**(1), 1–20.

Madoz-Escande, C., Henner, P. & Bonhomme, T. (2004), 'Foliar contamination of phaseolus vulgaris with aerosols of cs-137, sr-85, ba-133 and te-123m: influence of plant development stage upon contamination and rain', *Journal of Environmental Radioactivity* **73**(1), 49–71.

Madoz-Escande, C. & Santucci, P. (2005), 'Weather-dependent change of cesium, strontium, barium and tellurium contamination deposited as aerosols on various cultures', *Journal of Environmental Radioactivity* **84**(3), 417–439.

Mala, H., Rulik, P., Beckova, V., Mihalik, J. & Slezakova, M. (2013), 'Particle size distribution of radioactive aerosols after the fukushima and the chernobyl accidents', *Journal of Environmental Radioactivity* **126**(Sp. Iss. SI), 92–98.

Mamaev, L. A., Rybakov, K. A., Galkin, G. A., Ogulnik, P. G., Hrabrov, S. A., Karlin, N. E., Parhomenko, V. I., Davydov, Y. P., Voronik, N. I., Shatilo, N. N., Dmitrieva, Z. S., Efremenkov, V. M., Kupriyanova, I. V. & Kherovets, N. A. (1993), 'Development of technologies for decontamination of urban areas, techniques, motor transport, buildings, progress report on the european project ecp-4, development of strategy for decontamination', *Bochvar RIIM, Moscow, Russia / IREP of Ac. Sc, Belarus* .

Mamikhin, S. V. & Klyashtorin, A. L. (2000), 'Mathematical model of 137cs dynamics in the deciduous forest', *Journal of Environmental Radioactivity* **47**(1), 101–114.

Martin, W. E. (1963), 'Losses of sr90, sr89, and i131 from fallout-contaminated plants', *Radiation Botany* **4**(3), 275–284.

McConn Jr, R., Gesh, C., Pagh, R., Rucker, R. & Williams III, R. (2011), 'Radiation portal monitor project - compendium of material composition data for radiation transport modeling. pacific northwest national laboratory. piet-43741-tm-963, pnnl-15870 rev. 1'.

McMahon, T. A. & Denison, P. J. (1979), 'Empirical atmospheric deposition parameters - a survey', *Atmospheric Environment* **13**(5), 571–585.

Meckbach, R. & Jacob, P. (1988), 'Gamma exposures due to radionuclides deposited in urban environments. part ii: Location factors for different deposition patterns', *Radiation Protection Dosimetry* **25**(3), 181–190.

Meckbach, R., Jacob, P. & Paretzke, H. (1988), 'Gamma exposures due to radionuclides deposited in urban environments. part i: Kerma rates from contaminated urban surfaces', *Radiation Protection Dosimetry* **25**(3), 167–179.

Meckbach, R., Jacob, P. & Paretzke, H. G. (1987), 'Shielding of gamma radiation by typical european houses', *Nuclear Instruments and Methods in Physics Research Section A: Accelerators, Spectrometers, Detectors and Associated Equipment* **255**(1), 160 – 164.

Mercer, T. T. (1967), 'On the role of particle size in the dissolution of lung burdens', *Health Physics* **13**(11), 1211–1222.

Milbourn, G. & Taylor, R. (1965), 'The contamination of grassland with radioactive strontium—i initial retention and loss', *Radiation Botany* **5**(5), 337–347.

Mück, K., Prohl, G., Likhtarev, I., Kovgan, L., Meckbach, R. & Golikov, V. (2002), 'A consistent radionuclide vector after the chernobyl accident', *Health Physics* **82**(2), 141–56, 141–156.

Mück, K., Roth, K., Gerzabek, M. H. & Oberlander, H.-E. (1994), 'Effective half-lives of i- and cs-isotopes in grassland shortly after fallout', *Journal of Environmental Radioactivity* **24**(2), 127–43, 127–143.

Müller, H. & Pröhl, G. (1993), 'Ecosys-87: A dynamic model for assessing radiological consequences of nuclear accidents', *Health Physics* **64**(3), 232–252.

Nair, S. & Darley, P. J. (1986), 'A preliminary assessment of individual doses in the environs of berkeley, gloucestershire, following the chernobyl nuclear reactor accident', *Journal of the Society for Radiological Protection* **6**(3), 101–8, 101–108.

Neal, C., Robson, A. J., Bhardwaj, C. L., Conway, T., Jeffery, H. A., Neal, M., Ryland, G. P., Smith, C. J. & Walls, J. (1993), 'Relationships between precipitation, stemflow and throughfall for a lowland beech plantation, black-wood, hampshire, southern england - findings on interception at a forest edge and the effects of storm damage', *Journal of Hydrology* **146**(1-4), 221–233.

Nicholson, K. W. (1988), 'The dry deposition of small particles - a review of experimental measurements', *Atmospheric Environment* **22**(12), 2653–2666.

Nicholson, K. W. & Watterson, J. D. (1992), 'Dry deposition of particulate material onto wheat', *Precipitation Scavenging and Atmosphere-Surface Exchange vol. 2 (edited by Schwartz, S. E. & Slinn, W. G. N.), Hemisphere, Washington DC, pp. 673-682* .

Nygren, P., Hari, P., Raunemaa, T., Kulmala, M., Luokkanen, S., Holmberg, M. & Nikinmaa, E. (1994), 'Behaviour of 137cs from chernobyl fallout in a scots pine canopy in southern finland', *Canadian Journal of Forest Research* **24**(6), 1210–1215.

OCD (1962), 'Shelter design and analysis, volume 1 - fallout protection'.

OECD (2018), 'Oecd database', *The Organisation for Economic Co-operation and Development* .
URL: *http://www.oecd.org/els/family/database.htm*

Östlund, K., Samuelsson, C., Mattsson, S. & Rääf, C. L. (2017), 'The influence of (cs)-c-134 on the cs-137 gamma-spectrometric peak-to-valley ratio and improvement of the peak-to-valley method by limiting the detector field of view', *Applied Radiation and Isotopes* **128**, 249–255.

Owen, W. L., Sartor, J. D. & van Horn, W. H. (1960), 'Performance characteristics of wet decontamination procedures', *US Naval Radiological Defence Laboratory* .

Périé, C. & Ouimet, R. (2008), 'Organic carbon, organic matter and bulk density relationships in boreal forest soils', *Canadian Journal of Soil Science* **88**(3), 315–325.

Petroff, A. (2005), 'Mechanistic study of aerosol dry deposition on vegetated canopies', *Radioprotection* **40**, S443–S450.

Pryor, S. & Barthelmie, R. (2005), 'Liquid and chemical fluxes in precipitation, throughfall and stemflow', *Water, Air and Soil Pollution* **163**(1-4), 203–227.

Reineking, A., H, B. K., Porstendorfer, J. & Wicke, A. (1987), 'Air activity concentrations and particle-size distributions of the chernobyl aerosol', *Radiation Protection Dosimetry* **19**(3), 159–163.

Ritchie, L. T., Brown, W. D. & Wayland, J. R. (1978), 'Effects of rainstroms and runoff on consequences of atmospheric releases from nuclear-reactor accidents', *Nuclear Safety* **19**(2), 220–238.

Rodriguez, D., Van Oijen, M. & Schapendonk, A. (1999), 'Lingra-cc: a sink-source model to simulate the impact of climate change and management on grassland productivity', *New Phytologist* **144**(2), 359–368.

Roed, J. (1985), *Dry deposition of urban surfaces*, RisøReport R-515.

Roed, J. (1987*a*), 'Dry deposition in rural and in urban areas in denmark', *Radiation Protection Dosimetry* **21**(1-3), 33–36.

Roed, J. (1987*b*), 'Run-off from and weathering of roof material following the chernobyl accident', *Radiation Protection Dosimetry* **21**(1-3), 59–63, 59–63.

Roed, J. (1988), 'The distribution on trees of dry deposited material from the chernobyl accident', *Joint Cec/oecd(nea) Workshop on Recent Advances in Reactor Accident Consequence Assessment. Proceedings of the Second Part of the Workshop (eur 11408 En)* pp. 165–78, 165–178.

Roed, J. (1990), *Deposition and removal of radioactive substances in an urban area. Final report of the NKA project AKTU-245*, Nordisk kontaktorgan for atomenergispørgsmål.

Roed, J. & Jacob, P. (1991), 'Deposition on urban surfaces and subsequent weathering', *Proceedings of the Seminar on Methods and Codes for Assessing the Off-site Consequences of Nuclear Accidents. Preprint. Volume 1* pp. 335–356.

Ronneau, C., Cara, J. & Apers, D. (1987), 'The deposition of radionuclides from chernobyl to a forest in belgium', *Atmospheric Environment* **21**(6), 1467–8, 1467–1468.

Rotko, T., Oglesby, L., Kunzli, N. & Jantunen, M. (2000), 'Population sampling in european air pollution exposure study, expolis: comparisons between the cities and representativeness of the samples', *Journal of Exposure Analysis and Environmental Epidemiology* **10**(4), 355–364.

Rulik, P., Bucina, I. & Malátovlá, I. (1989), 'Aerosol particle size distribution in dependence on the type of radionuclide after the chernobyl accident and in the npp effluents', *The Radioecology of Natural and Artificial Radionuclides, Proc. XV Regional Congress of IRPA, Visby, Sweden, Verlag TÜV Rheinland GmbH, Köln, Germany, ISBN 3-88585-668-9* .

Salbu, B. (1988), 'Radionuclides associated with colloids and particles in rainwaters', *Oslo, Norway, in: von Philipsborn, H., Steinhäuser, F. (Eds.), Hot particles from the Chernobyl Fallout. Bergbau - und Industrimuseum, Theuern* pp. 83–84.

Salbu, B. (2001), 'Actinides associated with particles', *Radio Envir* **1**, 121–138.

Salbu, B., Krekling, T., Oughton, D. H., Ostby, G., Kashparov, V. A., Brand, T. L. & Day, J. P. (1994), 'Hot particles in accidental releases from chernobyl and windscale nuclear installations', *Analyst* **119**(1), 125–130.

Salinas, I. C. P., Conti, C. C., Rochedo, E. R. R. & Lopes, R. T. (2006), 'Gamma shielding factor for typical houses in brazil', *Radiation Protection Dosimetry* **121**(4), 420–424.

Sandalls, F. J. & Gaudern, S. L. (1988), 'Radiocaesium on urban surfaces in west cumbria five months after chernobyl', *Journal of Environmental Radioactivity* **7**(1), 87–91, 87–91.

Sartor, J. D., Boyd, G. B. & Agardy, F. J. (1974), 'Water-pollution aspects of street surface contaminants', *Journal Water Pollution Control Federation* **46**(3), 458–467.

Sartor, J. & Gaboury, D. (1984), 'Street sweeping as a water pollution control measure: Lessons learned over the past ten years', *Science of the Total Environment* **33**(33), 171–183.

Schell, W. R., Linkov, I., Myttenaere, C. & Morel, B. (1996), 'A dynamic model for evaluating radionuclide distribution in forests from nuclear accidents', *Health Physics* **70**(3), 318–335.

Schimmack, W., Bunzl, K., Kreutzer, K., Rodenkirchen, E. & Schierl, R. (1991), 'Einfluss von fichte (picea abies l. karst) und buchte (fagus sylvatica l.) auf die wanderung von radioceasium im boden (in german)', *Forstwissenschaftliche Forschung* (39), 242–251.

Schuller, P., Ellies, A. & Kirchner, G. (1997), 'Vertical migration of fallout 137cs in agricultural soils from southern chile', *Science of the Total Environment* **193**(3), 197–205.

Schwartz, G. (1986), 'Deposition and post-deposition radionuclide behaviour in urban environments, proceedings', *Workshop on methods for assessing off-site radiological consequences of nuclear accidents, CEC, Luxemburg, Report EUR 10397 (EN)* pp. 533–558.

Schweizer, C. (2004), 'Expolis annex', *Final report of WP1 of the EXPOLIS study funded by CEFIC* .

Scotsman, T. (2008), 'How long do we spend in bathroom?'.
URL: *https://www.scotsman.com/news/how-long-do-we-spend-in-bathroom-1-189-years-1-1072528*

Sehmel, G. A. (1973), 'Particle eddy diffusivities and deposition velocities for isothermal flow and smooth surfaces [aerosols]', *Journal of Aerosol Science* **4**(2), 125–38, 125–138.

Shaw, S. B., Walter, M. T. & Steenhuis, T. S. (2006), 'A physical model of particulate wash-off from rough impervious surfaces', *Journal of Hydrology* **327**(3-4), 618–626.

Sheppard, S., Long, J. & Sanipelli, B. (2009), 'Solid/liquid partition coefficients (kd) for selected soils and sediments at forsmark and laxemar-simpevarp', *SKB Report R-09-27, Sweden* .

Slinn, W. G. N. (1982), 'Predictions for particle deposition to vegetative canopies', *Atmospheric Environment* **16**(7), 1785–1794, 1785–1794.

Sørensen, J. H., Schönfeldt, F., Sigg, R., Pehrsson, J., Lauritzen, B., Bartnicki, J., Klein, H., Cordt Hoe, S. & Lindgren, J. (2018), 'Added value of uncertainty estimates of source term and meteorology (avesome)'.

Spencer, L. (1962), 'Structure shielding against fallout radiation from nuclear weapons', *United States Bureau of Standards – Monograph* **National Bureau of Standards Monograph 42**.

Spencer, L. V., Chilton, A. B. & Eisenhauer, C. M. (1980), 'Structure shielding against fallout gamma rays from nuclear detonations', *National Bureau of Standards, Special Publication* .

Steinhauser, G. (2014), 'Fukushima's forgotten radionuclides: A review of the understudied radioactive emissions', *Environmental Science and Technology* **48**(9), 4649–4663.

Terstriep, M. L., Bender, G. M. & Noel, D. C. (1982), 'Final report, nationwide urban runoff project, champaign, illinois: Evaluation of the effectiveness of muncipl street sweeping in the control of urban storm runoff pollution', *US Environmental Protection Agency* .

Tessier, A., Campbell, P. G. C. & Bisson, M. (1979), 'Sequential extraction procedure for the speciation of particulate trace metals', *Analytical Chemistry* **51**(7), 844–851.

Tschiersch, J. & Georgi, B. (1987), 'Chernobyl fallout size distribution in urban areas', *Journal of Aerosol Science* **18**(6), 689–692.

USDA (2018), 'How much time do americans spend eating?', *United States Department of Agriculture* .
URL: *https://www.thefreelibrary.com/How+much+time+do+Americans+spend+eating%3fa0190462486/*

Vargas, A., Camacho, A., Laubenstein, M. & Plastino, W. (2016), 'Dry deposition velocity of cs-137 and cs-134 in spain after the fukushima dai-ichi nuclear power plant accident', *Applied Radiation and Isotopes* **109**, 441–443.

Ver, N., Matus, L., Kunstar, M., Pintér, a., Osán, J., Hózer, Z. & Tóth, B. (2007), 'Oxidation and release of ruthenium from white inclusions', *European Commission, EUR 22730 EN, ISSN 1018-5593, Luxenbourg* .

Warming, L. (1982), 'Weathering and decontamination of radioactivity deposited on asphalt surfaces', *Risø-M-2273* .

Warming, L. (1984), 'Weathering and decontamination of radioactivity deposited on concrete surfaces', *Risø-M-2473* .

Watterson, J. & Nicholson, K. (1996), 'Dry deposition and interception of 4-22 μm diameter particles to a lettuce crop', *Journal of Aerosol Science* **27**(5), 759–767.

Wilkins, B. (1987), 'The retention behaviour of radiocaesium on common building materials under natural outdoor conditions', *Radiation Protection Dosimetry* **21**(1-3), 69–73.

Xiao, Q. F., McPherson, E. G., Ustin, S. L., Grismer, M. E. & Simpson, J. R. (2000), 'Winter rainfall interception by two mature open-grown trees in davis, california', *Hydrological Processes* **14**(4), 763–784.

Chapter 8

Publications

Paper I

Hinrichsen, Y., Finck, R., Östlund, K., Rääf, C., Andersson, K. G. Comparison of experimental and calculated shielding factors for modular buildings in a radioactive fallout scenario. Journal of Environmental Radioactivity 189 (2018) 146-155.

Journal of Environmental Radioactivity 189 (2018) 146–155

Contents lists available at ScienceDirect

Journal of Environmental Radioactivity

journal homepage: www.elsevier.com/locate/jenvrad

Comparison of experimental and calculated shielding factors for modular buildings in a radioactive fallout scenario

Yvonne Hinrichsen[a,*], Robert Finck[b], Karl Östlund[b], Christopher Rääf[b], Kasper Grann Andersson[a]

[a] Technical University of Denmark, Center for Nuclear Technologies, Denmark
[b] Lund University, Department of Translational Medicine, Medical Radiation Physics, Sweden

ARTICLE INFO

Keywords:
Shielding factor
Monte Carlo simulations
Experimental validation

ABSTRACT

Experimentally and theoretically determined shielding factors for a common light construction dwelling type were obtained and compared. Sources of the gamma-emitting radionuclides ^{60}Co and ^{137}Cs were positioned around and on top of a modular building to represent homogeneous fallout. The modular building used was a standard prefabricated structure obtained from a commercial manufacturer. Four reference positions for the gamma radiation detectors were used inside the building. Theoretical dose rate calculations were performed using the Monte Carlo code MCNP6, and additional calculations were performed that compared the shielding factor for ^{137}Cs and ^{134}Cs. This work demonstrated the applicability of using MCNP6 for theoretical calculations of radioactive fallout scenarios. Furthermore, the work showed that the shielding effect for modular buildings is almost the same for ^{134}Cs as for ^{137}Cs.

1. Introduction

After an airborne release of radionuclides to inhabited environments, external gamma irradiation from deposited radioactivity can contribute considerably to the radiation exposure of the population. The shielding of gamma radiation by buildings can, however, reduce this exposure and sheltering of inhabitants is one of the principal countermeasures considered for areas potentially affected by radioactive release. Detailed knowledge of the shielding properties of buildings is therefore an important component of risk assessment in radiological emergency preparedness. Representing the shielding effect of a single-storey building, the UNSCEAR used a location factor of 0.1 (UNSCEAR, 2016) which describes the reduction in ambient dose equivalent from external exposure to deposited material that is achieved when indoors.

As the geometry of building structures is too complex for simple methods such as the point kernel model (Spencer et al., 1980), Monte Carlo calculations are needed to calculate shielding factors as shown in a comparison performed by Jensen and Thykier-Nielsen (1989). The shielding properties can vary greatly for different types of buildings (e.g., Finck, 1991) leading to the use of Monte Carlo simulations in the late 1980s at the GSF (now the Helmholtz Zentrum München German Research Center for Environmental Health) (Jacob and Meckbach, 1987; Meckbach and Jacob, 1988; Meckbach et al., 1987, 1988) An early Monte Carlo code SAM-CE (Lichtenstein et al., 1979) was applied to calculations for four different types of houses. Inhabited area external dose estimates in the European standard decision support systems ARGOS and RODOS rely entirely on these few old datasets. Monte Carlo calculations were repeated for one of these building types using the modern code MCNP6 (Goorley et al., 2012), and agreements and deviations within the order of magnitude for different parts of the building are described in a report that is still to be published. Further Monte Carlo simulations were performed for an industrial area (Kis et al., 2003; 2004), for various scenarios of U.S. residential structures (Dickson and Hamby, 2014; 2016; Dickson et al., 2017), for typical houses in Brazil (Salinas et al., 2006), and typical buildings in Japan (Furuta and Takahashi, 2015). To the best of our knowledge this is the first occasion where Monte Carlo calculations of shielding factors have been experimentally verified, employing a building type with lightweight walls that is used in Scandinavia for e.g. preschools, schools and habitation.

The aim of this study was to compare numerical simulation results from a theoretical calculation with practical measurements in a modular building geometry by using point sources of ^{137}Cs and ^{60}Co distributed over an area of about 800 m^2 around the building to mimic a surface deposition. By doing so we aim to show the applicability of the Monte Carlo simulation for this purpose, both in terms of the accuracy of the shielding estimate as well as the ability to find suitable, representative indoor points for obtaining the shielding factor. The comparison study was performed for a lightweight prefabricated

* Corresponding author. Technical University of Denmark, Center for Nuclear Technologies, Frederiksborgvej 399, Bldg 201, Rm S56, 4000 Roskilde, Denmark.
E-mail address: yvhi@dtu.dk (Y. Hinrichsen).

https://doi.org/10.1016/j.jenvrad.2018.04.005
Received 30 January 2018; Received in revised form 6 April 2018; Accepted 6 April 2018

modular building which was selected because this type of construction is not uncommon in Scandinavia as solutions for kindergartens, office-complexes and habitation in areas with rapid population growth. Another aspect of this type of building is the poor shielding provided by the light walls, and are therefore of special concern in emergency preparedness. The focus was on the two cesium radionuclides ^{134}Cs and ^{137}Cs, which have been of main concern in connection with the Chernobyl and Fukushima incidents (Imanaka et al., 2015). ^{137}Cs is also represented among those important high-activity sealed sources that could become dispersed in an accident or as a consequence of a terrorist attack (Andersson et al., 2008). However, this study also considered ^{60}Co as a representative of higher-energetic sources, as it also is directly relevant to plausible terrorism scenarios (Ferguson et al., 2003).

2. Materials and methods

2.1. Concept of the shielding factor

The shielding factor represents the reduction of the absorbed dose rate by attenuation and scattering when the radiation passes through matter. The shielding factor at a point inside a building structure acting on a radiation source outside the building can be defined as

$$S_{bld} = \frac{\dot{D}_{bld}}{\dot{D}_{ref}}, \quad 0 \le S_{bld} \le 1 \tag{1}$$

where $\dot{D}_{bld}$ is the absorbed dose rate at a point inside the building and $\dot{D}_{ref}$ is the absorbed dose equivalent at the same point in air without the presence of the building for an identical source geometry (Finck, 1991). This factor is based on the barrier shielding factor concept that was originally defined by Spencer (1962) and compares the dose rate at one position caused by the same source to the dose rate at the same position replacing the building with air. A second concept developed by Spencer (1962) is geometry shielding, which compares the dose rate at one position caused by a given source and replacing the building by air to the dose above an infinite, uniformly contaminated plane-surface source at a reference height of 1 m. Geometry shielding can be combined with the barrier-shielding concept by multiplication. The resulting factor is also called reduction factor. In the theoretical calculation, the shielding factor can be determined by first calculating the absorbed dose rate with the building in place, and then dividing it by the absorbed dose rate calculated at the same point but with the building removed and replaced by air. Of course, this is not possible in an experimental situation for buildings that already exist.

When shielding factors are determined experimentally by measuring dose rates with a dose rate instrument, it is necessary to separate the natural background component as defined by IAEA (IAEA, 2007) from the signal originating from a specific radiation source. This is done in two steps. First, the natural background is measured both inside the building and outside using one location as a reference. Then, the shielding factor for the radiation from the source is calculated from the relationship

$$S_{bld} = \frac{\dot{D}_{tot,bld} - \dot{D}_{bgd,bld}}{\dot{D}_{tot,ref} - \dot{D}_{bgd,ref}} \tag{2}$$

where $\dot{D}_{tot,bld}$ and $\dot{D}_{tot,ref}$ are the total measured absorbed dose rates inside the building and outside at the location chosen as reference with the radiation sources present. $\dot{D}_{bgd,bld}$ and $\dot{D}_{bgd,ref}$ are the dose rate contributions from the natural background in the building and outside at the location chosen as reference as measured in the absence of the source.

The focus of this study was on the shielding factors considering contamination on outdoor horizontal surfaces (ground and roof). In fallout scenarios where the deposition mainly has arisen from rainout or washout of fission products from the passing plume, radionuclides on the ground and on the roof of buildings can be expected to contribute significantly to the total dose (Andersson, 2009), although buildings naturally also protect against radiation from contamination, e.g., on all vertical surfaces, on other indoor surfaces, on vegetation and in the air (primary contaminant plume or resuspended radioactive matter).

Fig. 1. Setup of the modular building.

2.2. Description of the experiment

The applied modular building consisted of two standard office modules with outer measurements 900 cm × 330 cm × 300 cm (L x W x H) rented by the company Bilsby®, that were fitted together side by side (Fig. 1). The modules were placed in an open field (> 100 m clear in all directions) and raised with wooden beams from the uneven ground to make them level. Each module had one window on each short side and one door on each long side. The outer measurements of the windows were 140 cm × 120 cm (W x H) and of the doors 90 cm × 200 cm (W x H), so the fraction of windows was about 7% of the wall surface of the entire modular building and that of the doors was about 4%. The outer wall thickness was 12.5 cm and consisted mainly of wood and mineral wool. The combination thus had four windows, two doors, and one opening between the modules. The inner wall thickness was 25 cm. Inside one of the modules an “inner room” of lightweight expanded clay aggregate (LECA) was set up (Fig. 2) to investigate the impact of heavier material for constructing buildings. This room had a wall thickness of 15 cm, height of 152 cm, and outer measurements of 103 cm × 88 cm due to the measures of the used bricks.

Dose rate instruments (Automess Dose Rate Meter 6150 AD 6/H with a plastic scintillator probe 6150 AD-b/H) were used to experimentally determinate the dose rates. They were calibrated to the ambient dose rate, H*(10), according to the ICRP definition (ICRP, 2010). This is the absorbed dose rate at a point 10 mm below the surface in the 300 mm diameter ICRU sphere (consisting of tissue-equivalent matter) subjected to a parallel and aligned radiation field. One detector was calibrated by the Swedish Radiation Safety Authority (SSM) for calibration factors regarding the ambient dose rate equivalent, H*(10), and the angular efficiency (30°, 60°, and 90°) for ^{241}Am, ^{137}Cs, and ^{60}Co. The calibration factors for the other detectors were determined by placing a source at 1 m distance from the center of a scintillator crystal at 0° in a low background level room, with the calibrated detector as a reference instrument for ^{60}Co and ^{137}Cs. The deviations were within a range of 10%. It is assumed that the ratio of ambient dose, with and without shielding, at a given observation point, is the same as the corresponding ratio of the absorbed dose at that point. In the same low-background-level room, sources were also placed at 30°, 60°, and 90°to assess the angular efficiency. The results of those measurements were within a range of 6%. Four detectors were positioned inside the modules (Fig. 2) and one detector outside, about 14 m away from the

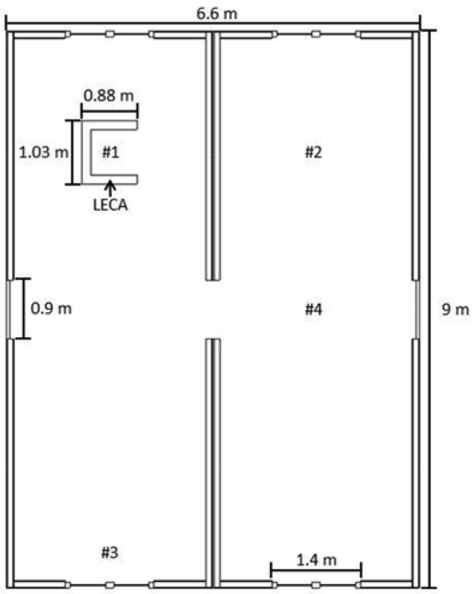

Fig. 2. Detector positions inside the modular building. The top and bottom wall have two windows each. The left and right wall have one door each, and there is a doorway connecting both modules where the modules are fitted together. The U-shape in the top-left corner represents the clay brick structure (LECA).

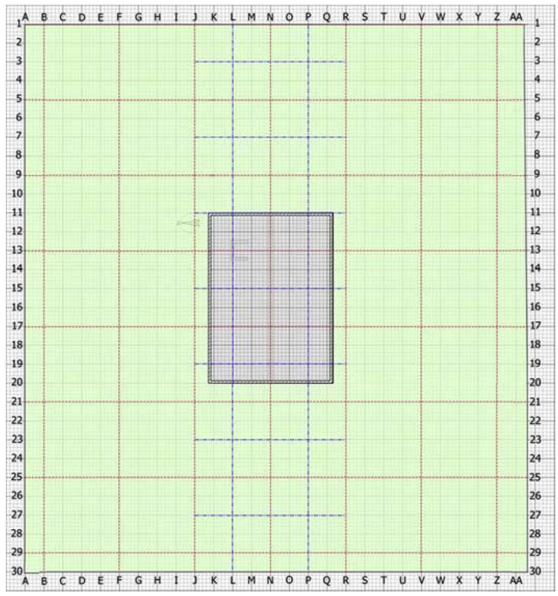

Fig. 3. Schematic overview of the measurement grid. All crossings of red and blue lines indicate source position points. The width of one row and column represented by the letters and numbers at the frame is 1 m. (For interpretation of the references to color in this figure legend, the reader is referred to the Web version of this article.)

modules. All detectors were placed 1 m above the floor surface in the modules. The bottom level of the modules was 26 cm beneath the floor surface and was used as ground surface, as the ground was uneven and thus the modules had to be put on beams.

^{137}Cs and ^{60}Co point sources as well as one point source with physical diameter 10 mm of ^{60}Co were used in the experiments. The respective details including uncertainties are presented in Table 1.

The measurement scheme used in the study followed a grid system that was 29 m × 26.5 m, as represented in Fig. 3 for the source positions. The red grid in Fig. 3 represents a distance between the source points of 4 m and the blue grid represents a subdivision of the red grid to a distance between the source points of 2 m. Every crossing between the red, blue, and red-blue lines in the figure represents a source point. Thus, the number of source points is denser along the short side of the module configuration in order to reduce systematic uncertainties for measurements of radiation penetrating the windows. The 4 m density of source points is also too coarse for measuring the shielding factor on the roof; hence, it was decreased to a 2 m density as seen by the crossings of the red, blue, and red-blue lines in Fig. 3. The height of the positioned sources was chosen to be on a plane that would have been level with the ground if the modules were placed on a level ground surface.

Table 1
Sources used for the measurement of shielding factors. The uncertainties represent a coverage factor of k = 2.

Radionuclide	Source number	Activity in MBq
^{137}Cs	1	1400 ± 200
	2	880 ± 80
	3	850 ± 150
^{60}Co	4	6100 ± 1600
	5	45 ± 4
	6	45 ± 4
	7	94 ± 9
	8	94 ± 9

To calculate the shielding factor, the background values for all detectors and their respective positions were recorded daily prior to the measurements with the sources present. These values were eventually subtracted from the instrument reading of the source points. The ambient dose rate was also corrected with the calibration factors and the angular efficiencies via a calculation of the incident angle from each source point.

The $H^*(10)$ rates measured with the detector outside the modules were also corrected using the same method mentioned above (subtraction of measured background values and correction with calibration factors and angular efficiencies). Ambient dose rates for different source points were compiled and the data set was used to fit a mathematical expression that displayed $H^*(10)$ as a function of distance. This expression was then used to extract the reference $H^*(10)$ for the exact distance from each detector to each source point. The measured $H^*(10)$ from each source point and each detector was then divided by this value to determine the shielding factor.

Measurements for the following four setups were performed:

Setup 1: All 92 grid points on the ground according to Fig. 3 were measured with three ^{137}Cs point sources totaling 3.1 GBq (Sources number 1–3 in Table 1) placed in a 200 mL plastic container (inner wall ∅ = 67 mm and inner wall thickness = 1.9 mm). This container was placed on a height-adjustable tripod in order to place the sources in the measurement plane.

Setup 2: ^{137}Cs measurements were taken of the 15 grid points on the roof of the modules (L11 to P19 in Fig. 3). The scintillators were now reoriented so that their front surfaces were directed towards the ceiling of the building, instead of downwards in the previous experiments with the center of the plastic crystal remaining 1 m above the floor surface. For these measurements, one point source was used with activity 880 MBq (Source number 2 in Table 1), and it was also placed in a 200 mL plastic container.

Setup 3: All 92 source points on the ground, according to Fig. 3, were measured with the point source of 6100 MBq (^{60}Co - source number 4 in

Table 1). Due to its high activity, complementary measurements were made with weaker sources at the points closer to the modules in order to avoid saturating the detectors. The source points where one or more detectors saturated and for which complementary measurements were necessary were N9, L9, P9, R9, J11, R11, J13, R13, J15, R15, J17, R17, J19, R19, J21, L21, N21, P21, J23, L23 and N23 (Fig. 3). Measurements were taken by using three point sources of ^{60}Co that contained a total 180 MBq (Sources number 5, 6, and 7 or 8 in Table 1). The sources were placed in a 200 mL plastic container with inner wall diameter 67 mm, which, in turn, was placed on a height-adjustable tripod.

Setup 4: For the ^{60}Co measurements of the 15 grid points on the roof of the modules (L11 to P19 in Fig. 3), the detectors were reoriented so that their front surfaces were directed towards the ceiling of the building, instead of downwards in the previous experiments with the center of the plastic crystal remaining 1 m above the floor surface. Two point sources totaling an activity of 190 MBq (Sources number 7 and 8 in Table 1) were used for the measurements on the roof. As in Setup 3, the sources were placed in a 200 mL plastic container.

For all the measurements that used the 200 mL plastic container, the maximum displacement of the sources within the container was 30 mm. Source number 4 in Table 1 was somewhat more difficult to place in exact position because of its higher activity and attached handling equipment. Because of this, the displacement varied from measurement point to measurement point, in the range 10 cm–40 cm.

2.3. Description of the calculations

The Monte Carlo calculations for the setup of the modular building were performed with the transport code MCNP6 (Goorley et al., 2012), using the nuclear cross-section data set ENDF/B-VII.0 (Chadwick et al., 2006). Among other processes, it accounts for photon creation and loss through relevant mechanisms such as bremsstrahlung, fluorescence, Compton scattering, photon capture, pair production and p-annihilation.

The code allows for the definition of complex three-dimensional geometries through a combinatorial geometry technique. The definition of the geometry is based on the construction drawings and descriptions made available by Bilsby®, and measurements for the real modules included an additional construction made of clay bricks (Fig. 4). The regions in space were constructed by a logical combination (union, intersection, difference) of elementary geometric bodies and surfaces. Different databases (McConn et al., 2011; Websides, 2016) were used to assign the material specifications with definite atomic compositions and densities as summarized in Table 2 to the input data for the different building structures and environmental regions.

For each setup separate computations were performed for the different source positions and for reference values without the building structure. The setups corresponded to the four different measurement setups. The source regions were defined in all calculations as cylinders

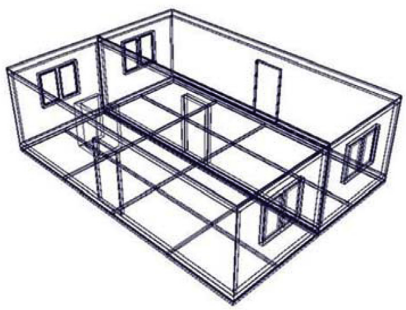

Fig. 4. Birds-eye view of the modular building model.

Table 2
Material specifications with definite atomic compositions (rounded) and densities that were used for the Monte Carlo calculations.

Material	Atomic composition	Density in kg/L
Particle board	46.24% H; 32.34% C; 0.28% N; 20.88% O;	0.7
Profile boards	0.06% Mg; 0.12% S; 0.04% K; 0.04% Ca	0.6
Plywood		0.5
Window frame		0.45
Mineral wool	42.5% O; 1.7% Na; 5.4% Mg; 10.6% Al; 18.2% Si; 1.9% K; 14.3% Ca; 0.5% Mn; $^{4.9\%\ Fe}$	0.167
Glas	60.39% O; 8.81% Na; 25.18% Si; 5.62% Ca	2.4
Plastic	50.00% H; 33.33 % C; 16.67% Cl	1.51
LECA bricks	63.33% O; 0.69% Na; 0.92% Mg; 9.47% Al; 21.91% Si; 0.01% P; 1.09% K; 0.99% Ca; 0.20% Ti; 0.01% Mn; 1.38% Fe	2.2
Steel	3.41% C; 4.87% N; 0.97% Si; 0.05% P; 0.03% S; 18.88% Cr; 8.69% Mn; 65.92% Fe; 4.65% Ni	7.86
Soil	31.69% H; 50.16% O; 4.00% Al; 14.16% Si	1.52
Air	0.02% C; 78.44% N; 21.07% O; 0.47% Ar	0.001205

with a diameter and height of 1 cm. The source energies were either monoenergetic sources of 0.662 MeV representing the ^{137}Cs sources, or they were multi-energetic sources with energies of 1.173 MeV and 1.332 MeV representing the ^{60}Co sources, also taking into account the emission probability of both energies. Internal scatter within the source material was neglected, and there was no extra material composition attached to the source regions apart from the surrounding air, but from a simple comparison calculation without building can be assumed that about 12% of the calculated ambient dose is caused by gamma radiation that was scattered by the soil for ^{137}Cs and about 8% for ^{60}Co.

To compare the shielding factors for the ^{134}Cs sources with those for the ^{137}Cs sources, additional Monte Carlo computations were performed for 70 source points on the roof (K11 to Q20 in Fig. 3) of the modules for the ^{137}Cs sources as well as poly-energetic gamma sources with energies of 0.475 MeV, 0.563 MeV, 0.569 MeV, 0.605 MeV, 0.796 MeV, 0.802 MeV, 1.039 MeV, 1.168 MeV, and 1.366 MeV. These latter represent the ^{134}Cs sources accounting for the emission probability of these energies, and they lead to a weighted mean value of 0.698 MeV. The reference values were determined as in the other setups without the building structure.

The detection regions were defined as air-filled spheres with a diameter of 30 cm. Four detector regions were positioned according to the detector positions in the real modular building 1 m above floor level of the modules (Fig. 2). In those regions, the number and energies of the gamma particles passing through were scored. By using conversion coefficients (ICRP, 2010), the fluence was transferred to the ambient dose equivalent $H^*(10)$ at the end of the calculation, as the applied dose rate instruments in the experiment were calibrated to the ambient dose rate $H^*(10)$.

In order to obtain sufficiently good statistics below a level of 5% standard deviation within acceptable computation times in MCNP6 various variation reduction techniques can be applied. The defined regions in space are called cells and for each of them a weight window was generated. The number of a particle's weight in MCNP6 represents the number of physical particles which in these calculations are photons with different random walks being represented by one MCNP particle. For each space cell, a lower weight bound is supplied by the user and the upper weight bound is a specified multiple of the lower. These weight bounds define a window of acceptable weights. If a particle emitted from the source and generated by interactions with the materials is below the lower weight bound, then “Russian roulette” is played and randomly the particle's weight is either increased to a value within the window or the particle is terminated. If a particle is above the upper weight bound, it is split so that its parts are within the window. No action is taken for particles within the window. The weight windows

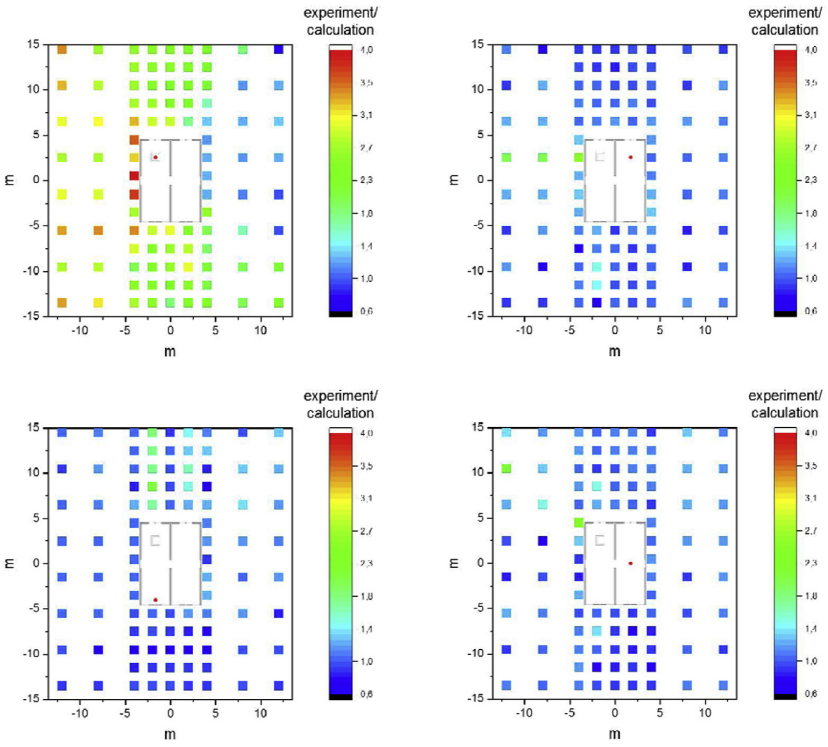

Fig. 5. Ratio of the experimentally determined to the theoretically calculated shielding factor according to source region position around the modules, for four different detector regions inside the modules (red spot) for Setup 1 (^{137}Cs). According to a material compendium (McConn et al., 2011), the density of the clay bricks in the calculations was assumed to be ρ = 2.20 kg/L, and it was later measured to be ρ = 0.65 kg/L. (For interpretation of the references to color in this figure legend, the reader is referred to the Web version of this article.)

were determined using the Weight Window Generator, which estimates the importance of the cells in the space. The importance of cells is defined as the expected score generated by a unit weight particle after entering the cell. By using the cell-based generator, the average importances of the space cells can be estimated.

3. Results

3.1. Comparison of the theoretical and experimental shielding factors

The shielding factors determined from the experiment were compared to those calculated theoretically. This was done by using the ratio of the experimentally and computationally determined shielding factors.

Setup 1: The resulting ratios of the experimentally determined to the theoretically calculated shielding factors for ^{137}Cs were plotted in heat maps, in which individual values are represented graphically by a color code, for the corresponding distances from the respective detector region. This allowed an investigation into any possible influence of the different source positions around the modules (Fig. 5) on the ratio. The ranges of the plotted ratios show that the clay bricks in the real modules provided less shielding than those in the theoretical model. Measurements of the real clay bricks showed that their density was ρ = 0.65 kg/L, which is lower than the clay density applied to the model: ρ = 2.20 kg/L taken from a material compendium (McConn et al., 2011). On average, the shielding factor over all source and detector regions was experimentally determined to be 0.66 ± 0.02 and theoretically calculated to be 0.60 ± 0.02. The overall ratio of the experimentally determined to the theoretically calculated shielding factors was determined to be 1.39 ± 0.04. If the combinations of source positions to detector regions are divided into those that cross the clay bricks looking at the direct line and those that do not cross the clay bricks at the direct line the ratios are determined to be 1.03 ± 0.02 without and 2.53 ± 0.06 with the clay bricks.

Setup 2: The resulting ratios of the experimentally determined to the theoretically calculated shielding factors for ^{137}Cs were plotted in heat maps for the corresponding source positions on top of the modules to the respective detector region. This allowed an investigation into any possible influence of different source positions on top of the modules (Fig. 6) on the ratio. The ranges of the plotted ratios show that the clay bricks in the real modules provide less shielding than those in the theoretical model, as the clay density was assumed to be higher in the model than that of the real bricks. The ranges of the plotted ratios also show that the sources that were positioned on the line where the two modules were fitted together lead to greater shielding from the real modules than that seen in the theoretical model. This can be explained because the edges of the real modules are encased in metal, which was not included in the model. The overall ratio of the experimentally determined to the theoretically calculated shielding factors was determined to be 1.24 ± 0.10. If the combinations of source positions to detector regions are divided into those that cross the clay bricks looking at the direct line and those that do not cross the clay bricks as well as those where the sources were positioned on the metal case the ratios are determined to be 1.10 ± 0.03 without the clay bricks or metal case, 2.68 ± 0.20 with the clay bricks and 0.64 ± 0.04 with the metal case.

Setup 3: The resulting ratios of the experimentally determined to the theoretically calculated shielding factors for ^{60}Co were plotted in heat maps as in Setup 1 (Fig. 7). The ranges of the plotted ratios show again that the clay bricks in the real modules provide less shielding than those in the theoretical model, as the clay density was assumed to be higher

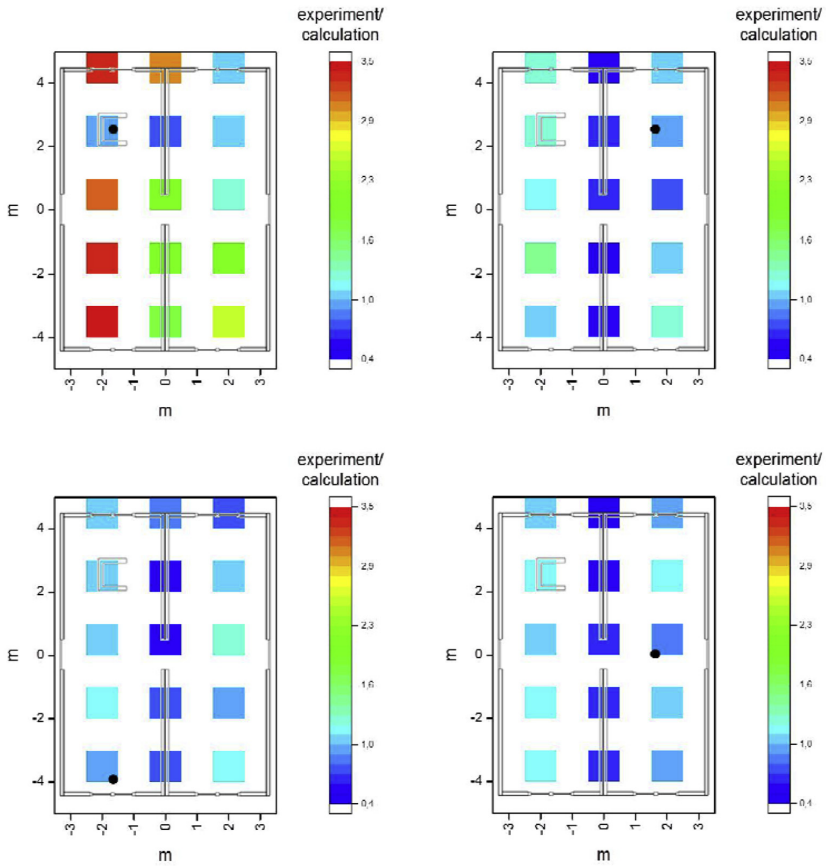

Fig. 6. Ratio of the experimentally determined to the theoretically calculated shielding factor according to source region position on top of the modules, for four different detector regions inside the modules (black spot) for Setup 2 (^{137}Cs). According to a material compendium (McConn et al., 2011), the density of the clay bricks in the calculations was assumed to be ρ = 2.20 kg/L, and it was later measured to be ρ = 0.65 kg/L.

in the model than that of the real bricks. On average, the shielding factor over all source and detector regions was experimentally determined to be 0.73 ± 0.02 and theoretically calculated to be 0.65 ± 0.02. This resulted in an overall ratio and the standard error of the mean of the experimentally determined to the theoretically calculated shielding factors of 1.33 ± 0.04. If the combinations of source positions to detector regions are divided into those that cross the clay bricks looking at the direct line and those that do not cross the clay bricks at the direct line the ratios are determined to be 1.04 ± 0.02 without and 2.22 ± 0.05 with the clay bricks.

Setup 4: The resulting ratios of the experimentally determined to the theoretically calculated shielding factors for ^{60}Co were plotted in heat maps as in Setup 2 (Fig. 8). The ranges of the plotted ratios show again that the clay bricks in the real modules provide less shielding than those in the theoretical model, as the clay density was assumed to be higher in the model than that of the real bricks. Furthermore, the ranges of the plotted ratios again show that the sources that were positioned on the line where the two modules were fitted together lead to greater shielding of the real modules than that seen in the theoretical model. This can be explained because the edges of the real modules are encased in metal which was not included in the model. The overall ratio of the experimentally determined to the theoretically calculated shielding factors was found to be 1.12 ± 0.07. If the combinations of source positions to detector regions are divided into those that cross the clay bricks looking at the direct line and those that do not cross the clay bricks, as well as those where the sources were positioned on the metal case the ratios are determined to be 1.02 ± 0.02 without the clay bricks or metal case, 2.17 ± 0.15 with the clay bricks and 0.67 ± 0.03 with the metal case.

Table 3 provides a summary of the ratios of the compared experimentally determined and theoretically calculated shielding factors.

To find a suitable and representative indoor point for the shielding factor the overall ratios were also determined per detector region and are summarized in Table 4. The ratios are the highest for detector #1 as it was almost surrounded by the clay bricks and thus its shielding factor was the most affected. The ratios determined for the source positions on the roof were lower than the respective ratios for source positions on the ground, since one third of the source positions on the roof were affected by the metal case.

3.2. Impact of the clay density on the result

For various brick clays, the firing temperature has a high impact on the development of their pore structure (Hill, 1960) and

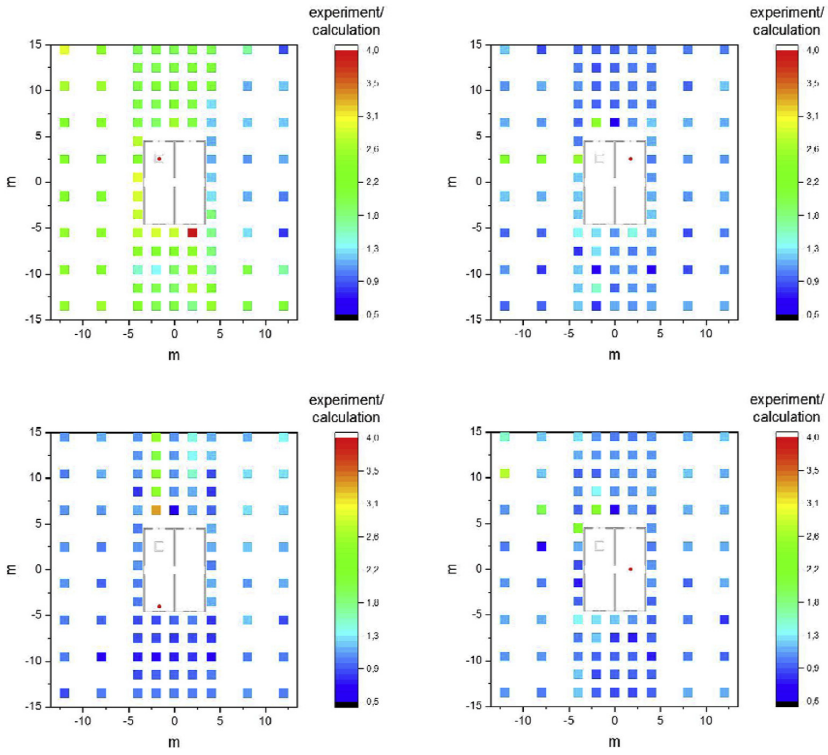

Fig. 7. Ratio of the experimentally determined to the theoretically calculated shielding factor according to source region position around the modules, for four different detector regions inside modules (red spot) for Setup 3 (^{60}Co). According to a material compendium (McConn et al., 2011), the density of the clay bricks in the calculations was assumed to be ρ = 2.20 kg/L, and it was later measured to be ρ = 0.65 kg/L. (For interpretation of the references to color in this figure legend, the reader is referred to the Web version of this article.)

correspondingly their density. Moreover, some clay brick types have large perforations that enhance their thermal insulating capacity (Gosmartbricks, 2017), which naturally also considerably reduces the bulk density of the brick. To investigate the impact of the different densities of clay bricks in this case and to show that the Monte Carlo calculations are also applicable for the clay brick structure, additional calculations were performed for clay brick densities of ρ = 2.20 kg/L and ρ = 0.65 kg/L. The ratio comparing H*(10) caused by ^{60}Co and ^{137}Cs crossing a clay brick for both densities was calculated using the MCNP6 code (Goorley et al., 2012). The ratios were determined for different thicknesses of clay brick (Fig. 10), as the radiation can cross the clay brick structure in the building model at different angles. The ratio of the difference of the shielding factor ratios for the respective source point detector combinations that were affected by the clay brick structure are in the right range.

Additionally, the calculations were repeated for all source points that were influenced by the clay brick structure according to Setup 1, but this time using the measured density of the clay brick structure. The resulting ratios of the experimentally determined to the theoretically calculated shielding factors for ^{137}Cs were plotted in heat maps for the corresponding distances from the respective detector region, as they were for the first calculations (Fig. 9). The presented results show good agreement with the measurements (slight variations will always be expected due to small imperfections in the model compared with real life, due to ground unevenness, surface texture, etc.). The ratio of the experimentally determined to the theoretically calculated shielding factors was now determined to be 0.95 ± 0.02 for detector #1, 1.02 ± 0.02 for detector #2, 0.99 ± 0.02 for detector #3, 1.03 ± 0.02 for detector #4 (Table 4), and 1.00 ± 0.01 averaging over all detector regions (Table 3). The results show that all detector regions are of similar quality. The average theoretical shielding factor increased with the new calculations to 0.68 ± 0.02.

3.3. Comparison of shielding factors for ^{137}Cs and ^{134}Cs

The comparison of the theoretically determined shielding factors for ^{137}Cs and ^{134}Cs is presented in Fig. 11. The ratio and the standard error of the mean of the shielding factor of ^{134}Cs and of ^{137}Cs was determined to be 1.02 ± 0.05 on average over all of the different source positions.

4. Discussion

In conclusion, the theoretically calculated shielding factors showed good agreement with the experimentally determined shielding factors for the modular building in case of source point and detector area combinations that were not directly influenced by the clay brick structure or the metal case. The ratios determined for the source points, for which the direct radiation path crosses the clay structure before reaching the detector, were within the predicted range, considering the clay density in the model and the density in the experiment. Further calculations also showed the agreement between the model and experiment. For future calculations, it will be important to know the actual density of bricks and other important construction elements used in building houses. If not properly accounted for, construction materials with highly deviating density or atomic composition may strongly affect the accuracy in the calculated shielding factors of a building, depending on the choice of reference point in the building. In the present study, however, the metal case only influenced the result when the source was directly positioned on top of it. For future models has to be considered, that a structure of this type might have to be included, especially when a major part of the unscattered radiation crosses the structure before reaching the detector, which is usually not the case as the metal case normally only covers a very small part of a modular building as in the presented case.

The difference between the calculated and experimentally

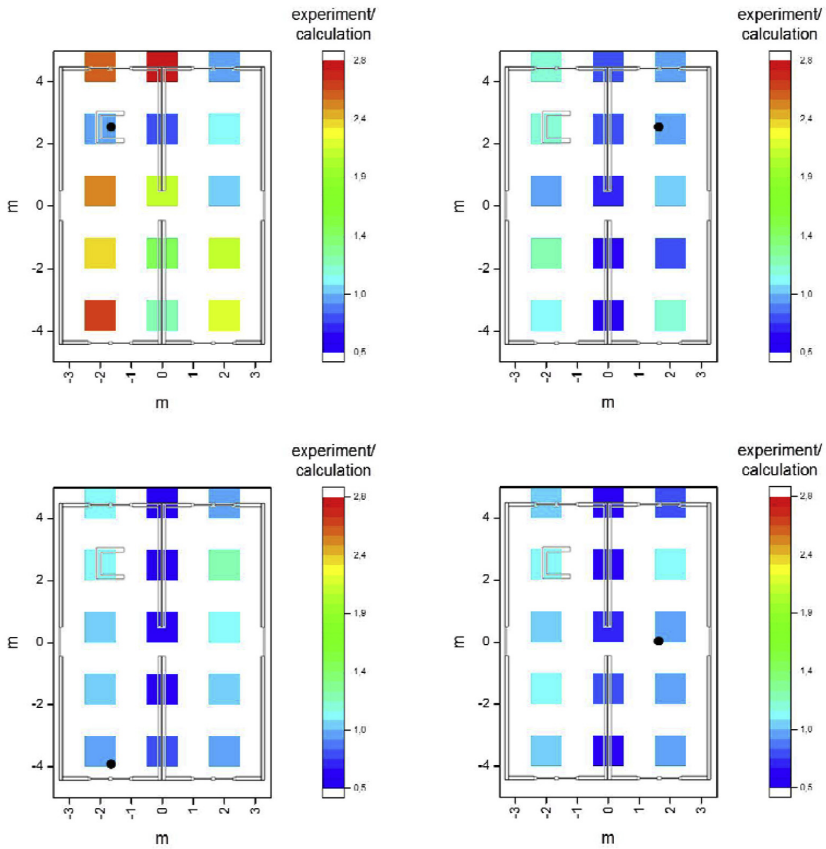

Fig. 8. Ratio of the experimentally determined to the theoretically calculated shielding factor according to source region position on top of the modules, for four different detector regions inside the modules (black spot) for Setup 4 (^{60}Co). According to a material compendium (McConn et al., 2011), the density of the clay bricks in the calculations was assumed to be ρ = 2.20 kg/L, and it was later measured to be ρ = 0.65 kg/L.

Table 3
Ratios and standard error of the mean of the experimentally determined and theoretically calculated shielding factors for different scenarios for a density of the clay bricks (LECA) of ρ = 2.20 kg/L if not a different value is mentioned.

Gamma source	Influence assumed	Source region Ground	Roof
^{137}Cs	None	1.39 ± 0.04 (ρ_{LECA} = 2.20 kg/L) 1.00 ± 0.01 (ρ_{LECA} = 0.65 kg/L)	1.24 ± 0.10
	Without clay bricks or metal case	1.03 ± 0.02	1.10 ± 0.03
	Clay bricks	2.53 ± 0.06	2.68 ± 0.20
	Metal case	–	0.64 ± 0.04
^{60}Co	None	1.33 ± 0.04	1.12 ± 0.07
	Without clay bricks or metal case	1.02 ± 0.05	1.02 ± 0.02
	Clay bricks	2.22 ± 0.05	2.17 ± 0.15
	Metal case	–	0.67 ± 0.03

determined shielding for two different radionuclides with primary gamma energies of 0.662–1.25 MeV appeared to be negligible for the reference points not directly affected by the clay bricks (Detector points #2–4). As an example, the ratio between the measured and calculated shielding factors ranged from 1.06 to 1.10 for the ground source geometry (Table 4). Hence, the results showed that the gamma energy, in practice, has no influence on the level of agreement between experiment and calculation, provided that the construction materials are accurately characterized in terms of density and atomic composition. Therefore, the applicability of theoretical calculations using MCNP6 for radioactive fallout scenarios has been demonstrated in practice.

Additionally, it was shown that the shielding effect for modular buildings is almost the same for ^{134}Cs as for ^{137}Cs, meaning that a common value for the shielding factor for this type of building can be used for the two radionuclides that dominate the external gamma fluence in connection with nuclear power plant fallout.

In future investigations that will also use MCNP6, methodologies will be demonstrated to, for example, enable optimization of dose reductive interventions in contaminated inhabited areas by calculating dose isolines. The influence on the dose rate of different building features will also be examined. Such calculation estimates are important, as the justification and optimization of an intervention should be based on estimates of residual dose (ICRP, 2007), and the dose rate conversion factors for the gamma exposure inside and outside resulting from radionuclides deposited on different surfaces at the required level of detail are at most available for 4 to 5 different building types. With modern day computing power, much less time is required to obtain reliable Monte Carlo model estimates with good statistics, and with constant improvements to model data libraries, tools such as MCNP6 will play an increasing role in the optimization of an intervention.

Table 4
Ratios and standard error of the mean of the experimentally determined and theoretically calculated shielding factors for the different setups and detectors for a density of the clay bricks (LECA) of ρ = 2.20 kg/L if not a different value is mentioned.

Setup		Detector			
		#1	#2	#3	#4
^{137}Cs	Ground (ρ_{LECA} = 2.20 kg/L)	2.38 ± 0.08	1.07 ± 0.03	1.05 ± 0.03	1.06 ± 0.03
	Ground (ρ_{LECA} = 0.65 kg/L)	0.95 ± 0.02	1.02 ± 0.02	0.99 ± 0.02	1.03 ± 0.02
	Roof	2.14 ± 0.25	0.96 ± 0.08	0.95 ± 0.06	0.91 ± 0.06
^{60}Co	Ground	2.02 ± 0.06	1.10 ± 0.04	1.10 ± 0.05	1.10 ± 0.04
	Roof	1.76 ± 0.18	0.92 ± 0.06	0.90 ± 0.06	0.88 ± 0.06

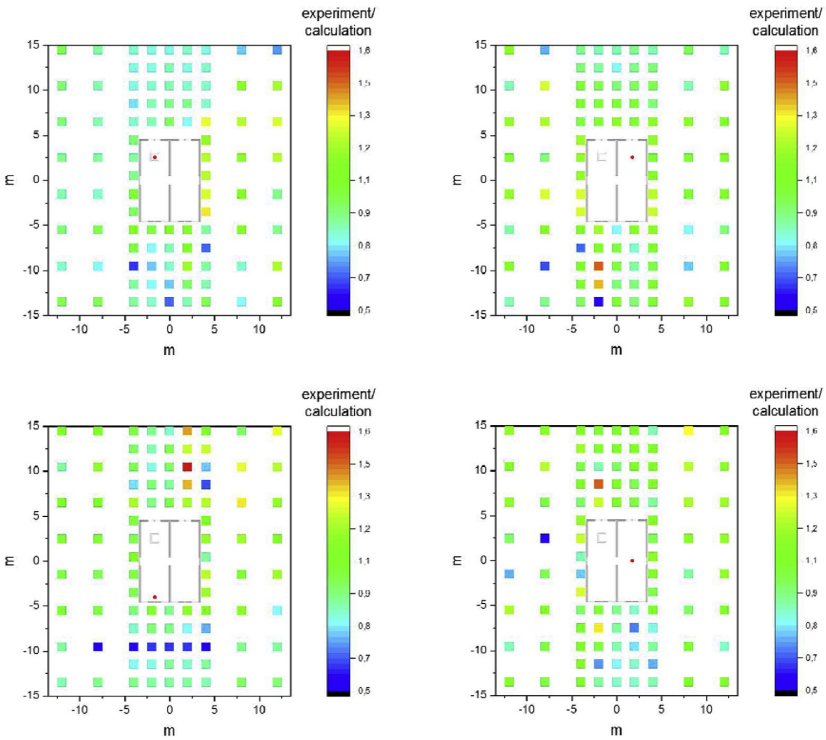

Fig. 9. Ratio of the experimentally determined to the theoretically calculated shielding factor according to source region position around the modules for four different detector regions inside the modules (red spot) for Setup 1 with corrected density of the clay bricks (^{137}Cs). (For interpretation of the references to color in this figure legend, the reader is referred to the Web version of this article.)

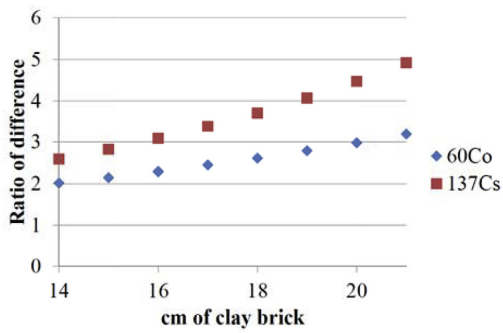

Fig. 10. Ratio of the difference in H*(10) after crossing clay bricks with a density ρ = 0.65 kg/L to bricks with density ρ = 2.20 kg/L.

Further Monte Carlo models will enable the computation of differential shielding factors, where the shielding of an incoming photon at a given angle of incidence and for a given construction material can be expressed.

5. Conclusions

An agreement within 2% between the measured and calculated shielding factor (Table 4) can be obtained using Monte Carlo simulations, provided that the atomic composition and density of the majority of the construction materials are accurately specified. This agreement appears to be independent of the primary photon energy of the surrounding gamma sources. The applicability of theoretical calculations using MCNP6 for radioactive fallout scenarios has thus been demonstrated in practice.

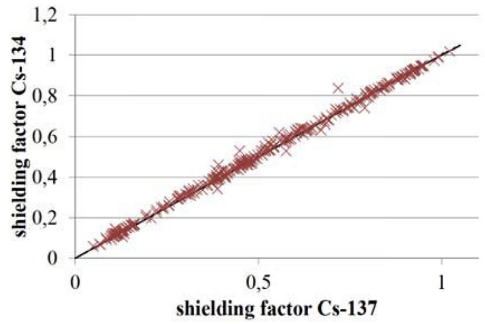

Fig. 11. Shielding factor of ^{134}Cs compared to the shielding factor of ^{137}Cs for source region positions on top of the modules (red crosses, the black line has a slope of 1). (For interpretation of the references to color in this figure legend, the reader is referred to the Web version of this article.)

Acknowledgements

This study was supported by the Swedish Radiation Safety Authority (SSM2016-1683 7030076-00).

Appendix A. Supplementary data

Supplementary data related to this article can be found at http://dx.doi.org/10.1016/j.jenvrad.2018.04.005.

References

Andersson, K.G., 2009. Chapter 10 Strategies for restoration of contaminated inhabited areas. In: Andersson, K.G. (Ed.), Airborne Radioactive Contamination in Inhabited Areas. Radioactivity in the Environment, vol. 15. Elsevier, pp. 297–326.

Andersson, K.G., Mikkelsen, T., Astrup, P., Thykier-Nielsen, S., Jacobsen, L., Schou-Jensen, L., Hoe, S., Nielsen, S.P., 2008. Estimation of health hazards resulting from a radiological terrorist attack in a city. Radiat. Protect. Dosim. 131 (3), 297–307.

Bilsby*, -. Snittegning Af Kontormoduler - Stabelbare; Konstruktionsbeskrivelse-Kontormoduler - Stabelbare (in Danish).

Chadwick, M., Obložinský, P., Herman, M., Greene, N., McKnight, R., Smith, D., Young, P., MacFarlane, R., Hale, G., Frankle, S., Kahler, A., Kawano, T., Little, R., Madland, D., Moller, P., Mosteller, R., Page, P., Talou, P., Trellue, H., White, M., Wilson, W., Arcilla, R., Dunford, C., Mughabghab, S., Pritychenko, B., Rochman, D., Sonzogni, A., Lubitz, C., Trumbull, T., Weinman, J., Brown, D., Cullen, D., Heinrichs, D., McNabb, D., Derrien, H., Dunn, M., Larson, N., Leal, L., Carlson, A., Block, R., Briggs, J., Cheng, E., Huria, H., Zerkle, M., Kozier, K., Courcelle, A., Pronyaev, V., van der Marck, S., 2006. ENDF/B-VII.0: next generation evaluated nuclear data library for nuclear science and technology. Nucl. Data Sheets 107 (12), 2931–3060 evaluated Nuclear Data File ENDF/B-VII.0.

Dickson, E.D., Hamby, D.M., 2014. Cloud immersion building shielding factors for us residential structures. J. Radiol. Prot. 34 (4), 853–871.

Dickson, E.D., Hamby, D.M., 2016. Building protection- and building shielding-factors for environmental exposure to radionuclides and monoenergetic photon emissions. J. Radiol. Prot. 36 (3), 579–615.

Dickson, E.D., Hamby, D.M., Eckerman, K.F., 2017. Contaminant deposition building shielding factors for us residential structures (vol. 35, pg 317, 2015). J. Radiol. Prot. 37 (4), 961–962.

Ferguson, C., Kazi, T., Perera, J., 2003. Commercial Radioactive Sources, Occasional Paper No. 11. Center for nonproliferation studies, Monterey institute of international studies.

Finck, R., 1991. Shielding factors for gamma radiation, experiments and calculations for Swedish dwellings. In: Moberg, L. (Ed.), Results from a Research Programme on Environmental Radioecology. The Swedish Radiation Protection Institute, pp. 489–526.

Furuta, T., Takahashi, F., 2015. Study of radiation dose reduction of buildings of different sizes and materials. J. Nucl. Sci. Technol. 52 (6), 897–904.

Goorley, T., James, M., Booth, T., Brown, F., Bull, J., Cox, L.J., Durkee, J., Elson, J., Fensin, M., Forster, R.A., Hendricks, J., Hughes, H.G., Johns, R., Kiedrowski, B., Martz, R., Mashnik, S., McKinney, G., Pelowitz, D., Prael, R., Sweezy, J., Waters, L., Wilcox, T., Zukaitis, T., 2012. Initial MCNP6 release overview. Nucl. Technol. 180 (3), 298–315.

Gosmartbricks, Nov. 2017. Why Bricks Have Holes? http://gosmartbricks.com/why-bricks-have-holes/.

Hill, R.D., 1960. A study of pore-size distribution of fired clay bodies. Trans. J. Br. Ceram. Soc. 59, 189–197.

IAEA, 2007. Terminology Used in Nuclear Safety and Radiation Protection. IAEA Safety Glossary.

ICRP, 2007. The 2007 recommendations of the international commission on radiological protection. Ann. ICRP 37 (2–7), 1–332 ICRP Publication 103.

ICRP, 2010. Conversion coefficients for radiological protection quantities for external radiation exposures. Ann. ICRP 40 (2), 1–257 ICRP Publication 116.

Imanaka, T., Hayashi, G., Endo, S., 2015. Comparison of the accident process, radioactivity release and ground contamination between Chernobyl and Fukushima-1. J. Radiat. Res. 56 (Suppl. 1), I56–I61 Sp. Iss. SI.

Jacob, P., Meckbach, R., 1987. Shielding factors and external dose evaluation. Radiat. Protect. Dosim. 21 (1–3), 79–85.

Jensen, P.H., Thykier-Nielsen, S., 1989. Shielding factor calculation for plume radiation. Radiation Protection Programme. Progress Report 1988, 1561–1565.

Kis, Z., Eged, K., Meckbach, R., Müller, H., 2003. Guidelines for Planning Interventions against External Exposure in Industrial Area after a Nuclear Accident. Pt. 2. Calculation of Doses Using Monte Carlo Method. Institut für strahlenschutz, GSF - Forschungszentrum für Umwelt und Gesundheit GmbH.

Kis, Z., Eged, K., Voigt, G., Meckbach, R., Müller, H., 2004. Modeling of an industrial environment: external dose calculations based on Monte Carlo simulations of photon transport. Health Phys. 86 (2), 161–173.

Lichtenstein, H., Cohen, M., Steinberg, H., Troubetzkoy, E., Beer, M., 1979. The SAM-ce Monte Carlo System for Radiation Transport and Criticality Calculations in Complex Configurations (Revision 7.0). Mathematical Application Group, Inc.

McConn Jr., R., Gesh, C., Pagh, R., Rucker, R., Williams III, R., 2011. Radiation Portal Monitor Project - Compendium of Material Composition Data for Radiation Transport Modeling. Pacific Northwest National Laboratory PIET-43741-TM-963, PNNL-15870 Rev. 1.

Meckbach, R., Jacob, P., 1988. Gamma exposures due to radionuclides deposited in urban environments. Part II: Location factors for different deposition patterns. Radiat. Protect. Dosim. 25 (3), 181–190.

Meckbach, R., Jacob, P., Paretzke, H.G., 1987. Shielding of gamma radiation by typical European houses. Nucl. Instrum. Methods Phys. Res. Sect. A Accel. Spectrom. Detect. Assoc. Equip. 255 (1), 160–164.

Meckbach, R., Jacob, P., Paretzke, H., 1988. Gamma exposures due to radionuclides deposited in urban environments. Part I: Kerma rates from contaminated urban surfaces. Radiat. Protect. Dosim. 25 (3), 167–179.

Salinas, I.C.P., Conti, C.C., Rochedo, E.R.R., Lopes, R.T., 2006. Gamma shielding factor for typical houses in Brazil. Radiat. Protect. Dosim. 121 (4), 420–424.

Spencer, L., 1962. Structure Shielding Against Fallout Radiation from Nuclear Weapons. United States Bureau of Standards NBS Monograph 42.

Spencer, L.V., Chilton, A.B., Eisenhauer, C.M., 1980. Structure Shielding against Fallout Gamma Rays from Nuclear Detonations. National Bureau of Standards (Special Publication).

UNSCEAR, 2016. Sources, Effects and Risks of Ionizing Radiation; Report to the General Assembly, with Scientific Annexes. UNSCEAR 2016 Report. United Nations Scientific Committee on the Effects of Atomic Radiation.

Websides, Jun. 2016. (in German). www.isola-mineralwolle.de https://de.wikipedia.org/wiki/N%C3%A4hrstoff_(Pflanze) http://www.kaiser-vrees.de/downloads/Ra40gew5chte.pdf https://de.wikipedia.org/wiki/Brettsperrholz https://de.wikipedia.org/wiki/Spanplatte http://www.wfg.be/cms/upload/.

Paper II

Hinrichsen, Y., Finck, R., Rääf, C., Andersson, K. G. Introducing the concept of the isodose for optimization of decontamination activities in a radioactive fallout scenario. Journal of Radiological Protection 38 (2018) 1293-1310.

IOP Publishing | Society for Radiological Protection Journal of Radiological Protection
J. Radiol. Prot. **38** (2018) 1293–1310 (18pp) https://doi.org/10.1088/1361-6498/aadd24

Introducing the concept of the isodose for optimisation of decontamination activities in a radioactive fallout scenario

Y Hinrichsen[1], R Finck[2], C Rääf[2] and K G Andersson[1]

[1] Technical University of Denmark, Center for Nuclear Technologies, Frederiksborgvej 399, 4000 Roskilde, Denmark
[2] Lund University, Department of Translational Medicine, Medical Radiation Physics, SUS Malmö, 205 02 Malmö, Sweden

E-mail: yvhi@dtu.dk

Received 1 June 2018, revised 16 August 2018
Accepted for publication 28 August 2018
Published 20 September 2018

Abstract

In the recovery phase after a radioactive release incident, it is important to be able to focus decontamination operations on the areas that contribute most to the radiation dose. Monte Carlo simulations were applied to determine the shielding effect of a building against radiation from various directions, also giving information on the dose contributions at various locations inside the building from specific areas outside. The concept of the isodose was developed to optimise decontamination activities, and was applied as isodose lines to define the smallest areas that lead to a certain dose reduction through decontamination of areas surrounding the building. The shape and position of the isodose lines depend on the building's geometry, wall thickness, and material, and on the observation point inside the building. Calculations have been made with a surface resolution of 1 m^2 for four observation points in a modular building, assuming depositions of ^{137}Cs and ^{60}Co on the ground surface and on the roof, as well as 1 cm below the ground surface to represent ground penetration. For example, a ten times as large area would have to be decontaminated to increase the dose reduction from 10% to 30%, if it is assumed that all the contamination is located at a depth of 1 cm.

Keywords: shielding factor, isodose, ground penetration, Monte Carlo simulations

(Some figures may appear in colour only in the online journal)

1. Introduction

After an airborne release of radionuclides to a populated area, external gamma irradiation from deposited radioactive material can contribute considerably to the radiation exposure of inhabitants. The shielding of gamma radiation by buildings can reduce this exposure, but since buildings generally have complex geometries their shielding properties will vary depending on where the radionuclides are deposited, and in which parts of the building the residents spend most of their time. Thorough and consistent removal of a topsoil layer can remove more than 90% of the contamination from the surface (Andersson 2009a), but equipment, consumables, and skilled personnel are required, and the resulting costs can be high depending on the area to be treated (Roed *et al* 2006). To minimise these costs while achieving a satisfactory dose reduction, it is useful to have information on exactly which areas it would be most beneficial to decontaminate, taking into account the shielding properties of local buildings.

Since the geometry of buildings is too complex for simple methods such as the point kernel model, Monte Carlo calculations are needed to calculate their shielding properties (Jensen and Thykier-Nielsen 1989). The applicability of the transport code MCNP6 (Goorley *et al* 2012) in determining exposure reduction for a modular building type has been experimentally verified in a previous study by our group (Hinrichsen *et al* 2018). The focus in that study was on the comparison of experimentally determined and theoretically calculated shielding factors for ^{137}Cs and ^{60}Co sources that were positioned around and on top of a modular building, showing that an agreement within 2% can be obtained. As the next step, the aim of this study was to use the MCNP6 code to illustrate how the shielding properties of a modular building vary depending on the source location with respect to a number of different observation points (selected points where people could be located) inside the building.

Furthermore, the isodose concept for the optimisation of decontamination activities is introduced. In its application as isodose lines for a two-dimensional source area, for example, a ground or roof surface, the concept illustrates the extent to which the surrounding areas contribute to the external radiation exposure at the observation points inside a building. This could, in turn, be used to show how the decontamination of surfaces or replacement of topsoil can be optimised in an emergency situation by determining the surfaces that contribute most to the external radiation exposure at the various observation points while taking ground penetration into consideration, which is especially relevant for wet deposition scenarios involving, for example, nuclear power plant releases and nuclear weapons fallout.

2. Materials and methods

2.1. Concept of the shielding factor

Buildings naturally provide some shielding against radiation from the ground and from miscellaneous contamination of all outdoor surfaces (including soil, roofs, walls, windows, and pavements), vegetation, and in the air (primary contaminant plume or resuspended radioactive matter). In the case of wet deposition of nuclear fallout, the contamination on the ground can generally be expected to contribute most to the total dose integrated over long periods of time (assuming that areas of soil in the local inhabited environment are not insignificant) (Andersson 2009b). Several different, and sometimes confusing, terms have been used to describe the shielding effect of a building, such as the shielding factor, reduction factor, or protection factor. The term shielding factor is used here to describe the reduction of the absorbed dose rate inside the building compared to the absorbed dose rate outside the

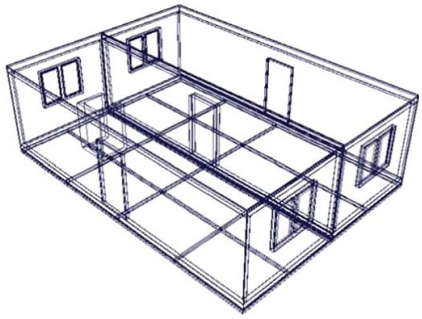

Figure 1. Bird's-eye view of the model of the modular building.

building, and represents the reduction of the absorbed dose rate by attenuation and scattering as the radiation passes through matter. Absorbed dose here refers to the absorbed dose free in air.

The shielding factor, S_{bld}, at a point inside a building acting on a radiation source outside the building is here defined as follows:

$$S_{\mathrm{bld}} = \frac{\dot{D}_{\mathrm{bld}}}{\dot{D}_{\mathrm{ref}}}, \quad 0 \leqslant S_{\mathrm{bld}} \leqslant 1 \tag{1}$$

where $\dot{D}_{\mathrm{bld}}$ is the absorbed dose rate at a point inside the building, and $\dot{D}_{\mathrm{ref}}$ is the absorbed dose rate that would be measured at the same point if the building were removed after the radionuclide deposition. This factor is based on the barrier shielding factor concept, which was originally defined by Spencer (1962) and compares the dose rate at a given position resulting from the same source to the dose rate at the same position when the building is replaced with air. Barrier shielding depends on the energy of the gamma radiation and on the composition and thickness of the absorbing material. Barrier shielding will also depend on the direction of the incident radiation on the building, since the attenuation will be higher when radiation is incident at oblique angles. Thus, barrier shielding varies with the angular direction of the photon fluence, and depends on the actual geometry of the source. The angular barrier shielding factor is therefore a function in two dimensions, the vertical and the horizontal.

For the sake of completeness it should be mentioned that a second concept was developed by Spencer (1962), called geometry shielding, which compares the dose rate at one position resulting from a given source when the building is replaced by air to the dose rate above an infinite, uniformly contaminated plane surface source at a reference height of 1 m. Geometry shielding can be combined with the barrier shielding concept by multiplication. The resulting factor is, amongst other terms, called the reduction factor.

The focus of this study is on barrier shielding and the angular contribution to the absorbed dose from ^{137}Cs and ^{60}Co sources on the surrounding ground, and on top of the same modular building (figure 1) as used in our previous study (Hinrichsen *et al* 2018). The term 'shielding factor' is used in the following sections because this study is concerned only with barrier shielding.

2.2. Introducing the concept of the isodose

Examination of the distribution of angular shielding factors around building structures leads to the conclusion that some contaminated areas have a higher influence on the radiation exposure inside the building than others. Considering that the distance between a given observation point inside the building and a given surface source element outside the building also influences the radiation exposure at the observation point, it is interesting to study which contaminated areas have the highest impact on the radiation exposure indoors. This could be helpful in optimising decontamination activities after the release of radioactive substances and reducing the resulting waste.

In this study, an observation point i is defined such that it can be inside or outside the building, and its position is described by the vector $\vec{r}_i$ in three-dimensional space. The absorbed dose resulting from gamma-emitting radionuclides over an infinitesimal volume, dV, located at the positions $\vec{r}$, can be determined at this point. The dose contribution from dV to the observation point i, here denoted by the dose contribution density $\rho_{\mathrm{D},i}(\vec{r})$, can be determined at each point in space by, for example, defining a certain radionuclide contamination on a surface, or by defining it as 0 inside the building. Thus, the total dose $D_{i,\infty}$ at observation point i can be determined by the following integral:

$$D_{i,\infty} = \int \rho_{\mathrm{D},i}(\vec{r})\mathrm{d}V \; IF \lim_{|\vec{r}_i - \vec{r}| \to \infty} \rho_{\mathrm{D},i}(\vec{r}) = 0. \tag{2}$$

To determine the areas with the highest dose contribution, the concept of the 'isodose' was developed in this study, and is defined below.

Definition. The isodose $ID_{i,k}$ is defined by the outer boundary of one or more zones in space that contribute, for the most part, a given fraction k to the dose at the observation point i. In the case where $\rho_{\mathrm{D},i}(\vec{r})$ is a continuous function with the maximum $\rho_{\mathrm{D},i,\max} < \infty$, the isodose $ID_{i,k}$ can be chosen from the range $0 < ID_{i,k} < \rho_{\mathrm{D},i,\max}$ and the fraction of dose contribution k_i resulting from the zone or zones determined by the isodose is given by

$$k_i = \int f(\rho_{\mathrm{D},i}(\vec{r}))\mathrm{d}V / D_{i,\infty} \quad FOR \quad f(\rho_{\mathrm{D},i}(\vec{r})) = \begin{cases} \rho_{\mathrm{D},i}(\vec{r}), & \rho_{\mathrm{D},i}(\vec{r}) \geqslant ID_{i,k} \\ 0, & \rho_{\mathrm{D},i}(\vec{r}) < ID_{i,k} \end{cases}. \tag{3}$$

When $\rho_{\mathrm{D},i}(\vec{r})$ is not a continuous function for the entire space, for example, due to limitations of the considered space, the concept of the isodose is still applicable for jump discontinuities. In such a case, the left- and right-hand limits exist, and the respective point can be applied over the entire range of dose contribution densities that lie within the left- and right-hand limits.

These equations apply to a single observation point inside the building, but in a real fallout situation, decontamination must be performed in such a way that a substantial dose reduction is achieved throughout the entire building. To obtain a measure of the effective shielding obtained in a building by a given decontamination measure, the times spent by the residents in various parts of the building must be accounted for. Therefore, so-called occupancy factors p_i for various observation points can be applied to equation (3), resulting in

Table 1. Overview of the relevant quantities in the determination of the isodose.

Symbol	Name
A_j	Size of subarea j
D_∞	Total dose weighted for several observation points
D_i	Dose at observation point i
$D_{i,j}$	Dose at observation point i resulting from contamination of subarea j
$D_{i,\infty}$	Total dose at observation point i
D_j	Dose weighted for several observation points resulting from contamination of subarea j
i	Observation point index
j	Subarea index
$ID_{i,k}$	Isodose for the fraction of dose contribution k to observation point i
ID_k	Isodose for the fraction of dose contribution k weighted for several observation points
k	Fraction of dose contribution weighted for several observation points
k_i	Fraction of dose contribution to observation point i
p_i	Occupancy factors
$\vec{r}$	Any point in the defined space
$\vec{r}_i$	Position of observation point i
ρ_D	Dose contribution density weighted for several observation points
$\rho_{\mathrm{D},i}$	Dose contribution density to observation point i
$\rho_{D,i,j}$	Dose contribution density for observation point i resulting from contamination of subarea j
$\rho_{\mathrm{D},j}$	Dose contribution density weighted for several observation points resulting from contamination of subarea j

$$k = \int f(\rho_\mathrm{D}(\vec{r}))\mathrm{d}V / \sum_i \mathrm{D}_{i,\infty} \cdot p_i \quad \forall \quad 1 = \sum_i p_i$$
$$FOR \quad f(\rho_\mathrm{D}(\vec{r})) = \begin{cases} \sum_i \rho_{\mathrm{D},i}(\vec{r}) \cdot p_i, & \sum_i \rho_{\mathrm{D},i}(\vec{r}) \cdot p_i \geqslant ID_k \\ 0, & \sum_i \rho_{\mathrm{D},i}(\vec{r}) \cdot p_i < ID_k \end{cases}. \tag{4}$$

Based on this definition, the concept of the isodose can also be applied to two-dimensional dose contribution densities $\rho_{\mathrm{D},i}(\vec{r})$, for example, on specific surfaces or on the ground surrounding the building. This can be done in some cases for the sake of simplification, when the depth distribution under a surface (e.g. fallout in the ground) is neglected.

2.3. Applying the concept of the isodose

In reality, we do not know the dose contribution density of the space (equations (2) to (4)), and thus the concept must be applied for different scenarios. The first scenario could be a contaminated ground surface around a building. The depth distribution is neglected for the sake of simplification because it differs from point to point in a real fallout situation (see e.g. Östlund *et al* 2017). Therefore, this application of the isodose concept is two-dimensional, and the areas giving the highest dose contribution for a given source–building geometry can be determined using the following step-by-step procedure. To provide a better understanding, the relevant quantities are listed in table 1.

Step 1. The dose resulting from the entire contaminated surface at observation point i, $D_{i,\infty}$ is determined, as well as the contribution to the dose from smaller parts of the surface $D_{i,j}$. The size of areas A_j is chosen by reasonability based on the applied scenario. The dose contribution density is then calculated for each subarea using the relation $\rho_{\mathrm{D},i,j} = D_{i,j} / A_j$. If more than one observation point is considered, this process must be repeated for all points, and the results weighted with their respective occupancy factors p_i: $D_j = \sum_i D_i \cdot p_i$ for the dose contribution, and $\rho_{D,j} = \sum_i D_{i,j} \cdot p_i / A_j$ for the dose contribution density.

Step 2. The subarea j with the highest dose contribution density for the observation point $\rho_{\mathrm{D},i,j}$ or weighted dose contribution density $\rho_{\mathrm{D},j}$ is then determined.

Step 3. The fraction of dose contribution k_i is then calculated by dividing the dose contribution $D_{i,j}$ by the dose resulting from the entire contaminated surface $D_{i,\infty}$ for one observation point, or for the weighted fraction of dose contribution k by dividing $D_{i,j}$ by $D_\infty = \sum_i D_{i,\infty} \cdot p_i$.

Step 4. This subarea j now represents the area with a fraction of dose contribution k_i or k surrounded by the isodose criterion $ID_{i,k}$ and ID_k. $ID_{i,k}$ and ID_k are in turn defined here by their respective dose contribution densities $\rho_{\mathrm{D},i,j}$ or $\rho_{\mathrm{D},j}$.

Step 5. The subarea j with the next highest dose contribution density for observation point $\rho_{\mathrm{D},i,j}$ or weighted dose contribution density $\rho_{\mathrm{D},j}$ is then determined.

Step 6. The fraction of dose contribution k_i is calculated by dividing the sum of all dose contributions from the subareas so far determined in steps 2 or 5, $\sum_j D_{i,j} \forall j$: $\rho_{\mathrm{D},i,j} \geqslant ID_{i,k}$, by the dose resulting from the entire contaminated surface $D_{i,\infty}$ for one observation point using the isodose $ID_{i,k}$ as the criterion equalling the dose contribution density $\rho_{\mathrm{D},i,j}$ of the subarea j that was determined in step 5. This must be done for the weighted fraction of dose contribution k by dividing the weighted sum of all dose contributions considered $\sum_j D_j \forall j$: $\rho_{\mathrm{D},j} \geqslant ID_k$ by the weighted dose resulting from the infinite contaminated surface D_∞, again using the isodose ID_k as the criterion equalling the dose contribution density $\rho_{\mathrm{D},j}$ of the subarea j that was determined in step 5.

Step 7. The subareas j: $\rho_{\mathrm{D},i,j} \geqslant ID_{i,k}$ or j: $\rho_{\mathrm{D},j} \geqslant ID_k$ that were determined in steps 2 or 5 now represent the area or areas with a fraction of dose contribution k_i or k surrounded by the isodose criterion $ID_{i,k}$ or ID_k, which are defined here by their respective dose contribution densities $\rho_{\mathrm{D},i,j}$ or $\rho_{\mathrm{D},j}$, as in step 6.

Step 8. Repeat steps 4–7 until all subareas have been considered.

These steps can be expressed more mathematically for one observation point by

$$k_i = \sum_j D_{i,j} / D_{i,\infty} \quad \forall \quad j\text{: } \rho_{\mathrm{D},i,j} \geqslant ID_{i,k} \tag{5}$$

and for more than one observation point by

$$k = \sum_j D_j / D_\infty \quad \forall \quad j\text{: } \rho_{\mathrm{D},j} \geqslant ID_k. \tag{6}$$

If the sizes of areas A_j are numerically equal, the procedure can be simplified because the determination of the dose contribution density for each subarea becomes unnecessary, and the dose contribution per subarea can be compared with the isodose $ID_{i,k}$ multiplied by the size of one subarea A. Mathematically, equation (5) for one observation point can be transformed into

$$k_i = \sum_j D_{i,j} / D_{i,\infty} \quad \forall \quad j\colon D_{i,j} \geqslant ID_{i,k} \cdot A \quad \wedge \quad A_j = A \tag{7}$$

and equation (6) for more than one observation point into

$$k = \sum_j D_j / D_\infty \quad \forall \quad j\colon D_j \geqslant ID_k \cdot A \quad \wedge \quad A_j = A. \tag{8}$$

2.4. Description of the calculations

The Monte Carlo calculations for the modular building scenario were performed with the transport code MCNP6 (Goorley *et al* 2012), using the cross-section data set ENDF/B-VII.0 (Chadwick *et al* 2006). Among other processes, it accounts for photon creation and loss through relevant mechanisms such as bremsstrahlung, fluorescence, Compton scattering, photon capture, pair production, and p-annihilation. The code allows for the definition of complex three-dimensional geometries through a combinatorial geometry technique. The definition of the geometry is based on the construction drawings and descriptions made available by Bilsby® (Bilsby®, n.d), and based on measurements of a real modular building, including an additional construction of breeze blocks that was used in our previous study (Hinrichsen *et al* 2018) (figure 1). The regions in space were constructed by a logical combination (union, intersection, difference) of elementary geometric bodies and surfaces. Data from various databases (McConn *et al* 2011) were used to assign the material specifications with definite atomic compositions and densities as the input for the different building structures and environmental regions.

^{137}Cs sources with a primary gamma energy of 0.662 MeV, and ^{60}Co sources with primary gamma energies of 1.173 MeV and 1.332 MeV, taking into account the emission probabilities of 0.998 5 photons per disintegration for a primary gamma energy of 1.173 MeV and 0.999 826 photons per disintegration for a primary gamma energy of 1.332 MeV, were assumed. The source regions were defined as cylinders with a diameter and height of 1 cm, on a 1 m × 1 m grid, up to a lateral distance of 10 m from the sides of the modular building at the bottom of the modules and, additionally, at the top of the modules. For the assumption of homogeneous contamination, interpolation methods were applied to the results of the grid points. Internal scattering within the source material was neglected, and no (extra) material composition was assigned to the source regions. Separate Monte Carlo computations were performed for reference values without the building, in the same way as in the calculations when the building was present ($\dot{D}_{\mathrm{ref}}$ in equation (1)). Calculations with an infinite surface source on ground level, excluding the area of the modular building, were performed to determine the isodose lines. Furthermore, calculations were performed for surface sources of various radii centred in the centre of the modular building on the ground and 1 cm beneath it, to determine the impact of ground penetration.

The composition of the soil surrounding the building was based on data in a material compendium (McConn *et al* 2011). The soil in the model was defined as a 5 m deep slab, and the air above as a 500 m high slab, to take possible scattering effects into account. The observation points were defined as air-filled spheres with a diameter of 30 cm, for which the

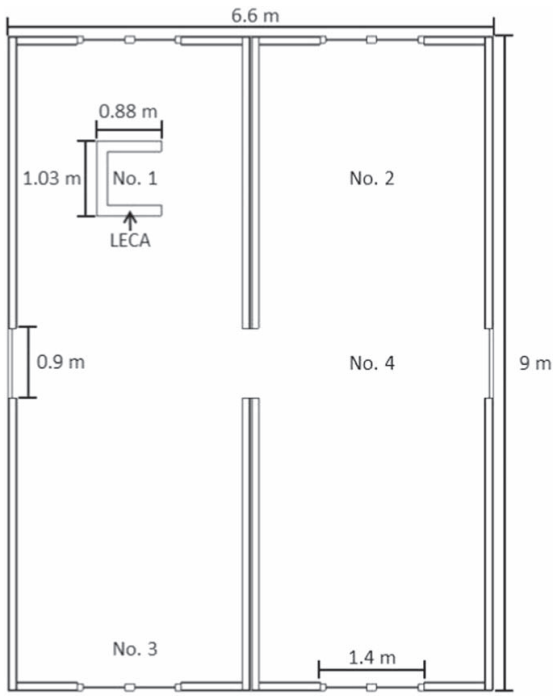

Figure 2. Observation points inside the modular building. The walls at each end of the building have two windows each. The left and right walls have one door each, and there is a opening connecting the two modules. The U-shape in the top-left corner represents the breeze block structure (lightweight expanded clay aggregate).

absorbed dose free in air was calculated. The four detector regions were centred at the corresponding observation points 1 m above the floor of the modules (figure 2). Detector region No. 1 was centred at the observation point in the middle of the breeze block structure, No. 2 in the middle of one half of one module, No. 3 0.5 m away from a window, and No. 4 opposite a doorway and an opening between the modules. These locations were chosen because they represent different parts of the building, and are the same as those used in our previous study (Hinrichsen *et al* 2018). The number and energies of the gamma particles passing through these regions were determined. The fluence was then transformed into dose using conversion coefficients (ICRP 2010).

Several techniques can be applied to reduce the variation in the results below a standard deviation of 5% with acceptable computation times in MCNP6. The defined regions in space are called cells, and weight windows were generated for each cell. The number of a particle's weight in MCNP6 represents the number of physical particles, which in these calculations are photons. Different random walks are represented by one MCNP particle. A lower bound on the weight of particles in each cell is defined by the user, and the upper weight bound is a specified multiple of the lower bound. These weight bounds define a window of acceptable weights. If the weight of a particle emitted from the source and generated by interactions with

the materials is below the lower weight bound, then the weight of the particle is randomly increased to a value within the window, or it is not included in the calculations. If the weight of a particle is above the upper limit, it is split so that its parts are within the window. No action is taken for particles with weights within the window. The weight windows were determined using Weight Window Generator, which estimates the importance of the cells in space. The importance of cells is defined as the expected score generated by a unit weight particle after entering the cell. The average importance of each cell can be estimated using the cell-based generator.

3. Results and discussion

3.1. Shielding factors around a modular building

In order to illustrate the influence of the position of the sources around the building on the shielding factor (equation (1)), the results for ^{137}Cs and ^{60}Co are plotted in heat maps for all four observation points defined above (figure 3). The shielding factor is substantially lower at observation point No. 1 (inside the breeze block construction) than at the other observation points. At this point, the overall average shielding factor is 0.29 ± 0.20 (1 SD) for ^{137}Cs and 0.37 ± 0.21 for ^{60}Co. The shielding factors at the other points were about 0.72 ± 0.22 for ^{137}Cs and 0.77 ± 0.21 for ^{60}Co.

For ^{137}Cs, the shielding factor of one module wall is 0.90 ± 0.01 and for one breeze block wall 0.25 ± 0.01; meanwhile, the corresponding values for ^{60}Co are 0.94 ± 0.01 and 0.32 ± 0.01, respectively. As can be seen from the plots in figure 3, even the doors and windows provide slightly better shielding than the module walls. The shielding factors determined for the doors and windows are 0.89 ± 0.01 and 0.85 ± 0.01 in the case of ^{137}Cs, and 0.93 ± 0.01 and 0.87 ± 0.01 in the case of ^{60}Co. All other shielding factors can be determined from combinations of these factors and the angles at which the radiation passes through the different materials. The impact of the angle of incidence at the observation point on the shielding factor depends on the increasing septum length of the material traversed by the gamma photons as the distance between the surface source element and the observation point decreases (close to the building). This effect is especially evident when the breeze block structure is in the line of sight between the source and the observation point. Hence, as the angle between the incoming radiation and wall approaches 90°, while moving farther away from the observation point, the radiation penetrates less material, and thus the shielding factor is higher.

3.2. Shielding factors on top of a modular building

In order to demonstrate the influence on the shielding factor of different source positions on top of the building, the results for ^{137}Cs and ^{60}Co are plotted for the four observation points in the case of surrounding deposition (figure 4). The shielding factor is substantially lower at observation point No. 1 (inside the breeze block construction) than for the other observation points. At this point, the overall average shielding factor is 0.32 ± 0.30 (1 SD) for ^{137}Cs and 0.38 ± 0.29 for ^{60}Co. The shielding factors for the other points were about 0.59 ± 0.22 for ^{137}Cs and 0.66 ± 0.19 for ^{60}Co.

All other shielding factors can be determined as combinations of radiation passing through the roof and then a module or brick wall, taking the angles at which the radiation passes through the different materials as well as backscattering effects into account.

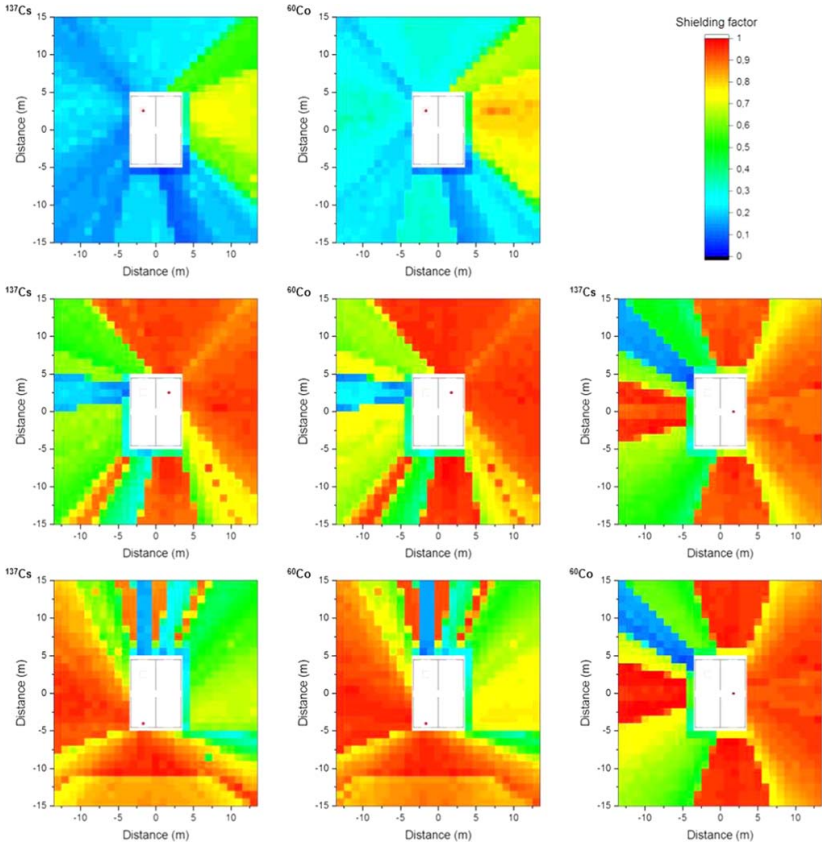

Figure 3. Computed angular shielding factors according to source region position around a modular building, at four different observation points inside the building (indicated by the red dots) for ^{137}Cs and ^{60}Co.

3.3. Monte Carlo computed isodose lines around a modular building

The concept of the isodose, in its simplified application for same-sized subareas, described in equation (7), was applied to a case where decontamination would lead to different reductions in the absorbed dose, depending on which of the four observation points is being considered. Homogeneous ground contamination surrounding the modular building was assumed. The results are presented graphically as isodose lines in figure 5 for ^{137}Cs and for ^{60}Co.

It can be seen in figure 5 that the shapes of the areas encompassed by the isodose lines for a given observation point are relatively similar for both radionuclides. The zones are larger for ^{60}Co since the source energy is higher than in the case of ^{137}Cs. To give a better idea of the size of the area that would have to be decontaminated to achieve a certain reduction in relative dose, the values are presented in table 2, together with the primary dose factor calculated for an infinite contaminated ground surface. The primary dose factor is directly related to the dose

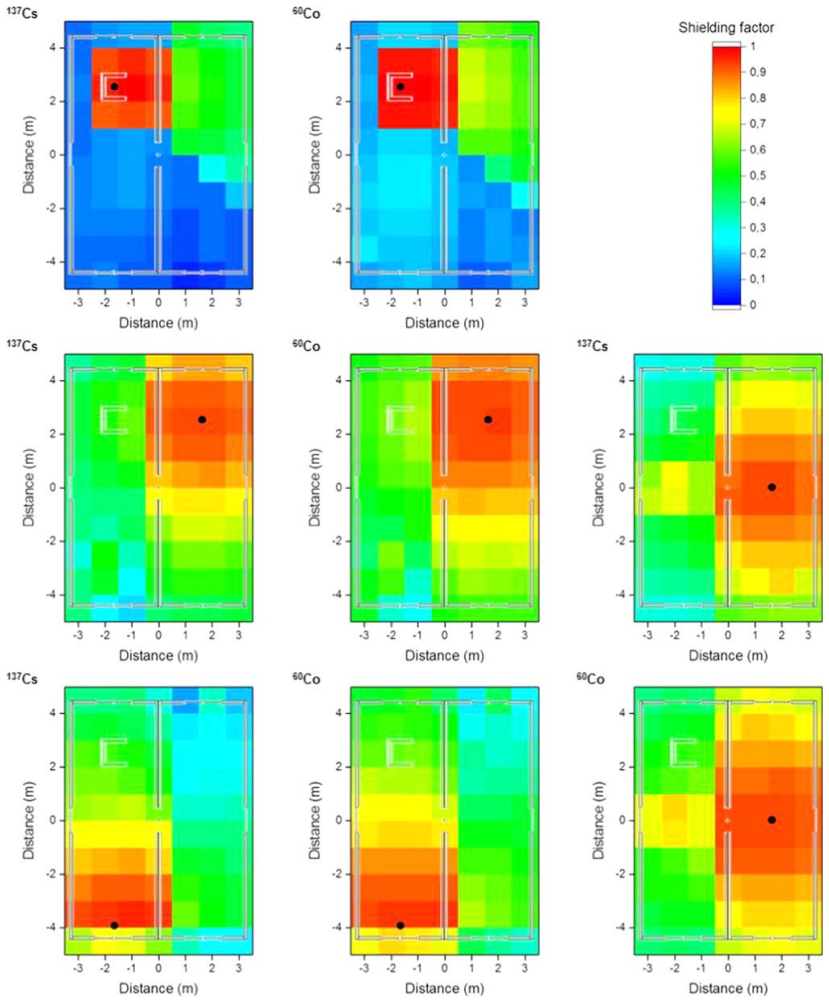

Figure 4. Computed angular shielding factors according to the source region position on top of a modular building at four different observation points inside the building (black dots) for ^{137}Cs and ^{60}Co.

to the residents when no decontamination measures are taken, and is given in pGy per γ mm^{-2} representing the dose (pGy) that would be caused by a homogeneous ground contamination for an source strength of one gamma photon per unit area (γ mm^{-2}).

The values vary significantly depending on the observation point, especially regarding the influence of the breeze block structure or walls, which cause radiation backscattering. There also appears to be an inverse correlation between the primary dose factor at a given

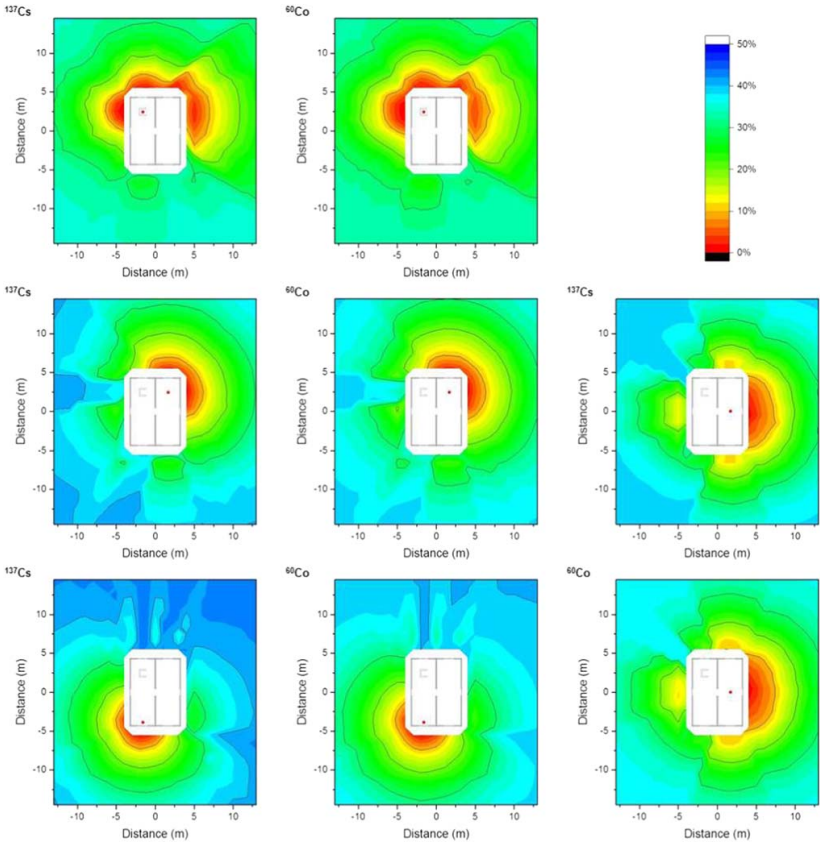

Figure 5. Isodose lines around a modular building at four different observation points inside the building (red dots) for ^{137}Cs and ^{60}Co. The shading indicates the fraction of dose contribution to the observation point including the areas that were determined for lower fractions of dose contribution. When the outside line for a certain dose reduction reaches the limit of the calculation grid, its shape might differ for a larger calculation grid.

observation point attributed to an infinite contaminated ground and the size of the decontaminated surface required to reduce this dose by a certain fraction. The lower the unremediated dose, the larger the size of the area that must be decontaminated to achieve a certain percentage of dose reduction.

3.4. Monte Carlo computed isodose lines on top of a modular building

The concept of the isodose applied to a two-dimensional area, as described by equation (5), was also applied to the roof of the building to determine the areas that would have to be decontaminated to achieve different degrees of reduction of the absorbed dose at the four

Table 2. Area (m^2) that would hypothetically have to be decontaminated to achieve various degrees of dose reduction at the four observation points in the case of ^{137}Cs and ^{60}Co contamination. All contamination is assumed to be on the soil surface.

Observation point	Radionuclide	Primary dose factor before decontamination (pGy per γ mm^{-2})	Dose reduction		
			10%	20%	30%
1	^{137}Cs	173	48	155	396[a]
	^{60}Co	394	51	168	450[a]
2	^{137}Cs	446	23	88	251
	^{60}Co	829	27	106	303
3	^{137}Cs	489	15	58	172
	^{60}Co	908	18	73	221
4	^{137}Cs	425	30	117	292
	^{60}Co	804	37	140	349

[a] The values for 30% dose reduction at observation point No. 1 were determined using a limited calculation grid; these results may differ with a larger calculation grid.

different observation points. The results are presented graphically as isodose lines in figure 6 for ^{137}Cs and for ^{60}Co.

It can be seen from the figure that most of the dose contribution from the roof results from a small area over each observation point. As in the case of ground penetration, the isodose lines for each observation point have similar shapes for the different zones and for both simulated radionuclides. Furthermore, the zones for ^{60}Co are larger since the emitted photon energy is higher than for ^{137}Cs.

3.5. Isodose lines based on more than one observation point

So far, four separate observation points representing different parts of the building have been used to determine isodose lines. In the next step, occupancy factors (p_i in equation (8)) are applied to determine isodose lines assuming a contaminated ground surface in order to obtain isodose lines that are more representative of the doses in the building as a whole. Since it was observed that a smaller area had to be decontaminated to achieve a given dose reduction in the case of a high unremediated absorbed dose $D_{i,\infty}$ at a given observation point, the occupancy factors were chosen in proportion to the primary dose factors $p_i = D_{i,\infty}/\sum_i D_{i,\infty}$. The results are presented graphically in figure 7. The size of the area that must be decontaminated to achieve dose reductions of 10%, 20%, and 30% are 39 m^2, 125 m^2, and 297 m^2 , respectively, for ^{137}Cs, and 45 m^2, 145 m^2, and 353 m^2, respectively, for ^{60}Co. For the modular building studied, the primary dose factor based on the occupancy factors was determined to be 423 pGy per γ mm^{-2} for ^{137}Cs and 788 pGy per γ mm^{-2} for ^{60}Co. In comparison with the values in table 2, it can be seen that the inverse relation between the primary dose factor and area size is still valid.

No isodose lines were determined for the roof taking all observation points into account since the results for the single observation points showed that the main dose contribution is from a small area over the observation point.

3.6. Impact of ground penetration

In order to study the impact of ground penetration on the size of an area encompassed by a given fraction of dose reduction, the absorbed doses resulting from contaminated circular

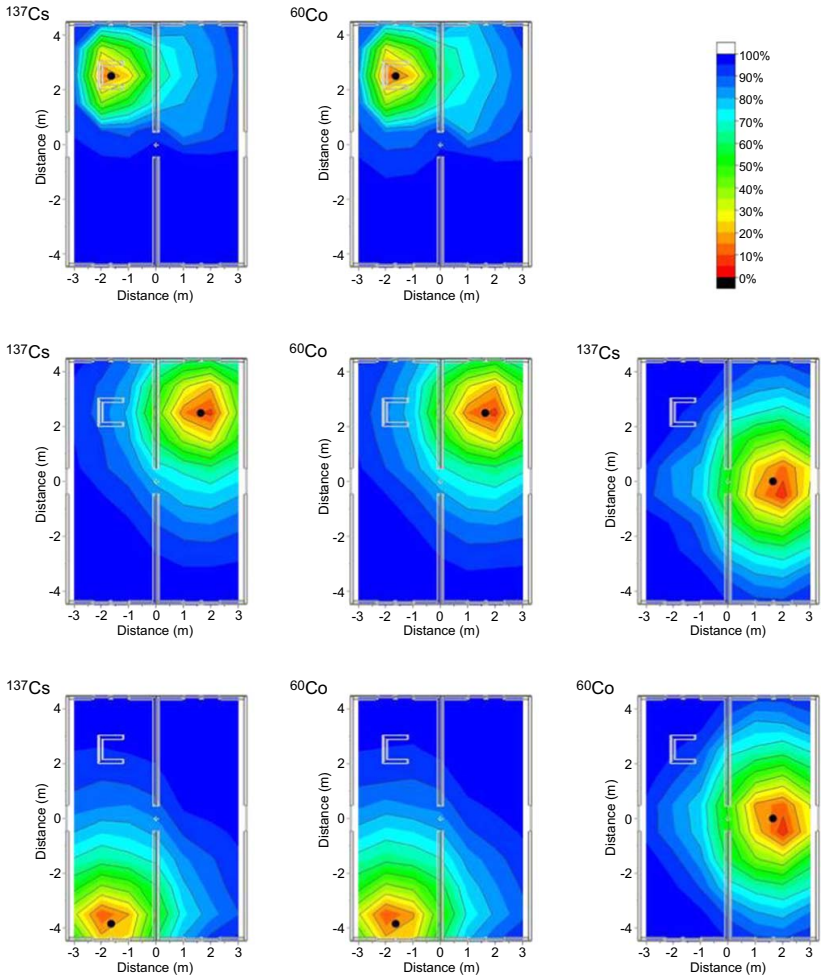

Figure 6. Isodose lines on top of a modular building at four different observation points inside the modules (black spot) for ^{137}Cs and ^{60}Co. The areas of different colours represent the fraction of dose contribution to the observation point including the areas that were determined for lower fractions of dose contribution.

areas of various sizes centred in the centre of the modular building on the ground were first calculated, and then divided by the absorbed dose resulting from an infinite ground source. The same calculations were then performed for a scenario with contamination to a depth of 1 cm beneath the ground surface to simulate ground penetration of the fallout some time after the initial deposition event, as was the case for ^{137}Cs fallout from the Fukushima release

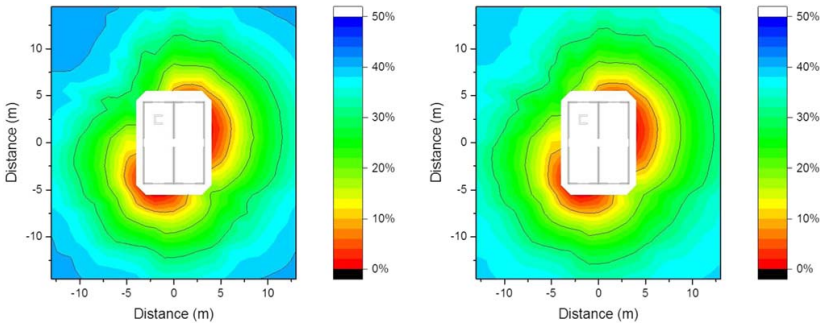

Figure 7. Isodose lines around a modular building for ^{137}Cs (left) and ^{60}Co (right) using occupancy factors according to the primary dose for the four observation points. The areas of different colours represent the fraction of dose contribution including the areas that were determined for lower fractions of dose contribution.

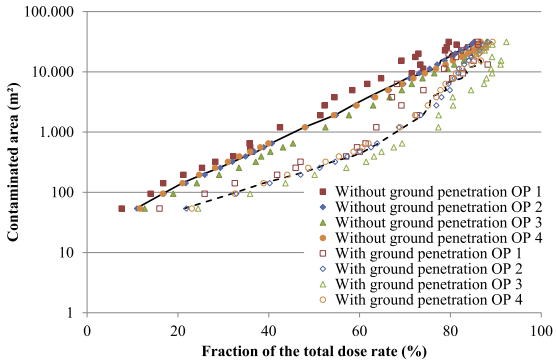

Figure 8. Size of a circular area that would have to be decontaminated to achieve a certain reduction in the total absorbed dose contribution at the four observation points (OP) inside the modular building. The continuous line indicates the average over all observation points without ground penetration, and the dashed line indicates the average over all observation points assuming ground penetration.

(e.g. Östlund *et al* 2017). Calculations were only performed for a ^{137}Cs source, and the results are presented in figure 8.

From figure 8 it can be seen that decontaminating an average area of 1000 m^2 would reduce the total absorbed dose contribution by about 45% without ground penetration, and by about 65%–70% with ground penetration. To study the impact of ground penetration in more detail, the size of circular area A that would have to be decontaminated to obtain a certain reduction in the dose contribution f can be described by the following mathematical expression:

$$A(f) = (a \cdot (-\ln(1-f))^b + c)^2 - 59.4, \quad a, b, c > 0. \tag{9}$$

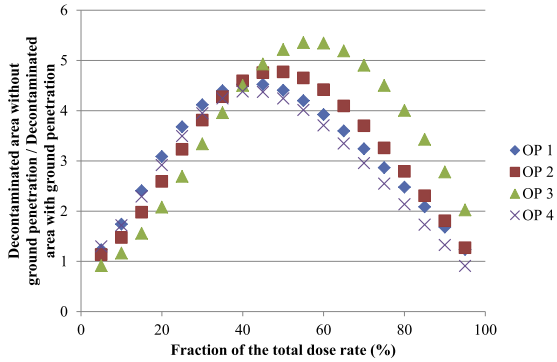

Figure 9. Ratio of the area that would have to be decontaminated without ground penetration to the area that would have to be decontaminated with 1 cm ground penetration to obtain the same fractional dose reduction at the four observation points (OP).

Table 3. Values of the variables in equation (9) describing the fraction of absorbed dose contribution for areas of various sizes.

Scenario	Observation point	Variable		
		a	b	c
Without ground penetration	1	68.6	1.72	9.57
	2	52.5	1.79	9.75
	3	44.4	1.82	9.57
	4	49.6	1.69	9.75
With 1 cm ground penetration	1	31.5	2.33	9.57
	2	21.3	2.50	9.75
	3	14.6	2.50	9.93
	4	22.9	2.44	9.57

Regression analysis can be used to obtain *a*, *b*, and *c* for each scenario, and the values are presented in table 3. The ground area of the modular building is 59.4 m^2.

Comparing the values in table 3 shows that a smaller area would have to be decontaminated in the case of ground penetration to obtain the same fractional dose reduction as in the case without ground penetration. Figure 9 shows the ratio of the area that would have to be decontaminated without ground penetration to the area that would have to be decontaminated with ground penetration to obtain the same fractional dose reduction.

The ratios in figure 9 vary between 1 and 5.5, showing a peak at a dose reduction in the range of 40% to 55%. In the case of real fallout situations, it should be kept in mind that according to the International Commission on Radiological Protection (ICRP) the key dose parameter to be considered in connection with decisions on interventions in a contaminated area is the residual dose, which is integrated over a long time for long-term interventions (ICRP 2007). Further factors are the costs and amount of generated waste that are caused by respective countermeasures, as well as the possible risk of erosion that could be increased by

topsoil removal over large areas and the resulting social, environmental, and ethical factors (Roed *et al* 2006). Downward migration of the contamination in soil over time can lead to different fractional contributions to the dose from contamination at different distances, as can be seen in figure 8. Therefore, to fully comply with the ICRP recommendations, in a 'real' situation, each calculated dose contribution at a given depth should be multiplied by the predicted fraction of the contamination present at that depth at each time, and it should all be integrated over time to give a committed dose over a given time span (e.g. 70 years). Downward penetration will depend greatly on the soil type and status, weather conditions, human and other impact, as well as on the physiochemical characteristics of the contaminants. These factors were neglected in this illustration of the method for the sake of simplicity, but they should be taken into account in realistic cases.

4. Conclusions

This study demonstrated the influence of various building materials and the angle of incidence of radiation on the shielding factor in a modular building, using the Monte Carlo model MCNP6. For example, the breeze block structure provides the most efficient shielding, with about a three times lower shielding factor than the walls of the modules. Even the doors and windows exhibit slightly lower shielding factors than the walls. Furthermore, the concept of the isodose, defining an area with a given dose contribution to a defined observation point inside the building, was introduced. Such isodose lines can be used to illustrate the extent of surrounding areas that must be decontaminated to achieve a certain dose reduction, depending on the observation point. It was found that the shape of the surface encompassed by the isodose lines did not change with increasing gamma energy of the incident photons, but the area requiring decontamination to achieve the same percentage of dose reduction increased with higher gamma energies. An inverse correlation was found between the primary dose factor and the size of the area that has to be decontaminated to achieve a certain dose reduction. To optimise decontamination activities for a residential building living habits inside the building must be considered, and a combination of primary dose factors for a number of observation points must therefore be used, depending on the occupancy times of the residents. When assuming 1 cm deep ground penetration, a decrease of up to 60% in the area requiring decontamination was found compared with surface deposition. This means that a substantially smaller area will have to be decontaminated to achieve a given reduction in dose after allowing time for the gradual migration of the deposition.

In conclusion, the isodose concept shows promise for comparing the effects of decontaminating different surface areas, of different primary gamma energies, and of different degrees of ground penetration. Further studies are required on the application of these findings to other types of buildings, as well as on the choice of a representative indoor observation points for such buildings, in order to develop this method into a practical and useful instrument for the optimisation of countermeasures in cases of radioactive fallout in inhabited areas.

Acknowledgments

This study was supported by the Swedish Radiation Safety Authority and by the Swedish Civil Contingencies Agency.

ORCID iDs

Y Hinrichsen https://orcid.org/0000-0002-1363-2002

References

Andersson K G 2009a Countermeasures for reduction of dose in contaminated inhabited areas *Airborne Radioactive Contamination in Inhabited Areas* (*Radioactivity in the Environment* vol 15) ed K G Andersson (Amsterdam: Elsevier) ch 8 pp 217–58

Andersson K G 2009b Strategies for restoration of contaminated inhabited areas *Airborne Radioactive Contamination in Inhabited Areas* (*Radioactivity in the Environment* vol 15) ed K G Andersson (Amsterdam: Elsevier) ch 10 pp 297–326

Bilsby® (n.d)., Snittegning af kontormoduler—stabelbare; konstruktionsbeskrivelse—kontormoduler - stabelbare (in Danish).

Chadwick M *et al* 2006 Endf/b-vii.0: Next generation evaluated nuclear data library for nuclear science and technology *Nucl. Data Sheets* **107** 2931–3060 Evaluated Nuclear Data File ENDF/B-VII.0.

Goorley T *et al* 2012 Initial MCNP6 release overview *Nucl. Technol.* **180** 298–315

Hinrichsen Y, Finck R, Östlund K, Rääf C and Andersson K G 2018 Comparison of experimental and calculated shielding factors for modular buildings in a radioactive fallout scenario *J. Environ. Radioact.* **189** 146–55

ICRP 2007 The 2007 recommendations of the international commission on radiological protection *Ann. ICRP* **37** 1–332 ICRP Publication 103.

ICRP 2010 Conversion coefficients for radiological protection quantities for external radiation exposures *Ann. ICRP* **40** 1–257 ICRP Publication 116.

Jensen P H and Thykier-Nielsen S 1989 Shielding factor calculation for plume radiation *Radiation Protection Programme. Progress Report 1988* 1561–5

McConn R Jr, Gesh C, Pagh R, Rucker R and Williams R III 2011 Radiation portal monitor project—compendium of material composition data for radiation transport modeling. pacific northwest national laboratory. piet-43741-tm-963, pnnl-15870 rev. 1 https://www.pnnl.gov/main/publications/external/technical_reports/PNNL-15870Rev1.pdf

Östlund K, Samuelsson C, Mattsson S and Rääf C L 2017 The influence of (cs)-c-134 on the cs-137 gamma-spectrometric peak-to-valley ratio and improvement of the peak-to-valley method by limiting the detector field of view *Appl. Radiat. Isot.* **128** 249–55

Roed J, Andersson K G, Barkovsky A, Fogh C, Mishine A, Ponamarjov A and Ramzaev V 2006 Reduction of external dose in a wet-contaminated housing area in the Bryansk Region, Russia *J. Environ. Radioact.* **85** 265–79

Spencer L 1962 Introduction to structure shielding analysis *Structure Shielding Against Fallout Radiation from Nuclear Weapons* (*United States Bureau of Standards–Monograph*) 42 (Gaithersburg, MD: United States Bureau of Standards Publications) 12–18

Paper III

Hinrichsen, Y., Andersson, K. G., Kerma conversion factors for modern urban glass buildings in radioactively contaminated areas. Accepted for publication by Journal of Radiological Protection.

Kerma conversion factors for modern glass buildings in radioactively contaminated areas

Y Hinrichsen, K G Andersson

Technical University of Denmark, Center for Nuclear Technologies, Frederiksborgvej 399, 4000 Roskilde, Denmark

E-mail: yvhi@dtu.dk

Abstract.

To improve the estimation of external gamma irradiation from deposited radioactivity in urban environments a model of a modern office or residential building with glass facades was set up with eleven different building heights. Kerma conversion factors for the floors inside the building from contamination on different types of surfaces were determined by using the Monte Carlo code MCNP6 for the primary gamma energies 0.3 MeV, 0.662 MeV and 3.0 MeV and for three different environmental scenarios. The kerma conversion factors were expressed as formulas for each possible deposition area for contaminants. The importance of the determined factors was shown by comparing them to previously generally used factors for multistorey house blocks.

Submitted to: *J. Radiol. Prot.*

1. Introduction

After an airborne release of radionuclides to inhabited environments, external gamma irradiation from deposited radioactivity can contribute considerably to the radiation exposure of the population (Golikov et al. 2002). The shielding of gamma radiation by buildings can, however, reduce this exposure and sheltering of inhabitants is one of the principal countermeasures considered for areas potentially affected by radioactive release. Detailed knowledge of the shielding properties of buildings is therefore an important component of risk assessment in radiological emergency preparedness.

As the geometry of building structures is too complex for simple methods such as the point kernel model (Spencer et al. 1980), Monte Carlo calculations are needed to calculate the kerma as shown in a comparison performed by Jensen & Thykier-Nielsen (1989). The shielding properties and the resulting kerma rate can vary greatly for different types of buildings depending on the size of the building and its construction characteristics, on the energy spectrum of the radionuclides, on the distribution of the contaminants on the different surfaces and on the type of environment (e.g. Meckbach et al. 1988) leading to the use of Monte Carlo simulations in the late 1980s at the GSF (now the Helmholtz Zentrum München German Research Centre for Environmental Health) (Meckbach et al. 1988, Jacob & Meckbach 1987, Meckbach & Jacob 1988, Meckbach et al. 1987). An early Monte Carlo code SAM-CE (Lichtenstein et al. 1979) was applied to calculations for four different types of houses. Inhabited area external dose estimates in the European standard decision support systems ARGOS and RODOS rely entirely on these few old datasets. Monte Carlo calculations were repeated for the semi-detached house by Meckbach et al. (1988) using the modern code MCNP6 (Goorley et al. 2012), and similarities and deviations within the order of magnitude for different parts of the building are described in a paper that is still to be published (Hinrichsen & Andersson 2018).

The applicability of the transport code MCNP6 in determining exposure reduction for a modular building type has been experimentally verified in a previous study by our group (Hinrichsen et al. 2018). Further Monte Carlo simulations were performed for an industrial area (Kis et al. 2003, Kis et al. 2004), for various scenarios of U.S. residential structures (Dickson & Hamby 2014, Dickson & Hamby 2016, Dickson et al. 2017), for typical houses in Brazil (Salinas et al. 2006), and typical buildings in Japan (Furuta & Takahashi 2015). To the best of our knowledge such simulations have not previously been performed for buildings with glass facades that can be found in many cities now as a part of modern architecture or buildings with similar shielding properties. Therefore, the aim of this study was to set up a model of a modern glass building, derive the kerma conversion factors from different contaminated surfaces and compare them with the respective values that were derived for a multistorey house block (Meckbach et al. 1988) that would so far be applied in emergency management decision support for any high rise urban building.

2. Materials and methods

The Monte Carlo calculations for the setup of modern buildings were performed with the transport code MCNP6 (Goorley et al. 2012), using the nuclear cross-section data

set ENDF/B-VII.0 (Chadwick et al. 2006). Among other processes, it accounts for photon creation and loss through relevant mechanisms such as bremsstrahlung, fluorescence, Compton scattering, photon capture, pair production and p-annihilation.

The code allows for the definition of complex 3-dimensional geometries through a combinatorial geometry technique. The definition of the geometry is leaned on the construction drawings and descriptions of a real glass building in the city of Copenhagen that were made available by the Technical and Environmental Administration of the Municipality of Copenhagen (Teknik- og Miljøforvaltning Københavns Kommune) and was applied to 11 different heights of the building from one storey till 11 storeys for a single house scenario that stands alone, for a park scenario with 3 houses in a row, and for a city scenario with a square of 3 x 3 houses (Figures 1 to 4). The outer walls are made of 2 layers of 1.2 cm thick glass with 97.6 cm air in between them. In the middle of the building (see Figures 1 and 2) is an atrium covered by a roof of 2.4 cm thick glass. It is not surround by any wall as it is usually surrounded by railings on the different floors. The house contains six shafts for stairs and elevators going from the basement up to the top of the building (see Figures 1 and 2). Their surrounding walls are made of 30 cm thick concrete. The building is furthermore based on sixty concrete columns (indicated by small circles in Figure 1) with a diameter of 60 cm going from the basement building. The intermediate floors and the roof are made 22 cm thick concrete and the basement is surrounded by 40 cm thick concrete to the bottom and to the sides. The spheres in Figures 1 to 4 indicate the positions of the tree canopies. As foliage on trees constitute a very efficient aerosol/rain filter, the contamination on the stem and braches will be of comparatively little importance (Roed 1988) and is not considered in the model.

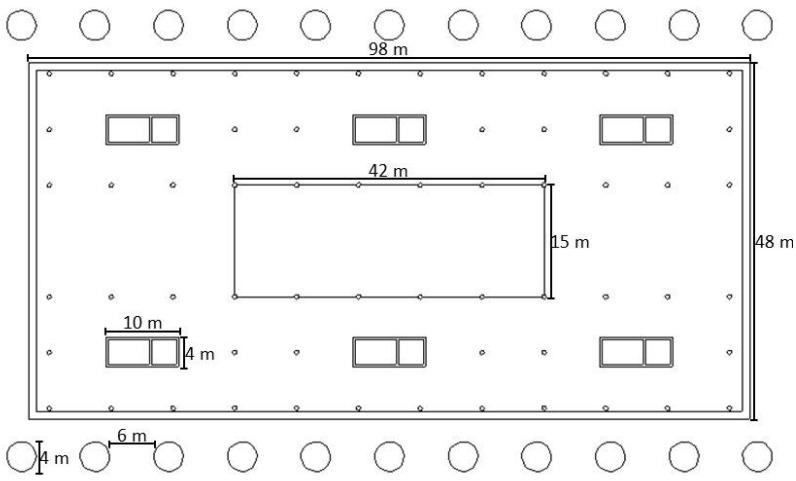

Figure 1. Horizontal cut of the glass building.

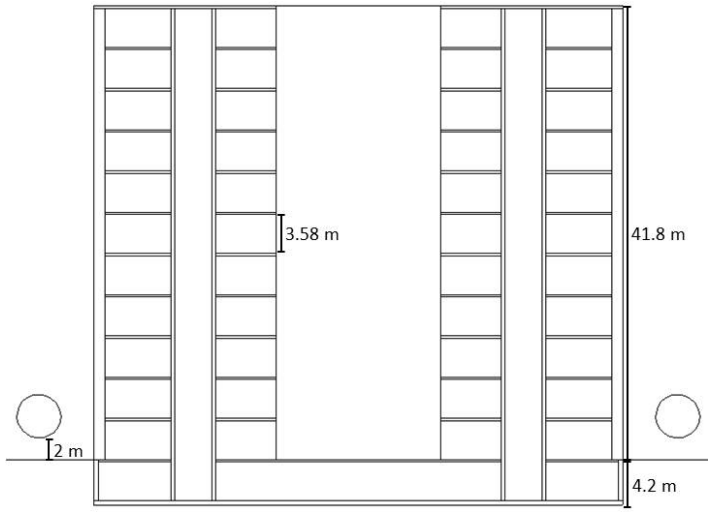

Figure 2. Vertical cut of the glass building for the largest height of eleven storeys.

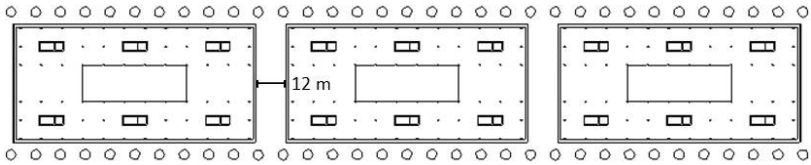

Figure 3. Horizontal cut of the park scenario.

The regions in space were constructed by a logical combination (union, intersection, difference) of elementary geometric bodies and surfaces. Data from a material compendium (McConn Jr et al. 2011) was used to assign the material specifications with definite atomic compositions and densities as summarized in Table 1 to the input for the different building structures and environmental regions.

Table 1. Material specifications with definite atomic compositions (rounded) and densities that were used for the Monte Carlo calculations.

Material	Atomic composition	Density in kg/l
Air	0.02 % C; 78.44 % N; 21.07 % O; 0.47 % Ar	0.001205
Concrete	8.47 % H; 60.41 % O; 1.25 % Na; 2.48 % Al; 24.19 % Si; 2.72 % Ca; 0.47 % Fe	2.25
Glass	60.39 % O; 8.81 % Na; 25.18 % Si; 5.62 % Ca	2.4
Soil	31.69 % H; 50.16 % O; 4.00 % Al; 14.16 % Si	1.52

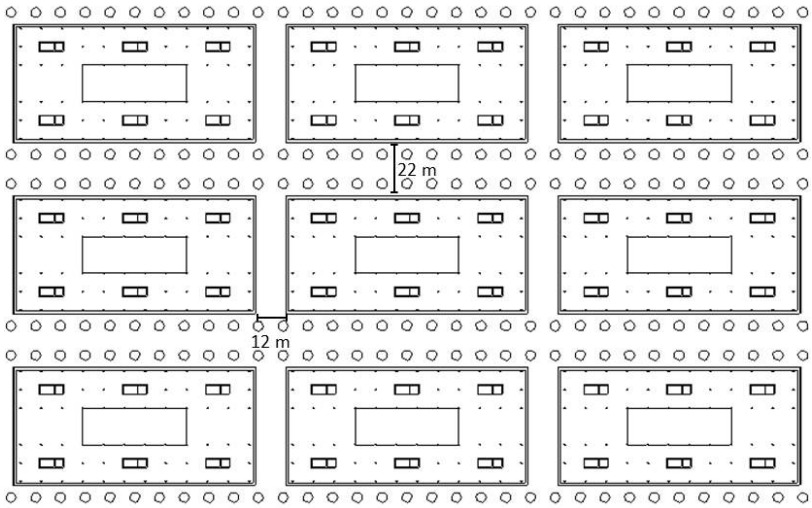

Figure 4. Horizontal cut of the city scenario.

For each height and scenario separate computations were performed for sources that were defined as surfaces on top of the ground, trees, walls, and roofs. The source energies were monoenergetic sources of 0.662 MeV representing ^{137}Cs, which has been of main concern regarding long term effects (Imanaka et al. 2015) in connection with the Chernobyl and Fukushima incidents, 0.3 MeV or 3.0 MeV to get an impression of the behaviour of the kerma for lower and higher primary gamma energies.

The detector regions were defined as air-filled spheres with a diameter of 30 cm and eighteen of them were positioned in various part of each floor 1 m above the level of the respective floor of the building. In those regions, the number and energies of the gamma 'particles' passing through were scored. By using conversion coefficients (ICRP 2010), the fluence was transferred to air kerma free-in-air and averaged over the eighteen detector regions in each floor. Furthermore, the code provides ten statistical tests that are performed on each defined detector region (called tally in MCNP). Those tests are a valuable tool to ascertain reliable statistical quality of the respective results.

Internal walls inside the building were not modelled, because in these modern buildings they are not part of the building. They are usually made of gypsum (around 12 cm thick) and can be built up and removed quickly. To get an idea about their shielding effect extra simulations were performed leading to the results that the kerma will be reduced by a factor of 0.72 for a primary gamma energy of 0.3 MeV, by 0.77 for a primary gamma energy of 0.662 MeV and by 0.86 for a primary gamma energy of 3.0 MeV after passing one gypsum wall of 12 cm thickness.

3. Results and discussion

3.1. Kerma conversion factors

With the Monte Carlo calculations the kerma (pGy) per emitted gamma photon (γ) on the source was determined. This factor was multiplied with the size of the respective source area (mm^2) to determine the kerma (pGy) for a source strength of one gamma photon per unit area (γ mm^{-2}) represented by K. These values were used as a basis to fit a mathematical model for the kerma over them for each type of surface at a given floor F inside a building of a height H with the smallest possible deviations.

The following mathematical expressions describe the kerma for all floors of the glass building for all building heights, environmental scenarios, source energies and source areas. H represents in the equations the height in terms of number of storeys above ground level (excluding the basement there are $H + 1$ storeys). F represents the floor inside the building from $F = -1$ (basement) through $F = 0$ (ground floor) to higher floors (e.g. $F = 5$ is the fifth floor). F is of course restricted by the height of the building (FH). All equations determine the kerma (pGy) for a source strength of one gamma photon per unit area (γ mm^{-2}) (K). By multiplying this factor with a given contamination level (Bq mm^{-2}) and the number of photons per disintegration (γ) of the respective gamma energy, the kerma rate contribution for each gamma energy emitted with determined kerma factors can be calculated. As the basement of the building is more shielded than the rest of the building, an extra equation is necessary for all contamination scenarios.

The development of the kerma per source strength inside a glass building caused by contamination on the roof can be described by Equation (1) with the values of the variables given in Table 2. The variable a expresses the kerma per source strength in the floor directly under the roof, the term $\exp\left(-b \cdot (H - F)^c\right)$ the decrease of the kerma with distance to the roof, and the term $(1 + d \cdot \exp(-e \cdot F^f))$ the backscattered radiation from the ground. The kerma in the basement decreases with the height of the building as the distance to the basement increases ($g \cdot \exp(-h \cdot H^i)$).

$$K(F,H) = \begin{cases} a \cdot \exp(-b \cdot (H - F)^c) \cdot (1 + d \cdot \exp(-e \cdot F^f)), & \forall F \geq 0 \\ g \cdot \exp(-h \cdot H^i), & \forall F = -1 \end{cases} \quad (1)$$

Equation (2) with the values of the variables given in Table 3 describes the development of the kerma per source strength inside a glass building caused by contamination on the walls. The variable a expresses the maximal kerma per source strength in a floor with several floors under and over it. The term $(1 - b \cdot \exp(-c \cdot F^d))$ expresses the decrease of the kerma because of decreasing distance to the ground and therefore smaller area of contaminated wall below this floor, and the term $(1 - e \cdot \exp(-f \cdot (H - F)^g))$ the same effect of decreasing distance towards the roof of the building. Furthermore, the term $(1 - h \cdot \exp(-i \cdot H^j))$ expresses the impact of the height of the building as the source area of the walls increases with height. The kerma in the basement increases with the height and source area of the building $(1 - l \cdot \exp(-m \cdot H^n))$ towards a maximum value of k.

Table 2. Values of the variables in Equation (1) describing the kerma per source strength inside a glass building caused by contamination on the roof. 'a' and 'g' have the dimension pGy per γ mm^{-2}. All other variables are dimensionless.

	0.3 MeV	0.662 MeV	3.0 MeV
a	4.70	15.3	126
b	0.80	1.05	1.33
c	0.78	0.74	0.70
d	0.11	0.073	0.018
e	1.29	1.27	0.95
f	1.03	0.63	0.30
g	0.040	0.39	14.6
h	0.35	0.59	0.96
i	0.87	0.69	0.60

$$K(F,H) = \begin{cases} a \cdot (1 - b \cdot \exp(-c \cdot F^d)) \cdot (1 - e \cdot \exp(-f \cdot (H-F)^g)) \cdot (1 - h \cdot \exp(-i \cdot H^j)), & \forall F \geq 0 \\ k \cdot (1 - l \cdot \exp(-m \cdot H^n)), & \forall F = -1 \end{cases} \tag{2}$$

Table 3. Values of the variables in Equation (2) describing the kerma per source strength inside a glass building caused by contamination on the walls. 'a' and 'k' have the dimension pGy per γ mm^{-2}. All other variables are dimensionless.

	0.3 MeV	0.662 MeV	3.0 MeV
a	17.0	36.7	132
b	0.066	0.065	0.098
c	1.76	2.64	1.41
d	0.0064	0.45	0.87
e	0.12	0.12	0.15
f	1.84	1.92	1.62
g	0.39	0.42	0.74
h	0.096	0.037	0.025
i	0.25	0.59	1.46
j	0.60	0.71	0.86
k	0.040	0.30	7.42
l	0.34	0.35	0.41
m	1.40	2.38	1.63
n	0.17	0.31	1.33

The development of the kerma per source strength inside a glass building caused by contamination on the ground can be described by Equations (3) and (4) with the respective values of the variables given in Tables 4 to 6 depending on the environmental scenario. The variable a represents the kerma at the ground floor and the term $\exp(-b \cdot F^c)$ the decrease of it towards the roof. In the scenarios with neighbouring buildings skyshine has an impact on the floors closest to the roof, which is expressed by the term $(1 + d \cdot \exp(-e \cdot (H-F)^f))$. The kerma in the basement is independent from the height of the buildings and therefore stable. It is expressed by the value d in the scenario without neighbouring buildings and by the value g in the scenarios with

neighbouring buildings.

$$K(F,H) = \begin{cases} a \cdot \exp(-b \cdot F^c), & \forall F \geq 0 \\ d, & \forall F = -1 \end{cases} \quad (3)$$

Table 4. Values of the variables in Equation (3) describing the kerma per source strength inside a glass building caused by contamination on the ground for a single house without any neighbouring buildings. 'a' and 'd' have the dimension pGy per γ mm^{-2}. 'b' and 'c' are dimensionless.

	0.3 MeV	0.662 MeV	3.0 MeV
a	41.1	115	572
b	0.64	0.67	0.62
c	0.51	0.53	0.58
d	0.019	0.093	0.63

$$K(F,H) = \begin{cases} a \cdot \exp(-b \cdot F^c) \cdot (1 + d \cdot \exp(-e \cdot (H-F)^f)), & \forall F \geq 0 \\ g, & \forall F = -1 \end{cases} \quad (4)$$

Table 5. Values of the variables in Equation (4) describing the kerma per source strength inside a glass building caused by contamination on the ground for a house in a park scenario with two neighbouring buildings. 'a' and 'g' have the dimension pGy per γ mm^{-2}. All other variables are dimensionless.

	0.3 MeV	0.662 MeV	3.0 MeV
a	34.5	95.7	475
b	0.70	0.73	0.69
c	0.50	0.51	0.54
d	0.035	0.026	0.015
e	0.37	0.48	0.52
f	1.88	1.51	1.33
g	0.017	0.082	0.55

Table 6. Values of the variables in Equation (4) describing the kerma per source strength inside a glass building caused by contamination on the ground for a house in a city scenario with eight neighbouring buildings. 'a' and 'g' have the dimension pGy per γ mm^{-2}. All other variables are dimensionless.

	0.3 MeV	0.662 MeV	3.0 MeV
a	23.8	61.5	267
b	1.18	1.36	1.46
c	0.49	0.48	0.49
d	0.12	0.13	0.084
e	0.60	0.68	0.88
f	1.56	1.49	1.57
g	0.011	0.056	0.36

Neighbouring buildings contribute to the kerma by contamination on their roofs and walls. Equation (5) with the respective values of the variables given in Tables 7

and 8 describe the development of the kerma per source strength inside a glass building caused by contamination on the roofs of those neighbouring buildings. The variable a expresses the kerma per source strength in the floor directly under the roof, the term $\exp(-b\cdot(H-F)^c)$ the decreasing of the kerma with distance to the roof, and the term $(1+d\cdot\exp(-e\cdot F^f))$ the backscattered radiation from the ground. The kerma in the basement decreases with the height of the building as the distance to the basement increases $(g\cdot\exp(-h\cdot H^i))$ for primary gamma energies of 0.3 and 0.662 MeV. For primary gamma energies of 3.0 MeV an extra of $-j\cdot\exp(-k\cdot H^l)$ has to be added to model the development of the kerma in the basement for different heights of the buildings. This may reflect a second relevant factor apart from the distance of source and detector position. By looking at the direct line between source and detector position can be seen that the distance of soil that has to be crossed, before the radiation reaches the basement, decreases with increasing height of the building. Therefore, the kerma in the basement at the beginning increases with increasing distance to the source as this shielding effect seems to have a higher impact on the kerma development in these ranges than the distance to the source which additionally seems to be only relevant for higher energies.

$$K(F,H)=\begin{cases} a\cdot\exp(-b\cdot(H-F)^c)\cdot(1+d\cdot\exp(-e\cdot F^f)), & \forall F\geq 0 \\ g\cdot\exp(-h\cdot H^i) & \forall F=-1(0.3 and 0.662 MeV) \\ g\cdot\exp(-h\cdot H^i)-j\cdot\exp(-k\cdot H^l) & \forall F=-1(3.0 MeV) \end{cases} \tag{5}$$

Table 7. Values of the variables in Equation (5) describing the kerma per source strength inside a glass building caused by contamination on the roof of two neighbouring buildings in a park scenario. 'a', 'g' and 'j' have the dimension pGy per γ mm^{-2}. All other variables are dimensionless.

	0.3 MeV	0.662 MeV	3.0 MeV
a	0.37	0.64	1.38
b	0.74	0.84	0.70
c	0.59	0.58	0.79
d	0.034	0.039	0.039
e	0.017	0.31	0.37
f	4.95	1.78	1.45
g	0.00043	0.0018	0.077
h	0.45	0.38	0.10
i	0.90	0.85	1.61
j	-	-	0.067
k	-	-	0.20
l	-	-	2.38

The development of the kerma per source strength inside a glass building caused by contamination on the walls of neighbouring buildings can be described by Equation (2) with the respective values of the variables given in Tables 9 and 10 depending on the environmental scenario. The variable a expresses the maximal kerma per source strength in a floor with several floors under and over it. The term $(1-b\cdot\exp(-c\cdot F^d))$ expresses the decrease of the kerma because of decreasing distance to the ground

Table 8. Values of the variables in Equation (5) describing the kerma per source strength inside a glass building caused by contamination on the roof of eight neighbouring buildings in a city scenario. 'a', 'g' and 'j' have the dimension pGy per γ mm^{-2}. All other variables are dimensionless.

	0.3 MeV	0.662 MeV	3.0 MeV
a	1.48	2.64	5.53
b	0.55	0.61	0.52
c	0.85	0.85	0.93
d	0.063	0.066	0.037
e	0.67	0.39	0.57
f	1.56	1.91	1.26
g	0.0014	0.0079	0.39
h	0.072	0.32	0.12
i	1.78	0.96	1.26
j	-	-	0.36
k	-	-	0.16
l	-	-	1.44

and therefore less area of contaminated walls on this side of the floor, and the term $(1 - e \cdot \exp(-f \cdot (H - F)^g))$ the same effect of decreasing distance towards the roof of the buildings. Furthermore, the term $(1 - h \cdot \exp(-i \cdot H^j))$ expresses the impact of the heights of the buildings as the source area of the walls increases with height. The kerma in the basement increases with the height and source area of the building $(1 - l \cdot \exp(-m \cdot H^n))$ towards a maximum value of k.

Table 9. Values of the variables in Equation (2) describing the kerma per source strength inside a glass building caused by contamination on the walls of two neighbouring buildings in a park scenario. 'a' and 'k' have the dimension pGy per γ mm^{-2}. All other variables are dimensionless.

	0.3 MeV	0.662 MeV	3.0 MeV
a	4.62	10.8	36.9
b	0.21	0.20	0.20
c	1.11	1.34	1.52
d	0.75	0.70	0.44
e	0.37	0.38	0.40
f	0.89	0.94	0.99
g	1.20	1.19	1.13
h	0.51	0.46	0.31
i	0.45	0.51	0.74
j	0.55	0.40	0.43
k	0.0071	0.053	1.61
l	0.92	0.94	0.98
m	0.19	0.15	0.11
n	1.24	1.60	1.88

Equation (6) with the respective values of the variables given in Tables 11 to 13 describe the development of the kerma per source strength inside a glass building

Table 10. Values of the variables in Equation (2) describing the kerma per source strength inside a glass building caused by contamination on the walls of eight neighbouring buildings in a city scenario. 'a' and 'k' have the dimension pGy per γ mm^{-2}. All other variables are dimensionless.

	0.3 MeV	0.662 MeV	3.0 MeV
a	15.3	36.4	142
b	0.23	0.22	0.22
c	0.85	1.02	1.06
d	0.90	0.99	1.07
e	0.41	0.43	0.47
f	0.51	0.51	0.50
g	1.11	1.15	1.07
h	0.61	0.56	0.46
i	0.41	0.47	0.66
j	0.69	0.64	0.62
k	0.024	0.24	6.42
l	0.94	0.97	0.99
m	0.079	0.061	0.039
n	1.47	1.40	1.73

caused by contamination on trees depending on the environmental scenario. The term $a \cdot \exp(-b \cdot F^c)$ describes the decreasing of the kerma with distance to the trees for buildings of heights $H \geq 1$ at the floors $F \geq 1$. The value of the variable d expresses the kerma at the ground floor for a building height of $H = 0$ and e the kerma at the ground floor for higher buildings. The kerma in the basement is independent from the height of the buildings and expressed by the value f.

$$K(F,H) = \begin{cases} a \cdot \exp(-b \cdot F^c), & \forall F, H \geq 0 \\ d & \forall F, H = 0 \\ e & \forall F = 0 \wedge H \geq 1 \\ f & \forall F = -1 \end{cases} \tag{6}$$

Table 11. Values of the variables in Equation (6) describing the kerma per source strength inside a glass building caused by contamination on trees for a single house without any neighbouring buildings. 'a', 'd', 'e' and 'f' have the dimension pGy per γ mm^{-2}. 'b' and 'c' are dimensionless.

	0.3 MeV	0.662 MeV	3.0 MeV
a	$1.42 \cdot 10^{17}$	$6.50 \cdot 10^{9}$	$1.12 \cdot 10^{10}$
b	39.4	21.6	20.8
c	0.048	0.10	0.12
d	1.07	2.66	10.2
e	1.12	2.77	10.6
f	0.0020	0.014	0.38

Table 12. Values of the variables in Equation (6) describing the kerma per source strength inside a glass building caused by contamination on trees for a house in a park scenario with two neighbouring buildings. 'a', 'd', 'e' and 'f' have the dimension pGy per γ mm^{-2}. 'b' and 'c' are dimensionless.

	0.3 MeV	0.662 MeV	3.0 MeV
a	$4.24 \cdot 10^{18}$	$3.58 \cdot 10^{9}$	$3.90 \cdot 10^{42}$
b	42.7	20.9	95.6
c	0.041	0.095	0.025
d	1.19	2.98	11.7
e	1.23	3.09	12.1
f	0.0020	0.015	0.39

Table 13. Values of the variables in Equation (6) describing the kerma per source strength inside a glass building caused by contamination on trees for a house in a city scenario with eight neighbouring buildings. 'a', 'd', 'e' and 'f' have the dimension pGy per γ mm^{-2}. 'b' and 'c' are dimensionless.

	0.3 MeV	0.662 MeV	3.0 MeV
a	$4.70 \cdot 10^{20}$	$3.01 \cdot 10^{9}$	$9.10 \cdot 10^{9}$
b	47.0	20.3	20.0
c	0.030	0.078	0.092
d	1.78	4.55	18.6
e	1.83	4.65	18.9
f	0.0025	0.017	0.41

3.2. Comparison with previous values for a multistorey house block

To show the relevance of the determined kerma factors they were compared to respective factors calculated by Meckbach et al. (1988) for a multistorey house block, which is the closest of the building models that were developed so far compared to the glass building model in this study. The multistorey house was five storeys high and therefore the values are compared to the values of the glass building with a height of $H = 4$. Furthermore, kerma factors inside the multistorey house block were determined for the basement ($F = -1$), the ground floor ($F = 0$), the second floor ($F = 2$), and the fourth floor ($F = 4$) and thus compared to the respective floors inside the glass building. Regarding the source areas on the building both factors for the roof were compared as well as the factor for the walls of the glass building with the sum of the factors for walls and windows of the multistorey house block. In case of the ground as source area the respective factors were compared for the park and the city scenario that were for the multistorey house block the sum of the factors for the street and the park in the park scenario and the factor for the street in case of the city scenario. For the neighbouring buildings (Meckbach et al. 1988) calculated factors for walls and windows as well as for the roof and for both park and city scenario. Therefore, all four could directly be compared to the respective ones determined for the glass building. Regarding the factors for the trees the respective ones for a park scenario were compared.

The comparison took place by dividing the factor for the glass building by the respective one for the multistorey house block for all values available. This was per-

formed for all three primary gamma energies and the resulting ratios are presented in Tables 14 to 16.

Table 14. Ratios of the kerma factor for the glass building divided by the respective factor for a multistorey house block (Meckbach et al. 1988). The figures are given according to source and detection area for a primary gamma energy of 0.3 MeV.

	Basement	Ground floor	Second floor	Forth floor
On the building:				
Roof	-	-	-	7.85
Walls and windows	12.3	4.39	4.49	4.38
Ground:				
Park scenario (street and park)	7.65	11.6	9.42	8.14
City scenario (street)	2.76	24.1	21.6	30.2
Neighbouring buildings:				
Roofs in a park scenario	-	2.25	2.88	3.68
Roofs in a city scenario	-	24.3	11.6	4.90
Walls and windows in a park scenario	1.62	4.16	4.91	5.83
Walls and windows in a city scenario	1.19	4.46	5.55	6.34
Trees:				
Park scenario	0.510	1.90	2.25	2.02

Table 15. Ratios of the kerma factor for the glass building divided by the respective factor for a multistorey house block (Meckbach et al. 1988). The figures are given according to source and detection area for a primary gamma energy of 0.662 MeV.

	Basement	Ground floor	Second floor	Forth floor
On the building:				
Roof	-	-	271	4.04
Walls and windows	17.5	3.94	4.20	3.77
Ground:				
Park scenario (street and park)	4.88	11.0	8.62	8.66
City scenario (street)	2.83	23.9	21.1	35.4
Neighbouring buildings:				
Roofs in a park scenario	-	1.86	2.09	2.55
Roofs in a city scenario	-	4.36	5.82	4.37
Walls and windows in a park scenario	1.77	3.47	4.12	5.95
Walls and windows in a city scenario	2.06	4.25	4.72	5.62
Trees:				
Park scenario	1.14	1.71	2.06	1.88

The numbers show that the kerma factor is larger, apart from nine cases for the glass building than for the multistorey house block. Two extreme cases were determined with a ratio of 271 for the roof to second floor factor for a primary gamma energy of 0.662 MeV and with a ratio of 383 for the roof to ground floor factor for a

Table 16. Ratios of the kerma factor for the glass building divided by the respective factor for a multistorey house block (Meckbach et al. 1988). The figures are given according to source and detection area for a primary gamma energy of 3.0 MeV.

	Basement	Ground floor	Second floor	Forth floor
On the building:				
Roof	-	383	27.7	2.26
Walls and windows	16.5	2.37	2.45	2.24
Ground:				
Park scenario (street and park)	2.03	6.13	4.74	5.06
City scenario (street)	1.14	11.2	9.47	16.3
Neighbouring buildings:				
Roofs in a park scenario	0.223	0.250	0.319	0.649
Roofs in a city scenario	0.412	0.838	1.27	1.64
Walls and windows in a park scenario	1.08	1.93	2.27	2.02
Walls and windows in a city scenario	1.39	2.98	3.19	3.21
Trees:				
Park scenario	1.93	1.21	0.635	0.665

primary gamma energy of 3.0 MeV. The other ratios vary between 0.22 and 35.4 with an averaged ratio and standard error of the mean of 6.11 ± 0.73 (excluding the two extreme values).

Looking into the details the average ratio over each primary gamma energy decreases with increasing primary energy excluding the two extreme values as the averaged values are 7.72 ± 1.34 for a primary gamma energy of 0.3 MeV, 6.76 ± 1.36 for a primary gamma energy of 0.662 MeV and 4.05 ± 0.99 for a primary gamma energy of 3.0 MeV. Looking at the source areas of course the roof of the building has the highest averaged ratio because of the two extreme values with 116 ± 77 (without them it is still 10.5 ± 5.1). This source area in term of the averaged ratio is followed by the ground in the city scenario with 16.7 ± 3.2, the ground in the park scenario with 7.32 ± 0.78, the walls and windows of the building with 6.54 ± 1.54, the roofs of neighbouring buildings in the city scenario with 5.95 ± 2.18, the walls and windows of neighbouring buildings in the city scenario with 3.75 ± 0.47, the walls and windows of neighbouring buildings in the park scenario with 3.26 ± 0.48, the roofs of neighbouring buildings in the park scenario with 1.67 ± 0.38 and at last the trees in the park scenario with 1.49 ± 2.18. The averaging of the ratio over the detection areas excluding the two extreme values shows less variety with the values for ground floor (6.60 ± 1.49), second floor (6.70 ± 1.38) and fourth floor (6.65 ± 1.56) being similar. Only the basement shew a lower averaged ratio of 4.04 ± 1.12.

Apart from the building material, the deviations of the two building models are caused e.g. by different building sizes. Furthermore, the glass building had an atrium instead of a courtyard inside multistorey house block and the multistorey house block had light-shafts to the basement apart from the glass building. Moreover, the calculations were performed with different code, but the influence is further described in a paper that is still to be published (Hinrichsen & Andersson 2018). Finally, those ratios

underpin the importance of the determined factors for decision support systems as the kerma factors for the multistorey house block were calculated for only one building height.

4. Conclusions

The knowledgebase for external dose estimations in inhabited areas was improved by determining kerma conversion factors for a modern glass building that can be found in a similar way in many modern cities now. Therefore, those factors support the progress of decision making in modern cities regarding managing the long term consequences of an airborne release of radionuclides as e.g. a nuclear power plant accident. The description as formulas allows the further application of the glass building model regardless of the height of the building and detection area. Furthermore, the importance of this building model was shown by comparing its results for kerma factors with those calculated by Meckbach et al. (1988) for a multistorey house block. The results of this comparison show the importance of taking into account adequate representations of construction geometries and materials when estimating kerma. The kerma conversion factors are given in a format that can in practice readily be implemented in the European decision support systems for management of the radiological consequences of airborne urban contamination.

References

Chadwick, M., Obložinský, P., Herman, M., Greene, N., McKnight, R., Smith, D., Young, P., MacFarlane, R., Hale, G., Frankle, S., Kahler, A., Kawano, T., Little, R., Madland, D., Moller, P., Mosteller, R., Page, P., Talou, P., Trellue, H., White, M., Wilson, W., Arcilla, R., Dunford, C., Mughabghab, S., Pritychenko, B., Rochman, D., Sonzogni, A., Lubitz, C., Trumbull, T., Weinman, J., Brown, D., Cullen, D., Heinrichs, D., McNabb, D., Derrien, H., Dunn, M., Larson, N., Leal, L., Carlson, A., Block, R., Briggs, J., Cheng, E., Huria, H., Zerkle, M., Kozier, K., Courcelle, A., Pronyaev, V. & van der Marck, S. (2006), 'Endf/b-vii.0: Next generation evaluated nuclear data library for nuclear science and technology', *Nuclear Data Sheets* **107**(12), 2931 – 3060. Evaluated Nuclear Data File ENDF/B-VII.0.

Dickson, E. D. & Hamby, D. M. (2014), 'Cloud immersion building shielding factors for us residential structures', *Journal of Radiological Protection* **34**(4), 853–871.

Dickson, E. D. & Hamby, D. M. (2016), 'Building protection- and building shielding-factors for environmental exposure to radionuclides and monoenergetic photon emissions', *Journal of Radiological Protection* **36**(3), 579–615.

Dickson, E. D., Hamby, D. M. & Eckerman, K. F. (2017), 'Contaminant deposition building shielding factors for us residential structures (vol 35, pg 317, 2015)', *Journal of Radiological Protection* **37**(4), 961–962.

Furuta, T. & Takahashi, F. (2015), 'Study of radiation dose reduction of buildings of different sizes and materials', *Journal of Nuclear Science and Technology* **52**(6), 897–904.

Golikov, V., Balonov, M. & Jacob, P. (2002), 'External exposure of the population living in areas of russia contaminated due to the chernobyl accident', *Radiation and Environmental Biophysics* **41**(3), 185–193.

Goorley, T., James, M., Booth, T., Brown, F., Bull, J., Cox, L. J., Durkee, J., Elson, J., Fensin, M., Forster, R. A., Hendricks, J., Hughes, H. G., Johns, R., Kiedrowski, B., Martz, R., Mashnik, S., McKinney, G., Pelowitz, D., Prael, R., Sweezy, J., Waters, L., Wilcox, T. & Zukaitis, T. (2012), 'Initial mcnp6 release overview', *Nuclear Technology* **180**(3), 298–315.

Hinrichsen, Y. & Andersson, K. G. (2018), 'European decision support modelling of longterm external doses received in inhabited areas contaminated by a nuclear power plant accident - 1: initial relative dose rate contributions from different contaminated outdoor surfaces (working title)', *to be published* .

Hinrichsen, Y., Finck, R., Östlund, K., Rääf, C. & Andersson, K. G. (2018), 'Comparison of experimental and calculated shielding factors for modular buildings in a radioactive fallout scenario', *Journal of Environmental Radioactivity* **189**, 146 – 155.

ICRP (2010), 'Conversion coefficients for radiological protection quantities for external radiation exposures', *Annals of the ICRP* **40**(2), 1 – 257. ICRP Publication 116.

Imanaka, T., Hayashi, G. & Endo, S. (2015), 'Comparison of the accident process, radioactivity release and ground contamination between chernobyl and fukushima-1', *Journal of Radiation Research* **56**(Suppl. 1, Sp. Iss. SI), I56–I61.

Jacob, P. & Meckbach, R. (1987), 'Shielding factors and external dose evaluation', *Radiation Protection Dosimetry* **21**(1-3), 79–85.

Jensen, P. H. & Thykier-Nielsen, S. (1989), 'Shielding factor calculation for plume radiation', *Radiation Protection Programme. Progress Report 1988* pp. 1561–1565.

Kis, Z., Eged, K., Meckbach, R. & Müller, H. (2003), 'Guidelines for planning interventions against external exposure in industrial area after a nuclear accident. pt. 2. calculation of doses using monte carlo method. institut für strahlenschutz, gsf - forschungszentrum für umwelt und gesundheit gmbh'.

Kis, Z., Eged, K., Voigt, G., Meckbach, R. & Müller, H. (2004), 'Modeling of an industrial environment: External dose calculations based on monte carlo simulations of photon transport', *Health Physics* **86**(2), 161–173.

Lichtenstein, H., Cohen, M., Steinberg, H., Troubetzkoy, E. & Beer, M. (1979), 'The sam-ce monte carlo system for radiation transport and criticality calculations in complex configurations (revision 7.0). mathematical application group, inc.'.

McConn Jr, R., Gesh, C., Pagh, R., Rucker, R. & Williams III, R. (2011), 'Radiation portal monitor project - compendium of material composition data for radiation transport modeling. pacific northwest national laboratory. piet-43741-tm-963, pnnl-15870 rev. 1'.

Meckbach, R. & Jacob, P. (1988), 'Gamma exposures due to radionuclides deposited in urban environments. part ii: Location factors for different deposition patterns', *Radiation Protection Dosimetry* **25**(3), 181–190.

Meckbach, R., Jacob, P. & Paretzke, H. (1988), 'Gamma exposures due to radionuclides deposited in urban environments. part i: Kerma rates from contaminated urban surfaces', *Radiation Protection Dosimetry* **25**(3), 167–179.

Meckbach, R., Jacob, P. & Paretzke, H. G. (1987), 'Shielding of gamma radiation by typical european houses', *Nuclear Instruments and Methods in Physics Research Section A: Accelerators, Spectrometers, Detectors and Associated Equipment* **255**(1), 160 – 164.

Roed, J. (1988), 'The distribution on trees of dry deposited material from the chernobyl accident', *Joint Cec/oecd(nea) Workshop on Recent Advances in Reactor Accident Consequence Assessment. Proceedings of the Second Part of the Workshop (eur 11408 En)* pp. 165–78, 165–178.

Salinas, I. C. P., Conti, C. C., Rochedo, E. R. R. & Lopes, R. T. (2006), 'Gamma shielding factor for typical houses in brazil', *Radiation Protection Dosimetry* **121**(4), 420–424.

Spencer, L. V., Chilton, A. B. & Eisenhauer, C. M. (1980), 'Structure shielding against fallout gamma rays from nuclear detonations', *National Bureau of Standards, Special Publication* .

Paper IV

Hinrichsen, Y., Andersson, K. G., European decision support modelling of long-term external doses received in inhabited areas contaminated by a nuclear power plant accident - 1: initial relative dose rate contributions from different contaminated outdoor surfaces. Submitted to Journal of Environmental Radioactivity.

European decision support modelling of long-term external doses received in inhabited areas contaminated by a nuclear power plant accident – 1: initial relative dose rate contributions from different contaminated outdoor surfaces

Yvonne Hinrichsen and Kasper G. Andersson*

Technical University of Denmark, Center for Nuclear Technologies, DK-4000 Roskilde, Denmark

*Corresponding author: kgan@dtu.dk

Abstract: Dose prediction tools making use of existing knowledge on the environmental behaviour of radiocontaminants are essential for justification and optimisation of recovery countermeasure strategies for contaminated inhabited areas. In this context, one necessary requirement is to estimate the relative initial contaminant distribution on different types of surfaces in the environment and the resultant initial dose rates to humans staying in the environment. This paper reports on the latest parametric refinements in this context for use in the ERMIN inhabited area dose model, which is an integral part of the European emergency management decision support systems ARGOS and RODOS.

1. Introduction

Prior to 1986, it was in general thought that any significant airborne environmental contamination resulting from nuclear power plant accidents would be restricted to rural areas very near the power plant. However, the Chernobyl accident demonstrated that inhabited environments and even cities at considerable distances from the release point could become strongly affected. On the basis of the measurements and learning points after the Chernobyl accident, relatively simple calculation models were soon created to enable rough estimation of the external doses to urban and suburban populations (e.g., Crick & Brown, 1989; Andersson, 1989). Subsequently these models were integrated with the much more comprehensive map based decision support systems ARGOS (2018) and RODOS (2018), which are today support emergency arrangements in practically all European countries as well as in, e.g., Canada, Brazil and Australia. Over the following decades, the common model for external dose in inhabited areas in the ARGOS and RODOS systems, known as the ERMIN (EuRopean Model for INhabited areas) model co-developed and coded at Public Health England (Charnock, 2018; Andersson et al., 2009; Charnock et al., 2009; Andersson et al., 2008), has been developed and considerably refined, for example through extended studies of long-term natural weathering parameter components of contaminants on different types of surface, and conceptual improvements (including representation of weather conditions and contaminant characteristics). Recently, the ERMIN databases were revised and updated again in the European projects PREPARE and CONFIDENCE to accommodate the newest available information, and expand the scope so that contaminant particles of a range of relevant characteristics can now be modelled (previously only two types could be modelled; Jones et al., 2007), and also rough estimates of uncertainties of relevant parameters in ERMIN have been addressed. This paper reports on the latest developments in relation to identification of the relative contamination levels on different outdoor surfaces in the inhabited environment and the air kerma rates that the presence of these contaminants would imply in different positions in an inhabited environment. In part 2 of the paper, the post-deposition mobility of contaminants on/in these surfaces in the inhabited

environment and the importance of all the described methods and parameters for external dose prognoses are dealt with.

2. Materials and methods

Model estimation of deposition of contaminants may be useful for several purposes in nuclear emergency management decision support, including rough early phase external dose prognoses when local measurements of deposits on different representative surfaces have not yet been made, drills and competence building training sessions to assess possible consequences of different contamination scenarios and possibly to dimension an operational preparedness accordingly (e.g., assess recovery capability and capacity).

The deposition is greatly dependent on the physicochemical properties of the contaminants and the types and orientations of the surfaces in the inhabited area to which the deposition occurs (Andersson, 2009). It should thus first be considered which physicochemical forms the various likely contaminants from a major NPP (nuclear power plant) accident could be expected to have. A 'consensus' list of contaminants considered potentially important by Slovakia, France, Germany, Finland, Czech Rep. and USA for evaluation of radiological consequences in case of severe NPP accidents comprises (apart from noble gases) radionuclides of the following elements: Am, Ba, Ce, Cs, Cm, I, La, Mo, Nb, Np, Pu, Rb, Ru, Sb, Sr, Te and Zr (Bujan, 2014). The physicochemical forms of these in future accidental releases will depend on a complex of processes and conditions during the release, and are difficult to predict. However, the experience from history's two large nuclear power plant accidents, the Fukushima and the Chernobyl accident, provide very useful information on what might be expected in some different types of scenarios, and for instance which sizes, materials and thus aerodynamic behaviour the produced aerosols might be expected to have under different conditions. A literature search has been made in this study on the characteristics of radiocontaminants that might be released to the environment in a nuclear power plant accident, and on which relative initial contamination levels on different surfaces in the inhabited environment would be likely to occur for contaminants with different characteristics.

By multiplication of initial relative contamination levels with dose rate conversion factors (dose rate in a given environmental location per photon emitted with a given energy per unit area of each contaminated surface), the initial relative dose rate contributions to persons staying in given types of inhabited areas from different contaminated surfaces in the area can be estimated. Apart from drills and training purposes, detailed dose rate modelling is an essential requirement in estimating any future doses to people living in a contaminated area, as these can obviously not be measured (e.g., residual doses when considering different recovery intervention strategies on different contaminated surfaces; ICRP, 2007).

After the contamination levels on different surfaces in an inhabited area from the passage of the contaminated plume have been estimated, an important next step in determining the associated long-term external doses to affected populations is to relate the contamination levels to dose rates to people present in different locations in different representative inhabited environments. Depending on the types and energies of the radiation, and the positions of people in the environment over time in relation to contaminated and shielding surfaces, dose rates per unit surface contamination on a given surface can vary

very widely. Due to the geometrical complexity of inhabited environments with potentially highly shielding structures and, e.g., low-shielding window areas that can vary considerably in number, location and size, simple point kernel models are inadequate in predicting resultant dose rates (Jensen and Thykier-Nielsen, 1989). Instead, the Monte Carlo method can be used to randomly model the propagation in a given environment of a large number of individual photons and probabilistically track their paths as they collide with atoms and cause secondary radiation in the media they pass through. Resultant dose rates can then be computed in various points in the environment, which might be occupied by humans. The most widely used, extensively validated and suitable Monte Carlo code available for calculation of complex gamma fields is probably the MCNP developed at Los Alamos National Laboratory in the USA (Goorley et al., 2012; Lin et al., 2011), and this was selected for the studies reported in this paper.

3. Results

3.1. Relative deposition of contaminants on different surfaces in inhabited areas

To shed light on possible physicochemical forms of different contaminants potentially released in a nuclear power plant accident, the experience from the Chernobyl and Fukushima accidents was first assessed.

The radionuclide composition of released contaminants will depend on the source, while contaminant characteristics such as particle/gas release fractions, particle size distribution, solubility and oxidation states will also depend on the release processes, in particular on the temperature, pressure and the presence of air/oxygen (Lind, 2006; Lind et al., 2009; Salbu, 2001).

One of the most volatile contaminants (except noble gases) is iodine, which may be released in its elemental gas form (which has a very high deposition velocity to surfaces), in organic gas forms (where the deposition velocity is comparatively insignificant and thus in practice unimportant), and as condensed vapour on ambient aerosols, typically resulting in an AMAD (activity median aerodynamic diameter) in the range of 0.5-1 μm, which would have an intermediate deposition velocity (Andersson, 2009). As expected, comparatively very high release fractions of iodine were reported in connection with both the Chernobyl (0.2; IAEA, 1991) and Fukushima (0.0002; Le Petit et al., 2014) accidents. Iodine aerosol spectra obtained at different distances after the Chernobyl accident show a perfect Gaussian distribution with no signs of bimodality (e.g., Reineking et al., 1987; Jost et al., 1986), with an AMAD of about 0.5 μm, which is slightly smaller than that of the corresponding Cs aerosol. This iodine aerosol size distribution compares well with that registered after the Fukushima accident (Kaneyasu et al., 2012). However in these measurements the size distribution is a complete match with that for caesium, indicating that insignificant quantities of larger (fuel fragment) particles containing traces of caesium were at the times of measurement released at Fukushima. This suggests that the aerosol iodine can essentially be assumed to be purely condensed mode (on ambient particles). This is in-line with the high solubility and initial post-deposition mobility recorded for all the deposited iodine from Chernobyl at different distances (see, e.g., Roed, 1990).

At the other end of the volatility spectrum, in the Chernobyl accident, contaminants of certain elements were only released to the atmosphere in the form of comparatively large low solubility fuel particles, indicating that these would in general be expected to be highly refractory (undepleted from the fuel). These elements comprised ^{95}Zr, ^{95}Nb, ^{140}Ba, ^{140}La, $^{141/144}$Ce, $^{237/239}$Np, $^{238\text{-}242}$Pu, $^{241/243}$Am and $^{242/244}$Cm

(Bobovnikova et al., 1990, Loschilov et al., 1992, Kuriny et al., 1993, Kashparov et al., 2003; Salbu et al., 1994). They were not reported after the Fukushima accident where the explosions were less powerful but it cannot be ruled out that future accident scenarios might lead to releases of fuel particles. Apart from the fuel particles with sizes allowing them to follow air streams, part of the released fuel from the Chernobyl accident was in the form of either very large fuel fragments spread ballistically by the power of the release process, or very large conglomerates of nuclear fuel fused with melted zirconium (Kashparov et al., 2003). This part of the contamination was mainly in a form with a size range from several tens to more than a thousand microns (Kashparov et al., 2003), and mostly deposited within the nearest 2 km (Kashparov et al., 2003) - a zone where it makes absolutely no sense to attempt to model the contaminant distribution through atmospheric dispersion modelling. These huge particles/fragments, although probably locally dominant in some areas over very small distances, are estimated to contain only a small fraction of the total contamination (Kashparov et al., 1999). It can thus be assumed that nearly all atmospherically dispersed particles carrying Zr, Nb, Ba, La, Ce, Np, Pu, Am and Cm are aerosol-sized fuel particles. Measurements made after the Chernobyl accident showed that the smallest of these particles (which reached great distances) had a size of about 4 µm (Reineking et al., 1987; Rulik et al., 1989, Mala et al., 2013). Kashparov et al. (1996, 1999) reported of a fuel aerosol particle median diameter of some 5-6 µm corresponding to a crystallite size of the fuel. This actually seems consistent with results of smaller explosive tests (although clearly much less powerful) interacting on a matrix of uranium dioxide (Harper et al., 2007), where the smallest particles were found to be some 4 µm, but the greatest part of the aerosolised mass was in the ca. 5-20 µm range. In addition to pure fuel (uranium oxides) particles, also fuel mixes with construction materials and fire extinguishing materials have been reported in the near zones after the Chernobyl accident, which could have a different environmental mobility (Dobrovolsky & Lyalko, 1995; Lind, 2006).

Quite large (and comparable) fractions of Cs, Te and Rb (and to a somewhat lesser extent Sb and Mo) were released in the Fukushima accident (Le Petit et al., 2014), and these should, based on Chernobyl data (e.g., Bobovnikova et al., 1990, Loschilov et al., 1992, Kuriny et al., 1993) be expected to a considerable extent (probably somewhat less for Sb and Mo) to be volatilised from the fuel, forming submicroneous condensation particles. In the Chernobyl case with powerful explosions, investigations by Kuriny et al. (1993) show that even at distances up to about 50-60 km in some directions from the Chernobyl NPP, most of the deposited caesium was in the form of fuel particles. This agrees with results of experimental investigations of the effect of decontamination operations (water hosing on impermeable surfaces) carried out in Pripyat and hundreds of km away from the Chernobyl NPP, where the contamination was much easier removed in the nearest areas where it was associated with large low-solubility fuel particles (Andersson, 2009). The data of Salbu et al. (1994) show that the relationship between ^{90}Sr and ^{137}Cs in fuel particle deposition dominated areas was roughly 10 times higher than that in condensation particle deposition dominated areas. This can be taken as an indication that the fuel particles may have been depleted about 10 times more with respect to Cs than with respect to Sr. Some association with fuel particles could explain the slightly bimodal ^{137}Cs aerosol distribution measured by Reineking et al. (1987) as far away as Göttingen in central Germany after the Chernobyl accident, clearly showing the presence of some supermicron particles, which would be expected to have low solubility (Andersson, 2009). Again, the depletion fraction would be expected to vary according to the exact accident scenario conditions. The caesium aerosol measured after the Fukushima accident was generally submicron and characteristic of

condensation mode (Kaneyasu et al., 2012), even though surprising processes some days after the start of the Fukushima accident also seem to have resulted in creation of some homogeneously caesium-containing spherical low solubility particles in the 2 µm range (Adachi et al., 2013). In connection with the Chernobyl accident, single element particles (e.g., ruthenium, caesium) were recorded more than a thousand km from Chernobyl (Salbu, 1988), indicating the complexity of processes during the release.

As for strontium, both fuel particle and small condensation aerosol fallout has been reported from the Chernobyl accident (Kashparov et al., 2003; Salbu et al., 1994). In the Chernobyl 30 km zone Konoplev et al. (1993) and Askbrant et al. (1996) reported that 80-90 % of the strontium was associated with fuel particles. Even more than a hundred km away from the Chernobyl NPP, fuel particles constituted a significant part of the strontium contamination (Kuriny et al., 1992). The 'duality' of the fuel particles and condensation aerosols carrying strontium from the Chernobyl accident can be illustrated through the results of modified 'Tessier type' sequential extractions (see Tessier, 1979) carried out on soils contaminated with Chernobyl Sr at various distances from the Chernobyl NPP (Salbu et al., 1994). In the nearest investigated areas (at 50 km distance), by far the greatest part of the strontium in the soil was in strongly bound forms that could only be extracted with hydrogen peroxide or nitric acid, whereas in areas at greater distances (170-450 km), by far the majority of the strontium was in much more easily soluble forms. Parallel tests with stable Sr were employed to rule out effects of the different specific soil types. It should be noted that since ^{89}Sr, ^{90}Sr and ^{90}Y cannot be determined in straightforward gamma spectrometry, but usually require chemical separation of strontium from other radionuclides in the sample, prior to radiometric analysis, they are 'inconvenient' to study for instance in aerosol samples, where they have to a large extent been ignored both after the Chernobyl and the Fukushima accident (Steinhauser, 2014). However, even in the Fukushima case ^{90}Sr contamination has been measured in the vicinity of the Fukushima NPP (Steinhauser et al., 2014) at reported levels of about 1 kBq/kg soil (note: as this figure was published without indications of the depth/dimensions of the soil sample taken, it only qualitatively indicates the presence of strontium).

Ruthenium is special in that it has a very high elemental boiling point (2700°C), which would in practically any conceivable incident scenario prevent it from being volatilised and depleted from fuel material. However, if oxygen is present, it can be oxidised to its tetraoxide form, which is highly volatile (Kashparov et al., 1996; Hunt et al., 1994). From the Chernobyl accident, ruthenium radionuclides were in great amounts dispersed as condensation particles. This would be expected to have occurred in connection with the fire that followed the explosion. In fact, more ruthenium than caesium was released in connection with the Chernobyl accident (IAEA, 1991), and this had a considerable impact on doses over the first few years (^{106}Ru has a half-life of very close to 1 year). The explanation offered by Le Petit et al. (2014) as to why only small amounts of ruthenium were measured in the environment after the Fukushima accident was that it seems that the fuel remained under water in the spent fuel pools (thus no air ingress). Instead the low volatility of ruthenium is reported to be consistent with overheating and fuel melting of reactor cores. Oxidation could in reality occur in all accident scenarios currently represented in RODOS (Bujan, 2014). However, since this is a critical parameter, and oxidation obviously may not always be expected, it would be useful to run the DSS with different assumptions in this respect, both for training purposes and for early prognostic runs, when actual scenario specific processes have not yet been disclosed through measurements. It is well known that ruthenium in irradiated UO_2 fuel appears in small metallic alloy precipitations together with other fission product elements such as molybdenum, technetium, rhodium,

and palladium (Ver et al., 2007). Such precipitations are in metallographic images seen as generally spherical white inclusions.

It is difficult to predict the physicochemical forms that would arise in any future nuclear power plant accidents, as these would be largely dependent on the exact inventory and accident processes at the NPP. Although for example the international Phebus Fission Product Programme (Gonfiotti and Paci, 2018) shed some new light on possible releases in different NPP accident processes, the results reflect specific conditions and do not provide the range of details needed in operational nuclear preparedness for a specific NPP construction. However, perhaps in the future, results of such investigations could be used together with for example the Rapid Source Term Prediction (RASTEP) system (Knochenhauer, 2013), focusing on estimating the state of the specific NPP at the time of the accident using a Bayesian belief network to provide a probabilistic overview of possible accident states. By estimating the processes at the NPP, also the physicochemical forms of the various potentially released contaminants could be estimated. In a recent publication Havskov Sørensen et al. (2018) comment on the requirements to do this.

3.1.1. Dry deposition

It is important to note that the background data for the derived deposition parameter values given in Table 1 may possibly not reflect the full range of possible parametric variation, as they are generally taken from a limited number of actual sets of environmental observations of deposition velocity of elemental iodine and relevant aerosols with different AMADs on different surfaces in connection with the Chernobyl accident, the Fukushima accident and various experimentation (Atkins, 1967; Belot, 1977; Bonka, 1989; Bonka & Horn, 1980; Chamberlain, 1953; Chamberlain, 1967; Clough, 1975; Collins et al., 2004; Freer-Smith et al., 2003; Garland, 2001; Horn et al., 1988; Jonas, 1984; Jonas & Vogt, 1982; Kashparov et al., 1999; Lai & Nazaroff, 2005; Little, 1977; McMahon & Denison, 1979; Mück et al., 2002; Nicholson, 1989; Nicholson & Watterson, 1992; Petroff, 2005; Roed, 1985; Roed, 1987; Roed, 1988; Roed, 1990; Schwartz, 1986; Sehmel, 1973; Tschiersch et al., 2009; Vargas et al., 2016; Watterson & Nicholson, 1996). However, these relations between deposition on different surfaces *in the same scenario* are obviously associated with comparatively much less variation than would relations between deposition velocities in general to these surfaces.

For example, deposition velocity depends on atmospheric stability. It has been demonstrated that under moderately stable atmospheric conditions (e.g., night time with clear sky), the friction velocity will only be about half of its value under neutral conditions (Jensen, 1981). This in turn means that the eddy diffusion part of the deposition velocity will be reduced to about a quarter (IAEA, 1994).

Also wind velocity can greatly influence deposition velocity. It has been demonstrated (Ahmed, 1979) that between wind velocities of 2 and 14 m s^{-1}, the deposition velocity of naturally occurring radioactive aerosols increases by about a factor of 3, both to smooth (e.g., filter paper) and rough (grass) surfaces. It has also been shown (Freer-Smith et al., 2003; Slinn, 1982) that deposition velocities of ca. 0.8 µm particles to trees can increase by a factor of 3-4 between wind velocities of 3-9 m s^{-1}. Even at moderate wind velocities (< 5 m s^{-1}), the deposition of particles on walls facing the wind direction can be several times higher than that on leeside walls, for particles of sizes between about 10^{-2} and 20 µm (Freer-Smith et al., 2003). As the particle size increases beyond about 20 µm, the influence of wind speed on deposition

increases markedly, due to the significance of the inertial impaction mechanism (Ahmadi & Li, 1999). However, such large particles will in any case only remain airborne for short time, due to their large mass, and radionuclides associated with these would thus only contaminate rather small areas, depending on, e.g., the initial plume rise height (Hage, 1961; Ivanov, 2009).

Finally, surface roughness is an important parameter. An indication of this influence can be seen from measurements made in the Roskilde area after the Chernobyl accident. Here deposition velocities to grassed surfaces varied rather widely (Roed, 1990) between 1.8 and 8.8 m s^{-1}. However, if the length of the grass is taken into account (by dividing with the grass mass per unit area), the results are consistent within 10 %. It should therefore be noted that grassed areas in inhabited environments must be well-defined with respect to roughness (grass length). Differences of up to about a factor of 2 have been recorded (Lai & Nazaroff, 2005) for deposition velocities of 0.9-9.1 µm particles to vertical sandpaper surfaces, ranging from Sand 60 to Sand 220. As shown in Table 1, dry deposition will vary to roof pavings of different materials having different roughness.

Deposition to coniferous trees and deciduous trees in leaf would according to available literature be similar (Jonas, 1984). However, during the winter period where deciduous trees are leafless, the deposition to these would be very low. According to measurements made after the Chernobyl accident (Roed, 1988), the needles or leaves receive some 98 % of the bulk 0.7 µm aerosol deposition on a tree. However, relatively not quite insignificant deposition velocities of trace particles have been reported to bare trees in forests (Höfken et al., 1981) (ca. 10-30 % of that to the same trees in leaf). This is explained by a higher wind speed in a forest with bare trees, but this effect would not be expected to be relevant for single trees in an inhabited area (Jonas, 1984). Only trees in leaf are thus considered in the table. In the period where they are not in leaf, the deposition to these surfaces may be assumed to be comparatively negligible. Note that in the surface contamination values for trees, shrubs, plants and grass in the tables of this report are given per projected area of ground covered by the vegetation canopy, and then normalised according to the contamination level value on the reference surface.

Unfortunately, no measurements of deposition velocities on surfaces in inhabited areas were reported after the Fukushima accident.

In the ERMIN model deposition on different surfaces in the inhabited environment is dealt with relatively to the deposition to a defined reference surface - in this case a newly shortcut lawn was selected (here a quick measurement the relationship between deposition on the grass and the underlying soil can also give a useful indication of the local extent of dry and wet deposition). In ARGOS and RODOS, the deposition process to the reference surface is dealt with in the applied atmospheric dispersion model tool, and not in ERMIN. ERMIN has been designed on the background of the Chernobyl and Fukushima experience to hold information for elemental iodine gas and for aerosols in four characteristic groups with different size ranges (AMAD less than 2 µm, 2 - 5 µm, 5 - 10 µm and 10 - 20 µm). The initial surface contamination relations within each group are all assumed to be representable by normal distributions. Typically reported values of the dry deposition velocity in units of 10^{-4} m/s to the reference surface are for these contaminant groups respectively of the order of 20, 4, 7, 30 and 130 (see references above), but case-specific factorial dependencies and thus overall uncertainties are large as explained above.

Table 1. Values for deposition to different surfaces relative to that on the grassed reference surface, for situations when dry deposition dominates. The term 'sd' denotes one standard deviation. All distributions are assumed to be normal. Values are given for elemental iodine gas and for particles with AMAD < 2 μm, 2-5 μm, 5-10 μm and 10-20 μm.

Surface	Elemental iodine		AMAD < 2 μm		AMAD 2-5 μm		AMAD 5-10 μm		AMAD 10-20 μm	
	Mean	sd	Mean	sd	Mean	sd	Mean	sd	Mean	sd
Short grass*	1.0	Ref. surf.	1.0	Ref. surf.	1.0	Ref. surf.	1.0	Ref. surf.	1.0	Ref. surf.
Bare soil	0.6	0.4	0.3	0.15	0.3	0.15	0.17	0.10	0.23	0.12
Soil and short grass*	1.0	-	1.0	-	1.0	-	1.0	-	1.0	-
Small plants*	0.8	0.5	1.4	0.7	1.6	0.8	1.0	0.5	1.2	0.7
Trees and shrubs*	0.4	0.25	2.5	1.2	4.3	2.5	1.7	1.2	1.5	1.1
Paved area	0.2	0.1	0.25	0.15	0.75	0.35	0.3	0.15	0.3	0.25
Clay tile roof	1.5	0.3	0.8	0.1	3.0	0.8	1.9	0.5	1.5	0.4
Concrete tile roof	1.8	0.4	1.0	0.2	4.0	1.0	2.2	0.6	1.6	0.4
Fibre cement roof	1.6	0.3	0.9	0.1	3.6	0.9	2.1	0.5	1.6	0.4
Silicon covered fibre cement roof	1.0	0.2	0.7	0.1	2.5	0.6	1.7	0.4	1.4	0.4
Glass roof	0.5	0.1	0.4	0.1	1.4	0.4	1.5	0.4	1.3	0.3
Smooth metal roof	0.7	0.1	0.5	0.1	1.6	0.4	1.6	0.4	1.3	0.3
External walls	0.15	0.1	0.03	0.02	0.07	0.04	0.1	0.07	0.05	0.03

*Values given per area of ground covered by the vegetation.

3.1.2. Wet deposition

Table 2 shows estimates of the relative wet depositions to the different surfaces for each type of contaminant (again, the modelling of deposition to the shortcut grassed reference surface is, in ARGOS and RODOS, included in the atmospheric dispersion estimation tool). Also shown in this table is the fraction of the deposition to each surface which is practically instantaneously carried away, e.g., to sewers, with run-off water. Even during periods of strong rain, deposition to surfaces occurs through a combination of wet and dry deposition. However, unless the rain is extremely light or brief during such a phase or only leads to slight contaminant scavenging from the plume (not assumed for this deposition weather category), wet deposition will clearly be the dominant contamination process. Dry deposition contributions can thus be assumed to be negligible for the deposition weather category covered in this section. The initial run-off of contaminants in rainwater during the wet deposition process may depend on the surface roughness/permeability/porosity and rainfall intensity immediately before as well as during the wet deposition episode (Bonka & Horn, 1980; Karlberg, 1986; Sartor et al., 1974; Shaw et al., 2006). Further, the surface material type has been reported to be able to influence run-off through pH (Göbel et al., 2007).

On roofs compared with the grassed reference surface, the rain intensity incident per unit roof area will be less by cos(v), where v is the roof angle. It is assumed that common roofs have a slope of between 0 and 45 degrees. The initial retention after wet deposition of a range of Chernobyl contaminants (^{134}Cs, ^{137}Cs, ^{103}Ru, ^{106}Ru, ^{140}La and ^{140}Ba) with different physicochemical characteristics was recorded on different types of roof pavements with different slopes in Denmark following the Chernobyl accident (Roed, 1987). Caesium, which is in cationic form retained selectively and strongly in many building materials (Andersson, 2009), seems to be somewhat more efficiently retained on the roof than other contaminants. In general, the initial retention after the deposition process varies greatly with the roof material. For a range of materials

and radionuclides, in the region of one-sixth to half of the contaminants were instantaneously removed with the run-off rain water. The exception from this was silicon-treated very smooth roofs with extremely low open porosity, where the run-off percentage was as high as 70-80 %. The main cause of variation here was by far the roof material and not the roof angle nor the radionuclide. Corresponding measurements made in Germany and the United Kingdom of wet-deposited Chernobyl radiocaesium on clay and concrete roofs showed similar values (Roed & Jacob, 1990; Sandalls & Gaudern, 1986). It should be noted that contaminant run-off in rainwater is likely to be more dominant when the roof pores are already filled by rain than when contaminated rain falls on a dry roof (Roed, 1987). Ritchie (1976) found that run-off from artificial surfaces in an urban area (e.g., roofs) would be virtually 100 % for all rainfall above an initially accumulated 3 mm, and if there has been rain within the previous hour the run-off will occur sooner.

Wet contamination levels on walls would in general be expected to be low, but associated with some variation according to factors such as the wind speed and direction during the contaminating process. In the Gävle area, which was wet-contaminated by the Chernobyl accident, a caesium contamination level on walls of slightly less than 1% relative to the reference surface was recorded in 1988 (Andersson, 1991). Figures reported by Roed & Jacob (1990) for the same location were by mistake somewhat higher (up to 3%), as the contamination estimate for the grassed reference surface originated from a direct measurement, not allowing for contaminant penetration.

Only a couple of weeks after the Chernobyl accident, the initial retention on street pavings of wet deposited contaminants was measured in Sweden (Karlberg, 1986; Karlberg, 1992). It was found that at this point, some 40-70 % of the radiocaesium incident on asphalt and differently textured concrete street pavings had been removed, most likely to a very high extent already during the deposition phase, with the run-off water. Somewhat less had been removed from rough concrete paving slabs. Similar figures were found for the more refractory ^{140}Ba and ^{110m}Ag that were according to Rulik et al. (1989) associated with particles with a size of several microns after Chernobyl, indicating that particle size within the range of interest has little influence on the fraction of contamination lost with run-off water. Also Jacob et al. (1990) reported results of measurements of wet deposition of Chernobyl caesium, on different urban pavings in Germany. After 32 days, 28-32% of the caesium remained on concrete pavings, and 36% in an asphalted parking lot. A measurement after 40 days in an asphalted square showed 32% retention. In a different area, the retention on concrete pavings after 160 days was found to be 33%. By extrapolation from the curves obtained for the different locations, it could be estimated that the initial retention was in the German region of 35-50%.

Experience with non-radioactive pollutants demonstrates that rain often leaves comparatively little contamination on vegetation (Gravenhorst & Höfken, 1982). The deposition before run-off for trees is interpreted as the deposition per unit ground area covered by the tree. Contaminants in the precipitation above the tree canopy will either be intercepted by the tree, lost by throughfall (falling directly through leaf gaps or dripping from leaves, needles, twigs and branches), or lost by stemflow (flow down stems or boles). It has been reported (Alexander & Cresser, 1994) that both for birch trees (Betula pubescens) and pine trees (Pinus sylvestris L.) the throughfall precipitation fraction is some 80% of the incident precipitation. This is an average figure for a two-year study in the English Midlands, in an area with an annual precipitation of 930 mm. The interception was greatest for the pine tree during summer. This is in agreement with findings of other workers of 80-90% throughfall and 2-5% stemflow (Carlyle-Moses, 2004;

Kryshev, 1996; Neal et al., 1993; Pryor & Barthelmie, 2005). However, contaminants do not follow the water fractions evenly. Ronneau et al. (1987) reported that for Belgian spruce contaminated by a 7.4 mm rainfall episode after the Chernobyl accident significantly less ruthenium and lanthanum than caesium was intercepted. The explanation offered was biological absorption, e.g., by caesium exchange with potassium. It is also known that the rate of penetration of cations through the cuticle of vegetation is inversely related to the radius of the ion, and thus strongly favours caesium (Carini & Bengtsson, 2001). Similar figures have been reported by other workers for caesium on spruce, whereas deciduous trees have somewhat lower caesium interception (Schell et al., 1996). Schimmack et al. (1991) have reported a caesium interception fraction of 20% for beech trees. Deciduous trees would in winter conditions be expected to intercept considerably less than indicated by the numbers in Table 2. A rain interception fraction for a leafless pear tree has been reported, which was about half of that of an evergreen oak (Xiao et al., 2000). The same workers stress that interception fractions vary significantly dependent on factors like the structure of the tree and amount of rainfall.

Small plants would in general in the context interception be expected to be well represented by agricultural crops, due to sizes, shapes and textures. It has been reported that interception fractions will depend on the amount of rainfall, and plant type, as well as the stage of plant development (Müller & Pröhl, 1993). It would seem that a likely interception range relevant to urban small plants would be 10-30% for most radionuclides (IAEA, 1994; Schell et al., 1996). This would correspond to assuming a leaf area index value of about 5; retention coefficient of 0.2-0.3 mm, and rainfall of 4-10 mm (Müller & Pröhl, 1993). The leaf area index is the total one-sided leaf canopy area per projected area ground covered by the plant.

For relatively short urban grass, the leaf area index would be of the order of 1-3 (Kammann et al., 2005; Müller & Pröhl, 1993; Rodriguez et al., 1999), and the retention coefficient would be 0.2 for most radionuclides (Müller & Pröhl, 1993). With the same assumptions as for small plants regarding rainfall, this would give the retention/run-off expressed by the values in Table 2 (Müller & Pröhl, 1993).

Table 2. Values for initial deposition to different surfaces relative to that on the grassed reference surface, for situations when wet deposition dominates. The term 'sd' denotes one standard deviation. Also given are the fractions of the contaminants that immediately run off the surface with rain water during the deposition process.

Surface	Elemental iodine		Cationic caesium		Other contaminants		Elemental iodine		Cationic caesium		Other contaminants	
	Rel. deposition		Rel. deposition		Rel. deposition		Runoff fraction		Runoff fraction		Runoff fraction	
	Mean	sd	Mean	sd	Mean	sd	Mean	sd	Mean	sd	Mean	sd
Short grass*	1	-	1	-	1	-	0.9	0.1	0.8	0.1	1	0.2
Bare soil	1	-	1	-	1	-	0	-	0	-	0	-
Soil and short grass*	1	Ref. surf.	1	Ref. surf.	1	Ref. surf.	0	-	0	-	0	-
Small plants*	1	-	1	-	1	-	0.99	0.01	0.7	0.2	0.8	0.2
Trees and shrubs*	1	-	1	-	1	-	0.99	0.01	0.5	0.3	0.8	0.2
Paved area	1	-	1	-	1	-	0.97	0.03	0.55	0.15	0.55	0.15
Clay tile roof	0.8	0.2	0.8	0.2	0.8	0.2	0.99	0.01	0.3	0.04	0.35	0.05
Concrete tile roof	0.8	0.2	0.8	0.2	0.8	0.2	0.99	0.01	0.4	0.05	0.45	0.06
Fibre cement roof	0.8	0.2	0.8	0.2	0.8	0.2	0.99	0.01	0.15	0.02	0.18	0.02
Silicon covered fibre cement roof	0.8	0.2	0.8	0.2	0.8	0.2	0.99	0.01	0.8	0.1	0.9	0.1
Glass roof	0.8	0.2	0.8	0.2	0.8	0.2	0.99	0.01	0.95	0.05	0.95	0.05
Smooth metal roof	0.8	0.2	0.8	0.2	0.8	0.2	0.99	0.01	0.9	0.07	0.9	0.07
External walls	0.01	0.01	0.01	0.01	0.01	0.01	0	-	0	-	0	-

*Values given per area of ground covered by the vegetation.

3.1.3. Equal amounts of wet and dry deposition

ERMIN also operates with a case, where contributions of wet and dry deposition are of approximately the same magnitude. Since precipitation is very effective in washing out contaminants from a plume, this case would be associated with very little rain, and comparatively rather little contamination would be removed with the run-off water during the deposition process. This is for instance clear from investigations in areas in Russia, which received some rain as the contaminated plume carrying primarily caesium condensation particles passed from Chernobyl. Here, dry deposition rarely contributed more than one or two percent to the total deposition on the reference surface (Andersson et al., 2002). It would thus in most cases only take very little precipitation during the plume passage to make wet deposition the dominant mechanism of contamination. Table 3 shows estimates of the relative depositions to the different surfaces for each type of contaminant assuming that half of the deposition is wet and the other dry (simple averaging with parameters described above). Also the fractions of the deposit removed by run-off water during the contamination process are estimated on the basis of the same literature as used for the wet deposition mode, but assuming very little water. The rainfall rate is here assumed to be well below 1 mm per hour. Experimental and theoretical work has demonstrated that at low precipitation values (< ca. 0.5 mm), the majority of a contamination deposited in solution on a grassed area will remain on the grass (Bonka & Horn, 1980).

Other modes of deposition (e.g., deposition in fog, deposition in snow and deposition to snow covered landscape) still remain to be implemented in the ERMIN model, although some parametric reviews have been conducted.

Table 3. Values for initial deposition of different contaminant groups to different surfaces relative to that on the grassed reference surface, for situations when wet and dry deposition are about equal in magnitude. The term 'sd' denotes one standard deviation. Also given are the fractions of the contaminants that immediately run off the surface with rain water during the deposition process.

Surface	Elemental iodine		AMAD < 2 µm		AMAD 2-5 µm		AMAD 5-10 µm		AMAD 10-20 µm		Elemental iodine		Cationic caesium (<2 µm fraction)		Other contaminants	
	Rel. deposition		Rel. deposition		Rel. deposition		Rel. deposition		Rel. deposition		Runoff fraction		Runoff fraction		Runoff fraction	
	Mean	sd	Mean	sd	Mean	sd	Mean	sd	Mean	sd	Mean	sd	Mean	sd	Mean	sd
Short grass*	1.0	Ref. surf.	1.0	-	1.0	--	1.0	-	1.0	-	0.3	0.1	0.2	0.1	0.2	0.2
Bare soil	0.8	0.2	0.7	0.2	0.7	0.2	0.6	0.2	0.6	0.2	0	-	0	-	0	-
Soil and short grass*	1.0	-	1.0	Ref. surf.	1.0	Ref. surf.	1.0	Ref. surf.	1.0	Ref. surf.	0	-	0	-	0	-
Small plants*	0.9	0.3	1.2	0.4	1.3	0.4	1.0	0.3	1.1	0.4	0.3	0.3	0.1	0.1	0.15	0.15
Trees and shrubs*	0.7	0.2	1.8	1.0	2.5	1.0	1.4	0.7	1.2	0.6	0.3	0.3	0.05	0.05	0.15	0.15
Paved	0.6	0.1	0.7	0.2	0.9	0.2	0.7	0.1	0.7	0.1	0.3	0.3	0.05	0.05	0.05	0.05

area																
Clay tile roof	1.2	0.8	0.8	0.3	1.8	0.5	0.3	0.4	1.2	0.4	0.3	0.2	0.1	0.06	0.1	0.06
Concrete tile roof	1.5	0.9	0.9	0.3	2.4	0.6	1.5	0.4	1.2	0.3	0.3	0.2	0.2	0.1	0.2	0.1
Fibre cement roof	1.3	0.8	0.8	0.3	2.2	0.5	1.5	0.4	1.2	0.3	0.3	0.2	0.03	0.02	0.03	0.02
Silicon treated fibre cement roof	1.4	0.8	0.7	0.2	1.7	0.4	1.3	0.3	1.1	0.2	0.5	0.3	0.4	0.2	0.4	0.2
Glass roof	0.7	0.2	0.5	0.1	0.7	0.2	0.6	0.2	1.0	0.3	0.6	0.5	0.6	0.2	0.6	0.2
Smooth metal roof	0.9	0.2	0.6	0.2	1.2	0.3	1.2	0.3	1.1	0.3	0.6	0.6	055	0.2	0.55	0.2
External walls	0.07	0.05	0.02	0.015	0.04	0.03	0.06	0.04	0.03	0.02	0	0	0	-	0	0

*Values given per area of ground covered by the vegetation.

3.2. Dose rate conversion factors for different locations in inhabited areas

Currently, the ERMIN model largely relies on a series of Monte Carlo computed dose rate conversion factors, which date more than 30 years back (Meckbach et al., 1988). The dose rate conversion factors were calculated for essentially four different types of inhabited environment, ranging from detached suburban houses of light construction to urban centres with 4-storey brick buildings with relatively thick walls. Since then, only a few specialised environments have been added to the ERMIN dose rate conversion factor database, involving industrial buildings and supermarkets (Kis et al., 2004). However, there are still a number of typical European inhabited environments that would not be well described by any of the data currently in the database. For instance, city centres contain many tall buildings of modern construction (e.g., with much glass). Therefore, dose conversion factors for a modern tall urban glass front construction house were calculated and will be published separately (Hinrichsen & Andersson, 2018).

The applicability of the Monte Carlo calculation code MCNP6 (Goorley et al., 2012) in calculating shieldingfactors for inhabited environments was validated through comparison with in situ measurements in the inhabited environment being modelled (Hinrichsen et al., 2018). Generally, a comparison between computed and determined dose rate factors (or shielding factors) for different target points for a contamination of ^{134}Cs and ^{137}Cs on different surfaces gave an average ratio of 1.02 ± 0.05. Among other processes the MCNP6 code accounts for photon creation and loss through bremsstrahlung, p-annihilation, fluorescence, Compton scattering, pair production and photon capture (Goorley et al., 2012). The code allows the definition of complex three-dimensional geometries through a combinatorial geometry technique. The regions in space were constructed by logical combination (union, intersection, difference) of elementary geometric bodies and surfaces.

A new re-calculation has been made with the MCNP6 code of one of the scenarios for which dose rate conversion factors were reported more than 30 years earlier by Meckbach et al. (1988) on the basis of Monte Carlo modelling using the code SAM-CE. The house type and the surfaces and neighbouring

buildings (see Figure 1) were modelled based on the data published by Meckbach et al (1988), who also provided, e.g., highly detailed descriptions of the assumed construction materials with dimensions, material specifications and densities. Atomic composition data of the different materials were added from a compilation by Pacific Northwest National Laboratory (McConn et al., 2011). The MCNP6 calculations were carried out using the cross section data set (ENDF/B-VII.0; Chadwick et al., 2006) that had been validated in comparison with in situ measurements for a different housing environment as described above. The source and detector regions were defined according to the data given by Meckbach et al. (1988). The number and energies of any radiation passing through the detector regions were scored and by using conversion coefficients (ICRP, 2010) transferred to kerma free-in-air at the end of the calculation.

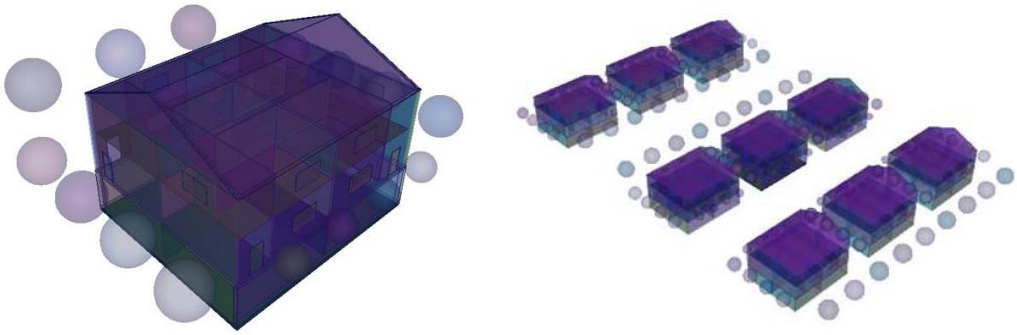

Figure 1. Birds-eye view of the semidetached house without (left) and with (right) neighbouring buildings. The spheres indicate the position of the trees.

The calculated air kerma values per photon emitted per unit source area were compared to those published at GSF (Meckbach et al., 1988). The ratios of the two data were calculated for different source and detector areas and averaged over three different photon energies – 0.3 MeV, 0.662 MeV and 3.0 MeV (Table 4). The new calculations only comprise indoor detection positions, as the publications of Meckbach did not disclose the positions assumed for detection in outdoor locations.

Table 4. Ratios of newly calculated air kerma rate conversion factors divided by those previously reported by Meckbach et al. for the same scenario. Figures are given according to source and detection area.

		Detection area			
		Basement	Ground floor	First floor	Attic
Source	On the house:				
	Windows	1.11	0.41	0.78	0.68
	Walls and doors	0.36	0.41	0.16	0.23

Roof	1.01	0.82	0.92	1.06
Without neighbouring buildings:				
Ground	0.51	0.37	0.27	0.81
With neighbouring buildings:				
Ground	0.42	0.36	0.13	0.13
Neighbouring buildings	0.35	0.22	0.35	0.53
Trees	0.38	0.28	0.06	0.24

Naturally, part of the difference may be attributable to differences in assumptions regarding atomic compositions of materials, which were not specified in the old publication. However, the rather substantial differences between the calculations for particularly walls and doors show that something more fundamental may be at play, possibly due to the old and perhaps incorrect cross-section libraries that were used with the SAM-CE code. The wall material in this case provides better shielding against radiation than does the roof, and comparatively smaller radiation tallies would thus be scored, and longer computing time required for a good result. However, the code provides ten statistical tests that are performed on each defined detector region. Those tests are a valuable tool to ascertain the statistical quality of the respective results.

Also estimates of contributions to the air kerma from radiation from neighbouring areas (where comparatively small radiation tallies would also be expected) are generally not in good agreement. The results of the new calculations of kerma rate conversion factors in the format applied by Meckbach et al. (1988) and used in the ERMIN data libraries are reported in Tables 5-7 for the photon energies 0.3 MeV, 0.662 MeV and 3.0 MeV.

Table 5. Contribution of the various deposition areas to the kerma at several locations inside a semi-detached house for a source energy of 0.3 MeV in pGy per γ mm^{-2}.

Source	Detection area			
	Basement	Ground floor	First floor	Attic
On the house:				
Windows	0.026	2.8	6.2	1.5
Walls and doors	0.008	4.0	1.4	1.2
Roof	0.116	7.3	24.0	84.0
Without neighbouring buildings:				
Ground	0.013	13.6	10.4	29.8
With neighbouring buildings:				
Ground	0.004	8.8	2.6	3.1
Neighbouring buildings	0.001	1.0	1.9	3.9
Trees	0.002	1.4	0.3	0.7

Table 6. Contribution of the various deposition areas to the kerma at several locations inside a semi-detached house for a source energy of 0.662 MeV in pGy per γ mm^{-2}.

	Detection area

Source	Basement	Ground floor	First floor	Attic
On the house:				
Windows	0.159	6.2	20.5	4.0
Walls and doors	0.054	7.9	3.0	3.5
Roof	0.753	17.5	57.5	198.8
Without neighbouring buildings:				
Ground	0.060	31.0	19.4	73.1
With neighbouring buildings:				
Ground	0.020	18.9	5.3	7.7
Neighbouring buildings	0.007	2.3	4.2	12.1
Trees	0.012	3.2	0.5	1.9

Table 7. Contribution of the various deposition areas to the kerma at several locations inside a semi-detached house for a source energy of 3.0 MeV in pGy per ɣ mm^{-2}.

	Detection area			
Source	Basement	Ground floor	First floor	Attic
On the house:				
Windows	2.37	20.9	66.2	14
Walls and doors	1.10	23.1	11.0	19
Roof	9.79	69.3	218.3	722
Without neighbouring buildings:				
Ground	0.95	108.2	46.4	416
With neighbouring buildings:				
Ground	0.71	59.8	16.7	31
Neighbouring buildings	0.15	7.9	14.5	66
Trees	0.31	11.2	1.2	9

As the contamination migrates downward in permeable surfaces (soil), the soil above it will shield against the radiation it emits, but in the calculations behind the kerma factors in the above tables, it is assumed that all contamination is on the very surface. The factors thus need to be modified according to contamination penetration depth in the soil. As shown in part 2 of the paper, ERMIN can dynamically calculate the contamination level at different soil depths. A series of pre-calculated modification factors are used to take into account the influence on kerma rate of contaminant penetration at different depths in the soil (Charnock, 2018; Andersson et al., 2008).

Conclusions

The latest developments for the inhabited areas dose estimation model, ERMIN, which is integrated in the European decision support systems ARGOS and RODOS, are described with respect to two important

parameters: the relative contamination level on different surfaces in the inhabited environment and the conversion factor from contamination level to dose rate.

An overview is given of primary contaminants with different physicochemical forms produced in the Chernobyl and Fukushima accidents. It should be noted that future accidents would be likely to have different features and might lead to different types of contaminants. Nevertheless, the lessons from these two major accidents are of great importance. On the basis of available knowledge, the relative deposition of various groups of possible contaminants on the different surfaces in the inhabited environment is estimated. This is an essential requirement in predicting initial dose rates to inhabitants from different contaminated surfaces in representative housing environments. The tables in this paper show that the relative distribution of contaminants on different surfaces can vary considerably according to the physicochemical form (notably elemental iodine gas fraction, aerosol sizes) of the contaminants. Although rough estimates of the expected variation in these parameters are given, it should be noted that ARGOS and RODOS currently do not have inherent options for full visualisation of the implications of uncertainty/variation of such parameters.

The other requirement in predicting initial dose rates in different environmental positions is reliable dose rate conversion factors for different types of inhabited areas. The MCNP6 Monte Carlo radiation transport estimation system, which was recently experimentally validated for dose rate estimation in inhabited areas, was used to re-calculate the ca. 30 year-old dose rate (kerma rate in air) conversion factor estimates (made with the Monte Carlo code SAM-CE) for one of the standard inhabited environments integrated in the European decision support systems. The new dose rate factors differed significantly from the old ones, particularly when the radiation passed through substantial masses like outer house walls. The number of tallies seems to have been adequate in both cases (judged from code statistics), and thus not the problem. The explanation might possibly lie in the programming (where MCNP is probably the most widely used and validated of all such codes), and could also reflect differences in cross-section data libraries or unreported case-specific assumptions. The new dose rate conversion factors are reported for use in the decision support systems.

The parameter requirements in predicting future time-integrated doses on this background are dealt with in the second part of the paper.

Acknowledgments

The authors would like to thank Dr. Thomas W. Charnock at Public Health England for valuable advice in drafting the paper.

Part of the research leading to these results was carried out in the CONFIDENCE project, which is part of the CONCERT project. This project has received funding from the Euratom research and training programme 2014-2018 under grant agreement No 662287.

An other part of the research leading to these results has received funding from the European Atomic Energy Community Seventh Framework Programme FP7/2012-2013 under grant agreement 323287.

Disclaimer

This publication reflects only the author's view. Responsibility for the information and views expressed therein lies entirely with the authors. The European Commission is not responsible for any use that may be made of the information it contains.

References:

Adachi, K., Kajino, M., Zaizen, Y. & Igarashi, Y., 2013. Emission of spherical caesium-bearing particles from an early stage of the Fukushima accident, Scientific reports, 3:2554, DOI: 10.1038/srep02554.

Ahmadi, G. & Li, A., 1999. Computer simulation of particle transport and deposition near a small isolated building, Journal of Wind Engineering and Industrial Aerodynamics 84, pp. 23-46.

Ahmed, A.-R. A.-A.,1979. Untersuchungen zur Aerosoldeposition an Oberflächen, Doktor Dissertation, Justus-Liebig-Universität Giessen (in German).

Alexander, C. E., Cresser, M. S., 1995. An assessment of the possible impact of expansion of native woodland cover on the chemistry of Scottish freshwaters. Forest Ecology and Management 73, 1-27.

Andersson, K.G., 1989. TACTUS: A Code for Simulation of the Flow of Caesium-137 in Urban Surroundings, in proceedings of the Symposium on Recovery Operations in the Event of a Nuclear Accident or Radiological Emergency, IAEA-SM-316/48, International Atomic Energy Agency, Vienna, Austria, ISBN 92-0-020290-x, pp. 217-228.

Andersson, K.G. 1991. Contamination and decontamination of urban areas, Ph.D. Thesis, Risø National Laboratory.

Andersson, K.G., 2009. Migration of radionuclides on outdoor surfaces, Chapter 5 (pp. 107-146) in K.G. Andersson (editor): Airborne radioactive contamination in inhabited areas, Book Series Radioactivity in the Environment vol. 15 (series editor: M.S. Baxter), Elsevier, ISBN 978-0-08-044989-0, ISSN 1569-4860.

Andersson, K.G., Brown, J., Mortimer, K., Jones, J.A., Charnock, T., Thykier-Nielsen, S., Kaiser, J.C., Proehl, G. & Nielsen, S.P., 2008. New developments to support decision-making in contaminated inhabited areas following incidents involving a release of radioactivity to the environment, J. Environmental Radioactivity, vol. 99, pp. 439-454.

Andersson, K.G., Jones, A. & Charnock, T., 2009. Estimation of doses in inhabited areas, Chapter 6 (pp. 147-185) in K.G. Andersson (editor): Airborne radioactive contamination in inhabited areas, Book Series Radioactivity in the Environment vol. 15 (series editor: M.S. Baxter), Elsevier, ISBN 978-0-08-044989-0, ISSN 1569-4860.

Andersson, K.G., Roed, J. & Fogh, C.L., 2002. Weathering of radiocaesium contamination on urban streets, walls and roofs, J. Environmental Radioactivity vol. 62, no.1, pp. 49-60.

ARGOS, 2018. ARGOS CBRN crisis management support system, PDC-ARGOS, Denmark, http://www.pdc-argos.com/.

Askbrant, S., Melin, J., Sandalls, J., Rauret, G., Vallejo, R., Hinton, T., Cremers, A., Vandecastelle, C., Lewyckyj, N., Ivanov, Y.A., Firsakova, S.K., Arkhipov, N.P. & Alexakhin, R.M., 1996. Mobility of

radionuclides in undisturbed and cultivated soils in Ukraine, Belarus and Russia six years after the Chernobyl fallout, J. Environ. Radioactivity 31(3), pp. 287-312.

Atkins, D.H.F., Chadwick, R.C. & Chamberlain, A.C., 1967. Deposition of radioactive methyl iodide to vegetation, Health Physics 13, pp. 91-92.

Belot, Y., 1977. Etude de la caption des pollutants atmospheriques par les végétaux, Report CEA-R-4786, Département de Protection, Centre d'Etudes Nucléaires de Fontenay-aux-Roses.

Bobovnikova, C.I., Virichenko, E.P., Konoplev, A.V., Siverina, A.A. & Shkuratova, I.G., 1990. Chemical forms of long-term radionuclides and their transformation in the soils of accidental zone of the Chernobyl NPP, Pochvovedenie, 10, 20–29.

Bonka, H., 1989. Measured radioecological parameters after the Chernobyl accident, In: The Radioecology of Natural and Artificial Surfaces (edited by W. Feldt), TUEV Rheinland, Germany.

Bonka, H. & Horn, M., 1980. Review on the dry and wet deposition of aerosol particles, Lehrgebiet Strahlenschutz in der Kerntechnik, Rhein-Westf. Technische Hochschule, Aachen.

Bujan, A., 2014. Personal communication within the European PREPARE project (FP7 Grant Agreement No. 323287). Albert Bujan, VUJE Inc., Nuclear Safety Division, Trnava, Slovak Republic.

Carini, F. & Bengtsson, G., 2001. Post-deposition transport of radionuclides in fruit, J. Environmental Radioactivity 52, pp. 215-236.

Carlyle-Moses, D.E., 2004. Throughfall, stemflow, and canopy loss fluxes in a semi-arid Sierra Madre Oriental matorral communuty, Journal of Arid Environments 58(2), pp. 181-202.

Chadwick, M. B., Oblozinsky, P., Herman, M., Greene, N. M., McKnight, R. D., Smith, D. L., Young, P. G., MacFarlane, R. E., Hale, G. M., Frankle, S. C., Kahler, A. C., Kawano, T., Little, R. C., Madland, D. G., Moller, P., Mosteller, R. D., Page, P. R., Talou, P., Trellue, H., White, M. C., Wilson, W. B., Arcilla, R., Dunford, C. L., Mughabghab, S. F., Pritychenko, B., Rochman, D., Sonzogni, A. A., Lubitz, C. R., Trumbull, T. H., Weinman, J. P., Brown, D. A., Cullen, D. E., Heinrichs, D. P., McNabb, D. P., Derrien, H., Dunn, M. E., Larson, N. M., Leal, L. C., Carlson, A. D., Block, R. C., Briggs, J. B., Cheng, E. T., Huria, H. C., Zerkle, M. L., Kozier, K. S., Courcelle, A., Pronyaev, V., van der Marck, S. C., 2006. ENDF/B-VII.0: Next generation evaluated nuclear data library for nuclear science and technology. Nuclear Data Sheets 107 (12), 2931–3060.

Chamberlain, A.C., 1953. Aspects of travel and deposition of aerosol and vapour clouds, AERE, HP/ R 1261, Harwell Lab., UK.

Chamberlain, A.C., 1967. Transport of lucopodium spores and other small particles to rough surfaces, Proc. R. Soc. A, vol. 296, pp. 45-70.

Charnock, T.W., Jones, J.A., Singer, L.N., Andersson, K.G., Roed, J., Thykier-Nielsen, S., Mikkelsen, T., Astrup, P., Kaiser, J.C., Müller, H., Pröhl, G., Raskob, W., Hoe, S.C., Jacobsen, L.H., Schou Jensen, L. & Gering, F., 2009. Calculating the consequences of recovery, a European model for inhabited areas, Radioprotection vol. 44, No.5, pp. 407-412, ISSN 0033-8451.

Charnock, T.W., 2018. Concise description of ERMIN 2.1. The European inhabited dose and decontamination model, Draft report, Centre for Radiation, Chemical and Environmental Hazards, Public Health England, Chilton, Didcot, Oxfordshire, OX11 0RQ, UK.

Clough, W.S., 1975. The deposition of particles on moss and grass surfaces, Atmospheric Environment 9, pp. 1113-1119.

Collins, C.D., Gravett, A.E. & Bell, J.N.B., 2004. The deposition and translocation of methyl iodide by crops, Health Physics 87(5), pp. 512-516.

Crick, M. J. and Brown, J., 1990. EXPURT – a model for evaluating exposure from radioactive material deposited in the urban environment. Chilton. NRPB-R235.

Dobrovolsky, E., Lyalko, V., 1995. Acidification of soils and radioactive hot particles behavior: A macrokinetic approach. Water Air and Soil Pollution 85, 767-772.

Freer-Smith, P.H., El-Khatib, A.A. and Taylor, G., 2004. Capture of particulate pollution by trees: a comparison of species typical of semi-arid areas (Ficus Nitida and Eucalyptus Globulus) with European and North American species, Water, Air and Soil Pollution 155 (1-4): pp. 173-187.

Garland, J.A., 2001. On the size dependence of particle deposition, Water, Air and Soil Pollution, Focus 1, 323-332.

Gonfiotti, B. & Paci, S., 2018. Stand-alone containment analysis of Phébus FPT tests with ASTEC and MELCOR codes: the FPT-2 test, Helyon 4(3), doi: 10-1016/j.helyon.2018.e00553.

Goorley, T., James, M., Booth, T., Brown, F., Bull, J., Cox, L. J., Durkee, J., Elson, J., Fensin, M., Forster, R. A., Hendricks, J., Hughes, H. G., Johns, R., Kiedrowski, B., Martz, R., Mashnik, S., McKinney, G., Pelowitz, D., Prael, R., Sweezy, J., Waters, L., Wilcox, T., Zukaitis, T., 2012. Initial MCNP6 Release Overview. Nuclear Technology 180, 298–31.

Gravenhorst, G., Höfken, K. D., 1982. Concentration of aerosol constituents above and beneath a beech and a spruce forest canopy, in H. W. Georgii & J. Pankrath: Deposition of Atmospheric Pollutants, D. Reidel, Dordrecht, the Netherlands.

Göbel, P., Dierkes, C. & Coldewey, W.G., 2007. Storm water runoff concentration matrix for urban areas, Journal of Contaminant Hydrology 91, pp. 26-42.

Hage, K. D., 1961. On the dispersion of large particles from a 15-m source in the atmosphere. J. Meteorol. 18, 534–539.

Harper, F.T., Musolino, S.V. & Wente; W.B., 2007. Realistic radiological dispersal device hazard boundaries and ramifications for early consequence management decisions, Health Physics 93(1), 1-16.

Havskov Sørensen, J., Schönfeldt, F., Sigg, R., Pehrsson, J., Lauritzen, B., Bartnicki, J., Klein, H., Hoe, S.C., Lindgren, J., 2018. Added Value of uncertainty Estimates of SOurce term and Meteorology (AVESOME), NKS report 402, NKS, Roskilde, Denmark, ISBN 978-87-7893-490-1, http://www.nks.org/en/nks_reports/view_document.htm?id=111010214694197.

Hinrichsen, Y. & Andersson, K. G., 2018. Gamma conversion factors for modern glass buildings in radioactively contaminated areas, paper submitted for publication in J. Radiological Protection.

Hinrichsen, Y., Finck, R., Östlund, K., Rääf, C. & Andersson, K.G., 2018. Comparison of experimental and calculated shielding factors for modular buildings in a radioactive fallout scenario, J. Environmental Radioactivity 189, pp. 146-155.

Horn, H.G., Maqua, M. & Bonka, H., 1988. Nasse und trockene Ablagerung radioaktiver Stoffe auf die Vegetation und den Erdboden. Schriftenreihe Reaktorsicherheit und Strahlenschutz, BMU 199 –195, ISSN 0724-3316 (in German).

Hunt, C.E.L., Cox, D.S. & Iglesias, F.C., 1994. Fission-product release during accidents – an accident management perspective, Nuclear Engineering and Design 148(2-3), pp. 205-216.

Höfken, K.D., Georgii, H.W. & Gravenhorst, G., 1981. Untersuchung über die Deposition atmosphärischer Spurenstoffe an Buchen- und Fichtenwald, Berichte des Instituts für Meteorologie und Geophysik der Universität Frankfurt/Main, Nr. 46, Frankfurt.

IAEA, 1991. The International Chernobyl Project, Technical Report, Report by an Advisory Committee, IAEA, International Atomic Energy Agency, Vienna, ISBN 92-0-129191-4.

IAEA, 1994. Modelling the deposition of airborne radionuclides into the urban environment, First report of the VAMP Urban Working Group, IAEA TECDOC 760, International Atomic Energy Agency, Vienna.

ICRP, 2007. The 2007 recommendations of the International Commission on Radiological Protection, ICRP Publication 103, Annals of the ICRP, Vienna, Austria, ISSN 0146-6453.

ICRP, 2010. Conversion Coefficients for Radiological Protection Quantities for External Radiation Exposures. ICRP Publication 116, Annals of the ICRP 40(2–5), Vienna, Austria, ISSN 0146-6453.

Ivanov, Y., 2009. Migration of fuel particles of ChNPP fallout and leached radionuclides in soils and soil-to-plant system, In: 'Radioactive Particles in the Environment', Proceedings of the NATO Advanced Research Workshop on Hot Particles Released from Different Nuclear Sources, Yalta, Ukraine, 7-10 May 2007, Springer, Dordrecht, The Netherlands, ISBN 978-90-481-2949-2.

Jacob, P., Meckbach, R. & Müller, H.M., 1987. Reduction of external exposure from deposited Chernobyl activity by run-off, weathering, street cleaning and migration in the soil, Radiation Protection Dosimetry 21(1/3), 51-57.

Jensen, N.O., 1981. A micrometeorlogical perspective on deposition, Health Physics 40(6), pp. 887-891.

Jensen, P. H., Thykier-Nielsen, S., 1989. Shielding factor calculation for plume radiation. Radiation Protection Programme. Progress Report 1988, 1561– 1565.

Jonas, R., 1984. Ablagerung und Bindung von Luftverunreinigungen an Vegetation und anderen atmosphärischen Grenzflächen, Kernforschungsanlage Jülich GmbH, Abteilung Sicherheit und Strahlenschutz, Jül-1949, ISSN 0366-0885.

Jonas, R. & Vogt, K.J., 1982. Untersuchungen zur Ermittlung der Ablagerungsgeschwindigkeit von Aerosolen auf Vegetation und anderen Probenahmeflächen, Kernforschungsanlage Jülich GmbH, Abteilung Sicherheit und Strahlenschutz, Jül-1780, ISSN 0366-0885.

Jost, D.T., Gäggeler, H.W., Baltensperger, U., Zinder, B. & Haller, P., 1986. Chernobyl fallout in size-fractionated aerosol, Nature 324, pp. 22-23.

Kammann, C., Grünhage, L., Gruters, U., Janze, S. & Jäger, H.J., 2005. Response of aboveground grassland biomass and soil moisture to moderate long-term CO2 enrichment, Basic and Applied Ecology 6 (4), pp. 351-365.

Kaneyasu, N., Ohashi, H., Suzuki, F., Okuda, T. & Ikemori, F., 2012. Sulfate aerosol as potential transport medium of radiocesium from the Fukushima nuclear accident, Environmental Science and Technology 46, 5720-5726.

Karlberg, O., 1986. Avrinning och retention av Chernobyl nedfallet i stadsmiljö – Fält-mätningar med gamma spectrometer (in Swedish), Technical Note (6 pages), Studsvik AB, Nyköping, Sweden.

Karlberg, O., 1992. The environmental behaviour of Chernobyl deposition in a high fallout region of Sweden – Measurements and analysis of the urban programme 1986-1989, Studsvik Nuclear, Stockholm, Sweden, Report NS-92/1, ISBN 91-7010-184-1.

Kashparov, V.A., Ivanov, Y.A., Zvarisch, S.I., Protsak, V.P., Khomutinin, Y.V., Kurepin, A.D. & Pazhukin, E.M., 1996. Formation of hot particles during the Chernobyl nuclear power plant accident, Nuclear Technology 114(2), pp. 246-253.

Kashparov, V.A., Lundin, S.M., Zvarych, S.I., Yoschenko, V.I., Levchuk, S.E., Khomutinin, Y.V., Maloshtan, I.M. & Protsak, V.P., 2003. Territory contamination with the radionuclides representing the fuel component of the Chernobyl fallout, Sci. Tot. Environment 317, 105-119.

Kashparov, V.A., Protsak, V.P., Ahamdach, N., Stammose, D., Peres, J.M., Yoschenko, V.I. & Zvarich, S.I., 2000. Dissolution kinetics of particles of irradiated Chernobyl nuclear fuel: influence of pH and oxidation state on the release of radionuclides in the contaminated soil of Chernobyl, J. Nucl. Materials 279, 225-233.

Kis, Z., Eged, K., Voigt, G., Meckbach, R., Müller, H., 2004. Modeling an industrial environment: External dose calculations based on Monte Carlo simulations of photon transport, Health Physics, 86, pp. 161-173.

Knochenhauer, M., Hedtjärn Swaling, V., Di Dedda, F., Hansson, F., Sjökvist, S. & Sunnegård, K., 2013 . Using Bayesian Belief Network (BBN) Modelling for Rapid Source Term Prediction – Final Report. NKS report 293, NKS, Roskilde, Denmark, ISBN 978-87-7893-369-0. http://www.nks.org/en/nks_reports/view_document.htm?id=111010111846390.

Konoplev, A.V., Bulgakov, A.A., Popov, V.E. & Bobovnikova, T.I., 1993. Behaviour of long-lived Chernobyl radionuclides in a soil-water system, Analyst 117, pp. 1041-1047.

Kryshev, I.I., 1996. Dose reconstruction for the areas of Russia affected by 131I contamination, Radiation Protection Dosimetry 64 (1/2), 93-96.

Kuriny, V.D., Ivanov, Yu. A., Kashparov, V.A., Loshchilov, N.A., Protsak, V.P., Yudin, E.B., Zhurba, M.A., Parshakov, A.E., 1993. Particle-associated Chernobyl fallout in the local and intermediate zones, Ann. Nucl. Energy 20(6), 415-420.

Lai, A.C.K. & Nazaroff, W.W., 2005. Supermicron particle deposition from turbulent chamber flow onto smooth and rough vertical surfaces, Atmospheric Environment 39, pp. 4893-4900.

Le Petit, G., Douysset, G., Ducros, G., Gross, P., Achim, P., Monfort, M., Raymond, P., Pontillon, Y., Jutier, C., Blanchard, X., Taffary, T. & Moulin, C., 2014. Analysis of radionuclide releases from the Fukushima Dai-ichi nuclear power plant accident part I, Pure Applied Geophys. 171, 629-644.

Lichtenstein, H., Cohen, M., Steinberg, H., Troubetzkoy, E. & Beer, M., 1979. The SAM-CE Monte Carlo system for radiation transport and criticality calculations in complex configurations (Revision 7.0). A computer code manual (Mathematical Application Group inc., 3 Westchester Plaza, Elmsfort, NY 10523, USA.

Lin, Y.C., Liu, Y.H., Nievaart, S., Chen, Y.F., Wu, S.W., Chou, W.T., Jiang, S.H., 2011. Simulation of the Mg(Ar) ionization chamber currents by different Monte Carlo codes in benchmark gamma fields, Nuclear Instruments & Methods in Physics Research Section A – Accelerators Spectrometers Detectors and Associated Equipment, pp. 559-563.

Lind, O.C., 2006. Characterisation of radioactive particles in the environment using advanced techniques. PhD thesis. Norwegian University of Life Sciences, pp. 1-191.

Lind, O.C., Salbu, B., Skipperud, L., Janssens, K., Jaroszewicz, J., De Nolf, W., 2009. Solid state speciation and potential bioavailability of depleted uranium particles from Kosovo and Kuwait. Journal of Environmental Radioactivity 100, 301-307.

Little, P., 1977. Deposition of 2.75, 5.0 and 8.5 μm particles to plant and soil surfaces, Environ. Pollution 12, 293-305.

Loschilov, N.A., Kashparov, V.A., Yudin, Ye. B., Protsak, V.P., Zhurba, M.A.& Parshakov, A.E., 1991. Experimental assessment of radioactive fallout from the Chernobyl accident, Sicurezza e protezione 25-26, 46-50.

Mala, H., Rulík, P., Becková, V., Mihalík, J. & Slezáková, M., 2013. Particle size distribution of radioactive aerosols after the Fukushima and the Chernobyl accidents, J. Environ. Radioactivity 126, 92-98.

McConn Jr, R. J., Gesh, C. J., Pagh, R. T., Rucker, R. A., Williams III, R.G., 2011. Radiation Portal Monitor Project - Compendium of Material Composition Data for Radiation Transport Modeling. Pacific Northwest National Laboratory, PIET-43741-TM-963; PNNL-15870 Rev. 1.

McMahon, T.A. & Denison, P.J., 1979. Empirical atmospheric deposition parameters – a survey, Atmospheric Environment 13, pp. 571-585.

Meckbach, R., Jacob, P., Paretzke, H. G., 1988. Gamma exposures due to radionuclides deposited in urban environments. Part I: kerma rates from contaminated urban surfaces. Radiation Protection Dosimetry 25, 167-179.

Mück, K., Pröhl, G., Likhtarev, I., Kovgan, L., Meckbach, R. & Golikov, V., 2002. A consistent radionuclide vector after the Chernobyl accident, Heakth Physics 82(2), pp. 141-156.

Müller, H. & Pröhl, G., 1993. ECOSYS-87: A dynamic model for assessing radiological consequences of nuclear accidents, Health Physics 64(3), pp. 232-252.

Neal, C., Robson, A.J., Bhardwaj, C.L., Conway, T., Jeffery, H.A., Neal, M., Ryland, G.P., Smith, C.J. & Walls, J., 1993. Relationships between precipitation, stemflow and throughfall for a lowland beech plantation, black-wood, Hampshire, Southern England – Findings on interception at a forest edge and the effect of storm damage, Journal of Hydrology 146(1-4), pp. 221-233.

Nicholson, K.W., 1988. The dry deposition of small particles – a review of experimental measurementsAtmospheric Environement 22 (12), pp. 2653-2666.Nicholson, K.W. & Watterson, J.D. (1992). Dry deposition of particulate material onto wheat: in Precipitation Scavenging and Atmosphere-Surface Exchange vol. 2 (edited by Schwartz, S.E. & Slinn, W.G.N.), Hemisphere, Washington DC, pp. 673-682.

Petroff, A. 2005. Mechanistic study of aerosol dry deposition on vegetated canopies, Radioprotection, Suppl.1, vol. 40, pp. S443-S450.

Pryor, S.C. & Barthelmie, R.J., 2005. Liquid and chemical fluxes in precipitation, throughfall and stemflow: Observations from a deciduous forest and a red pine plantation in the midwestern USA, Water Air and Soil Pollution 163 (1-4), pp. 203-227.

Reineking, A., Becker, K.H., Porstendörfer, J. & Wicke, A., 1987. Air activity concentrations and particle size distributions of the Chernobyl aerosol, Radiat. Protect. Dosimetry 19, pp. 159-163.

Ritchie, L.T., 1976. Effects of rainstorms and runoff on consequences of nuclear reactor accidents, Sandia Lab. report SAND76-0429.

RODOS, 2018. Realtime Online Decision Support System for nuclear emergency management. RODOS system home page, Karlsruhe Institute of Technology, Germany, https://resy5.iket.kit.edu/RODOS/.

Rodriguez, D., van Oijen, M. & Schapendonk, A.H.M.C., 1999. LINGRA-CC: a sink-source model to simulate the impact of climate change and management on grassland productivity, New Phytol. 144, pp. 359-368.

Roed, J., 1985. Dry deposition of urban surfaces, Risø Report R-515, ISBN 87-550-1069-5.

Roed, J., 1987. Dry deposition in rural and urban areas in Denmark, Rad. Prot. Dos. 21(1/3), pp. 33-36.

Roed, J., 1988. The distribution on trees of dry deposited material from the Chernobyl accident, paper NKA/AKTU-245 (88)2, presented at the Joint CEC/OECD (NEA) Workshop on Recent Advances in Reactor Accident Consequence Assessment, Rome, Italy, 25-30 January 1988.

Roed, J., 1990. Deposition and removal of radioactive substances in an urban area, Final Report of the NKA Project AKTU-245, Nordic Liaison Committee for Atomic Energy at Risø, Denmark, ISBN 87 7303 514 9.

Roed, J. & Jacob, P., 1990. Deposition on urban surfaces and subsequent weathering, Proceedings of a seminar on methods and codes for assessing the off-site consequences of nuclear accidents (vol. 1), Athens, Greece, 1990, EUR13013, pp. 335-356.

Ronneau, C., Cara, J. & Apers, D., 1987. The deposition of radionuclides from Chernobyl to a forest in Belgium, Atmospheric Environment 21 (6), pp. 1467-1468.

Rulik, P., Bucina, I. & Malatova, I., 1989. Aerosol particle size distribution in dependence on the type of radionuclide after the Chernobyl accident and in NPP effluents, The Radioecology of Natural and Artificial Radionuclides, Proc. XV Regional Congress of IRPA, Visby, Sweden, Verlag TÜV Rheinland GmbH, Köln, Germany, ISBN 3-88585-668-9.

Salbu, B., 1988. Radionuclides associated with colloids and particles in rainwaters, Oslo, Norway, in: von Philipsborn, H., Steinhäuser, F. (Eds.), Hot particles from the Chernobyl Fallout. Bergbau - und Industrimuseum, Theuern, pp. 83-84.

Salbu, B., 2001. Actinides associated with particles, in: Kudo, A. (Ed.), Plutonium in the environment. Elsevier, Tokyo, pp. 121-138.

Salbu, B., Krekeling, T., Oughton, D.H., Østby, G, Kashparov, V.A., Brand, T.L.& Day, J.P., 1994. Hot particles in accidental releases from Chernobyl and windscale nuclear installations, Analyst, 199, 125-130.

Sandalls, F.J. & Gaudern, S.L., 1988. Radiocaesium on urban surfaces in West Cumbria five months after Chernobyl, J. Environ. Radioactivity 7, pp. 87-91.Sartor, J.D., Boyd, G.B. & Agardy, F.J. (1974). Water pollution aspects of street surface contaminants, Journal WPCF vol. 46, no. 3, pp. 458-466.

Schell, W.R., Linkov, I., Myttenaere, C. & Morel, B., 1996. A dynamic model for evaluating radionuclide distribution in forests from nuclear accidents, Health Physics 70(3), pp. 318-335.

Schimmack, W., Bunzl, K., Kreutzer, K., Rodenkirchen, E. & Schierl, R., 1991. Einfluss von Fichte (Picea abies L. Karst) und Buchte (Fagus sylvatica L.) auf die Wanderung von radiocaesium im Boden (in German), Forstwiss Forsch. 39, pp. 242-251 (as referenced by Schell et al., 1996).

Schwartz, G., 1986. Deposition and post-deposition radionuclide behaviour in urban environments, Proc. Workshop on methods for assessing off-site radiological consequences of nuclear accidents, CEC, Luxemburg, Report EUR 10397 (EN), pp. 533-558.

Sehmel, G.A. 1973. Particle eddy diffusitivities and deposition velocities for isothermal flow and smooth surfaces, Aerosol Science 4, pp. 125-138.

Shaw, S.B., Walter, M.T. & Steenhuis, T.S., 2006. A physical model of particulate wash-off from rough impervious surfaces, Journal of Hydrology 327, pp. 618-626.

Slinn, W.G.N., 1982. Predictions for particle deposition to vegetative canopies, Atmospheric Environment 16(7), pp. 1785-1794.

Steinhauser, G., 2014. Fukushima's forgotten radionuclides: a review of the understudied radioactive emissions, Environmental Science and Technology 48, 4649-4663.

Tessier, A., Campbell, P.G.C. & Bisson, M,. 1979. Sequential extraction procedure for the speciation of particulate trace metals, Analytical Chemistry 51, pp. 844-851.

Tschiersch, J. & Georgi, B., 1987. Chernobyl fallout size distribution in urban areas, J. Aerosol Sci. 18(6), pp. 689-692.

Vargas, A., Camacho, A., Laubenstein, M., Plastino, W., 2016. Dry deposition velocity of Cs-137 and Cs-134 in Spain after the Fukushima Dai-ichi nuclear power plant accident, Applied Radiation and Isotopes, vol. 109, pp. 441-443.

Ver, N., Matus, L., Kunstar, M., Pintér, A., Osán, J., Hózer, Z. & Tóth, B., 2007. Oxidation and release of ruthenium from white inclusions, European Commission, EUR 22730 EN, ISSN 1018-5593, Luxembourg.

Watterson, J.D. & Nicholson, K.W.,1996. Dry deposition and interception of 4-22 μm diameter particles to a lettuce crop, J. Aerosol Sci. 27(5), pp. 759-767.

Xiao, Q., McPherson, E.G., Ustin, S.L., Grismer, M.E. & Simpson, J.R., 2000. Winter rainfall interception by two mature open-grown trees in Davis, California, Hydrological Processes 14, pp. 763-784.

Paper V

Hinrichsen, Y., Andersson, K. G., European decision support modelling of long-term external doses received in inhabited areas contaminated by a nuclear power plant accident - 2: post deposition contaminant mobility on outdoor surfaces. Submitted to Journal of Environmental Radioactivity.

European decision support modelling of long-term external doses received in inhabited areas contaminated by a nuclear power plant accident – 2: post deposition contaminant mobility on outdoor surfaces

Yvonne Hinrichsen and Kasper G. Andersson*

Technical University of Denmark, Center for Nuclear Technologies, Frederiksborgvej 399, DK-4000 Roskilde, Denmark

*Corresponding author: kgan@dtu.dk

Abstract: To enable estimation of time-integrated external doses to persons staying in an inhabited area radioactively contaminated by aerosols and gases released in connection with a large nuclear power plant accident, additional knowledge to that described in the first part of this paper is needed on the post-deposition migration of different types of contaminants on the various relevant types of environmental surface. This part of the paper describes how the migration processes are modelled dynamically in the European standard inhabited area dose model, ERMIN, and presents the newest parametric datasets. It is explained how the total information in both parts of the paper may be used to estimate doses received over time by populations in radioactively contaminated inhabited areas.

Keywords: external dose, nuclear power plant accident, radioactive, caesium, weathering, contamination

1. Introduction

According to a recent publication (Howard et al., 2017), the long term ingestion and external dose contributions received by inhabitants of areas contaminated by the Chernobyl accident was estimated to be about equal in magnitude, whereas the long term external dose contribution to the public in areas contaminated by the Fukushima accident has been estimated to be of the order of 80-90 %, and the corresponding ingestion dose only 10-20 %. In preparedness for possible future nuclear power plant accidents, it is thus highly important to be able to implement effective recovery strategies for contaminated inhabited areas. However, as per tradition, radioecology studies have over many decades to a very great extent focused on studies of mechanisms and parameters governing the post-deposition transfer of various radionuclides to man via foodchains. Therefore, these processes are today in general better understood than those determining external doses in inhabited areas. For example, the International Atomic Energy Agency has published a report of more than 600 pages on radionuclide transfer parameters for terrestrial and freshwater environments (IAEA, 2009), in which the terrestrial environments are all rural or natural (food producing).

Although a counterpart describing parameters and processes relevant to inhabited areas does not exist, there are of course also a range of publications that describe post-deposition transfer and natural removal of radiocontaminants deposited in inhabited areas. Many of these are based on studies of contamination from the Chernobyl accident. Unfortunately, measurements have not been made of the post-deposition migration of radioactive matter from the Fukushima accident on each of the various types of man-made surfaces representative of inhabited areas. Instead, the focus of the Japanese authorities has been on rapid carborne surveillance of dose rate in affected areas using KURAMA II detection systems (Kinase et al.,

2015), which measure an uncollimated dose rate in a position close to the road surface. This provided valuable rough indications of the contamination pattern over large land areas. In relation to the actual average exposure of the local population, however, this measurement geometry would give an overrepresentation of the radiation from the nearby contaminated street surface. And since the natural decline in radioactivity on street surfaces has previously been found to be comparatively very rapid (Andersson, 2009), such repeated measurements would lead to overestimation of the rate at which the average dose rate declines in the area through natural processes. Qualitatively, however, these Japanese measurements illustrate that the decline in dose rate is as expected faster in urban areas, comprising surfaces with rapid natural weathering processes, than in rural areas, where the decline in dose rate level is largely dependent on the slow downward contaminant migration in soil (Kinase et al., 2015).

Identifying appropriate time functions representing the natural weathering and migration processes of contaminants on each type of surface is essential in enabling estimation of future time integrated doses and for instance residual doses received by people after treatment in a prescribed way of a given type of surface in the inhabited environment. The ERMIN dose model co-developed and coded at Public Health England (Charnock et al., 2009; Charnock, 2018; Andersson et al., 2008) that is used in the European decision support systems, RODOS (2018) and ARGOS (2018), to estimate external doses in inhabited areas, includes a system of formulae reflecting the post deposition mobility of radiocontaminants on the different types of outdoor surface (Jones et al., 2007). This paper describes the most recent methods and parameter sets that have been developed for implementation in ERMIN, e.g., considering contaminants with an expanded range of possible physicochemical forms compared to earlier versions, and including the latest available information. As in part 1 of the paper, the focus is on describing external dose contributions from contamination on outdoor surfaces. Other processes modelled in ERMIN that can contribute to dose in inhabited areas after airborne releases, such as contaminant deposition on indoor surfaces, contaminant deposition on humans, and inhalation of contaminants are outside the scope of this paper, and described elsewhere (e.g., Jones et al., 2007; Andersson et al., 2004; Byrne, 2009; Andersson et al., 2008). Also naturally occurring contaminant resuspension processes are omitted in this paper as they are generally not expected to lead to significant redistribution of contamination deposited on urban surfaces after a nuclear power plant accident (Ramzaev et al., 2006; Andersson et al., 2004). Forced dose reduction processes are in general not considered in the models in this paper, although they are an integral part of ERMIN.

2. Materials and methods

As described in part 1 of the paper, experience from Chernobyl and Fukushima has shown that a large nuclear power plant accident can lead to airborne releases of a wide range of radionuclides with different physicochemical forms (more or less reactive gases, aerosols of different sizes and with different features with respect to environmental mobility). For the purpose of modelling post-deposition migration processes it is important to distinguish between elemental iodine, which may deposit in large amounts, but will in general be rapidly removed by natural processes (precipitation) on impermeable surfaces (Roed, 1987), and deposited contaminant particles with different characteristics. Radioiodine dose rate contributions may be high in an early phase, but due to the short physical half-life of the most abundant iodine isotopes in a nuclear power reactor, radioiodine would not be likely to have important influence on

external doses in later (recovery) time phases, particularly if other radionuclides than iodine and noble gases (notably caesium isotopes) are released.

If we, as argued in part 1 of the paper, concentrate on those particles that have a size that allows them to follow air streams over longer distances, these may be split into four different categories or model 'bins' (the general approach adopted in the ERMIN model). This includes a group of particles ranging in size between 0 and 2 μm, which is particularly representative of condensation mode contamination attached to ambient particles (Andersson, 2009). As mentioned in part 1 of the paper these typically had a radius of the order of half a micron in the Chernobyl and Fukushima cases. The contaminants associated with condensation mode particles are assumed to be rather readily soluble and would thus rapidly be in ionic form after deposition in the outdoor environment, as frequently reported after the Chernobyl accident (Andersson, 2009; Roed, 1987). Nevertheless, to illustrate the complexity of these issues, it should be mentioned that in an area very far from the release point from the Chernobyl accident, some low solubility caesium particles of this size range have been found, and increasing soil to milk contaminant transfer factors in that area over the first two years after the accident suggested that natural particle dissolution in the environment took considerable time (Hansen & Hove, 1991). However, focusing on external dose, contaminants embedded in low solubility particles would in general be expected to be more rapidly weathered away from an impermeable surface than caesium on cationic form (Andersson, 2009). Therefore, modelling post-deposition mobility of such small low solubility particles in the same way as cationic caesium, which will be very strongly fixed in upper layers of many types of urban surface, may make the dose contribution estimates somewhat conservative.

Radiocaesium has a particularly great importance in modelling external doses after nuclear power plant accidents, as it will evaporate at comparatively low temperatures, and thus be likely to be released in great quantities from large accidents. At the same time, the decays of the key isotopes of concern in this context, ^{134}Cs and ^{137}Cs, lead to emission of gamma photons with quite high energy and photon yield, particularly ^{137}Cs has a long physical half-life of ca. 30 years and the caesium cation has a rare marked tendency to be fixed in a range of minerals and also to be retained in the upper soil layers (Andersson, 2009). External dose rate contributions from caesium thus only slowly decline through natural processes, and would be of major concern in recovery (late phase) decisions for management of contaminated inhabited areas, as seen after both the Fukushima and Chernobyl accidents.

There is currently insufficient data available to enable specific detailed modelling of the retention of other radionuclides in ionic form on urban surfaces. However, high specific binding strength of caesium compared with any other potentially relevant ions has also been reported in laboratory studies of many urban construction materials (De Preter, 1990). Further, it has been demonstrated in field studies after the Chernobyl accident that the retention of cationic caesium in a variety of construction materials is considerably greater than that of, e.g., ruthenium (Roed, 1987), which was released in even greater quantity from the Chernobyl accident than was caesium (IAEA, 1991), but where the relevant isotopes, ^{103}Ru and ^{106}Ru are considerably more short-lived (physical half-lives of respectively 39.5 d and 1.0 y). Strontium deposited in water solution has for example been found to weather off a clay roof with a half-life of only ca. 2.5 months (Brown et al., 2016), whereas most of the caesium deposited in solution on a clay roof would remain over decades (Andersson, 2009). Thus modelling retention of all ionic contaminants

using parameters derived for caesium would be expected to make the dose estimates somewhat conservative.

Larger low solubility particles will generally be expected to be removed from impermeable surfaces at a much faster rate than cationic caesium (Andersson, 2009). The main mechanisms driving the 'natural' removal of all contaminants are in general precipitation and anthopogenic impact such as traffic and routine cleaning (Wilkins, 1987; Andersson, 2009). Although time, rain intensity and rain frequency all have importance (Madoz-Escande et al., 2004; Madoz-Escande et al., 2005), data is currently not available to allow quantitative modelling according to these factors, and in any case, weather predictions over long time periods would be too uncertain to make use of such data. Therefore empirical formulae based on typical observations of the overall natural weathering process are used in the ERMIN model. The following sections report on the newest version of weathering parameter formulae and datasets, which have been derived for use in ERMIN. In the event of a new contaminating incident, case specific parameter studies should be made to continuously further improve and target model parameters. Also, an investigation of aerosol characteristics (including solubility) should be made so that the user could for the purpose of long-term dose prediction target the model assumptions for different aerosol groups to the specific case.

3. Results

3.1. Contaminant mobility from paved areas

For modelling the mobility of contaminants on paved areas, such as streets and walkways, the primary dataset of interest reflects the results of in situ measurements on such surfaces of radiocaesium in the town of Gävle, Sweden, which received one of the highest levels of contamination outside the former Soviet Union from the Chernobyl accident (Andersson, 2009). These measurements were made with collimated germanium detectors over a period stretching from the first week after the accident to more than ten years later (Karlberg, 1988; Andersson, 1991; Andersson et al., 2002).

The weathering process has generally been found to be rapid on such surfaces, although a bit of variation has been observed due to differences in traffic intensity, and also precipitation rates and routine street cleaning would play a role. Experiments have shown that there are no strong binding mechanisms of cationic caesium in asphalt bitumen (Andersson, 1991), as there are in for example soil or common roof tiles. It has also been demonstrated that the downward penetration of caesium into an asphalted road surface can over a 2-year weathering period be expected to be less than one millimetre (Andersson, 1991). Although the caesium may be selectively bound to street dust (De Preter, 1990), this does not slow down the removal rate, as the street dust is not strongly attached to the road surface (Andersson, 1991).

As there does not appear to be significant contaminant ion specific fixation mechanisms at play on these surfaces, the results recorded for cationic caesium should apply also to other contaminant ions. This agrees with the results of Warming (1982; 1984) in a tracer experiment where ^{86}Rb, ^{103}Ru and ^{140}Ba were sprayed onto asphalt and concrete pavements in a solution, and a very large part of all tracers could be removed by simple firehosing some days later.

The empirical weathering formula that was derived from the measurement time series recorded in Gävle was found to be generally consistent with information from in situ measurements over shorter periods of time of Chernobyl caesium weathering in Bavaria (Jacob et al., 1987). This formula is used for all contaminants deposited in more or less readily soluble form (Andersson et al., 2002):

$$C(t) = C_0 \cdot \exp(-\mathrm{Ln}2 \cdot t / T_{½}) \cdot (f_1 \cdot \exp(-\mathrm{Ln}2 \cdot t / T_{w1}) + f_2 \cdot \exp(-\mathrm{Ln}2 \cdot t / T_{w2})), \quad (1)$$

where C(t) is the contaminant concentration at time t, C_0 is the initial contaminant concentration after the deposition process, $T_{½}$ is the physical half-life of the radionuclide, f_1 is the fraction (on average ca. 0.7 on streets; estimated standard deviation 0.2) of the contamination removed with a short half-life of T_{w1} (ca. 120 days on streets; estimated standard deviation 40 days), and f_2 is the fraction (1- f_1) of the contamination removed with a longer half-life of T_{w2} (on average ca. 3 years on streets; estimated standard deviation 1 year). The weathering process may take considerably longer, if there is very little human activity in the area, as recorded in areas deserted after the Chernobyl accident (Andersson, 2009).

The case is different if low solubility fuel particles are present. Sartor et al. (1974) found experimentally that removal of contaminants in particle form from impermeable road surfaces was largely independent of particle size, when the particles were larger than about 10 µm. Smaller particles are however increasingly difficult to remove, as they can enter cavities in structures, and be less prone to weathering. According to aerosol spectra recorded after the Chernobyl accident, ^{140}La and ^{140}Ba were representatives of the more refractory element radionuclides released (in fuel particles), having a contaminant AMAD (activity median aerodynamic diameter) of several microns (typically 2-5) even in the most remote areas to which dispersion was recorded (Rulik et al., 1989; Nair & Darley, 1986). This indicates that fuel particles may be expected to be supermicroneous, in-line with findings from explosions impacting on materials that do not undergo phase transition during the explosion (Andersson et al., 2008a). This would also be expected to have been the case in Denmark, where ^{140}La and ^{140}Ba contaminants were recorded to have different characteristics with respect to surface weathering, than did for instance the radiocaesium isotopes that predominantly deposited in readily soluble submicron particle form. Over the first 22 days that followed the initial contamination deposition in Roskilde, Denmark, from the Chernobyl accident, some 22 % of the lanthanum and barium was washed off concrete surfaces through natural processes (Roed, 1987, 1990). This corresponds to a weathering half-life of about 60 days. It is likely that routine street cleaning would speed up this process further, so that the value of T_{w3} of 60 days (with an estimated standard deviation of 20 days) may be seen as a conservative estimate for dose estimation from particles in the 2-5 µm range.

On the basis of experimental investigations of attachment of particles of different sizes to street surfaces (Sartor & Gaboury, 1984; Sartor et al., 1974; Bender & Terstriep, 1984; Owen et al., 1960; Terstriep et al., 1982), it would be expected that particles in the 5-10 µm range (and thus according to Sartor et al., 1974, also likely the particles in the 10-20 µm range) would have a half-life, T_{w3}, of the order of 30 days (standard deviation estimated to 15 days). The environmental dissolution timespans in soils reported by Kashparov et al. (2004) are long compared with the time constants determining natural removal of deposited fuel particles, and may thus be ignored in this context.

The general formula for contaminants deposited in fuel particle form becomes:

$$C(t) = C_0 \cdot \exp(-\mathrm{Ln}2 \cdot t / T_{½}) \cdot \exp(-\mathrm{Ln}2 \cdot t / T_{w3}) \quad (2)$$

3.2. Contaminant mobility from roofs

Measurement series performed in Denmark over a period of nearly 15 years after the Chernobyl accident of the level of radiocaesium contamination level on a range of common roof materials (concrete, slate, clay tile) showed that whereas the initial retention on the roof of contaminants after a wet deposition process varies considerably between roofing materials (see part 1 of this paper), the subsequent long-term weathering rates were after the Chernobyl accident found to vary rather little between the examined range of materials (Andersson, 2009). A shorter time-series of measurements made on German roofs (Roed & Jacob, 1990) support the general validity of these findings, although only done for concrete and clay tile roofs. Common to these materials is that they generally contain minerals, which selectively and strongly fix and retain caesium cations (De Preter, 1990; Andersson, 1991). Other radionuclide ions would be expected to be less strongly held (Andersson, 2009; Brown, 2016), although it has been demonstrated that ruthenium in representative ionic forms is not very easily removed from a roof clay or concrete tile surface (Andersson, 1991). ERMIN uses weathering data based on the Chernobyl time series caesium measurements (Andersson, 2009) for all radionuclides in ionic form for these types of roof materials. This may lead to conservative estimates of long term doses for other radionuclides, which are in reality weathered off faster. However, the physical half-lives of other radionuclides that would on the basis of past experience be expected to be potentially released in relatively large amounts and could impinge on external dose (see part 1 of the paper) are considerably shorter than that of ^{137}Cs, and caesium is among the more volatile elements with generally comparatively high release probability.

The empirical formula thus applied in ERMIN for all contaminant ions deposited in more or less readily soluble form on many types of roofs (clay, concrete, slate) is:

$$C(t) = C_0 \cdot \exp(-\mathrm{Ln}2 \cdot t / T_{½}) \cdot (f_1 \cdot \exp(-\mathrm{Ln}2 \cdot t / T_{w1}) + f_2 \cdot \exp(-\mathrm{Ln}2 \cdot t / T_{w2})), \quad (3)$$

where C(t) is the contaminant concentration at time t, C_0 is the initial contaminant concentration after the deposition process, $T_{½}$ is the physical half-life of the radionuclide, f_1 is the fraction (on average ca. 0.5 on these roof types; estimated standard deviation 0.1) of the contamination removed with a short half-life of T_{w1} (ca. 730 days; estimated standard deviation 85 days), and f_2 is the fraction (1- f_1) of the contamination removed with a longer half-life of T_{w2} (on average ca. 35 years; estimated standard deviation 7 years). Also sandstone roof tiles contain intact micaceous substances (De Preter, 1990), and would be expected to retain caesium in the same way.

The exception regarding radionuclide ions concerns very smooth (non-porous) surfaces, where experimentation suggests that the weathering of cationic caesium (and very likely also other ions) on a glass roof would occur with a half-life of the order of 95 days (Brown et al., 2016), and investigations from the European ECP-4 project (Mamaev et al., 1993) suggest a similar value for smooth (uncorroded) metal roof covers.

Regarding low solubility particle contamination, these types of surfaces would not constitute an environment that could over a reasonable time (compared with weathering half-lives) lead to very much fuel particle dissolution (Kashparov et al., 2004). For the parameterisation time series data exists for Chernobyl lanthanum and barium, associated with 2-5 µm particles, as measured on roof pavings (concrete,

slate, clay tile) in Denmark. These contaminants were found to be weathered off the surface much more rapidly than caesium (Roed, 1987). A reasonable weathering half-life, T_{w3}, would on the basis of that data seem to be of the order of 100 days. A probably dose conservative estimate of the weathering half-life for 5-10 µm (and larger) particles would judging from the data for paved horizontal surfaces be expected to be of the order of 60 days.

The general formula for contaminants deposited in fuel particle form becomes:

$$C(t) = C_0 \cdot \exp(-Ln2 \cdot t / T_{½}) \cdot \exp(-Ln2 \cdot t / T_{w3}) \quad (4)$$

3.3. Contaminant mobility from outer walls

For weathering of contamination on outdoor walls, generally very sparse information is available, primarily from measurements over time in Gävle (Andersson et al., 2002). It is clear that the weathering function on walls is not subject to strong fixation mechanisms, as construction bricks used for building walls are typically fired at such high temperatures that no specific strong ionic fixation sites remain (Andersson, 2009), and no significant difference was recorded in Gävle between plastered walls and clay brick walls (Andersson et al., 2002). The slow removal is largely due to wind abrasion and any horizontal precipitation components. It cannot be ruled out that larger particles may be more prone to wind-driven abrasion than small ones, which might be more protected in material cavities of suitable sizes, but the required data is not available to allow distinguishing on this parameter. Again a dose conservative approach is used, assuming that the larger particle contamination is weathered off walls at the same rate as is small particle contamination.

The generally assumed formula for contaminants deposited walls is (Andersson et al., 2002):

$$C(t) = C_0 \cdot \exp(-Ln2 \cdot t / T_{½}) \cdot \exp(-Ln2 \cdot t / T_{w1}), \quad (5)$$

where C(t) is the contaminant concentration at time t, C_0 is the initial contaminant concentration after the deposition process, $T_{½}$ is the physical half-life of the radionuclide, and T_{w1} is the weathering half-life of ca. 7 years (estimated standard deviation 2 years).

3.4. Contaminant mobility from grass and small plants

A large number of workers have over the years estimated the weathering half-life of contaminants on grass and small plants from experimentation, as such data is needed in traditional radioecology studies. The majority of experiments were carried out prior to the Chernobyl accident, but also some later studies have been made (Martin, 1964; Cline et al., 1965; Milbourn & Taylor, 1965; Heinemann & Vogt, 1980; Kirchmann et al., 1966; Chadwick & Chamberlain, 1970; Krieger & Burmann, 1969; Aarkrog et al., 1988; BIOMOVS, 1991; Mück et al., 1994; Eriksson et al., 1998; IAEA, 2009). There is no clear trend from this data with respect to dependence on physicochemical characteristics, where these have been specified, and it is thus assumed in the modelling that all the contaminant material is washed off vegetation at the same rate. Based on the above references, the default value in the ERMIN model of the natural weathering half-life of

contaminants from grass is T_w = 16 days (with a standard deviation of 7 days). This value is somewhat shorter than the value of 25 days that has been recommended by Müller & Pröhl (1993) for the purpose of the ECOSYS ingestion dose model. However, the 25 days correspond to the results of a field study where the field was completely protected against rain (Krieger & Burmann, 1969). It should be noted that in case of prolonged rain, the natural weathering half-life may be shortened considerably (Madoz-Escande et al., 2004; Madoz-Escande et al., 2005; Madoz-Escande & Santucci, 2005). On small plants, a similar typical value of T_w = 12 days (estimated standard deviation of 5 days) was derived from the same literature.

The formula applicable to describe the concentration of contaminants on these surfaces at any time t is of the form

$$C(t) = C_0 \cdot \exp(-\mathrm{Ln}2 \cdot t / T_{½}) \cdot \exp(-\mathrm{Ln}2 \cdot t / T_w), \quad (6)$$

where C(t) is the contaminant concentration at time t, C_0 is the initial contaminant concentration after the deposition process, $T_{½}$ is the physical half-life of the radionuclide, and T_w is the weathering half-life.

3.5. Contaminant mobility from trees and shrubs

Nearly half of the contamination on trees or shrubs will according to literature generally be removed with a short half-life, of about 30 days with a standard deviation of about 2 weeks (Mamikhin & Klyashtorin, 2000; Nygren et al., 1994; Roed, 1988). It would seem reasonable to assume that the mechanism largely responsible for this transfer is the first heavy rainshowers (Roed, 1988). A small part of the order of 4 % (estimated standard deviation of 4 %) is assumed to remain on the tree/shrub largely until it is felled (Mamikhin & Klyashtorin, 2000; Roed, 1988), and the rest is assumed to have a weathering half-life of some 1.7 years, with an estimated standard deviation of about 1 year (Mamikhin & Klyashtorin, 2000; Linkov et al., 1997). There may possibly be some species of trees for which this is not quite true, but the data available is sparse. On top of this, for coniferous trees, the shedding of needles will occur continuously with a half-life that depends on the exact species and climate, but can be assumed to be of the order of 4 years, with a standard deviation of about 2 years (Horticulture Diagnostic Laboratory, 2018). For deciduous trees/shrubs (in leaf at deposition), it is assumed that they shed their leaves during the first autumn, where nearly all the contamination is on the leaves (Roed, 1988). The time may here be assumed to vary rather homogeneously within about 8 weeks of the autumn.

It should be noted that the above parameter values were based almost exclusively on data for deposited soluble radiocaesium aerosols, and only Roed (1988) reported directly applicable information for garden trees. The mechanisms and/or rates of loss may well be different in forests. However, the values for caesium fit reasonably with results obtained after artificial contamination of respectively pine and birch forest tree crowns with ^{90}Sr in soluble form (Alexakhin & Naryshkin, 1977). It is assumed that all contaminants behave in this way on trees and shrubs. No data is available for large low solubility contaminant particles, but these would be assumed to be removed somewhat more easily from the trees by precipitation, as they are on for example street surfaces. Applying values for caesium in solution would thus make the tree/shrub dose contribution estimates somewhat conservative. The methodology is thus here largely unchanged since the first parameterisation of ERMIN, where less emphasis was placed on physicochemical forms of the contaminants (Jones, et al., 2007).

Small amounts of long-lived radionuclides in soil will be transferred from the soil to trees/shrubs by root uptake. This will correspond to only few percent of the material initially deposited directly on the tree (Linkov et al., 1997), and is not considered in ERMIN. Unlike forested areas, leaves/needles in urban areas are generally not left to form a litter layer after they are shed. Therefore urban tree/shrub soil uptake will be much less than that in forests. The focus in the context of urban external dose is on the initially potentially very high tree/shrub canopy contamination due to the very effective aerosol filter constituted by foliage if the tree/shrub was in leaf at deposition (Roed, 1990). Only trees in leaf during deposition are considered in ERMIN, as the contamination level will otherwise be much less significant.

The formula applied to describe the concentration of contaminants on these surfaces at any time t is of the form (Jones et al., 2007):

$$C(t) = C_0 \cdot \exp(-\mathrm{Ln2} \cdot t / T_{½}) \cdot (f_1 \cdot \exp(-\mathrm{Ln2} \cdot t / T_{w1}) + f_2 \cdot \exp(-\mathrm{Ln2} \cdot t / T_{w2}) + f_3), \quad (7)$$

where C(t) is the contaminant concentration at time t, C_0 is the initial contaminant concentration after the deposition process, $T_{½}$ is the physical half-life of the radionuclide, f_1 is the fraction (on average ca. 0.46, standard deviation of ca. 0.07) of the contamination removed with a half-life of T_{w1} = ca. 30 days, f_2 is the fraction ($1 - f_1 – f_3$) of the contamination removed with a half-life of T_{w2} (on average ca. 1.7 years for deciduous and ca. 1.2 years for coniferous trees/shrubs taking into account continuous needle shedding), f_3 is the fraction (0.04) of the contamination assumed to stay until the tree/shrub is removed, and T_{w1} and T_{w2} are the corresponding removal half-lives, as given above. Deciduous foliage shedding in the first autumn after the deposition occurred is assumed to change f_1 and f_2 to 0.

3.6. Contaminant mobility in soils

The concentration of contaminants in soil is described in ERMIN as a function of time and vertical soil depth by a convection-dispersion model (Andersson et al., 1998; Jones et al., 2007), in-line with methodology suggested by, e.g., Schuller et al. (1997) and Bunzl et al (2000):

$$C(x,t) = C_0 \exp(-\ln(2)\, t/T_{½}) \left(\frac{1}{\sqrt{\pi D_s t}} \exp\left(-\frac{(x-v_s t)^2}{4\, D_s t}\right) - \frac{v_s}{2\, D_s} \exp\left(\frac{v_s}{D_s} x\right) erfc\left(\frac{x+v_s t}{2\sqrt{D_s t}}\right) \right) \quad (8)$$

Here $T_{½}$ is again the physical half-life, whereas D_s is the effective dispersion coefficient, and v_s is the convective velocity, defined respectively as

$$D_s = \frac{D}{1 + K_d \frac{\rho}{\varepsilon}} \quad (9) \qquad \text{and} \qquad v_s = \frac{v_w}{1 + K_d \frac{\rho}{\varepsilon}} \quad (10)$$

where D is the dispersion coefficient, v_w is the mean pore water velocity, K_d is the distribution coefficient of the contaminant in the soil, ρ is the bulk soil density, and ε is the soil porosity.

Bossew and Kirchner (2004), and Kirchner et al. (2009) have made thorough reviews of D_s and v_s by soil type on the basis of numerous assessments over different parts of Europe. For radiocaesium from Chernobyl, the resultant values were found to be as shown in Table 1. These values are in agreement with those reported by Ivanov (2009).

Of course the downward migration of contaminants in fuel particles is governed by entirely different physicochemical processes. Ivanov (2009) recorded much lower effective diffusion coefficients for contaminants contained in dispersed fuel particles deposited on soil. For sandy, loamy and peaty soils, these were all found to be of the order of 0.015 cm^2 per year. The dispersed fuel particles measured by Ivanov (2009) were found to range up to about 18 µm in size, and the larger of these (>4 µm) seem as might be expected to be somewhat better retained in very top layers of undisturbed soils. Based on these results, the downward migration of fuel particles is seen to be exceedingly slow, and it could only lead to limited conservatism in external dose estimates to assume that the particles remain in the very top of the soil until they dissolve over months or years.

However, once the radionuclides are released from the fuel particles, other relevant contaminants can generally be expected to migrate faster than caesium (Andersson, 2009) as reflected by the differences in Table 2 of soil K_d. The dissolution of fuel particles in soil has in the Chernobyl case been reported by Kashparov et al. (2004) to take place according to the formulae below, which will be included in ERMIN:

If the material was initially oxidised, the dissolution rate constant after deposition in soil will be:

$$k\ (years^{-1}) = 0.6 * 10^{(-0.15*pH)} \text{ at } pH < 7.0, \text{ and } k = 0.05 \text{ at } pH > 7.0 \quad (11)$$

If the material was NOT initially oxidised, the dissolution rate constant after deposition in soil will be:

$$k\ (years^{-1}) = 40 * 10^{(-0.45*pH)} \text{ at } pH < 6.5, \text{ and } k = 0.05 \text{ at } pH > 6.5 \quad (12)$$

The pH values to be used in Kasparov et al.'s formulae would be based on easily made actual measurements in case of an accident, but may be assumed to mostly be in the range of 5.0-6.5 for mineral soils and 6.5-8.0 for more organic soils.

Theoretically, there should be some dependence of particle dissolution rates on particle sizes (Mercer, 1967). However, such data are not apparent from the data published by Kashparov et al. (2004).

Table 1. Results of a review of values of D_s and v_s by soil type in different types of soil, based on Chernobyl (cationic) caesium assessment (Bossew and Kirchner, 2004; Kirchner et al., 2009).

Soil group	GM	GSD	AM	SD	Min	Max
Parameter: D_s (cm^2 per year)						
All soils	0.22	3.1	0.37	0.4	0.02	1.9
Clay/Loam	0.20	4.6	0.36	0.3	0.02	0.8
Sand	0.11	2.3	0.16	0.2	0.03	0.6
Organic	0.94	1.8	1.07	0.7	0.63	1.9
Unspecified	0.27	2.6	0.37	0.3	0.04	0.8
Parameter: v_s (cm per year)						
All soils	0.18	3.3	0.27	0.2	0.00	0.9
Clay/Loam	0.06	17.5	0.24	0.3	0.00	0.6

Sand	0.15	1.7	0.17	0.1	0.07	0.6
Organic	0.69	1.6	0.73	0.3	0.40	0.9
Unspecified	0.22	1.6	0.24	0.1	0.09	0.5

GM: geometric mean; GSD: geometric standard deviation; AM: arithmetic mean; SD: arithmetic standard deviation.

It may be noted that values for the groups 'all soils' and 'unspecified soil type' are generally in reasonable agreement, as they would be if the unspecified category in reality spans representatively over different soil types. Also values reported for weapons fallout have been reported by Kirchner (2009), and these are in most cases comparable with those for Chernobyl data. A lognormal distribution (using the geometric mean) is assumed (as favoured by Kirchner et al., 2009) in the uncertainty evaluation feature that is prepared for ERMIN. Minimum and maximum values are used as boundaries.

Values of D_s and v_s for other radioelements than caesium can be found by multiplying the values in Table 1 for caesium by the 'retardation factor' relationship (R = $1+K_d\frac{\rho}{\varepsilon}$) (Kirchner et al., 2009) (i.e. by the 'retardation factor' for the new element divided by that for caesium), applying appropriate values for all parameters (see above) for the soil type and element in question.

For the K_d values in equations 9 and 10, a wide range of data is available (also by soil type) from a relatively recent review by IAEA (2009). Table 2 shows the values for the 3 radioelements that would be thought to be of primary importance for external dose, but data for other elements of any potential significance (Am, Ba, Ce, Cm, La, Mo, Nb, Np, Pu, Rb, Sb, Sr, Te, U and Zr) are also available for use in the specified format from the report from IAEA (2009), although generally based on much fewer data and often without soil type specific data or standard deviations. All values of K_d are assumed to be lognormally distributed based on the Central Limit Theorem, and the assumption of lognormal is generally supported by empirical evidence (Sheppard et al., 2009).

As for bulk soil density, this normally varies within a short range of 1.4-1.7 g/cm^3 for sandy soil, whereas it is typically 1.1-1.4 g/cm^3 for clay/loam soil (Brewer, 1964; Chesworth, 2008). An assumption of uniform distribution seems reasonable over these rather small intervals. The relationship between bulk soil density and porosity is given by:

Soil porosity = 1 – (Bulk soil density / particle density) (13)

(Blake & Hartge, 1986; Brady & Weil, 1996). In most soils the particle density can be assumed to be around 2.65 g/cm^3 (Brady & Weil, 1996). This is the density of quartz, which is the dominant mineral in most soils.

For organic soils, the porosity has on the basis of 180 soil samples been shown to have the following dependence on soil organic carbon (SOC) (Franzluebbers, 2011):

Soil porosity (m^3/m^3) = -0.20 + 0.89 (1-exp(-0.067 · SOC[g/kg])), (14)

whereas the bulk soil density depends on the soil organic C in the following way (Hossain et al., 2015):

Bulk soil density (g/cm^3) = 1.56 exp (-0.0063 · SOC[g/kg]). (15)

By including these formulas in ERMIN the user can specify the values for organic soils directly from the soil organic C content, which is easily measurable by ignition (remembering the rule of thumb – the van Bemmelen factor - that organic matter generally contains about 58 percent organic carbon (Périé & Ouimet, 2008)).

Table 2 Results of a review of values of K_d for 3 important elements by soil type in different types of soil, based on hundreds (for Cs and I) of field assessments (in units of L/kg = cm^3/g).

Soil group	GM	GSD	AM	SD	Min	Max
Contaminant: Cs						
All soils	1.2E3	7	6.1E3	2.1E4	4.3	3.8E5
Clay/Loam	5.5E3	4	2.2E4	6.7E4	5.7E2	3.8E5
Sand	5.3E2	6	2.2E3	5.0E3	1.0E1	3.5E4
Organic	2.7E2	7	3.0E3	1.2E4	4.3	9.5E4
Unspecified	1.7E3	5	6.7E3	1.5E4	4.0E1	5.5E4
Contaminant: I						
All soils	5.4	6	2.5E1	7.0E1	1.0E-2	5.8E2
Clay/Loam	6.8	6	2.1E1	3.0E1	1.0	1.2E2
Sand	3.6	8	1.3E1	2.0E1	1.0E-2	1.3E2
Organic	3.6E1	4	9.3E1	1.8E2	8.5	5.8E2
Unspecified	2.6	6	2.0E1	7.0E1	1.0E-1	3.7E2
Contaminant: Ru						
All soils	2.7E2	8	4.7E3	1.7E4	5.0	6.6E4
Clay/Loam	5.0E2	2	6.0E2	3.6E2	2.0E2	9.9E2
Sand	3.6E1	6	7.7E1	9.0E1	5.0	6.6E4
Organic	-	-	6.6E4	-	-	-
Unspecified	1.4E2	3	2.3E2	2.1E2	3.4E1	4.9E2

GM: geometric mean; GSD: geometric standard deviation; AM: arithmetic mean; SD: arithmetic standard deviation.

3.7. Combining the information for external dose prediction

This section gives a short description of how the information in both parts of this paper may be applied in prognoses of how the dose rate will vary with time after a contaminating event. For simplicity assume that a dry deposition of only ^{137}Cs (relevant emitted gamma energy: 0.662 MeV) has taken place to an area that may be adequately described by the type of semi-detached house environment described in part 1 of the paper (dose factors for a range of other types of environments exist in ERMIN (Jones et al., 2007), and the list of available data that may be used was recently expanded (Hinrichsen & Andersson, 2018). The following describes in crude terms the way ERMIN operates.

The initial contamination level on the short-cut grassed reference surface is assumed to have been measured (or if measurements are not available, estimated using a dispersion/deposition model in the decision support system). This contamination level (unit: Bq mm^{-2} on the reference surface) is multiplied by the set of factors for relative deposition on different surfaces for dry deposition from Table 1 of part 1 of the paper (for the relevant measured or assumed physicochemical form). This gives the initial contamination level on each type of surface in the environment (unit: Bq mm^{-2}).

For each type of contaminated surface, Table 6 in part 1 of the paper gives the normalised contribution to kerma (unit: pGy per γ mm^{-2} on the relevant surface type) in a detection point, where people may be staying (e.g., on the ground floor or first floor). By multiplying these kerma values by the gamma yield constant (unit: γ s^{-1} per Bq) for the radionuclide in question (0.85 for ^{137}Cs daughter nuclide ^{137m}Ba) a kerma rate contribution (unit: pGy s^{-1} per Bq mm^{-2}) is obtained. This kerma rate contribution can be multiplied by the initial contamination level on the given surface to obtain the initial contribution of the type of surface to kerma rate in the given position (unit: pGy s^{-1}). By multiplying this by the time function given in this paper for the relevant surface type and physicochemical form, the kerma rate contribution of the type of surface at any point in time can be estimated. Conversion factors from air kerma to effective dose are given by ICRP (1997) and are for most relevant energies of the order of unity.

As an example, Figure 1 shows the decline with time of kerma contributions (essentially kerma rate contributions) per unit initial level of contamination on each type of surface in the semi-detached house environment. The detection area is here indoors on the ground floor. Note that the figures here only show the natural decline due to contaminant mobility and do not include the decay due to the physical half-life (for ^{137}Cs: ca. 30 years). It is seen that due to the different initial deposition and environmental mobility of contaminants with different physicochemical forms on different surfaces, some kerma rate contributions comparatively quickly become unimportant, whereas other remain high over very long periods. It should be noted that in this example, all ground areas have been assumed to be grassed. The comparatively rapid natural removal of large low solubility contaminant particles on impermeable surfaces is also visible in Figure 1.

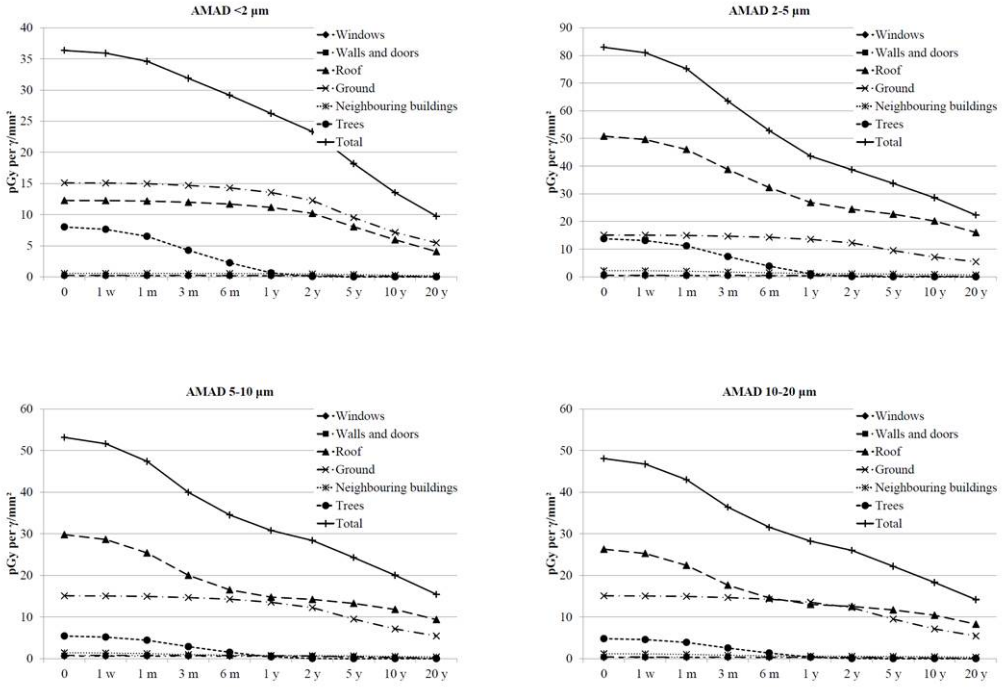

Figure 1. Natural decline with time in kerma contributions from different contaminated surface types per gamma initially emitted from the contamination on that surface per unit area. The detection point is here located on the ground floor of the building and all ground areas are assumed to be grassed. The physical half-life of ^{137}Cs is here not included in the calculations.

As can be seen, which of the contaminated surfaces contribute most to the kerma depends on the physicochemical form. Figure 2 shows the results of similar calculations, but here all ground areas were assumed to be paved.In comparison to the grassed ground areas, the deposition velocity is considerably lower (as seen in the tables of the paper), and the decline in the ground kerma rate contribution is comparatively faster (Andersson et al., 2009).

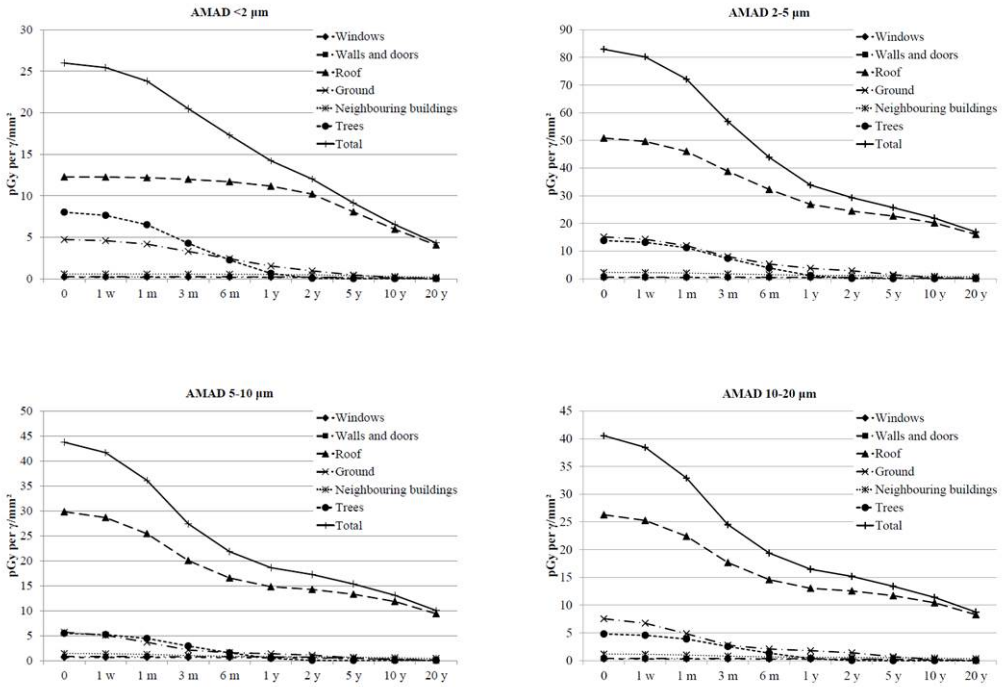

Figure 2. Natural decline with time in kerma contributions from different contaminated surface types per gamma initially emitted from the contamination on that surface per unit area. The detection point is here located on the ground floor of the building and all ground areas are assumed to be paved. The physical half-life of ^{137}Cs is here not included in the calculations.

It should be noted that due to the high shielding effect of this type of brick building towards radiation coming from the outdoor environment, the kerma rate is for 0.662 MeV radiation from the ground areas reported by Meckbach et al. (1987) to be of the order of ten times higher outdoors than indoors in this type of building. Of course the dose contributions calculated on the basis of this type of information are for specific locations indoors and outdoors and must be weighted by the fractions of time spent by people on different floors and outdoors in the different representative positions. An average figure for European urban populations of the percentage of time spent indoors is 87 %, with a 95th percentile of 75 % (Andersson, 2013). If the contaminated environment contains large grassed areas or areas of soil, it has been demonstrated that these will often contribute most to doses integrated over years (Andersson et al., 2009).

The importance of parameter uncertainties for important ERMIN calculation endpoints is currently being studied through calculations made at Public Health England in the European CONFIDENCE project.

Conclusion

Whereas part 1 of this paper described the relative deposition on a range of different surfaces in the inhabited environment of a wide range of contaminants with different physicochemical characteristics, as well as resultant initial kerma rates in air in the environment, this second part is aimed at providing an overview of the approaches behind modelling the system of processes that determine the fate over time of radioactive substances after deposition.

Formulae are given for the decline in contamination level on different surfaces in the inhabited environment, under different conditions. The most recent parameter datasets derived for use in the European inhabited area decision support model, ERMIN, are reported, including estimates of uncertainties, which are often rather rough, due to the scarcity of available relevant data. Recently, refinements to the modelling have also been made to reduce overall uncertainties by better distinguishing between for instance construction material types, and soil type categories. Also, data libraries have been created for ERMIN with values reflecting the latest state of knowledge. A few calculation examples are given, to illustrate that the post-deposition migration, and thereby doses to affected persons, may greatly depend on contaminant characteristics and assumptions regarding the surface characteristics.

Brief information is given on how to apply the information from the two parts of the paper in estimating doses.

Acknowledgments

The authors would like to thank Dr. Thomas W. Charnock at Public Health England for valuable advice in drafting the paper.

Part of the research leading to these results was carried out in the CONFIDENCE project, which is part of the CONCERT project. This project has received funding from the Euratom research and training programme 2014-2018 under grant agreement No 662287.

An other part of the research leading to these results has received funding from the European Atomic Energy Community Seventh Framework Programme FP7/2012-2013 under grant agreement 323287.

Disclaimer

This publication reflects only the author's view. Responsibility for the information and views expressed therein lies entirely with the authors. The European Commission is not responsible for any use that may be made of the information it contains.

References

Aarkrog, A., Bøtter-Jensen, L., Chen, Q.J., Dahlgaard, H., Hansen, H., Holm, E., Lauridsen, B., Nielsen, S.P. & Søgaard-Hansen, J., 1988. Environmental Radioactivity in Denmark in 1986, Riso Report R-549, ISBN 87-550-1339-2

Alexakhin R. M. & Naryshkin, M.A., 1977. Migration of radionuclides in forest biogeocenoses, Science, p. 144

Andersson, K.G., 1991. Contamination and decontamination of urban areas, Ph.D. Thesis, Risø National Laboratory.

Andersson, K.G., 2009. Migration of radionuclides on outdoor surfaces, Chapter 5 (pp. 107-146) in K.G. Andersson (editor): Airborne radioactive contamination in inhabited areas, Book Series Radioactivity in the Environment vol. 15 (series editor: M.S. Baxter), Elsevier, ISBN 978-0-08-044989-0, ISSN 1569-4860.

Andersson, K.G., 2013. On the current needs in European decision support tools for contaminated areas, Radioprotection Vol. 48, No. 5, pp. 57-64, ISSN 0033-8451.

Andersson, K.G., Brown, J., Mortimer, K., Jones, J.A., Charnock, T., Thykier-Nielsen, S., Kaiser, J.C., Proehl, G. & Nielsen, S.P., 2008. New developments to support decision-making in contaminated inhabited areas following incidents involving a release of radioactivity to the environment, J. Environmental Radioactivity, vol. 99, pp. 439-454.

Andersson, K.G., Roed, J. & Fogh, C.L., 2002. Weathering of radiocaesium contamination on urban streets, walls and roofs, J. Environmental Radioactivity vol. 62, no.1, pp. 49-60.

Andersson, K.G., Roed, J., Byrne, M.A., Hession, H., Clark, P., Elahi, E., Byskov, A., Hou, X.L., Prip, H., Olsen, S.K. & Roed, T., 2004. Airborne contamination in the indoor environment and its implications for dose, Risoe-R-1462(EN), Risoe National Laboratory, Roskilde, Denmark, ISBN 87-550-3317-2, 100 p.

Andersson, K.G., Mikkelsen, T., Astrup, P., Thykier-Nielsen, S., Jacobsen, L.H., Schou-Jensen, L., Hoe, S.C. & Nielsen, S.P., 2008a. Estimation of health hazards resulting from a radiological terrorist attack in a city, Radiation Protection Dosimetry, Vol. 131, No. 3, pp. 297-307.

Andersson, K.G., Jones, A. & Charnock, T., 2009. Estimation of doses in inhabited areas, Chapter 6 (pp. 147-185) in K.G. Andersson (editor): Airborne radioactive contamination in inhabited areas, Book Series Radioactivity in the Environment vol. 15 (series editor: M.S. Baxter), Elsevier, ISBN 978-0-08-044989-0, ISSN 1569-4860.

ARGOS, 2018. PDC-ARGOS CBRN Crisis Management website. , www.pdc-argos.com/.

Bender, G.M. & Terstriep, M.L., 1984. Effectiveness of street sweeping in urban runoff pollution control, Science of the Total Environment 33, 185-192.

BIOMOVS, 1991. Scenario 4. Multiple Model Testing using Chernobyl fallout data of I-131 and Cs-137 in forage, milk, beef and grain. H. Kohler, S.-R. Peterson & F.O. Hoffmann (eds.). Technical Report 13, vols. I and II, Stockholm: National Institute of Radiation Protection.

Blake, G.R., & Hartge, K.H., 1986. Bulk density. p. 363-375. In A. Klute (ed.): Methods of soil analysis. Part 1. (2nd ed.). Agron. Monogr. 9. ASA and SSSA, Madison, WI.

Bossew, P. & Kirchner, G., 2004. Modelling the vertical distribution of radionuclides in soil. PartI: the convection-dispersion equation revisited, J. Environ. Radioactivity 73, 127-150.

Brady, N.C. and Weil, R.R., 1996. The nature and properties of soils (11th ed.). Prentice Hall, New York.

Brewer, R., 1964. Fabric and mineral analysis of soils. Huntington, N.Y.: R.E. Krieger. ISBN 0882753142.

Brown, J., Ewers, L. & Youngman, M., 2016. An experimental study on natural weathering of radionuclides from urban surfaces for aerosols deposited in wet and dry conditions, Radioprotection 51´(HS2), S109-S112.

Bunzl, K., Schimmack, W., Zelles, L. & Albers, B.P., 2000. Spatial variability of the vertical migration of fallout ^{137}Cs in the soil of a pasture, and consequences for long-term predictions, Radiat. Environ. Biophys. 39, pp. 197-205.

Byrne, M.A., 2009. Airborne contamination inside dwellings, Chapter 3 (pp. 55-75) in K.G. Andersson (editor): Airborne radioactive contamination in inhabited areas, Book Series Radioactivity in the Environment vol. 15 (series editor: M.S. Baxter), Elsevier, ISBN 978-0-08-044989-0, ISSN 1569-4860.

Chadwick, R.C. & Chamberlain, A.C., 1970. Field loss of radionuclides from grass; Atmospheric Environment 4, pp. 51-56.

Charnock, T.W., 2018. Concise description of ERMIN 2.1. The European inhabited dose and decontamination model, Draft report, Centre for Radiation, Chemical and Environmental Hazards, Public Health England, Chilton, Didcot, Oxfordshire, OX11 0RQ, UK.

Charnock, T.W., Jones, J.A., Singer, L.N., Andersson, K.G., Roed, J., Thykier-Nielsen, S., Mikkelsen, T., Astrup, P., Kaiser, J.C., Müller, H., Pröhl, G., Raskob, W., Hoe, S.C., Jacobsen, L.H., Schou Jensen, L. & Gering, F., 2009. Calculating the consequences of recovery, a European model for inhabited areas, Radioprotection vol. 44, No.5, pp. 407-412, ISSN 0033-8451.

Chesworth, W., 2008. Encyclopedia of soil science. Dordrecht, Netherlands: Springer. p. 694. ISBN 1402039948.

Cline, J.F., Wilson, D.O. & Hubgate, F.P., 1965. Effect of physical and biological conditions on deposition and retention of 131I on plants, Health Physics 11, pp. 713-717.

De Preter, 1990. Radiocaesium retention in the aquatic, terrestrial and urban environment: a quantitative and unifying analysis, Doktoraatsproefschrift Nr. 190 aan de Fakulteit der Landbouwwetenschappen, Katholieke Universiteit te Leuven, Belgium.

Eriksson, Å, Rosén, K. & Haak, E., 1998. Retention of simulated fallout nuclides in agricultural crops, Swedish University of Agricultural Sciences, Uppsala (SE), Report SLU-REK-80, ISSN 0280-7963

Franzluebbers, A.J. , 2011.Stratification of soil porosity and organic matter, in Encyclopedia of Agrophysics, pp. 858-861, ISBN 978-90-481-3584-4, Springer Netherlands.

Hansen, H.S. & Hove, K., 1991. Radiocesium bioavailability – transfer of Chernobyl and tracer radiocesium to goat milk, Health Physics 60, 665-673.

Heinemann, K. & Vogt, K.J., 1980. Measurements of the deposition of iodine onto vegetation and the biological half-life of iodine on vegetation, Health Physics 39, pp. 463-474.

Hinrichsen, Y. & Andersson, K.G., 2018. Kerma factors for modern glass buildings in contaminated areas, paper submitted for publication in J. Radiological Protection.

Horticulture Diagnostic Laboratory, 2018. Normal Needle & Foliage Shedding On Evergreens, Cornell University, Cooperative Extension of Suffolk University, NY https://s3.amazonaws.com/assets.cce.cornell.edu/attachments/2182/Normal-Needle-And-Foliage-Shedding-On-Evergreens.pdf?1408632735.

Hossain, M.F., Chen, W & Zhang, Y, 2015. Bulk density of mineral and organic soils in the Canada's arctic and sub-arctic. Information Processing in Agriculture 2 (3-4) 183-190.

Howard, B.J., Fesenko, S., Balonov, M.I., Pröhl, G. & Nakayama, S., 2017. A comparison of remediation after the Chernobyl and Fukushima Daiichi accidents, Rad. Prot. Dosimetry 173, 170-176.

IAEA, 1991. The International Chernobyl Project , Technical Report, Report by an Advisory Committee, IAEA, International Atomic Energy Agency, Vienna, ISBN 92-0-129191-4.

IAEA, 2009. Quantification of radionuclide transfer in terrestrial and freshwater environments for radiological assessments, IAEA-TECDOC-1616, ISBN 978-92-0-104509-6, IAEA, Vienna.

ICRP, 1997. Conversion coefficients for use in radiological protection against external radiation, Annals of the ICRP, ICRP Publication 74, Pergamon Press, Oxford/ New York/ Tokyo, ISSN 0146-6453.

Ivanov, Y., 2009. Migration of fuel particles of ChPP fallout and leached radionuclides in soils and soil-to-plant system, In D.H. Oughton & V. Kashparov (eds.): Radioactive particles in the environment, Proceedings of the NATO Advanced Research Workshop on Hot Particles Released from Different Nuclear Sources, Yalta, Ukraine, 7-10 May 2007, Springer, Dordrecht, The Netherlands, ISBN 978-90-481-2949-2.

Jacob, P., Meckbach, R. & Müller, H.M., 1987. Reduction of external exposure from deposited Chernobyl activity by run-off, weathering, street cleaning and migration in the soil, Rad. Prot. Dosimetry 21, pp. 51-57.

Jones, A., Charnock, T., Singer, L., Roed, J., Andersson, K.G., Thykier-Nielsen, S., Mikkelsen, T., Astrup, P., Kaiser, J.C., Müller, H., Pröhl, G., Raskob, W., Hoe, S., Jacobsen, L.H., Schou-Jensen, L. & Gering, F., 2007. Description of the modelling of transfer and dose calculations within ERMIN, Deliverable report D5C2R2 of the CEC-EURANOS project, EURANOS(CAT2)-TN(05)-04.

Karlberg, O., 1988. Weathering and migration of Chernobyl fallout in Sweden, Studsvik report NP 216 EA, Studsvik, Sweden.

Kashparov, V.A., Ahamdach, N., Zvarich, S.I., Yoschenko, V.I., Maloshtan, I.M. & Dewiere, L., 2004. Kinetics of dissolution of Chernobyl fuel particles in soil in natural conditions, J. Environmental Radioactivity 72, 335-353.

Kinase, S., Takahashi, T., Sato, S., Yamamoto, H. & Saito, K., 2015. Prediction of ambient dose equivalent rates for the next 30 years after the accident, In Takahashi, T., Yamana, H., Tsukada, H., Sato, N., Nakatani, M.: Proceedings of the International Symposium on Radiological Issues for Fukushima's Revitalized Future, Paruse Iizaka, Fukushima City, Japan, May 30-31, 2015, KUR Research Program for Scientific Basis of Nuclear Safety, Osaka, Japan, ISBN 978 4 9906815-3-1.

Kirchmann, R., Fagniart, E. & van Puymbroeck, S., 1966. Studies on foliar contamination by radiocaesium and radio-strontium, In: Radioecological concentration processes, Proceedings of an international symposium held in Stockholm, Sweden, 25-29 April 1966, Pergamon Press, London, pp. 475-483.

Kirchner, G. Strebl, F., Bossew, P., Ehlken, S. & Geerzabek, M.H., 2009. Vertical migration of radionuclides in undisturbed grassland soils, J. Environ. Radioactivity 100, pp. 716-720.

Krieger, H.L. & Burmann, F.J., 1969. Effective half-times of 85-Sr and 134-Cs for a contaminated pasture; Health Physics 17, pp. 811-824.

Linkov, I., Morel, B. & Schell, W.R., 1997. "Remedial policies in radiologically-contaminated forests: environmental consequences and risk assessment", Risk Analysis 17, 67-75.

Madoz-Escande, C., Henner, P. & Bonhomme, T., 2004. Foliar contamination of Phaseolus vulgaris with aerosols of 137Cs, 85Sr, 133Ba and 123mTe: influence of plant development stage upon contamination and rain, J. Environ. Radioactivity 73(1), pp. 49-71.

Madoz-Escande, C., Garcia-Sanchez, L., Bonhomme, T. & Morello, M., 2005. Influence of rainfall characteristics on elimination of aerosols of caesium, strontium, barium and tellurium deposited on grassland, J. Environ. Radioactivity 84, pp. 1-20.

Madoz-Escande, C. & Santucci, P., 2005. Weather-dependent change of caesium, strontium, barium and tellurium contamination deposited as aerosols on various cultures, J. Environ. Radioactivity 84, pp. 417-439.

Mamaev, L.A., Rybakov, K.A., Galkin, G.A., Ogulnik, P.G., Hrabrov, S.A., Karlin, N.E., Parhomenko, V.I., Davydov, Yu.P., Voronik, N.I., Shatilo, N.N., Dmitrieva, Z.S., Efremenkov, V.M., Kupriyanova, I.V. & Kherovets, N.A., 1993. Development of technologies for decontamination of urban areas, techniques, motor transport, buildings, Progress report on the European Project ECP-4, Development of strategy for decontamination, Bochvar RIIM, Moscow, Russia / IREP of Ac. Sc, Belarus.

Mamikhin, S.V. & Klyashtorin, A.L., 2000. Mathematical model of 137Cs dynamics in the deciduous forest, J. Environmental Radioactivity vol. 47, pp. 101-114.

Martin, W.E., 1964. Losses of Sr-90, Sr-89 and I-131 from fallout contaminated plants, Radiat. Bot. 4, pp. 275-284.

Mercer, T.T., 1967. On the role of particle size in the dissolution of lung burdens, Health Physics 13, 1211-1221.

Milbourn, G.M. & Taylor, R., 1965. The contamination of grassland with radioactive strontium - I: Initial retention and loss; Radiat. Bot. 5, pp. 337-347.

Mück, K., Roth, K., Gerzabek, M.H. & Oberlander, H.-E., 1994. Effective half-lives of I- and Cs- isotopes in grassland shortly after fallout; J. Environ. Radioactivity 24(2), pp. 127-143.

Müller, H. & Pröhl, G., 1993. ECOSYS-87: A dynamic model for assessing radiological consequences of nuclear accidents, Health Physics 64(3), pp. 232-252.

Nair, S. & Darley, P.J.A., 1986. Preliminary assessment of individual doses in the environs of Berkeley, Gloucestershire, following the Chernobyl nuclear reactor accident, J. Soc. Radiol. Prot. 6(3), pp. 101-108.

Nygren, P., Hari, P., Raunemaa, T., Kulmala, M., Luokkanen, S., Holmberg, M. & Nikinmaa, E., 1994. Behaviour of ^{137}Cs from Chernobyl fallout in a Scots pine canopy in southern Finland, Can. J. For. Res., 24, 1210-1215.

Owen, W.L., Sartor, J.D. and van Horn W.H., 1960. Performance characteristics of wet decontamination procedures, US Naval Radiological Defence Laboratory.

Périé, C., Ouimet, R.,2008. Organic carbon, organic matter and bulk density relationship in boreal forest soils, Soil Science 88, 315-325.

Ramzaev, V., Andersson, K.G., Barkovsky, A., Fogh, C.L., Mishine, A. & Roed, J., 2006. Long-term stability of decontamination effect in recreational areas of the town Novozybkov, Bryansk Region, Russia, J. Environmental Radioactivity, vol. 85 (2-3), pp. 280-298.

RODOS, 2018. Realtime Online Decision Support System for nuclear emergency management. RODOS system home page, Karlsruhe Institute of Technology, Germany, https://resy5.iket.kit.edu/RODOS/.

Roed, 1987. Run-off from and weathering of roof material following the Chernobyl accident, Rad. Protection Dosimetry 21(1/3), 59-63.

Roed, J., 1988. The distribution on trees of dry deposited material from the Chernobyl accident, paper presented at the Joint CEC/OECD(NEA) Workshop on Recent Advances in Reactor Accident Consequence Assessment, Rome, Italy, 25-30 January, 1988.

Roed, J., 1990. Deposition and removal of radioactive substances in an urban area, Final report of the project NKA AKTU-245, NKA, ISBN 87 7303 514 9.

Roed, J. & Jacob, P., 1990. Deposition on urban surfaces and subsequent weathering, Proceedings of a seminar on methods and codes for assessing the off-site consequences of nuclear accidents (vol. 1), Athens, Greece, 1990, EUR13013, pp. 335-356.

Rulik, P., Bucina, I. & Malátová, I., 1989. Aerosol particle size distribution in dependence on the type of radionuclide after the Chernobyl accident and in the NPP effluents, Proceedings of the XVth Regional Congress of IRPA, Visby, Gotland, Sweden, pp. 102-107, ISBN 3-88585-668-9, TÜV Verlag Rheinland GmbH, Köln.

Sartor, J.D., Boyd, G.B., Agardy, F.J., 1974. Water pollution aspects of street surface contaminants, Journal WPCF, Water Pollution Control Federation, January 1974, pp. 456-467.

Sartor, J.D. & Gaboury, D.R., 1984. Street sweeping as a water pollution control measure: lessons learned over the past ten years, Science of the Total Environment 33, 171-183.

Schuller, P., Ellies, A. & Kirchner, G., 1997. Vertical migration of fallout ^{137}Cs in agricultural soils from Southern Chile, The Science of the Total Environment 193, 197-205.

Sheppard, S., Long, J., Sanipelli, B,2009. Solid /liquid partition coefficients (Kd) for selected soils and sediments at Forsmark and Laxemar-Simpevarp, SKB Report R-09-27, Sweden, ISSN 1402 3091.

Terstriep, M.L., Bender, G.M. & Noel, D.C., 1982. Final report, Nationwide urban runoff project, Champaign, Illinois: Evaluation of the effectiveness of municipal street sweeping in the control of urban storm runoff pollution, US Environmental Protection Agency.

Warming, L., 1982. Weathering and decontamination of radioactivity deposited on asphalt surfaces, Risø National Laboratory, Risø-M-2273.

Warming, L., 1984. Weathering and decontamination of radioactivity deposited on concrete surfaces, Risø National Laboratory, Risø-M-2473.

Wilkins, B.T., 1987. The retention behaviour of radiocaesium on common building materials under natural outdoor conditions, Rad. Prot. Dosimetry vol. 21, no.1/3, pp. 69-73.

Paper VI

Hinrichsen, Y., Finck, R., Martinsson, J., Rääf, C., Andersson, K. G., Influence of the migration of radioactive contaminants in soil, resident occupancy, and variability in contamination on isodose lines for typical Swedish houses. Submitted to Scientific Reports.

Influence of the migration of radioactive contaminants in soil, resident occupancy, and variability in contamination on isodose lines for typical Swedish houses

Yvonne Hinrichsen[1,*], Robert Finck[2], Johan Martinsson[2], Christopher Rääf[2], and Kasper Grann Andersson[1]

[1]Technical University of Denmark, Center for Nuclear Technologies, Roskilde, 4000, Denmark
[2]Lund University, Department of Translational Medicine, Medical Radiation Physics, Malmö, 205 02, Sweden
[*]yvhi@dtu.dk

ABSTRACT

In the remedial phase following an accidental radioactive release, it is important that soil decontamination measures are carried out on the areas that contribute most to the radiation dose. In this study, the newly developed concept of isodose lines was applied to the area around typical Swedish dwellings to identify these areas. The influence of the most common building materials in Sweden, wood and brick, and the importance of the positions of doors and windows on the isodose lines were demonstrated for specific positions inside the houses, as well as for the entire house, assuming the residents exhibit typical resident occupancy. Decontamination of the areas within certain isodose lines was shown to result in a greater dose reduction than decontaminating the same area of soil within a certain distance of the house. Furthermore, the impact of vertical migration of the radioactive contaminants in the soil on the isodose lines was studied, showing that the area enclosed by isodose lines decreases over time as the contaminants migrate deeper into the soil. The resulting isodose lines and their change over time are dominated by the downward movement of the contamination in the upper layer of soil. The impact of the variability in contamination on the final isodose lines and their dependence on building materials are demonstrated.

Introduction

The external radiation exposure is an important contribution to the radiation exposure of the population after the release of gamma-ray-emitting radionuclides into the air and their deposition on the ground and on other structures[1]. In inhabited environments, this radiation exposure can be reduced by building structures, depending on the geometry of the buildings, the deposition distribution on the different surfaces, and resident occupancy. The removal of a thin layer of soil on unpaved areas can reduce the contamination by as much as 90 %, provided the depth is optimized according to the vertical distribution of the contaminants[2]. The cost of employing skilled personnel, as well as equipment and consumables for such measures can be very high, and the construction of complex waste repositories may also be necessary[3]. It is therefore important to concentrate decontamination activities on the areas that have the greatest impact on the radiation exposure of the population, taking into account the reduction in exposure provided by various buildings.

The isodose concept was recently developed for this purpose[4]. When considering the dose contribution resulting from radionuclides deposited on the ground, this concept illustrates the extent to which the surrounding areas contribute to the external radiation exposure at different representative observation points inside a building, and can thus be used to optimize topsoil removal following a radioactive release. The aim of this study was to apply the isodose concept to two typical Swedish residential houses, constructed different materials, and to determine isodose lines at various locations in the houses, as well as for the entire the houses by applying data on typical resident occupancy. The impact of vertical migration of the contaminants in the soil and variability in the contaminants on the isodose lines was also studied.

Results

Monte Carlo computed isodose lines around typical Swedish houses

The isodose concept as described in Equation 1 in the Method section was applied to a case in which decontamination would lead to different reductions in the absorbed dose, depending on which of the eleven different observation points is considered.

Homogeneous ^{137}Cs contamination was assumed on the ground surrounding the wooden and the brick houses, as well as 2.5 cm and 5 cm below ground level. The results are presented graphically as isodose lines in Figures 1-3 for the wooden house and in Figures 4-6 for the brick house.

It can be seen from the Figures above that the shape of the areas encompassed by the isodose lines for a given observation point are relatively similar for all depths of the contamination, and for both the wooden and brick houses. The shapes of the isodose lines reflect the different materials, as well as the positions of doors and windows as they shield less than the walls. The zones for deposited contamination below ground level are smaller as fewer gamma photons from remote areas reach the observation point, as they lose energy through interactions with the soil. To obtain a better estimate of the size of the area that would have to be decontaminated to achieve a certain relative dose reduction for contamination at different depths, values of the primary dose factor were calculated for an infinite contaminated surface, and are presented in Table 1. The primary dose factor is directly related to the dose to the residents when no decontamination measures are implemented, and is expressed in pGy per γmm^{-2}, representing the dose (pGy) that would result from a homogeneous plane source at ground level, and at 2.5 cm and 5 cm below ground level, for a source with a strength of one gamma photon per unit area (γmm^{-2}). When determining isodose lines, it represents the total dose at the observation point i, $D_{i,\infty}$, in Equation 1 described in the Method section. It should be borne in mind that the isodose lines illustrate relative dose reduction and not the actual dose reduction.

Table 1. Primary dose factors before decontamination (pGy per γmm^{-2}) for the eleven observation points inside the wooden house and the brick house resulting from contamination at ground level, and 2.5 cm and 5 cm below ground level.

	Wooden house			Brick house		
	Contamination depth			Contamination depth		
Observation point	0 cm	2.5 cm	5 cm	0 cm	2.5 cm	5 cm
1	216	42.4	23.5	94.0	16.8	10.1
2	99.0	17.2	9.87	54.0	8.60	5.16
3	201	40.9	21.4	85.0	15.2	8.54
4	93.1	15.1	9.07	54.9	8.45	5.03
5	84.1	12.3	6.04	34.6	5.55	3.04
6	108	20.4	12.5	66.5	11.0	6.73
7	156	26.7	15.4	112	19.1	10.1
8	132	21.9	12.1	80.5	11.6	6.05
9	246	51.6	27.0	134	26.1	13.9
10	183	29.3	16.1	131	22.3	11.6
11	208	34.2	18.6	110	18.3	9.76

The values of the primary dose factors at the different observation points vary by up to a factor of five. Furthermore, the primary dose factors for contamination at ground level are about 5-6 times higher than the respective factors for contamination 2.5 cm below ground level, and those about 2 times higher than the corresponding factors for contamination 5 cm below ground level. Moreover, the primary dose factors inside the wooden house are about twice those in the brick house.

Isodose lines according to resident occupancy

The occupancy factors, p_i, as described in Equation 2 in the Method section were applied to determine isodose lines that are more representative of the dose to which a resident is exposed inside the house. The occupancy factors were chosen based the data published in the European EXPOLIS project[5,6,7]), in which thousands of people in seven European cities (Athens, Basel, Grenoble, Helsinki, Milan, Oxford, and Prague), were studied with respect to their time budgets, and the hours they spent in various microenvironments. From these data it was found that people spend about 14 h indoors at home, and about 1 of these 14 h preparing food in the kitchen. Further surveys show that people spend about 1 h eating[8] (i.e. in the dining room), about 8 h sleeping[9] (i.e. in the bedroom), and about 0.5 h in the bathroom[10], leaving about 3.5 h which it is assumed is spent in the living room. The resulting isodose lines taking into account the occupancy factors determined by the named occupancy times are presented graphically in Figure 7.

The isodose lines in Figure 7 show the combination of the influence of the time spend in one room (e.g. bedroom) and continuous influence of building materials (e.g. door and window in the kitchen). It can be seen that the isodose lines for a wooden house are gentler than those for a brick house, as timber provides less shielding, and therefore has less impact on the

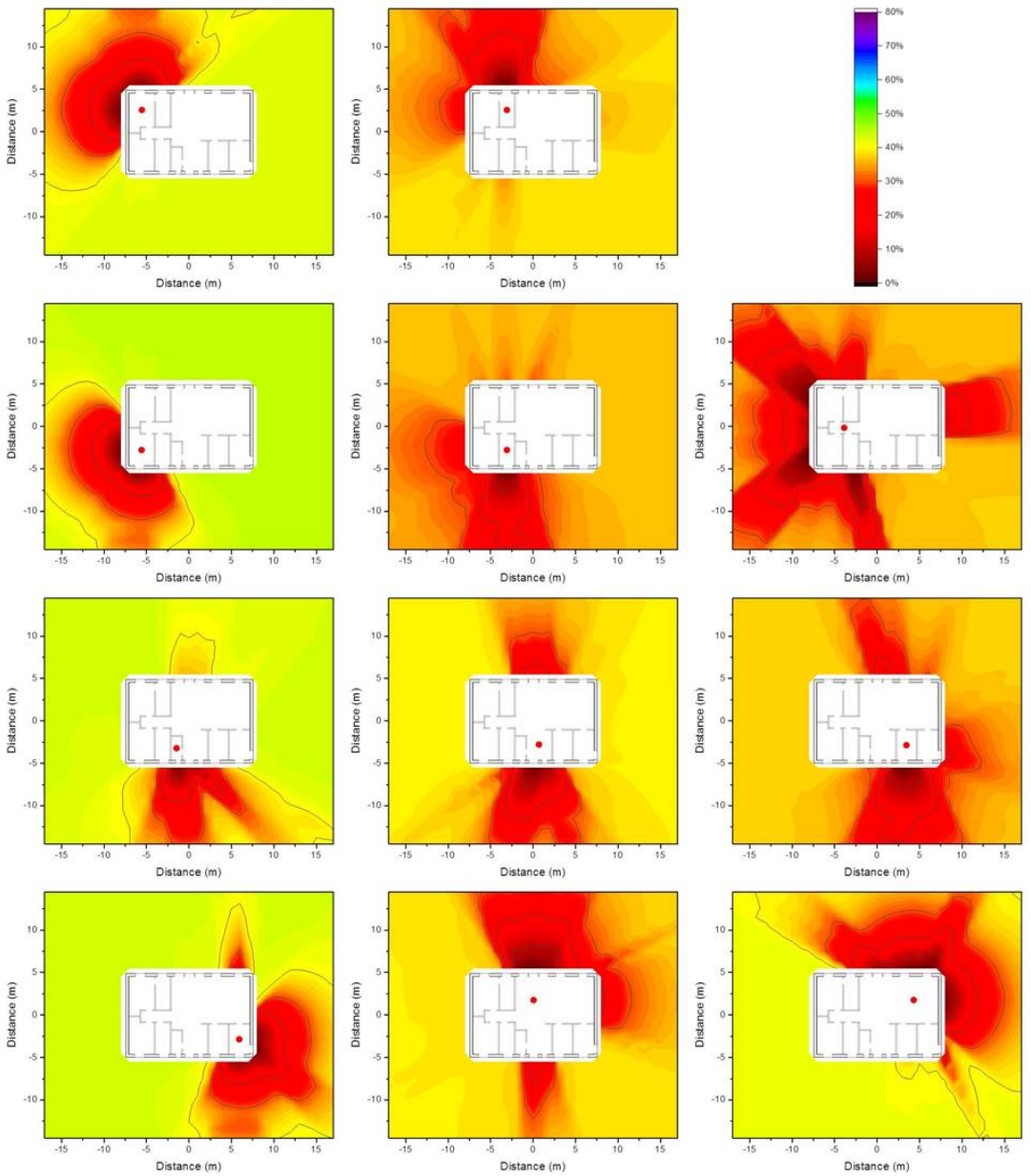

Figure 1. Isodose lines around the wooden house at the eleven observation points defined above (red dots) resulting from homogeneous ^{137}Cs contamination at ground level. The shading indicates the fraction of dose contribution to the observation point including the areas that are surrounded by the respective one. When the outside line for the isodose line of a certain relative dose reduction reaches the limit of the calculation grid, its shape may differ for a larger calculation grid.

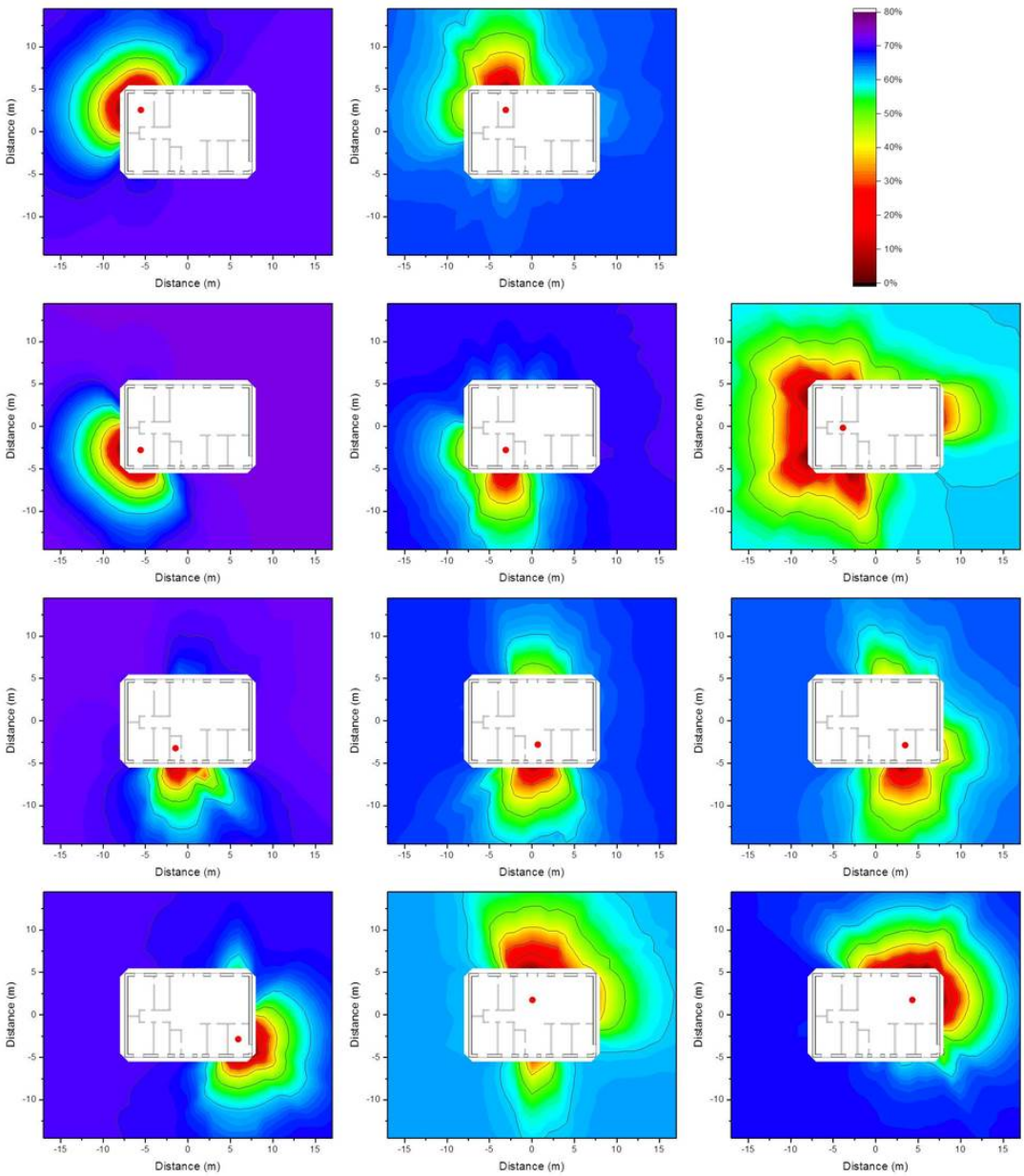

Figure 2. Isodose lines around the wooden house at the eleven observation points defined above (red dots) resulting from homogeneous ^{137}Cs contamination 2.5 cm below ground level. The shading indicates the fraction of dose contribution to the observation point including the areas that are surrounded by the respective one. When the outside line for the isodose line of a certain relative dose reduction reaches the limit of the calculation grid, its shape may differ for a larger calculation grid.

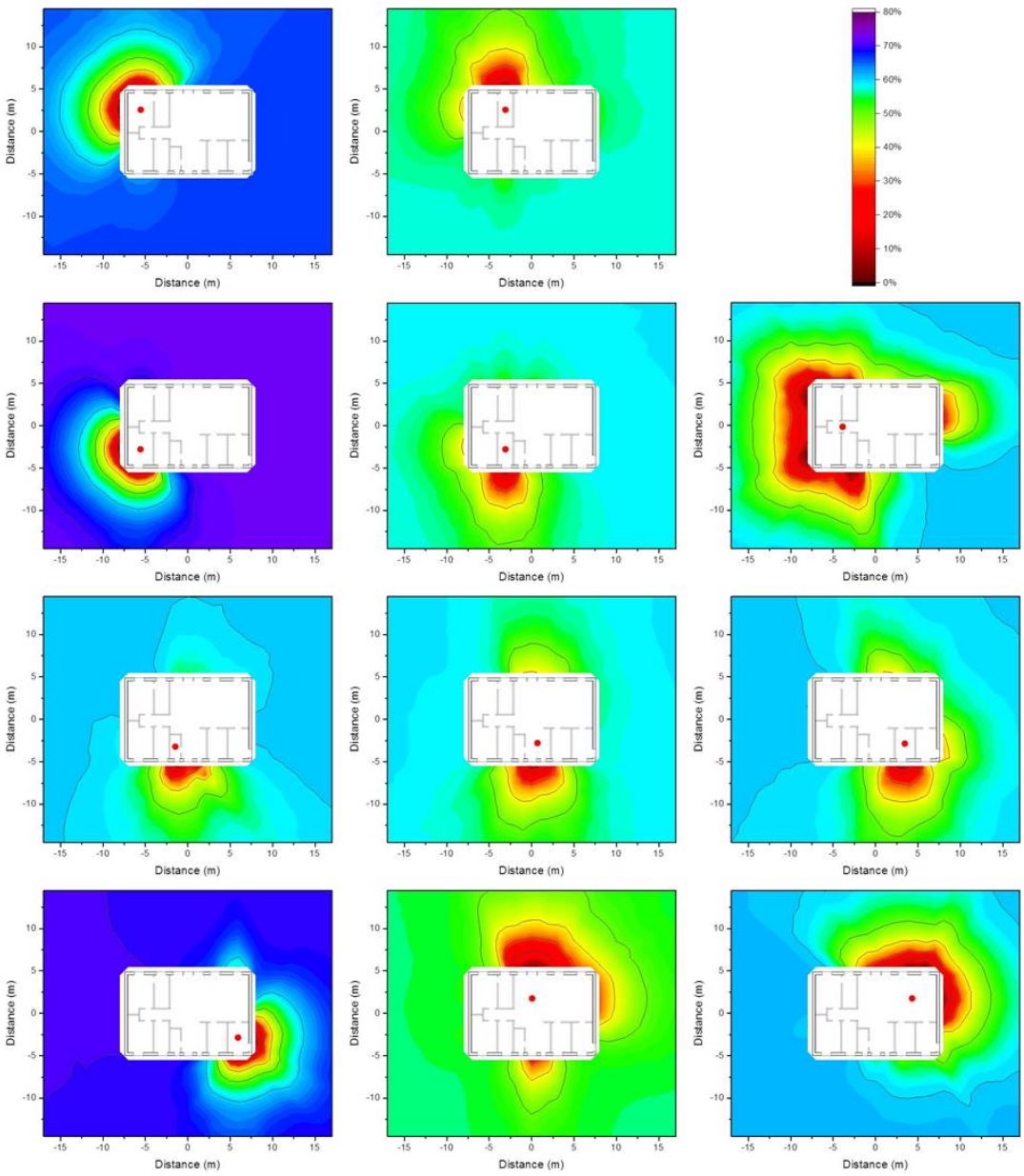

Figure 3. Isodose lines around the wooden house at the eleven observation points defined above (red dots) resulting from homogeneous ^{137}Cs contamination 5 cm below ground level. The shading indicates the fraction of dose contribution to the observation point including the areas that are surrounded by the respective one. When the outside line for the isodose line of a certain relative dose reduction reaches the limit of the calculation grid, its shape may differ for a larger calculation grid.

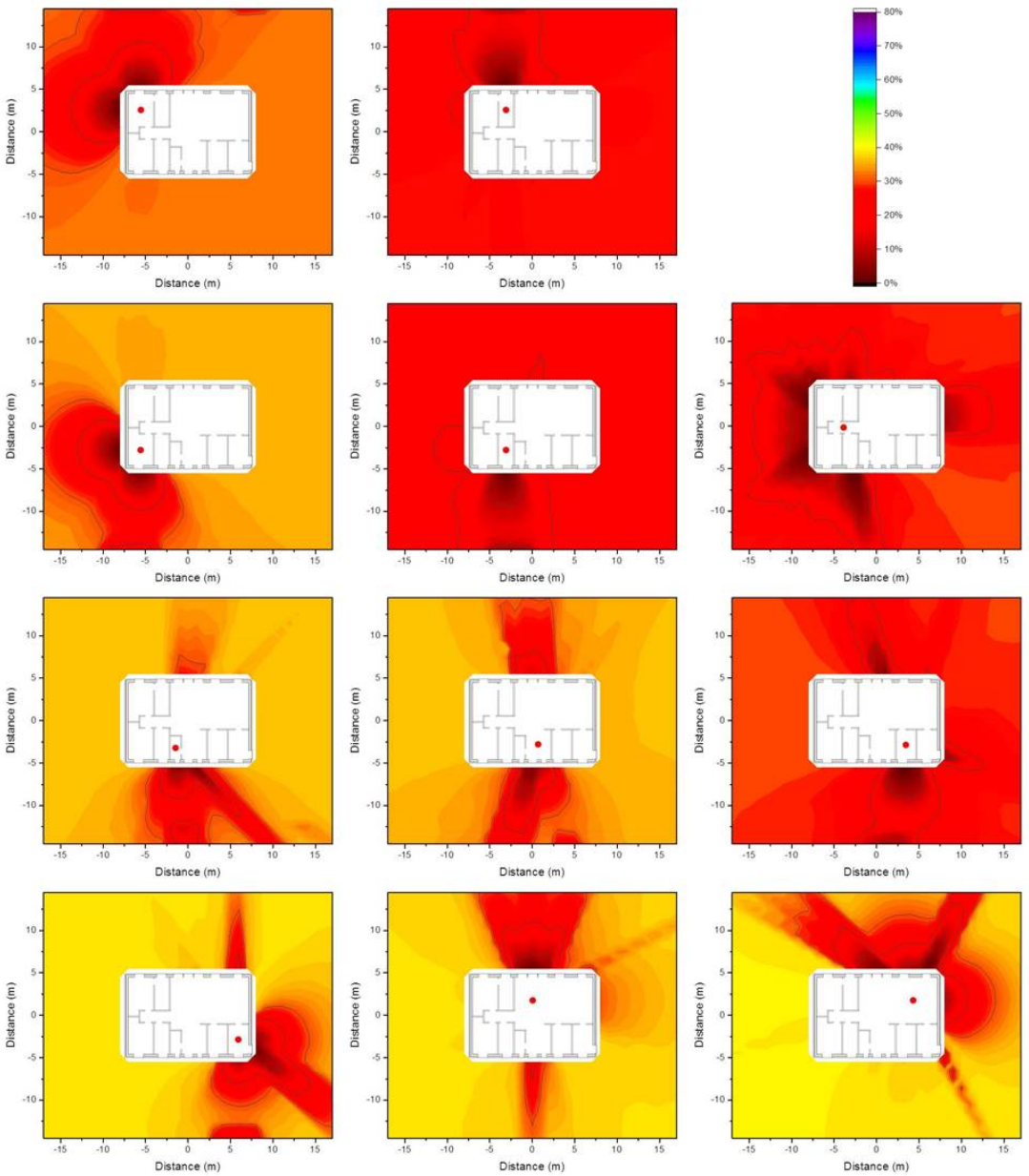

Figure 4. Isodose lines around the brick house at the eleven observation points defined above (red dots) resulting from homogeneous ^{137}Cs contamination at ground level. The shading indicates the fraction of dose contribution to the observation point including the areas that are surrounded by the respective one. When the outside line for the isodose line of a certain relative dose reduction reaches the limit of the calculation grid, its shape may differ for a larger calculation grid.

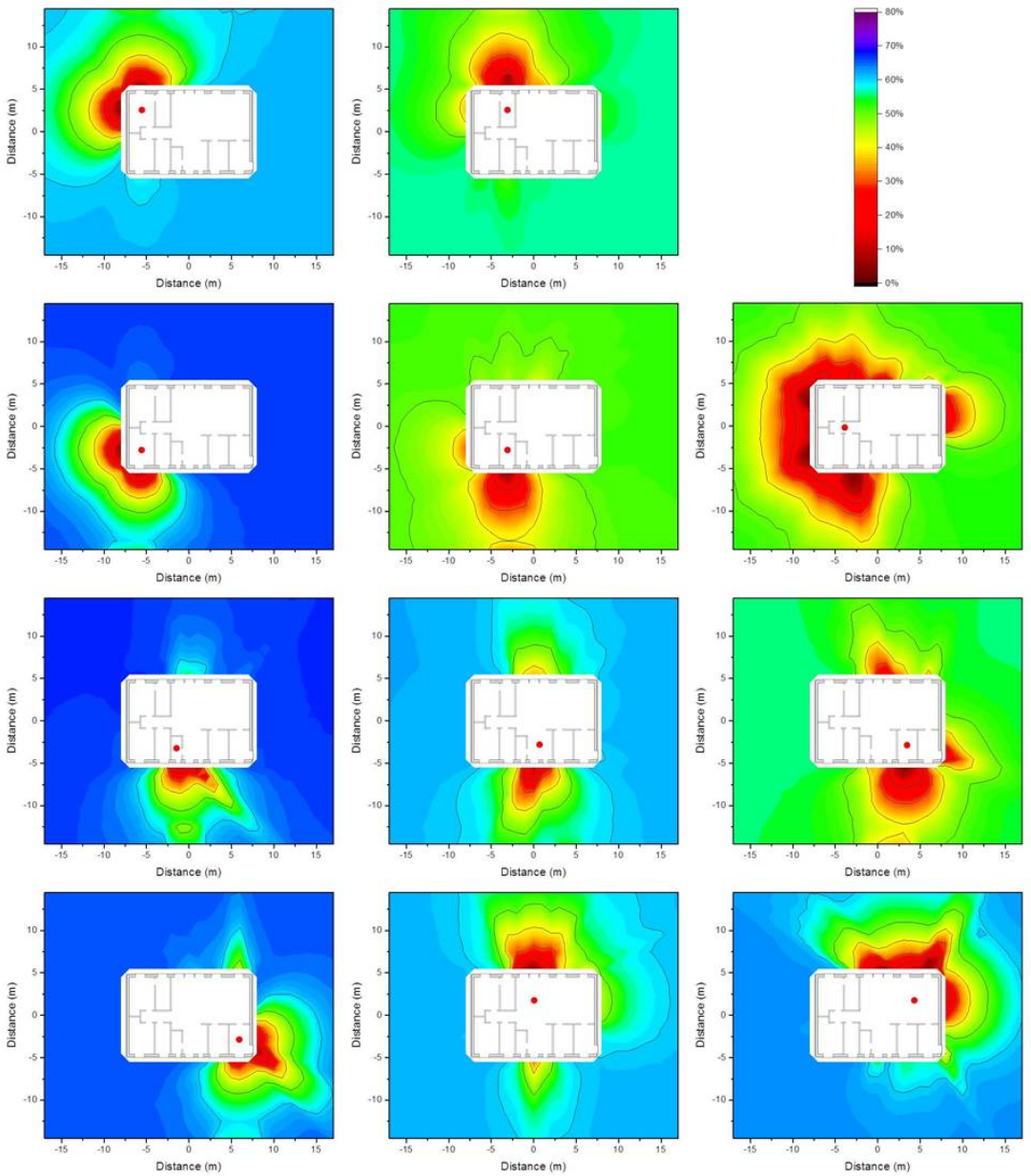

Figure 5. Isodose lines around the brick house at the eleven observation points defined above (red dots) resulting from homogeneous ^{137}Cs contamination 2.5 cm below ground level. The shading indicates the fraction of dose contribution to the observation point including the areas that are surrounded by the respective one. When the outside line for the isodose line of a certain relative dose reduction reaches the limit of the calculation grid, its shape may differ for a larger calculation grid.

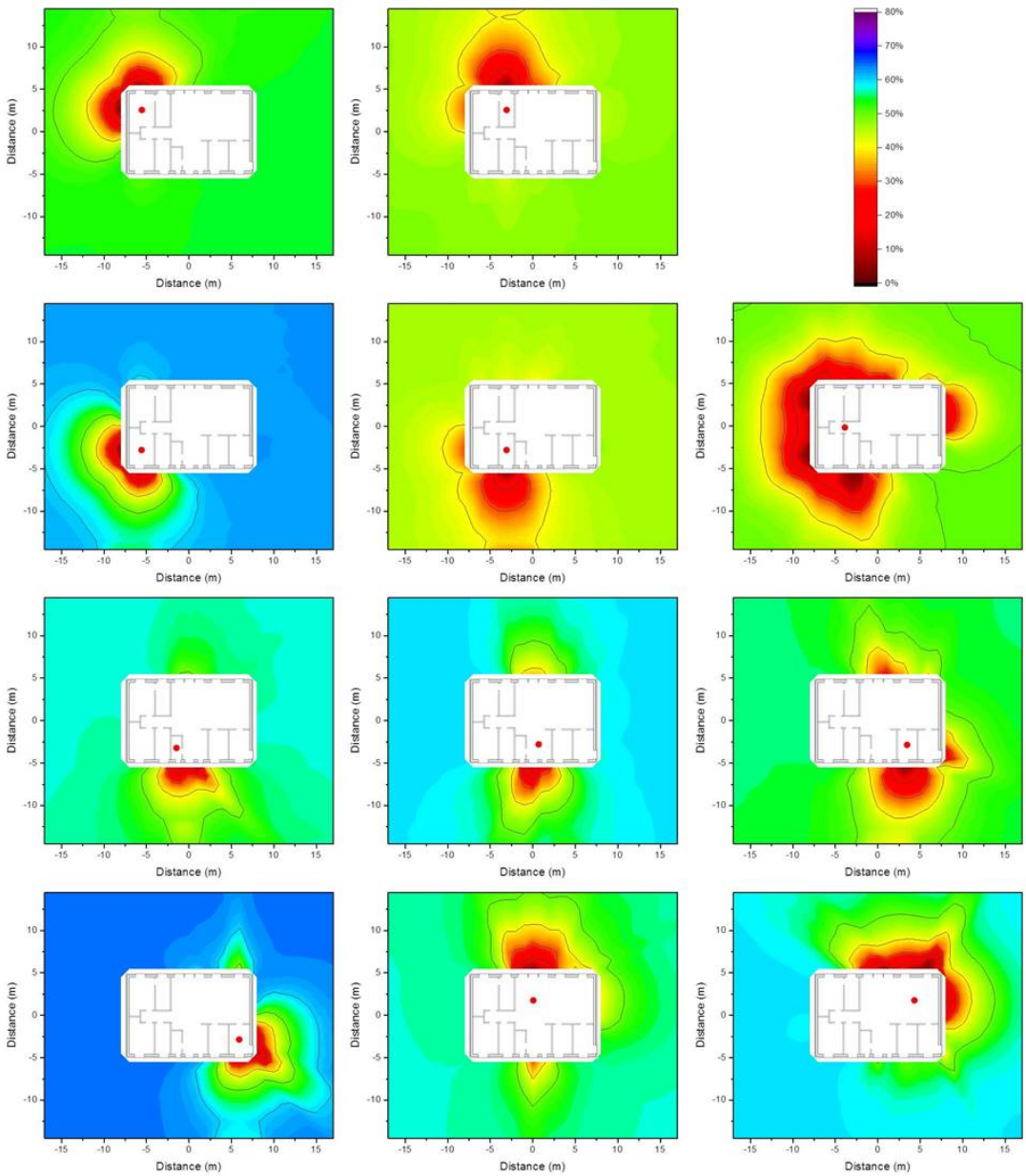

Figure 6. Isodose lines around the brick house at the eleven observation points defined above (red dots) resulting from homogeneous ^{137}Cs contamination 5 cm below ground level. The shading indicates the fraction of dose contribution to the observation point including the areas that are surrounded by the respective one. When the outside line for the isodose line of a certain relative dose reduction reaches the limit of the calculation grid, its shape may differ for a larger calculation grid.

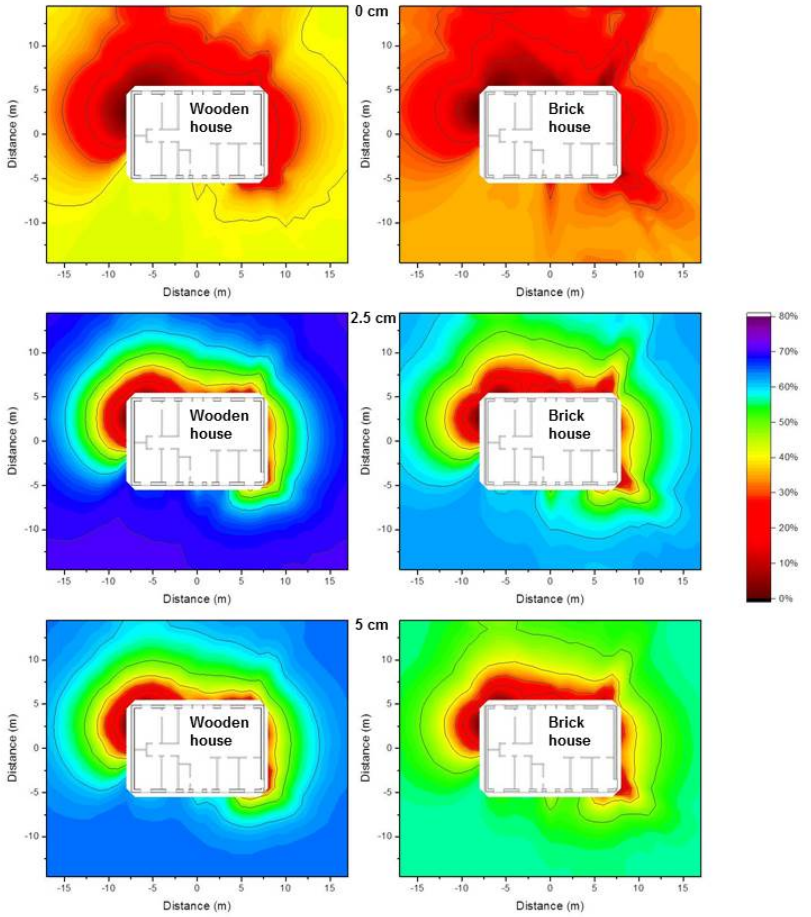

Figure 7. Isodose lines around the wooden house (left) and the brick house (right) using typical resident occupancy factors resulting from homogeneous ^{137}Cs contamination at ground level (top), 2.5 cm below (middle), and 5 cm below ground level (bottom). The shading indicates the fraction of dose contribution to the observation point including the areas that are surrounded by the respective one. When the outside line for a certain dose reduction reaches the limit of the calculation grid, its shape might differ for a larger calculation grid.

isodose lines. Furthermore, the corresponding zones for the brick house are larger than those for the wooden house. The size of the zone 2.5 cm below ground level is only half of that at ground level. However, at a depth of 5 cm the zones appear to increase slightly, as the contribution from areas far away becomes insignificant.

Impact of vertical migration of contaminants in the soil on the isodose lines

As contaminants migrate downwards in the ground over time, the impact of the depth of the contamination on the isodose lines is of interest. The most extreme combinations of the values of the effective dispersion coefficient D_s and the convective velocity v_s (Equation 3 in the Method section) determined for ^{137}Cs by Almgren and Isaksson[11] for sampling sites in western Sweden (D_s=0.06 cm^2 a^{-1}, v_s=0.17 cm a^{-1}and D_s=2.63 cm^2 a^{-1} and v_s=0.00 cm a^{-1}) were chosen. The contaminant distributions were calculated for the first 5 cm of soil for times of 0.1 a, 1 a, and 5 a after deposition and multiplied by the air kerma free-in-air values interpolated from the calculations at ground level, and depths of 2.5 cm and 5 cm. The results are presented graphically as isodose lines for the wooden house in Figure 8 and for the brick house in Figure 9.

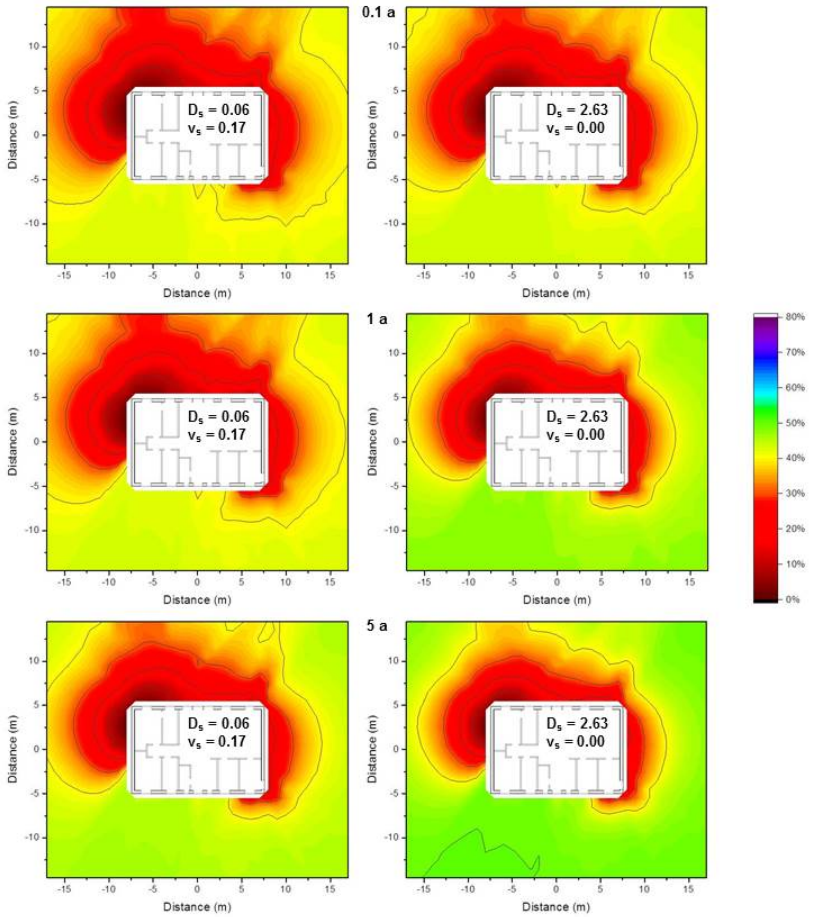

Figure 8. Isodose lines around the wooden house using typical resident occupancy factors resulting from homogeneous ^{137}Cs contamination for a vertical distribution, 0.1 years (top), 1 year (middle), and 5 years after deposition (bottom), based on the two most extreme parameter combinations determined for western Sweden[11]. The shading indicates the fraction of dose contribution at the observation point including the areas that are surrounded by the respective one. When the outside line for a certain dose reduction reaches the limit of the calculation grid, its shape might differ for a larger calculation grid.

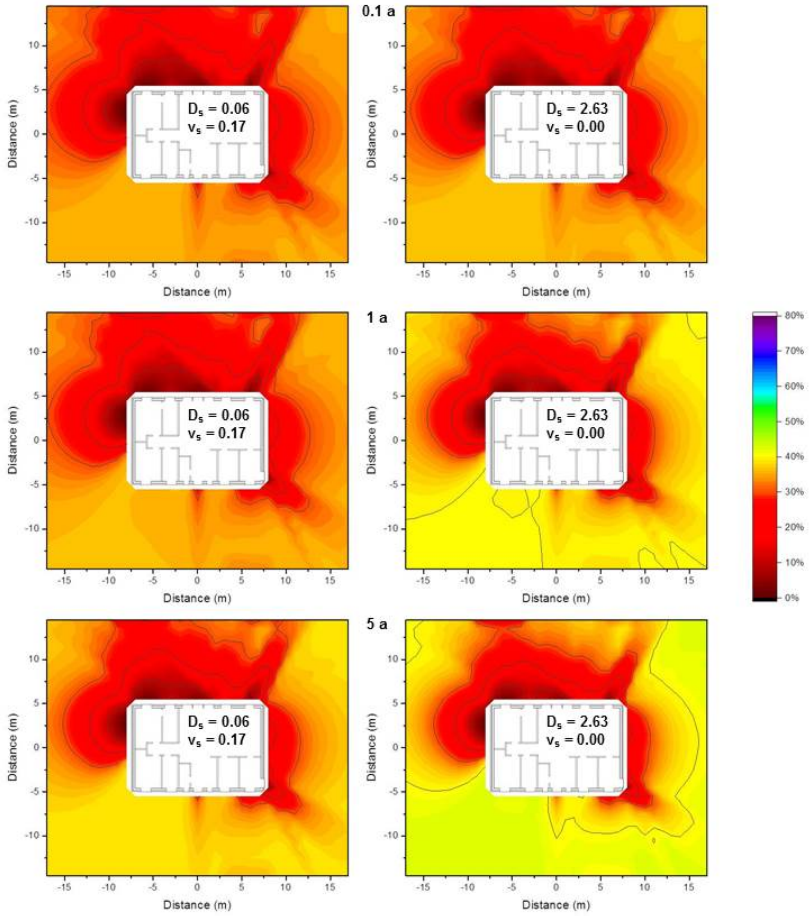

Figure 9. Isodose lines around the brick house using typical resident occupancy factors resulting from homogeneous ^{137}Cs contamination for a vertical distribution, 0.1 years (top), 1 year (middle), and 5 years after deposition (bottom), based on the two most extreme parameter combinations determined for western Sweden[11]. The shading indicates the fraction of dose contribution at the observation point including the areas that are surrounded by the respective one. When the outside line for a certain dose reduction reaches the limit of the calculation grid, its shape might differ for a larger calculation grid.

From Figures 8 and 9 it can be seen that the differences in the isodose lines for the wooden and brick houses are similar to those observed in the Figure 7. It can also be seen that for these parameter combinations the isodose lines are similar on the short timescale of 0.1 a. Over longer timescales the respective zones become smaller as the contaminants migrate deeper into the soil. This effect is stronger for the parameter combination of D_s=2.63 cm^2 a^{-1} and v_s=0.00 cm a^{-1} than for D_s=0.06 cm^2 a^{-1}, v_s=0.17 cm a^{-1}. Moreover, it can be seen that the upper layer of soil dominates as it contributes more to the air kerma free-in-air than the lower soil layer of soil, as indicated by the primary dose factors presented in Table 1.

In the comparison of the wooden and the brick house similar differences can be seen as described before. The parameter combination shows that the isodose lines are similar for a short timescale like 0.1 a. Over longer timescales the respective zones become smaller as the contaminants migrate to deeper soil level. This effect is stronger for the parameter combination D_s=2.63 cm^2 a^{-1} and v_s=0.00 cm a^{-1} than for D_s=0.06 cm^2 a^{-1}, v_s=0.17 cm a^{-1}. Moreover, the dominance of the top soil layer can be seen as it contributes more to the air kerma free-in-air than the lower soil level as shown for the primary dose factor presented in 1.

Impact of contamination variability on the isodose lines

The model for contamination variability is based on measurements of ^{137}Cs fallout in settlements in Russia and Belarus following the Chernobyl nuclear power plant accident[12], where dose rate levels represented by ^{137}Cs peak gamma signals ranging from 0 till 5 kcps were measured 0.1 m above a 9 m x 9 m open, untouched grass surface. A random number generator picking values from 0 till 5 was applied to the 1 m x 1 m grid that was used for the Monte Carlo calculations described in the Method section with the restriction that the values in all neighboring fields on a horizontal or vertical line are allowed to differ by at most ± 1, and on a diagonal line by at most ± 1.4. These values were applied as dimensionless scaling factors by multiplication of the Monte Carlo calculated air kerma free-in-air values for the respective fields that were determined for contamination at ground level (as this dominates the radiation dose to residents), for the wooden and the brick house. The primary dose factors were determined by subtracting the one for homogeneous contamination by the sum of the air kerma free-in-air values determined without the scaling factor, then multiplied by the average of the randomly generated multiplication factors and finally the sum of determined air kerma free-in-air values with multiplication factor was added. This was done for three different contamination variability scenarios obtained with the random number generator (Figure 10). The resulting isodose lines are presented graphically in for the wooden house in Figure 11 and for the brick house in Figure 12.

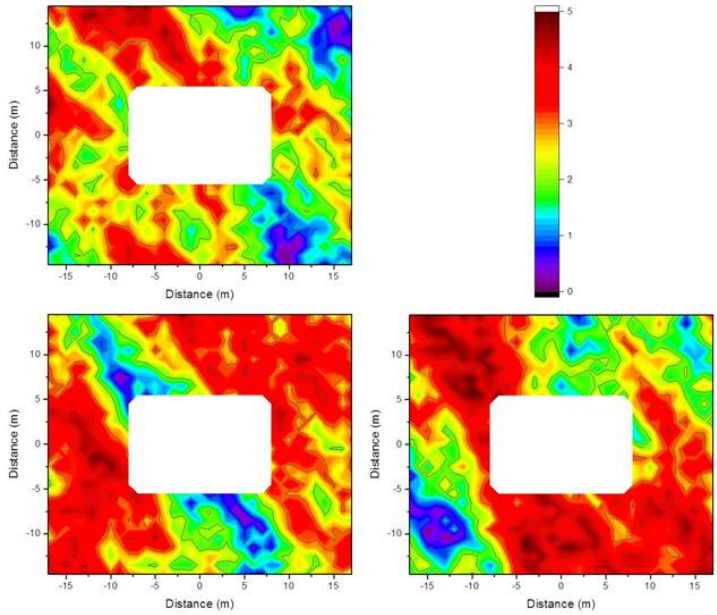

Figure 10. Three different variations in ^{137}Cs contamination obtained using a random number generator.

Comparing the isodose lines for the three contamination variability scenarios with those determined for homogeneous contamination (First line in Figure 7) shows that the original shape is still visible. However, as the shielding of the wooden house is lower, the effect of contamination variability on the isodose lines is greater than in the case of the brick house. This is supported by the values of the Pearson correlation coefficient, being 0.96, 0.93, and 0.95 for the wooden house and 0.96, 0.94, and 0.95 for the brick house, for the three different contamination variability scenarios.

To investigate the impact of contamination variability on the zones determined by isodose lines for homogeneous contamination in more detail, the dose factors were calculated after decontamination of an area up to 2 m from the houses (116 m^2), as well as the respective dose factor after decontamination of 116 m^2 according to the isodose lines that were determined for homogeneous contamination. The values obtained are given in Table 2 for both types of houses. The primary dose factors, the relative dose reduction, and the ratio comparing the relative dose reductions for optimized decontamination according to isodose lines and for normal decontamination within 2 m from the houses are also included in Table 2.

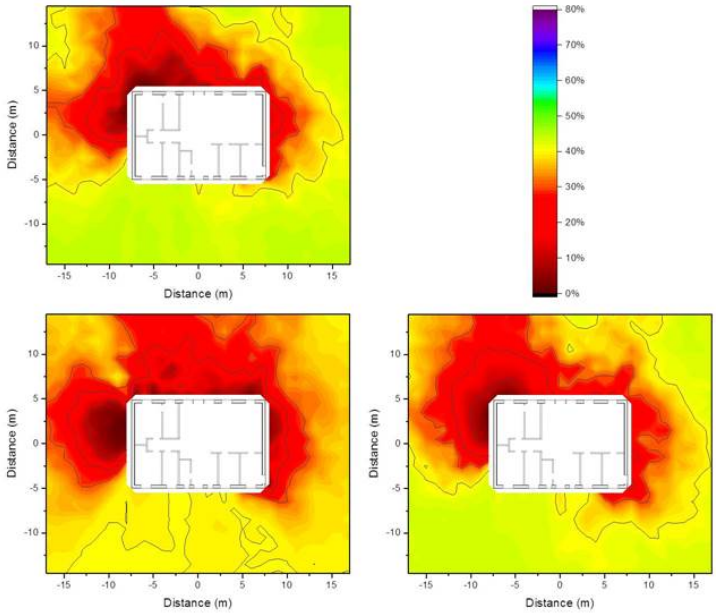

Figure 11. Isodose lines around the wooden house using typical resident occupancy factors for three different variability scenarios of ^{137}Cs contamination, according to Figure 10. The shading indicates the fraction of dose contribution to the observation point including the areas that are surrounded by the respective one. When the outside line for a certain dose reduction reaches the limit of the calculation grid, its shape might differ for a larger calculation grid.

The values in Table 2 show that the relative dose reduction following optimized decontamination is on average 51±8 % higher than that after normal decontamination for a fixed area of 116 m^2 to the same distance around the house being decontaminated. This leads to the conclusion that in an authentic fallout scenario where the contamination varies, the decontamination of areas determined with isodose lines for homogeneous contamination is still a better option than decontaminating within a certain distance surrounding a building.

Discussion

This study demonstrates the influence of the two most common building materials in Sweden, wood and brick, on the shape of the isodose lines, as well as the influence of the positions of doors and windows on the isodose lines. Including factors describing typical resident occupancy in the various rooms of the houses shows the mixture of the influence of the time spent in a specific room of the house and the continuous influence of building materials as well as positions of doors and windows. In addition, including a model for the vertical migration of contaminants in soil revealed the effects of different source depths in the soil on the decrease rate of the zones that are encompassed by the isodose lines, as well as the dominance of the contamination in the upper layer of the soil on the final isodose lines. Finally, the impact of variability in the contamination on the final result was demonstrated, and its dependence on building materials. It was shown that optimized decontamination according to isodose lines determined for homogeneous contamination is also a better choice than normal decontamination within a certain radius of the house.

In conclusion, it has now been demonstrated that the isodose concept presented in a previous study is useful for the comparison of the effects of decontaminating different surface areas, for houses constructed with different types of building materials. Downward migration of contaminants in the soil, resident occupancy, and variability in contamination were also included in the model. Further studies are required to further develop this method into a practical and useful tool for the optimization of countermeasures in cases of radioactive fallout in populated environments.

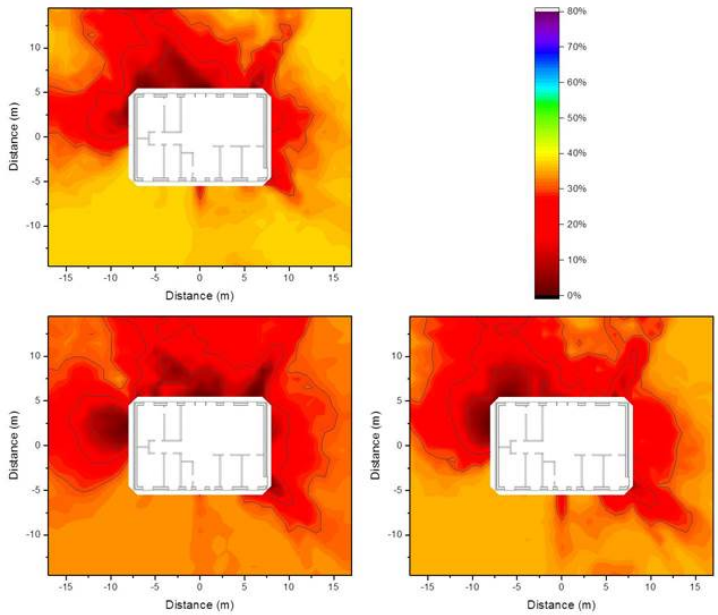

Figure 12. Isodose lines around the brick house using typical resident occupancy factors for three different variability scenarios of ^{137}Cs contamination, according to Figure 10. The shading indicates the fraction of dose contribution to the observation point including the areas that are surrounded by the respective one. When the outside line for a certain dose reduction reaches the limit of the calculation grid, its shape might differ for a larger calculation grid.

Methods

The isodose concept

The concept of the isodose was recently introduced by Hinrichsen et al.[4], where the isodose, $ID_{i,k}$, is defined by the outer boundary of one or more zones in space that contribute, for the most part, a given fraction k to the total dose $D_{i,\infty}$ at the observation point i. If $\rho_{D,i}(\vec{r})$ is a continuous function of the dose contribution density with the maximum $\rho_{D,i,max} < \infty$, the isodose can be chosen from the range $0 < ID_{i,k} < \rho_{D,i,max}$ and the fraction k_i resulting from the zone or zones determined by the isodose is given by:

$$k_i = \int f(\rho_{D,i}(\vec{r}))dV/D_{i,\infty} \quad FOR \quad f(\rho_{D,i}(\vec{r})) = \begin{cases} \rho_{D,i}(\vec{r}), & \rho_{D,i}(\vec{r}) \geq ID_{i,k} \\ 0, & \rho_{D,i}(\vec{r}) < ID_{i,k} \end{cases} \tag{1}$$

The concept can also be applied to more than one observation point[4] by introducing so-called occupancy factors, p_i, for the various observation points into Equation 1 leading to:

$$k = \int f(\rho_D(\vec{r}))dV/\sum_i D_{i,\infty} \cdot p_i \quad \forall \quad 1 = \sum_i p_i \quad FOR \quad f(\rho_D(\vec{r})) = \begin{cases} \sum_i \rho_{D,i}(\vec{r}) \cdot p_i, & \sum_i \rho_{D,i}(\vec{r}) \cdot p_i \geq ID_k \\ 0, & \sum_i \rho_{D,i}(\vec{r}) \cdot p_i < ID_k \end{cases} \tag{2}$$

Vertical migration of contaminants in soil

The vertical transport of radioactive contaminants in soil can be described as a function of time and vertical soil depth by a convection–dispersion model, as suggested by Schuller et al.[13], Bunzl et al.[14], and Kirchner et al.[15]:

$$C(x,t) = C_0 \exp(-\ln(2) \cdot t/T_{1/2}) \cdot \left(\frac{1}{\sqrt{\pi D_s t}} \cdot \exp\left(-\frac{(x - v_s t)^2}{4 D_s t}\right) - \frac{v_s}{2D_s} \cdot \exp\left(\frac{v_s}{D_s} x\right) \cdot erfc\left(\frac{x + v_s}{2\sqrt{D_s t}}\right)\right) \tag{3}$$

Table 2. Primary dose factors before decontamination (pGy per γmm^{-2}) for homogeneous ^{137}Cs contamination and three variability scenarios at ground level, using typical resident occupancy factors in the wooden and the brick house, together with the dose factors obtained after normal decontaminating an area of 116 m^2 directly around the houses, or optimized decontamination of the same area but according to the isodose lines presented in the first line of Figure 7, including relative dose reductions, and ratio of the relative dose reductions.

	Primary dose factor	After normal decontamination		After optimized decontamination		Ratio of the relative dose reductions
		Dose factor	Relative dose reduction	Dose factor	Relative dose reduction	
Wooden house:						
Homogeneous contamination	209	177	15.5 %	165	21.2 %	1.37
Variability scenario 1	217	184 6	15.3 %	167	23.0 %	1.50
Variability scenario 2	202	178	12.1 %	168	17.1 %	1.42
Variability scenario 3	213	178	16.3 %	165	22.8 %	1.39
Brick house:						
Homogeneous contamination	102	90	12.3 %	84	18.4 %	1.47
Variability scenario 1	106	93	12.5 %	85	20.3 %	1.62
Variability scenario 2	100	90	9.6 %	85	15.2 %	1.55
Variability scenario 3	103	90	12.1 %	84	18.4 %	1.50

where C_0 is the initial contaminant concentration (Bq cm^{-3}), $T_{1/2}$ is the physical half-life (a), D_s is the effective dispersion coefficient (cm^2 a^{-1}), and v_s is the convective velocity (cm a^{-1}).

Description of the calculations

Monte Carlo calculations were performed using the transport code MCNP6[16], and the nuclear cross-section data set ENDF/B-VII.0[17]. Among other processes, this code accounts for photon creation and loss through relevant mechanisms such as bremsstrahlung, fluorescence, Compton scattering, photon capture, pair production and p-annihilation. The code allows for the definition of complex 3-dimensional geometries through a combinatorial geometry technique. The applicability of MCNP6 in determining the reduction in exposure due to shielding inside a building has been experimentally verified in a previous study on a modular building[18].

Two typical Swedish houses were considered, constructed with the most common building materials in Sweden, namely wood and brick. The definition of the geometries of the houses, which had similar designs, are based on the construction drawings and descriptions of actual Swedish houses made available by the Urban Planning Department of the Municipality of Hässleholm (Stadsbyggnadskontoret, Hässleholms kommun) (Figure 13). The houses cover an area of 10 m x 15 m, and the building materials and dimensions are given in 3. The protection of wooden frames was assumed to be negligible and thus they are not included in the calculations. The windows and exterior doors comprise an area of 25.3 m^2 of the total vertical area.

The regions in space were constructed by logical combinations (union, intersection, difference) of elementary geometric bodies and surfaces. Data from a material compendium[19] were used to assign atomic compositions and densities to the materials, as summarized in Table 4. These were used as the input for the different building structures and environmental regions.

A radioactive source energy of 0.662 MeV was assumed in the calculations as this is the energy of the gamma-rays emitted

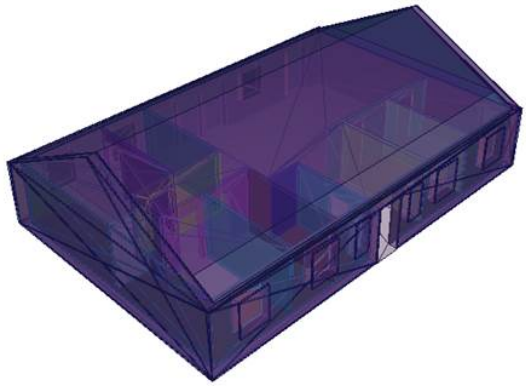

Figure 13. Birds-eye view of a typical Swedish house.

Table 3. Construction materials and dimensions for typical Swedish wooden and brick houses.

	Wooden house	Brick house
External walls	2.2 cm wood, 4 cm air, 0.9 cm gypsum, 26 cm mineral wool, 2.8 cm air, 1.1 cm wood, 1.3 cm gypsum	12 cm brick, 4 cm air, 0.9 cm gypsum, 23 cm mineral wool, 1.3 cm gypsum
Inner walls	12 cm or 17 cm gypsum	
Roof	5.4 cm concrete, 2.7 cm wood	5.4 cm concrete, 3.5 cm wood
Ceiling	1.3 cm gypsum, 2.8 cm air, 40 cm mineral wool	
Windows and doors	0.8 cm glass	

by ^{137}Cs, which is the radionuclide of greatest concern in connection with the Chernobyl and Fukushima nuclear power plant accidents. Source regions were defined as 1 m x 1 m plane squares in a 1 m x 1 m grid up to a lateral distance of 10 m from the sides of the houses, at ground level, and 2.5 cm and 5 cm below ground level. Separate Monte Carlo computations were performed to obtain reference values for an infinite horizontal plane source at ground level, and 2.5 cm and 5 cm below ground level.

The detector regions were defined as air-filled spheres with a diameter of 30 cm, positioned 1 m above ground level, at the observation points defined in different parts of the house (Figure 14). Observation point # 1 represents a bedroom, # 2 the bathroom, # 3 a second bedroom (for example, for a child or guests), # 4 a dressing room , # 5 the corridor, # 6 a restroom , # 7 the hall, # 8 a study, # 9 the kitchen, # 10 the living room, and # 11 the dining room. The number and energies of the gamma 'particles' passing through these detector were determined with the Monte Carlo code. The fluence was transformed into air kerma free-in-air using conversion coefficients[20].

A number of variation reduction techniques can be applied to MCNP6 to obtain results with a standard deviation below 5 % within acceptable computation times. The defined regions in space are called cells, and a 'weight window' was generated for each of them in the following way. The weight of a particle in MCNP6 represents the number of physical 'particles', which in these calculations are photons with different random walks , represented by one MCNP particle. A lower limit on the weight is supplied by the user for each cell, and the upper limit is a specified multiple of the lower limit. These upper and lower weight limits define a window of acceptable weights. If the weight of the particle emitted from the source and generated by interactions with the materials is below the lower weight limit, then "Russian roulette" is applied and the particle's weight is randomly increased to a value within the window, or the particle is terminated. If the weight of the particle is above the upper weight limit, it is divided so that its parts are within the window. No action is taken for particles within the window. The weight windows were determined using the Weight Window Generator included in MCNP6, which estimates the importance of the cells in the space. The importance of cells is defined as the expected score generated by a particle of unit weight after entering the cell. The average importance of the cells can thus be estimated using this cell-based generator.

Table 4. Material specifications in terms of atomic compositions (rounded) and densities used in the Monte Carlo calculations.

Material	Atomic composition	Density (kg/l)
Air	0.02 % C; 78.44 % N; 21.07 % O; 0.47 % Ar	0.001205
Brick	66.34 % O; 0.37 % Al; 32.32 % Si; 0.71 % Ca; 0.25 % Fe	1.8
Concrete	8.47 % H; 60.41 % O; 1.25 % Na; 2.48 % Al; 24.19 % Si; 2.72 % Ca; 0.47 % Fe	2.25
Glass	60.39 % O; 8.81 % Na; 25.18 % Si; 5.62 % Ca	2.4
Gypsum	33.33 % H; 50.00 % O; 8.33 % S; 8.33 % Ca	2.32
Mineral wool	42.50 % O; 1.70 % Na; 5.40 % Mg; 10.60 % Al; 18.20 % Si; 1.90 % K; 14.30 % Ca; 0.50 % Mn; 4.90 % Fe	0.1666667
Soil	31.69 % H; 50.16 % O; 4.00 % Al; 14.16 % Si	1.52
Wood	46.24 % H; 32.34 % C; 0.28 % N; 20.88 % O; 0.06 % Mg; 0.12 % S; 0.04 % K; 0.04 % Ca	0.64

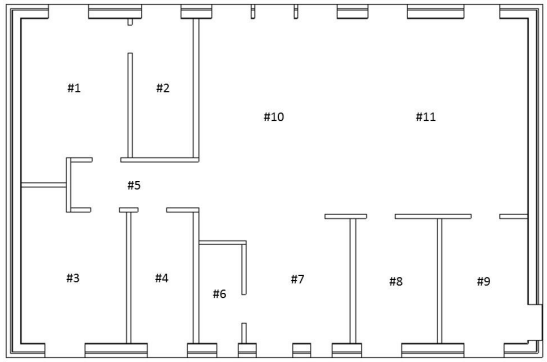

Figure 14. Observation points inside a typical Swedish house. # 1 indicates a bedroom, # 2 the bathroom, # 3 a second bedroom (for example, for a child or guests), # 4 a dressing room , # 5 the corridor, # 6 a restroom , # 7 the hall, # 8 a study, # 9 the kitchen, # 10 the living room, and # 11 the dining room.

References

1. Golikov, V. Y., Balonov, M. I., Jacob, P., 2002. External exposure of the population living in areas of Russia contaminated due to the Chernobyl accident. Radiation and Environmental Biophysics 41, 185-193.

2. Andersson, K. G., 2009. Chapter 8 countermeasures for reduction of dose in contaminated inhabited areas. In: Andersson, K. G. (Ed.), Airborne Radioactive Contamination in Inhabited Areas. Vol. 15 of Radioactivity in the Environment. Elsevier, 217 – 258.

3. Roed, J., Andersson, K. G., Barkovsky, A., Fogh, C., Mishine, A., Ponamarjov, A., Ramzaev, V., 2006. Reduction of external dose in a wet-contaminated housing area in the Bryansk region, Russia. Journal of Environmental Radioactivity 85 (2-3), 265–279.

4. Hinrichsen, Y., Finck, R., Rääf, C., Andersson, K. G., 2018a. Introducing the concept of the isodose for optimisation of decontamination activities in a radioactive fallout scenario. J. Radiol. Prot. 38, 1293-1310.

5. Jantunen, M. J., O. Hanninen, Katsouyanni, K., Knoppel, H., Kuenzli, N., Lebret, E., Maroni, M., Saarela, K., Sram, R., Zmirou, D, 1998. Air pollution exposure in European cities: The "EXPOLIS" study. Journal of Exposure Analysis and Environmental Epidemiology 8(4), 495-518.

6. Rotko, T., L. Oglesby, Kunzli, N., Jantunen, M. J., 2000. Population sampling in European air pollution exposure study, EXPOLIS: comparisons between the cities and representativeness of the samples. Journal of Exposure Analysis and Environmental Epidemiology 10(4), 355-364.

7. Schweizer, C. ,2004. EXPOLIS annex (Final report of WP1 of the EXPOLIS study funded by CEFIC)

8. USDA, 2018. United States Department of Agriculture, How much time do Americans spend eating?, https://www.thefreelibrary.com/How+much+time+do+Americans+spend+eating%3f-a0190462486 /

9. OECD, 2018. OECD database, The Organisation for Economic Co-operation and Development (OECD), http://www.oecd.org/els/family/database.htm

10. The Scotsman, 2008. How long do we spend in bathroom? Published Friday 4 January 2008, https://www.scotsman.com/news/how-long-do-we-spend-in-bathroom-1-189-years-1-1072528.

11. Almgren, S., Isaksson, M., 2006. Vertical migration studies of ^{137}Cs from nuclear weapons fallout and the Chernobyl accident, J. Environ. Radioactivity 91, 90-102.

12. Bernhardsson, C., Rääf, C. L., Mattsson, S., 2015. Spatial variability of the dose rate from 137Cs fallout in settlements in Russia and Belarus more than two decades after the Chernobyl accident, J. Environ. Radioactivity 149, 144-149.

13. Schuller, P., Ellies, A., Kirchner, G., 1997. Vertical migration of fallout 137Cs in agricultural soils from Southern Chile, The Science of the Total Environment 193, 197-205.

14. Bunzl, K., Schimmack, W., Zelles, L., Albers, B.P., 2000. Spatial variability of the vertical migration of fallout 137Cs in the soil of a pasture, and consequences for long-term predictions, Radiat. Environ. Biophys. 39, 197-205.

15. Kirchner, G. Strebl, F., Bossew, P., Ehlken, S., Gerzabek, M.H., 2009. Vertical migration of radionuclides in undisturbed grassland soils, J. Environ. Radioactivity 100, 716-720.

16. Goorley, T., James, M., Booth, T., Brown, F., Bull, J., Cox, L. J., Durkee, J., Elson, J., Fensin, M., Forster, R. A., Hendricks, J., Hughes, H. G., Johns, R., Kiedrowski, B., Martz, R., Mashnik, S., McKinney, G., Pelowitz, D., Prael, R., Sweezy, J., Waters, L., Wilcox, T., Zukaitis, T., 2012. Initial MCNP6 release overview. Nuclear Technology 180 (3), 298–315.

17. Chadwick, M., Obložinský, P., Herman, M., Greene, N., McKnight, R., Smith, D., Young, P., MacFarlane, R., Hale, G., Frankle, S., Kahler, A., Kawano, T., Little, R., Madland, D., Moller, P., Mosteller, R., Page, P., Talou, P., Trellue, H., White, M., Wilson, W., Arcilla, R., Dunford, C., Mughabghab, S., Pritychenko, B., Rochman, D., Sonzogni, A., Lubitz, C., Trumbull, T., Weinman, J., Brown, D., Cullen, D., Heinrichs, D., McNabb, D., Derrien, H., Dunn, M., Larson, N., Leal, L., Carlson, A., Block, R., Briggs, J., Cheng, E., Huria, H., Zerkle, M., Kozier, K., Courcelle, A., Pronyaev, V., van der Marck, S., 2006. ENDF/B-VII.0: Next generation evaluated nuclear data library for nuclear science and technology. Nuclear Data Sheets 107 (12), 2931 – 3060, evaluated Nuclear Data File ENDF/B-VII.0.

18. Hinrichsen, Y., Finck, R., Östlund, K., Rääf, C., Andersson, K. G., 2018b. Comparison of experimental and calculated shielding factors for modular buildings in a radioactive fallout scenario. J. Environ. Radioactivity 189, 146 – 155.

19. McConn Jr, R., Gesh, C., Pagh, R., Rucker, R., Williams III, R., 2011. Radiation portal monitor project - Compendium of material composition data for radiation transport modeling. Pacific northwest national laboratory.

20. ICRP, 2010. Conversion coefficients for radiological protection quantities for external radiation exposures. Annals of the ICRP 40 (2), 1 – 257, ICRP Publication 116.

Acknowledgements

This study was supported by the Swedish Civil Contingencies Agency and the Municipality of Hässleholm (Stadsbyggnadskontoret, Hässleholms kommun).

Author contributions statement

Y.H. conceived the study, designed and performed the simulations, and analyzed the results. R.F., J.M., C.R. and K.G.A. gave advise on the applied methods. Y.H. wrote the paper with input from all authors. All authors reviewed the manuscript.

Additional information

Competing interests

The authors declare no competing interests.

Data availability statement

The datasets generated during and analyzed during the current study are available from the corresponding author on reasonable request.